ILLINOIS CENTER FOR TRANSPORTATION

Report No. FHWA-ICT-25-003

Impact of Heavy Commercial Electric Vehicles on Flexible Pavements

Angeli Jayme
Jaime Hernandez
Imad L. Al-Qadi
Johann J. Cardenas
Murryam Hafeez
William Villamil

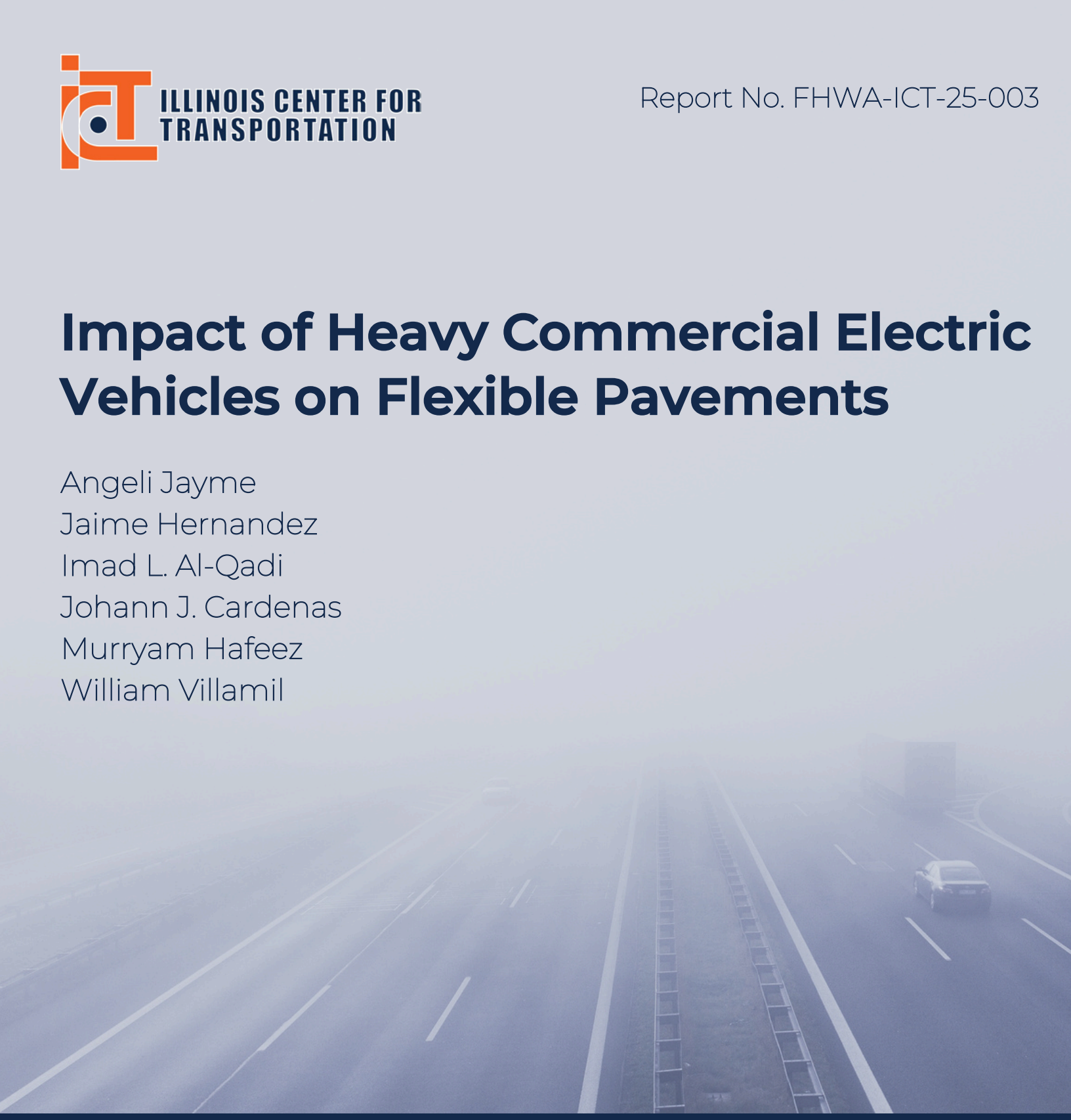

ICT Project R27-252

May 2025

ISSN: 0197-9191
ICT Series Report No. 25-003
https://doi.org/10.36501/0197-9191/25-003

TECHNICAL REPORT DOCUMENTATION PAGE

1. Report No.	2. Government Accession No.	3. Recipient's Catalog No.
FHWA-ICT-25-003	N/A	N/A

4. Title and Subtitle	5. Report Date
Impact of Heavy Commercial Electric Vehicles on Flexible Pavements	May 2025
	6. Performing Organization Code N/A

7. Authors	8. Performing Organization Report No.
Angeli Jayme (https://orcid.org/0000-0003-3640-4317), Jaime Hernandez (https://orcid.org/0000-0002-9665-0408), Imad L. Al-Qadi (https://orcid.org/0000-0002-5824-103X), Johann J. Cardenas (https://orcid.org/0000-0002-4695-7639), Murryam Hafeez (https://orcid.org/0000-0002-9826-1019), and William Villamil (https://orcid.org/0009-0003-1839-2807)	ICT-25-003 UILU-2025-2003

9. Performing Organization Name and Address	10. Work Unit No.
Illinois Center for Transportation Department of Civil and Environmental Engineering University of Illinois Urbana-Champaign 205 North Mathews Avenue, MC-250 Urbana, IL 61801	N/A
	11. Contract or Grant No. R27-252

12. Sponsoring Agency Name and Address	13. Type of Report and Period Covered
Illinois Department of Transportation (SPR) Bureau of Research 126 East Ash Street Springfield, IL 62704	Final Report 8/16/22–5/15/25
	14. Sponsoring Agency Code

15. Supplementary Notes

Conducted in cooperation with the US Department of Transportation, Federal Highway Administration.

https://doi.org/10.36501/0197-9191/25-003

16. Abstract

Heavy-duty electric vehicles (HDEV) pose challenges to flexible pavements. This study evaluated four Illinois pavement structures to quantify HDEV impacts on pavements. Compounding factors included increases in load and acceleration, which escalated critical strains and reduced repetitions to failure. Various distresses were considered: bottom-up cracking, shear-driven top-down cracking, and shear-driven shoving. A proposed framework is presented, which includes a new metric—e-truck adjustment factor—that enables a full truck comparison of internal combustion engine vehicles (ICs) with HDEVs. The driving factor for HDEV's effect was the additional shear strain in the pavement structure. For pavements with relatively thin hot-mix asphalt (HMA) layers (e.g., low volume and typical thick), the increased load impact was prominent. In addition, the impact adversely affected the subgrade and base layer with higher induced structural rutting. Pavement sections with either a relatively thick HMA layer (e.g., full depth) or supported by a high-modulus layer (e.g., stone matrix asphalt [SMA] overlay on Portland cement concrete) were impacted by the increasing acceleration. In that case, the horizontal shear strain near the surface aligned with the increased longitudinal contact stresses. Hence, determining HDEVs' impact on pavement should consider battery placement and acceleration increase as well as pavement's structural configuration, which define governing distresses. Full-depth and SMA-overlay sections displayed an increase in near-surface shearing, which may increase maintenance and rehabilitation frequency or warrant the use of shear-resistant materials. The environmental and economic impacts of the scenarios considered were assessed. HDEVs may reduce use-stage costs due to vehicle design efficiency but may escalate pavement maintenance expenses. In addition, the impact of reduced truckload capacity of HDEVs compared to ICs may warrant additional trips to transport the same amount of freight.

17. Key Words	18. Distribution Statement
Electric Truck, Pavement Distress, Acceleration, Finite Element, Asphalt Pavement, Pavement Design, Life Cycle Assessment, Life Cycle Cost Analysis	No restrictions. This document is available through the National Technical Information Service, Springfield, VA 22161.

19. Security Classif. (of this report)	20. Security Classif. (of this page)	21. No. of Pages	22. Price
Unclassified	Unclassified	79+ appendices	N/A

Form DOT F 1700.7 (8-72) **Reproduction of completed page authorized**

ACKNOWLEDGMENT, DISCLAIMER, MANUFACTURERS' NAMES

This publication is based on the results of **ICT-R27-252: Impact of Commercial Electric Vehicles on Flexible Pavement Performance**. ICT-R27-252 was conducted in cooperation with the Illinois Center for Transportation; the Illinois Department of Transportation; and the Federal Highway Administration.

Members of the Technical Review Panel (TRP) were the following:

- John Senger, TRP Chair, Illinois Department of Transportation
- David Adedokun, Federal Highway Administration
- Justin Belue, Illinois Department of Transportation
- Tiffany Brase, Illinois Department of Transportation
- Kevin Burke, Illinois Asphalt Pavement Association
- Brian Hill, Illinois Department of Transportation
- David Hunt, TransChicago Truck Group
- Stephen Jones, Illinois Department of Transportation
- Steven Karamihas, Applied Pavement Technology
- Geno Koehler, Illinois Department of Transportation
- Marshall Metcalf, Illinois Department of Transportation
- Tim Peters, Illinois Department of Transportation
- Don Schaefer, Mid-West Truckers Association
- Charles Wienrank, Illinois Department of Transportation

EXECUTIVE SUMMARY

As new vehicle technologies emerge, so do transportation agencies' challenges to adequately prepare and maximize infrastructure investments. This study evaluated long-term impacts of heavy-duty electric vehicles (HDEVs) on Illinois' current road infrastructure. HDEVs apply relatively larger axle load and more significant torque because of the battery weight and electric motor. As original equipment manufacturers are still designing how to balance battery weight with respect to truck load, this study assumed various battery placement scenarios. In addition, increased axle load for HDEVs was further exacerbated with increased acceleration level, due to HDEVs' higher torque than conventional internal combustion engine vehicles (ICs). Four common pavement structures across Illinois were selected to represent various functional levels.

The methodology of the proposed framework included a two-pronged model to generate tire-pavement contact stress inputs for both IC and HDEV scenarios and to simulate a loaded flexible pavement structure. Critical strain outputs were then utilized to estimate the number of repetitions to failure for bottom-up cracking, shear-driven top-down cracking, and shear-driven shoving. A new metric—e-truck adjustment factor—was proposed to enable a combined distress analysis for full IC and HDEV truck configurations. Such analysis is vital, as pavement damage is driven by a combination of distress mechanisms, not just one. The new e-truck adjustment factor scaled the International Roughness Index (IRI) progression curve to define earlier rehabilitation triggers and imposed a means to adjust the traffic factor in the Illinois Department of Transportation's full-depth mechanistic design. The framework also offers flexibility to account for other emerging technologies in transportation, such as truck platoons. The presented holistic framework also checked the resulting shear stresses at layer interfaces to ensure that the tack coat strength was not exceeded.

Increased load due to HDEV battery placement led to increased strains, reducing pavement service life. This load impact was especially prominent in pavement sections with relatively thin hot-mix asphalt (HMA) layers (e.g., low volume and typical thick) and adversely affected underlying layers with higher rutting. On the other hand, pavement sections with either a relatively thick HMA layer (e.g., full depth) or supported by a high-modulus layer (e.g., stone-matrix asphalt [SMA] overlay on Portland cement concrete [PCC]) were impacted by the increasing acceleration level. The near-surface horizontal shear strain is aligned with the increased longitudinal contact stresses. Hence, determining HDEVs' impact on pavement should factor in battery placement and acceleration increase as well as pavement's structural configuration, which define governing distresses. Increasing near-surface shearing, observed for full depth and SMA-overlay sections, may require increased frequency of maintenance and rehabilitation or warrant using shear-resistant materials.

The study focused on two realistic scenarios to estimate reductions in emissions: placing HDEV batteries on drive axles or evenly distributing them along a semi cab's steer and drive axles. In general, the total emissions from HDEVs are significantly less that those from ICs. For HDEVs, use stage emissions are significantly lower due to the relatively cleaner electricity grid in Illinois, where approximately 55% of energy is produced by nuclear power. For HDEVs, the use stage contributes approximately 44% of total emissions. Despite the increase in maintenance and rehabilitation (M&R) emissions, the substantial reductions in use-stage emissions underscore the potential environmental

benefits of adopting HDEVs in freight transportation. However, these results are highly dependent on the energy mix of the electricity grid. In states with higher reliance on fossil fuels for electricity generation, the emissions reduction potential of HDEVs may be lower, altering the overall life cycle impact.

At a 25% HDEV market penetration, the use-stage emissions decreased approximately 66%. On the other hand, M&R stage emissions increased due to their greater frequency, increasing the corresponding cost. Furthermore, because of the reduced hauling capacity of HDEVs compared to ICs, additional trips may be required to transport the same amount of freight—leading to increased traffic and pavement M&R frequency. The life cycle assessment (LCA) and life cycle cost analysis (LCCA) results highlighted a trade-off, where HDEVs may reduce use-stage costs due to energy efficiency but may escalate pavement maintenance expenses. This is impacted by energy efficiency and cost and HDEV market penetration.

TABLE OF CONTENTS

LIST OF FIGURES

LIST OF TABLES

CHAPTER 1: INTRODUCTION

BACKGROUND

Truck electrification is expected to grow significantly to reduce the dependency on fossil energy and reach complete energy independence by 2050. According to the Environmental Protection Agency (EPA, 2024), medium-duty (MD) and heavy-duty (HD) vehicles use a third of total transportation energy, resulting from ground transportation producing a third of greenhouse gas emissions in 2020. However, only 11% of the vehicle miles traveled on US highways are attributed to MD and HD vehicles (BTS, 2025). In addition, electric vehicles and heavy-duty electric vehicles (HDEVs) have been encouraged through the *Inflation Reduction Act* (Congress, 2022b) and the *Bipartisan Infrastructure Law* (Congress, 2022a) through tax incentives, funds for strengthening battery supply, and expansion of charging infrastructure (DOE, 2022).

In Illinois, 43 incentives are related to infrastructure planning, charging station manufacturing, electric vehicle purchase, retrofit reimbursement, smart grid infrastructure development, transportation electrification infrastructure projects, and utilities. The goal is to achieve 100% clean electricity generation by 2045 and one million battery-powered cars and trucks on the road by 2030. Currently, there are 3,823 stations with alternative fuels, wherein 2,930 public and 370 private EV supply equipment service exist. In 2021, approximately 269,100 vehicles registered in the state were EVs, plug-in hybrids, and hybrid EVs.

Adopting electric transportation requires evaluating economic and environmental impacts. The net environmental impact of electric transportation is linked to energy sources. Electricity sources in Illinois comprise nuclear, coal, natural gas, wind, solar, biomass, hydro, and oil. In contrast to the US national average, the top three electricity sources in Illinois are nuclear (54.4%), natural gas (15.9%), and coal (15.1%), as illustrated in Figure 1. Regarding the economic impact, HDEVs may induce additional pavement damage. The additional weight of the battery pack would impose greater axle loads than internal combustion counterparts. In addition, instantaneous torque application might increase pavement deterioration.

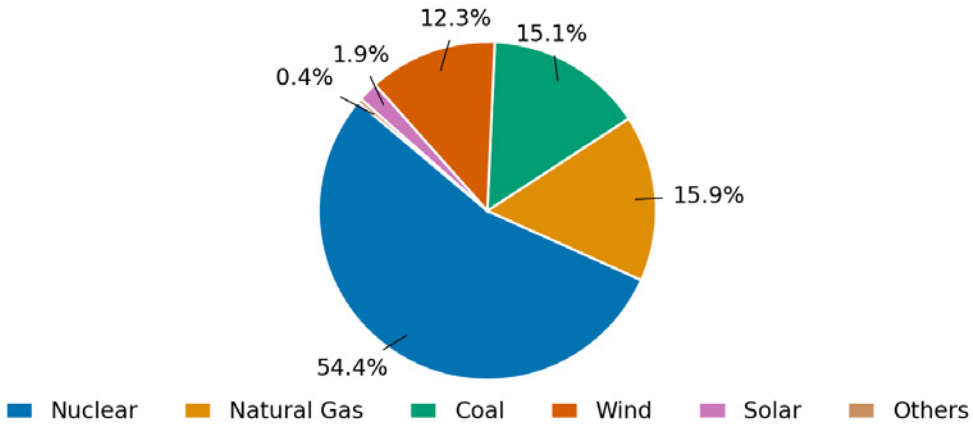

Figure 1. Graph. Breakdown of electricity sources in Illinois (AFDC, 2023).

In general, there are five aspects that must be considered when studying HDEVs.

Feasibility of Heavy-Duty Electric Vehicles

Some pertinent issues in delaying the transition to HDEVs include inadequate availability of technology, limited travel range, constraints about payload and volume, partial economy of scale, and insufficient charging stations (Moultak et al., 2017). As part of the *Inflation Reduction Act* (Congress, 2022b) and *Bipartisan Infrastructure Law* (Congress, 2022a), recommendations are provided to address and mitigate the aforementioned issues. Hence, there are efforts to enhance the use of clean energy in long-haul trucking technologies (e.g., electric plug-in, electric catenary, overhead line, hydrogen fuel cell, and dynamic inductive charging). Moultak et al. (2017) reported that in comparison with diesel in 2030 projections, overhead catenary would result in 25%–30% lower costs, in-road induction would reduce costs by 15%–25%, and hydrogen fuel costs would decrease by 5%–30% in capital, maintenance, and fuel costs.

Identified limitations for plug-in EVs include limited range, battery cost, charging time, and cargo weight and size. This technology is likely applicable to light commercial urban delivery vans, MD regional delivery trucks, and refuse trucks. On the other hand, catenary or in-road charging segments, geared for MD and HD tractor-trailers on medium-distance routes and drayage trucks around ports, are faced with challenges related to infrastructure cost and standardization across regions. Last, hydrogen fuel cell technology has been reported to have a durability status of 10,000 hours (Zhao et al., 2018). It was conducive to HD long-haul truck operation and drayage trucks around ports, albeit with barriers related to refueling infrastructure, renewable hydrogen, and fuel cell costs.

Recently, Zhou et al. (2024) assessed the life cycle analysis (LCA) and life cycle cost assessment (LCCA) for HD trucks. The authors considered fuel, natural gas, and battery, in addition to the energy cycle, truck manufacturing, truck operation, truck maintenance, and end of life. Contrasting the scenarios between states (Delaware, Illinois, Washington, and West Virginia) that have different electricity-mix characteristics, the LCA and LCCA revealed that EVs were cleanest in contrast to diesel and natural gas. Moreover, electric trucks led to the lowest environmental and economic impact relative to natural gas and diesel, with an associated global warming potential reduction up to 86%.

Economic Impact of Heavy-Duty Electric Vehicles

One component in the economic assessment of EVs is the balance between the cost of energy and batteries. Energy savings for EVs compared to internal combustion engine vehicles (ICs) can vary between 29% and 44%. However, such savings may be nullified by the battery cost (Gao et al., 2017). Gao et al.'s measured data included energy consumption, vehicle speed and acceleration, engine speed and torque, vehicle weight, and location using GPS with typical driving cycles in Knoxville, Tennessee, for HD and MD electric vehicles and plug-in hybrid electric vehicles. They used a simulation tool to calculate tractive energy and component efficiency and assess a system's components and performance. Energy savings were attributed to braking energy recovery, and the battery pack weights caused payload issues for Class-7 vehicles but not for Class 8. (The vehicle class is based on the National Highway Traffic Safety Administration vehicle classification.)

More recently, the effect of extra weight from battery packs and dynamic loading was included in an analysis of flexible pavements using a 3D finite-element (FE) model (Zhou et al., 2024). The study implemented AASHTOWare Pavement ME transfer functions to estimate pavement distresses and roughness progression from pavement responses. A 3D FE model provided pavement responses. Four types of pavements, additional weight of 2 and 8 kips, and market penetration of HDEVs of 0%, 25%, 50%, 75%, and 100% were included. The study found the impact of the extra weight was not significant (Zhou et al., 2024).

Torque and Pavement Responses

Extra battery weight and higher wheel torque from HDEVs may impact pavement performance. The additional weight may result in a larger axle load. Research since the 1950s at the American Association of State Highway Officials Road Test has consistently shown that as axle load increased, pavement damage accelerated. A few studies that investigated this issue concluded the extra weight of the battery pack does not result in significant pavement damage (Harvey et al., 2020; Zhou et al., 2024).

The second factor, wheel torque, may result in higher longitudinal tire-pavement contact stresses. In-plane contact stresses have been often overlooked in traditional flexible pavement analysis, in part because quantifying tire-pavement contact stresses is challenging. However, previous studies by the Illinois Center for Transportation (ICT) on contact stresses at different rolling conditions (braking and acceleration) have provided some insights into the impact of torque on flexible pavements (Al-Qadi et al., 2008, 2018; Hernandez et al., 2016; Wang et al., 2014; Yoo et al., 2006).

Wang and Al-Qadi (2010) developed a pneumatic tire FE model to predict contact stresses under various rolling conditions, including braking and acceleration (Wang et al., 2012). They calibrated material properties by comparing predicted and measured load-deflection curves and validated the model using measured contact stresses in the vertical and transverse directions. In the model development, the authors controlled the degree of braking and acceleration via the slip ratio parameter. In contrast to free-rolling conditions, braking induced higher shear stresses and lower compressive stresses, which might increase the likelihood of shear failure. The relevance of shear strain in the analysis was reiterated and confirmed by performing an analysis that included pre-existing cracks. In addition, the effect of various tire-pavement surface friction models on the same FE pavement model was assessed (Wang et al., 2014).

Hernandez and Al-Qadi (2016b) further improved the tire model by Wang et al. (2012). They incorporated measured tire geometry, rubber material properties provided by the tire manufacturer, lab-measured reinforcement materials properties, the effect of speed and uniform temperature (Hernandez & Al-Qadi, 2016a), and pavement deformability (Hernandez & Al-Qadi, 2017a, 2017b). Jayme and Al-Qadi added thermomechanical interaction between the tire and pavement to quantify the impact of nonuniform temperature distribution within the tire and interaction with ambient and pavement surface temperatures (Jayme & Al-Qadi, 2021, 2022). In 2021, an extensive ICT database of contact stresses was generated from truck tire FE models. The data were used to develop a deep-learning-based approach to predict contact stresses in a fast and accurate fashion in lieu of FE modeling (Liu & Al-Qadi, 2022b).

A parallel effort in pavement FE modeling incorporated viscoelastic HMA layers, a stress-dependent granular layer and subgrade, continuously moving load, layer interaction properties, and infinite boundary conditions for far-field behavior (Al-Qadi et al., 2008, 2018; Hernandez et al., 2016; Hjelmstad et al., 1997; Wang & Al-Qadi, 2013; Yoo et al., 2006). The simulation outcome has been validated using measurements from field and accelerated pavement test sections across the United State. Last, the post-processing scheme has been extended from the evaluation of single-point responses to bulk/volumetric pavement behavior via domain analysis, especially the 3D impact at the near-surface region (Gamez et al., 2018).

Hot-Mix Asphalt Mix Design for Higher Torque

HMA design modifications have been applied to address the effect of larger torque. A study in Nevada combined numerical modeling, forensic investigation, and laboratory testing to recommend HMA designs that account for high torque (Hajj et al., 2007). Vehicle acceleration, deceleration, and turning were identified as impactful factors, and rutting was estimated using empirical functions dependent on resilient response. A study recommended modifying aggregate gradation for intersections (Hajj et al., 2011). Follow-up research was completed in 2021 and had three components: (i) a forensic study encompassed 32 field cores from a 10-year-old intersection (Hajj et al., 2011); (ii) a proposed a balanced mix design and suggested performance thresholds; and (iii) a mechanistic approach using 3D-MOVE to evaluate HMA rutting for an 18-wheel truck traversing a 4% grade downhill section, with and without braking.

Loading from Heavy-Duty Electric Vehicles

Contact stresses depend not only on the material and structural configurations of the tire and pavement, but also on the vehicle drivetrain—controlling imposed rolling/driving conditions. The difference in vertical wheel load between HDEVs and ICs lies in the magnitude and distribution of the battery pack weight. However, wheel torque determines the difference between in-plane contact stresses. For HDEVs, wheel torque is governed by the electric motor and the characteristics of the power train. Although there are typical power train configurations in HDEVs, optimization is an active research topic. For instance, Verbruggen et al. (2020) optimized the topology of the electric design to minimize the total cost of ownership and energy consumption by looking at the hardware and the control design. The optimization model included factors such as the tractive force the vehicle needs (rolling friction, aerodynamic friction, and gradient resistance), transmission model (multi-speed gearbox with fixed efficiency for each gear), battery model, vehicle mass (mass without power train, mass of trailer, payload, and power train mass), and driving cycles.

In the absence of information regarding the power train configuration components, some assumptions are needed to estimate wheel torque based on motor torque. For instance, a Volvo VNR Electric reported maximum electric-motor torque as 4,051 lb-ft (Volvo, 2023), a two-driving wheel model with a final drive ratio of 3.50, and a gear ratio ranging from 0.5 to 4.50, yielding a wheel torque range from 3,545 to 31,902 lb-ft. Hence, automated torque control is an extensive research area with a large focus on safety (Adeleke et al., 2022). Several algorithms and models have been developed and tested. Additionally, torque distribution has affected electric motor efficiency, given that drivetrain power loss characteristics are positive and strictly monotonically increasing functions of wheel torque (Dizqah et al., 2016).

Although the federal allowance for natural gas and electric battery-powered tractor trailers has increased to 82,000 lb, the battery pack configuration of an HDEV poses a question on its impact on axle weight distribution. Electric battery packs for HDEVs may change axle load distribution in several ways:

- Weight distribution: The battery pack is typically located in the chassis of the truck, which can shift the weight distribution and affect the load distribution on the axles.
- Center of gravity: The placement of the battery pack can also alter the center of gravity of the truck, affecting its stability and handling characteristics.
- Axle loads: The weight of the battery pack can increase the total weight of the truck, leading to increased loads on the axles and suspension system.
- Load distribution: The distribution of weight between the front and rear axles can also change with the addition of an electric battery, potentially requiring adjustments to the suspension system to maintain optimal load distribution.

PROJECT OBJECTIVE

This project aimed to assess the impact of electric trucks on flexible pavements in Illinois, with a focus on potential changes in pavement structural design. The objectives of this study were as follows: (i) determine the overall impact of increased torque and axle loading of electric trucks on tire-pavement contact stresses compared to internal combustion trucks; (ii) quantify flexible pavement responses to electric truck loading; (iii) identify the impact of electric truck loading on pavement life-cycle cost analysis and life-cycle assessment; and (iv) recommend modifications to IDOT's flexible pavement design approach.

RESEARCH SCOPE

This study provides a framework that allows a detailed evaluation of flexible pavement behavior under commercial electric truck loading for representative Illinois Department of Transportation (IDOT) pavement sections. Various pavement distress mechanisms were evaluated per pavement functional class to determine key triggering mechanisms that may lead to early failure under HDEV loading. The proposed framework, although preliminary and limited to four structures, enables IDOT and other state agencies to conduct a holistic assessment of pavement systems under emerging vehicle technologies through combined distress evaluation, life cycle assessment, and life cycle cost analysis.

To achieve the objectives of this project, the research team conducted an in-depth assessment of electric trucks' increased torque and load on flexible pavements. Chapter 1 presents background about the subject, while Chapter 2 presents the impact of HDEV and IC loading and slip ratios on pavement contact stresses. To understand the implications of HDEVs on flexible pavement systems, Chapter 3 details the selection of representative Illinois pavement sections considering varying functional classes, structures, and material properties. Using FE analysis, the flexible pavement

sections were simulated under various HDEV loading and acceleration conditions relative to IC trucks. Pavement behavior analysis included the evaluation of critical strains and associated distresses alongside a proposed full-truck evaluation metric. Utilizing the findings, Chapter 4 discusses a possible adjustment to IDOT's full-depth pavement design guidelines. Chapter 5 expands the study's assessment of HDEV effects on flexible pavements by quantifying environmental and economic impacts through a general life cycle assessment and cost analysis, respectively. A summary of the study's findings and conclusions is presented in Chapter 6.

POTENTIAL IMPLEMENTATION

The study proposes a framework for modifying existing flexible pavement design methodologies to better account for the impact of HDEVs in Illinois. This framework would enable IDOT and other agencies to assess pavement distress, life cycle assessment, and life cycle cost analysis as HDEV penetration increases. A damage metric is proposed that evaluates the combined effect of fatigue cracking and near-surface damage (i.e., shear-induced top-down cracking and shoving/rutting). The proposed outcome will allow for the prediction of HDEV-related effects on pavement responses, distresses, costs, and environmental impact. This will empower IDOT and other agencies to optimize structural configurations and material selection. Additionally, the implementation of this framework will help IDOT and other agencies prepare for future HDEV penetration by developing new pavement designs and timely rehabilitation strategies.

CHAPTER 2: IMPACT OF AXLE WEIGHT AND TORQUE ON PAVEMENT CONTACT STRESSES

INTRODUCTION

Axle load is a determining factor in pavement damage. However, some situations warrant accounting for in-plane contact stresses, such as comparing different tire designs (e.g., wide-base tires, dual-tire assembly), analyzing intersections and road sections with stop-and-go operations (e.g., acceleration and braking), and considering curved roadways under turning or cornering tire maneuvers. Similarly, due to the extra weight of HDEV batteries and their instant access to higher wheel torque, quantifying the effect of HDEVs on pavement damage requires the use of nonuniform 3D contact stresses.

This chapter presents an evolved version of the tire model developed over the past two decades at ICT by Al-Qadi and his coauthors (Wang & Al-Qadi, 2010; Wang et al., 2012; Wang et al., 2014; Hernandez & Al-Qadi, 2016a, 2016b, 2017a, 2017b; Jayme & Al-Qadi, 2021, 2022; Liu et al., 2023; Liu & Al-Qadi, 2022b) to determine HDEV tire-pavement contact stresses, as influenced by the addition of higher loads (due to battery placement) and torque (level of acceleration). Appendix B presents details of the tire FE model, originally developed for IC vehicles, and discusses its applicability to HDEVs. HDEVs are expected to retain the same nominal tire sizes as ICs.

TRUCK AXLE LOADING

The loading scenarios consisted of various assumed placements of the battery pack on the truck tractor, and a baseline case scenario represents a standard IC. A total limit weight of 46 kips was considered in the IC's tractor, distributed across the axles as 26% (12.0 kips) for the steering axle and 37% (17.0 kips) for each tandem axle, per IDOT axle-load limits. Considering that regulations allow an additional 2 kips for electric trucks; the research team considered a total maximum weight of 48 kips for HDEV scenarios.

For calculating the net weight difference between a standard IC and HDEV scenarios, the research team subtracted 4.6 kips from the IC truck's weight (accounting for the engine, tank, exhaust, and fuel) and added 13.6 kips to represent the additional weight from a 900-kWh battery, electric motor, and electronics. This adjustment resulted in a net weight increase of 9 kips for the HDEV scenarios relative to the IC baseline case. It is worth noting that this increase in gross weight reduces the payload capacity of the HDEV. To illustrate this, if an IC truck has an empty weight of 35 kips, its payload capacity would be 45 kips provided a maximum gross weight of 80 kips. In contrast, an HDEV, with an empty weight of 44 kips (9 kips more than the IC counterpart), would only have a payload capacity of 38 kips, even after accounting for the additional 2-kip allowance (total gross weight of 82 kips). Therefore, it could be stated that the payload capacity of an IC truck is 1.184 times higher than any of the selected HDEV scenarios, implying that HDEV fleets might require a greater number of trips to carry to the same payload.

The placement of battery pack(s) remains a challenge, as original equipment manufacturers (OEMs) are contemplating optimal locations and logistic considerations for battery placement. Studies have investigated the effect of battery pack placement on mass distribution and driver comfort (Suriyamoorthy et al., 2019). Arora et al. (2021) recommended placing the battery at the center of the truck chassis to avoid frequent crash zones. In addition, to maximize profit and truck load-carrying capacity, the impact of battery weight on the trailer's gross freight load must be minimized.

Figure 2 illustrates the assumed scenarios of battery pack placement in this study: (i) steering axle, (ii) rear tandem axles of the tractor, and (iii) uniformly distributed along the tractor axles. The research team assumed HDEV trailer axles kept the same load distributions as those for ICs. The net weight increase when switching from ICs to HDEVs was assumed to be 9 kips as previously stated, which included the battery, electric motor, and electronics. Given the 2-kip allowance increase, the total weight of the HDEV was maintained at 82 kips (Figure 2). For the first scenario (S1), trailer weight was maintained at 34 kips, and the remaining 48 kips were distributed, with 19 kips on the steering and 14.5 kips on each tractor axle. For the second scenario (S2), the tractor's 48 kips were distributed, with 10 kips on the steering and 19 kips on each tractor axle. In scenario three (S3), the steering axle carried 14 kips, while all other axles each carried 17 kips. The change in battery location was intended to optimize freight capacity while maintaining the total weight of the truck at 82 kips.

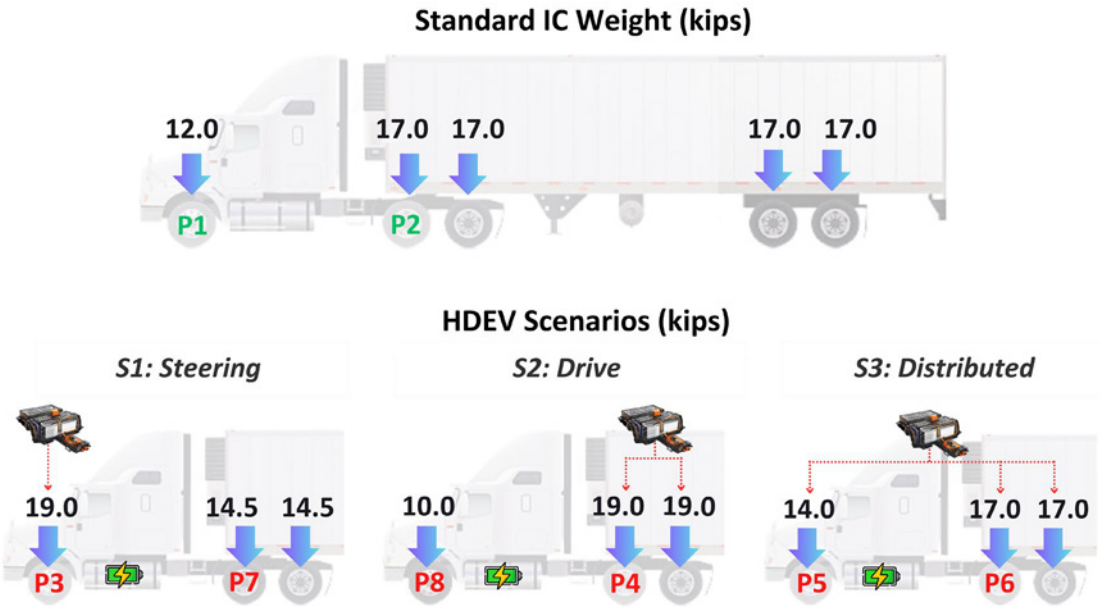

Figure 2. Schematic. Analysis scenarios of battery pack placement.

Table 1 summarizes the axle and half-axle weights for each scenario (with additional scenarios for later use in the full-truck analysis, as noted in the bottom four rows, highlighted grey). Table 2 enumerates the load inputs and nomenclatures for the numerical analysis matrix. Both drive axles were assumed to have equal loads and dual tires. Only one tire of the dual-tire assembly (DTA) was used as a tire load input in the analysis of this chapter, owing to the assumed symmetry between the two tires.

Table 1. Axle Loads per Various Scenario

Description	Steering axle	Drive axles (1 = 2)	Total
IC and HDEV without battery weight (%)	26	37	100
IC weight (kips)	12.0	17.0	46
HDEV weight without battery (kips)	10.0	14.5	39
HDEV scenario 1: battery weight in steering axle (kips)	19.0	14.5	48
HDEV scenario 2: battery weight in drive axle (kips)	10.0	19.0	48
HDEV scenario 3: battery weight evenly distributed (kips)	14.0	17.0	48
Base scenario: IC half axle (kips)	6.0	8.5	23
HDEV scenario 1 half axle (kips)	9.5	7.2	24
HDEV scenario 2 half axle (kips)	5.0	9.5	24
HDEV scenario 3 half axle (kips)	7.0	8.5	24

Table 2. FE Simulation Load Inputs

Vehicle	Axle	Scenario	Label	FEM Load (kips)
IC	Steering	Base	P1	6.0
IC	Drive	Base	P2	4.2
HDEV	Steering	1	P3	9.5
HDEV	Drive	2	P4	4.7
HDEV	Steering	3	P5	7.0
HDEV	Drive	3	P6	4.2
HDEV	Drive	1	P7	3.6
HDEV	Steering	2	P8	5.0

WHEEL TORQUE

It is essential to note that *motor torque* and *wheel torque* differ. While manufacturers often promote motor torque values for marketing EVs, the torque that reaches the wheels is a product of the power train's design. In a typical configuration—composed of a motor, gearbox, propeller shaft, and differential—the overall gear ratio and final drive ratio define how the motor torque translates into the axle torque before being distributed to each wheel (a standard in Class-9 truck tractors with a 6 × 2 layout). Because of the influence of the drivetrain setup, the wheel torque can vary from roughly equal to significantly more than the motor torque, as evident in published specifications for HDEVs like the Freightliner eCascadia (Freightliner Trucks, 2023) and XOS HDXT (XOS, 2023), which exhibit maximum wheel torques of 23.01 kips-ft and 36.58 kips-ft, respectively. At the same time, published maximum motor torques vary enormously—from 0.66 kips-ft for the BYD 8YTT (BYD, 2023) to 5.97 kips-ft for the Battle Motors LETII HDEV (Battle Motors, 2023). Thus, the multiplication effect of the power train's gear ratios can often compensate for lower inherent motor torque.

Because the development of HDEVs is still ongoing, technical details for HDEVs may not be as publicly available as for conventional ICs. As a result, certain assumptions about the power train must be made to estimate wheel torque values for HDEVs. For instance, the Volvo VNR Electric features a maximum motor torque of 4.06 kips-ft (VOLVO, 2023). If a two-wheel drive configuration with a final drive ratio of 3.50 and gear ratios from 0.5 to 4.50 were assumed, then the corresponding wheel torque would range between 3.55 and 31.90 kips-ft—almost an order of magnitude difference.

Figure 3 showcases the reaction torque over time from the FE simulation under the frequency of free-rolling conditions ($P1$, $P2$, $P3$, $P4$, $P5$, and $P6$) and at a 6% slip ratio ($P2$ and $P6$). These FE-derived wheel torque outputs aligned with ones displayed in the OEM reported values (Table 3). Specifically, the tire model was driven by the prescribed linear and angular velocities at its axis, and the corresponding reaction torque at the wheel was recorded for six distinct loads, covering all HDEV and IC scenarios.

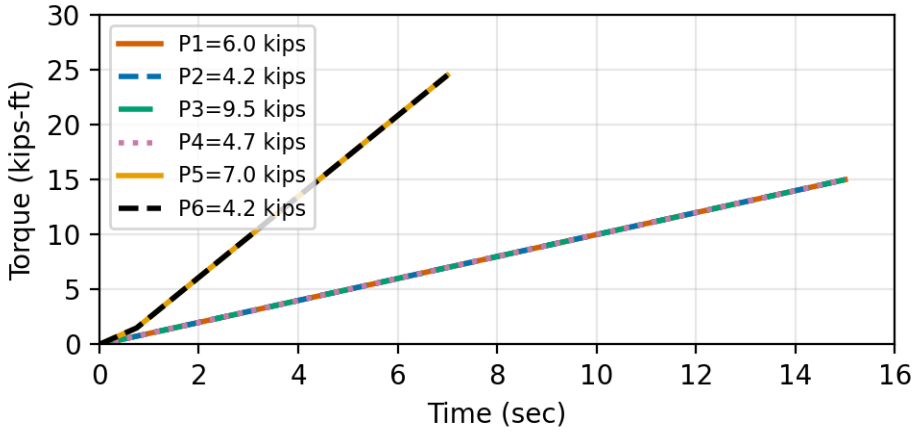

(a) Free rolling

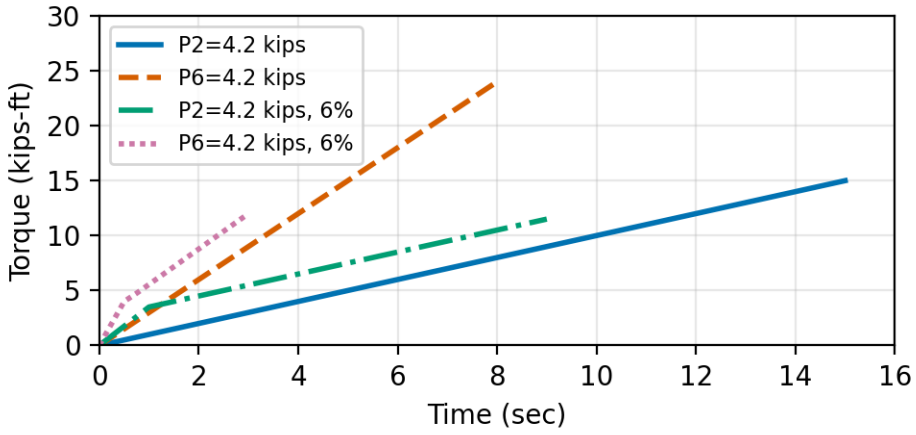

(b) Varied slip ratio

Figure 3. Graph. Reaction torque over time for (a) free rolling and (b) 6% slip ratio.

Table 3. NHSTA Vehicle Class 8 HD Design Operating Conditions

IC			HDEV		
Manufacturer	**Model**	**Torque (kips-ft)**	**Manufacturer**	**Model**	**Torque (kips-ft)**
Kenworth	T680	19.21–28.76	Battle Motors	LETII EV	3.50–6.00
Western Star	4900	26.06	BYD	8TT	0.66
Volvo	VNL 760	17.61	Freightliner	eCascadia	23.00
Peterbilt	579	23.03	Kenworth	T680E	1.62
Mack	Pinnacle	28.51	Lion Electric	Lion 8	2.51
Freightliner	Cascadia	28.71	Nikola	Tre BEV	–
International	LoneStar	31.09	Tesla	Semi	1.60
			Volvo	VNR Electric	4.05
			XOS	HDXT	30.54–36.58

Two key trends were observed. First, HDEV loads revealed torque values that were approximately triple those of IC loads. At 8 sec, the HDEV torque measured at 24.19 kips-ft, in contrast to 8.11 kips-ft for the IC. Second, the vertical load did not influence the reaction torque when 0% slip ratio was implemented, as indicated by the identical torque curves within each vehicle category ($P1$ and $P2$ for the IC and $P3$ through $P6$ for the HDEV on Figure 3-a). The results were intuitionally reasonable as the HDEV battery pack's additional load acted in the vertical direction rather than the direction in which the tire was moving. However, higher vertical loads correlated with increased in-plane forces at the tire-pavement interface (higher rolling resistance). This will be further explained in the next section, where the impact of axle loading on contact stresses is discussed.

Furthermore, Figure 3-b displays that increasing the slip ratio from 0% to 6% augments the reaction torque in distinct levels for HDEV and IC cases. For the HDEV case, at *t* = 3 sec, the torque increased by 2.58 kips-ft or 28%, from 9.07 to 11.65 kips-in. On the other hand, at *t* = 3 sec, the IC torque grew by 2.22 kips-in or over 70%, from 3.02 to 5.24 kips-ft. Because results obtained at *t* = 3 sec were statistically analogous to the ones obtained at *t* = 8 sec, the latter was not performed to reduce computation cost. This is further explained via the kernel density estimate analysis in Appendix C.

ANALYSIS OF TIRE-PAVEMENT CONTACT STRESSES

The analysis of resulting tire-pavement σ_{11}, σ_{33}, and σ_{22} contact stresses—f_{11}, f_{33}, and f_{22} for the corresponding contact forces, respectively—are presented. The 1-direction, 3-direction, and 2-direction correspond to longitudinal, transversal and vertical directions, respectively. The stresses were influenced by the additional loading and acceleration imposed by HDEVs. Although the analysis was focused on contact forces, similar trends could be observed for the contact stresses.

Longitudinal Direction

Figure 4 depicts the change in the longitudinal contact force f_{11} over time and specifically at *t* = 3 sec for all HDEV and IC load cases. The horizontal axis represents the distance along the tire-pavement

contact length. A positive f_{11} signifies a force acting at the tire node in the direction of travel (i.e., pushing backward on the pavement surface), whereas a negative value indicates the opposite direction. The variations in f_{11} stemmed from the tire's outer surface deformation as each node entered and exited the contact region (i.e., nodes "pushed" against the pavement at the leading edge of the contact patch and "pulled" away at the trailing edge). During the rolling process, tire-surface elements were compressed as they moved into the contact patch and then stretched as they departed, generating longitudinal stresses that were governed by road surface constraints and friction at the tire-pavement interface.

Figure 4-a highlights the most significant changes in the contact load, which occurred early in the simulation, particularly between the initial standstill and the first second (from 0 to 3.11 mph for the HDEV), when inertia forces were highest (transient condition). Moreover, Figure 4-b showcases the contact force increase with load. The load cases $P1$, $P2$, $P4$, $P6$, $P7$, and $P8$ ($P1$ and $P2$ corresponding to IC cases and the rest to HDEV cases) clustered together as the corresponding applied loads ranged between 4.23 and 6 kips. In contrast, *P5* and *P3* diverged substantially owing to heavier loads of 7 kips and 9.5 kips, respectively.

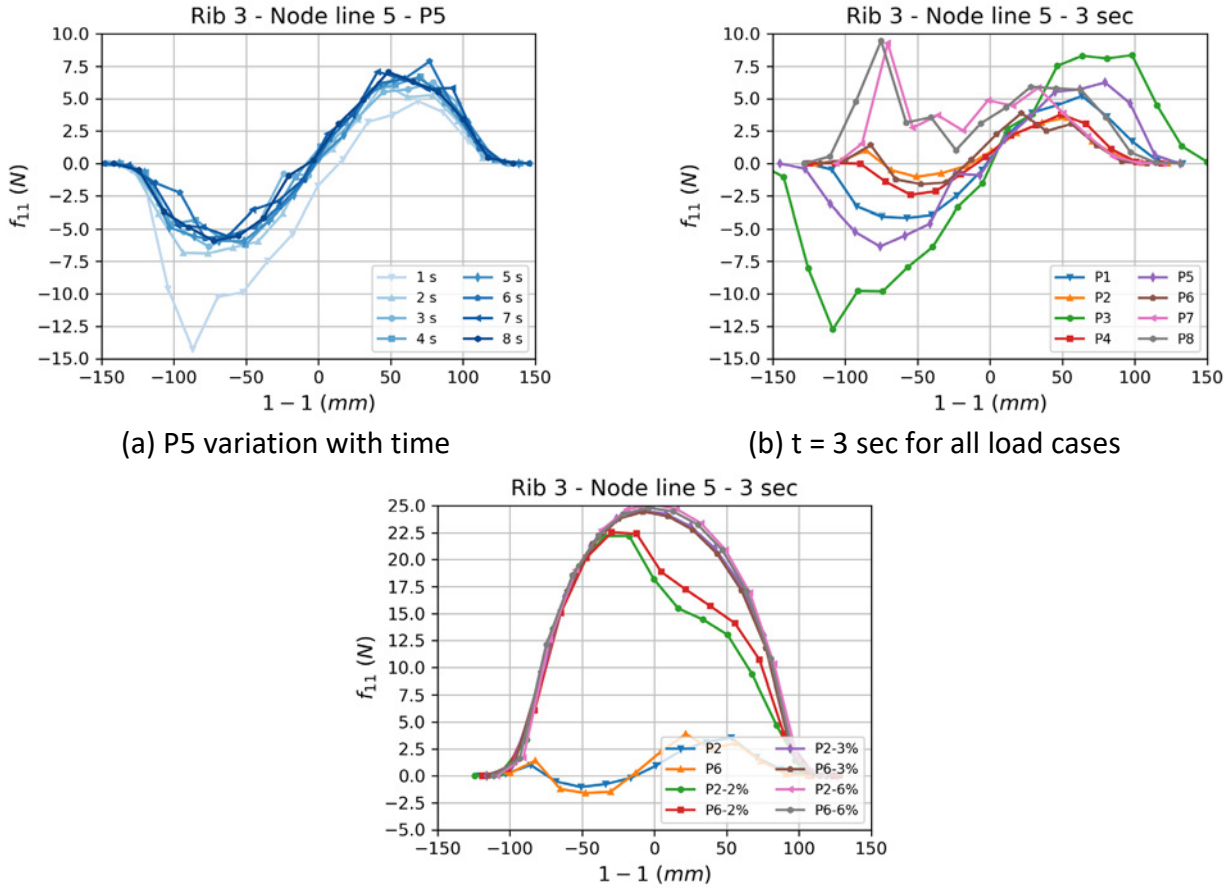

(a) P5 variation with time

(b) t = 3 sec for all load cases

(c) Effect of 2%, 3%, and 6% slip ratio for $P2$ and $P6$

Figure 4. Graph. Longitudinal contact forces at the mid-rib (rib 3, node line 5): (a) $P5$ variation with time, (b) t = 3 sec for all load cases, and (c) effect of 2%, 3%, and 6% slip ratio for $P2$ and $P6$.

The positive and negative portions of f_{11} also depended on the rib's position along the 1-direction (i.e., the traveling direction). For instance, the outer ribs (1 and 5) exhibited higher positive forces than negative ones, whereas ribs 2, 3, and 4 resulted in an opposite pattern. Moreover, under $P5$ load at *t* = 8 sec, rib 1 produced forces of 151.86 lb and −24.03 lb, and rib 5 produced forces of 153.93 lb and −24.05 lb. The middle ribs yielded smaller positive forces (31.61, 45.39, and 37.07 lb for ribs 2–4, respectively) and larger negative ones (−76.73, −61.60, and −86.91 lb). This distribution indicated that the outer edges supported higher contact forces in the rolling direction than the interior ribs, which resulted in higher force magnitudes at the tire edges.

As expected, the total positive force exceeded the total negative force, which aligned with the fact that a net forward push was applied against the pavement as the tire traveled in the positive 1-direction. Under the same conditions ($P5$, *t* = 8 sec), the overall positive force reached 419.88 lb, while the negative total force was −269.30 lb. Over time, positive f_{11} increased while negative f_{11} diminished, mirroring the tire's progression from rest to rolling. Figure 5 illustrates the evolution of the total forward contact force (for $P1$ to $P6$ load cases) obtained by summing the forces directed in the travel direction. The force grew most rapidly within the first two seconds, and higher vertical loads yielded higher forward forces. Case $P3$ (9.5 kips for the steer tire) notably resulted in the highest f_{11}. Moreover, $P2$ and $P6$ (both assumed similar loads, but from IC and HDEV scenarios, respectively) demonstrated comparable longitudinal force levels. These findings suggested that under a 0% slip ratio, the vertical load distribution—mainly influenced by battery placement—played a more substantial role in determining longitudinal forces than the wheel torque.

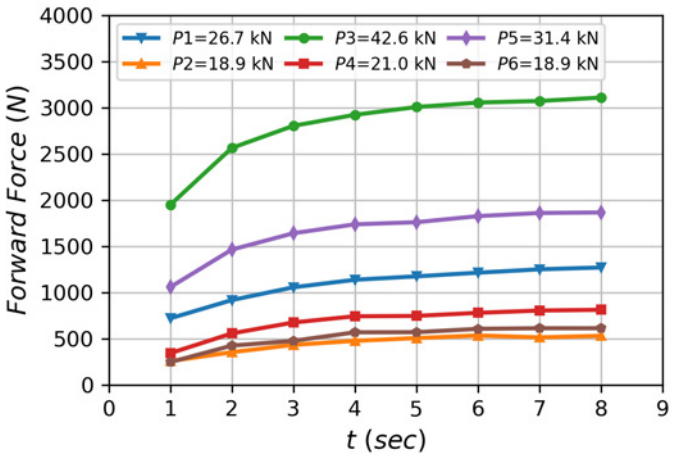

Figure 5. Graph. Evolution of total forward force with time.

However, regardless of the vertical load, longitudinal contact forces for a 0% slip ratio were very small compared to cases that included other slip ratios. Figure 4-c illustrates the amplification of f_{11} under 2%, 3%, and 6% slip ratio assumptions. Given a 6% slip ratio rolling condition, the maximum force reached 5.62 lb, which was approximately five times higher than that in free-rolling scenarios. Moreover, all forces remained positive, and the net longitudinal load was 1240.50 lb and 1221.84 lb at *t* = 3 sec for $P2$ and $P6$, respectively. Therefore, the tire's accelerating condition, represented by the slip ratio, impacted the longitudinal contact stress magnitude more significantly than the torque.

Vertical Direction

Figure 6 illustrates the evolution of vertical contact stresses with time for the mid-rib (rib 3, node line 5) with no slip ratio imposed, which followed a similar pattern to other ribs and node lines. Because the vertical load remained constant throughout the simulation, the vertical force component f_{22} at any given node changed marginally between 1 and 8 sec. Most loading cases produced a symmetrical distribution of the vertical stress σ_{22} relative to the midpoint of the contact path, except for the highest load case, $P3$ = 9.5 kips, which shifted the peak stress slightly toward the leading edge of the tire. Figure 6-b demonstrates that comparing $P2$ and $P6$ revealed very similar f_{22} distributions for HDEV and IC under the same tire load. This similarity stemmed from the fact that vertical load, tire inflation pressure, and tire characteristics (material, geometry, and reinforcement) govern the vertical stress distribution, which is influenced at a lower level by rolling conditions (Hernandez & Al-Qadi, 2016b; Liu & Al-Qadi, 2022b).

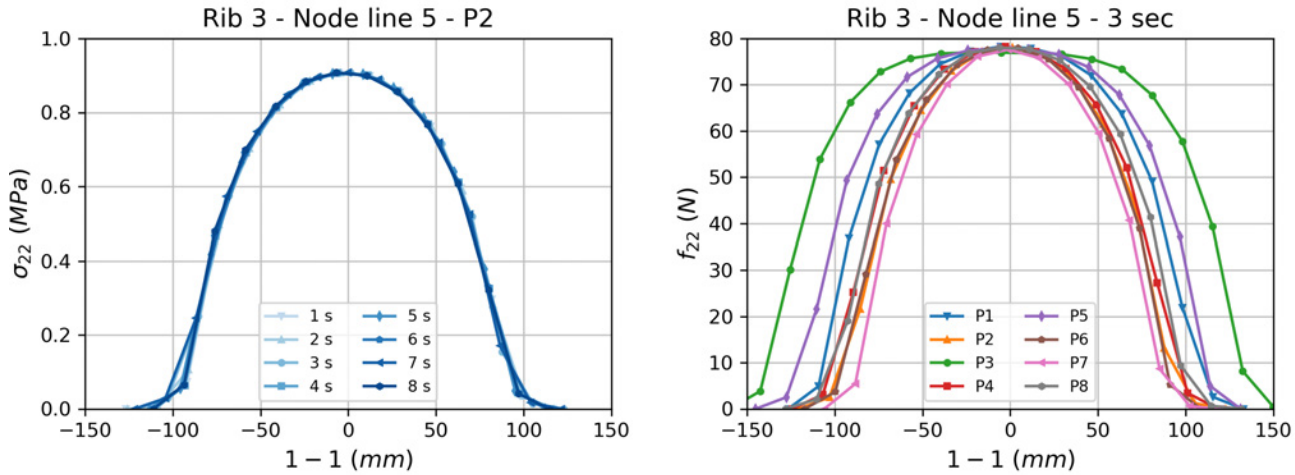

(a) P2 evolution with time

(b) Evolution at t = 3 sec

Figure 6. Graph. Vertical contact forces/stresses—rib 3 node line 5 (midrib): (a) P2 case evolution with time, and (b) evolution at t = 3 sec for the eight load cases.

Consistent with results from prior tire studies (Hernandez et al., 2015; Hernandez & Al-Qadi, 2016a, 2016b, 2017a, 2017b; Jayme & Al-Qadi, 2021; Wang et al., 2012), the maximum contact stress exceeded the inflation pressure (e.g., 100 psi vs. 130 psi in Figure 6-a). This challenges the typical pavement design assumption that these two values match exactly. The contact path length also increased as the load became higher, but the peak σ_{22} remained unchanged for different tire loads. This behavior implied that the vertical stress was redistributed over a broader contact region, manifesting a wider or flatter σ_{22} curve. Under the same inflation pressure, the stress profile evolved from having a pronounced peak around the center of the path (as seen in $P2$ in Figure 6-b) to a more uniform spread of stress at higher loads (e.g., $P3$ in Figure 6-b). This is because more rubber surface area was engaged in carrying the additional load. In general, for both HDEV and IC, outer ribs consistently exhibited higher values of σ_{22} than those of the inner ribs.

Transverse Direction

Transverse contact forces f_{33} followed a similar pattern as the longitudinal and vertical forces, as illustrated in Figure 7 (for a slip ratio equal to 0%). Specifically, Figure 7-a demonstrates the evolution of f_{33} over time for load case $P2$, while Figure 7-b displays the distribution of f_{33} along the contact length at *t* = 3 sec for all loads considered. Transverse forces manifested as the tire rubber is laterally constrained at the rib edges during contact, causing equal but oppositely directed reactions along the edges, evident in the "outward push" that is visible in Figure 7.

Figure 7-a demonstrates that the rolling time exerted only a minimal influence on f_{33}. The relationship between vertical and transverse contact forces largely explains this observation. As noted earlier, the restriction of the rib's lateral motion generated f_{33}. Such lateral motion resulted from a combination of the vertical load carried by each rib and the Poisson effect, which converted vertical compression into lateral expansion. Because the total vertical load remained constant while the tire accelerated from 0 mph to its final speed, the load distribution among the ribs remained unchanged. Consequently, any tendency for lateral movement—and thus f_{33}—remained consistent throughout the simulation.

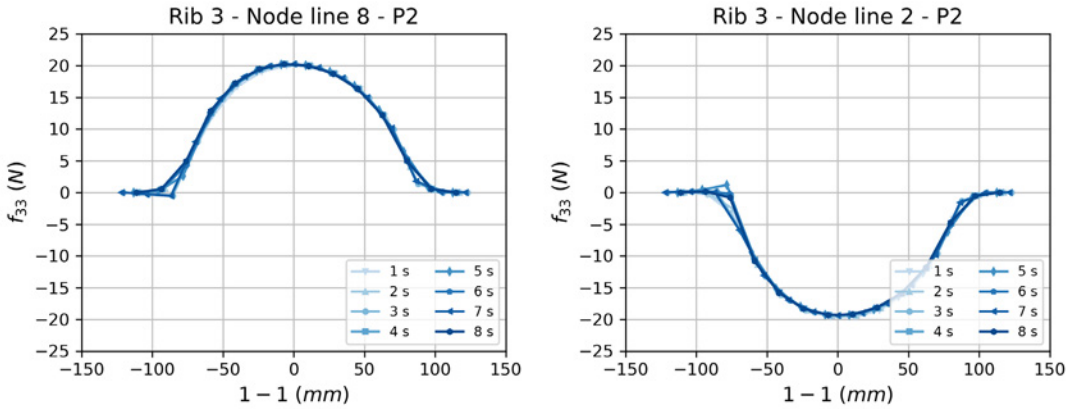

(a) P2 case evolution with time

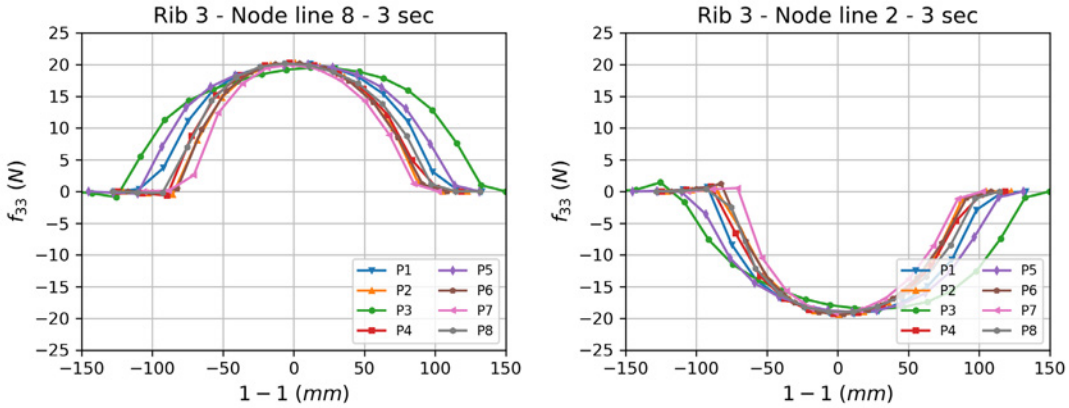

(b) Evolution at t = 3 sec

Figure 7. Graph. Transverse contact forces/stresses at rib 3, node lines 8 and 2: (a) $P2$ case evolution with time, and (b) evolution at t = 3 sec for the eight load cases.

Similar to the vertical force component, f_{33} was sensitive to an increased applied load as the contact length expanded without significantly altering the peak force. This effect was more pronounced at the outer ribs (1 and 5) than at the inner ribs (2, 3, and 4). Furthermore, a comparison of $P2$ (4.2 kips, IC) and $P6$ (4.2 kips, HDEV) indicated that different torque conditions for HDEVs and ICs did not noticeably affect the f_{33} magnitude. This result suggested that, as with vertical contact forces, the battery's positioning and the resulting vertical loading governed the transverse contact stress values rather than the impact of varied torque.

Even though the analyses of the contact forces and stresses presented above are based on the analysis along a given location at a rib, the findings apply to the distribution on the whole contact area. This was verified by comparing the variation along all ribs and node lines, alongside performing statistical analyses. The statistical analyses were based on statistical moments and Kernel density estimates, which are detailed in Appendix C.

SUMMARY

This chapter presented an FE model of a dual-tire assembly developed in Abaqus to analyze the effects of increased load and faster access to higher torque / acceleration in HDEVs compared with ICs. In the HDEV scenarios, battery placement along the tractor was varied, which shifted the overall weight distribution and altered axle-specific tire loads (including the allowable increased load per regulation). Three configurations were considered to account for various battery placements: one where extra weight was placed mainly on the steering axle, another where it was placed on the drive axle, and a third with an even load distribution along the tractor. Eight loading conditions were considered for both IC and HDEV cases, with speeds progressing from 0 to 15.5 mph for ICs and 0 to 24.9 mph for HDEVs. A dynamic implicit analysis was employed on the DTA model to generate 3D contact forces and stresses, assuming identical tire-pavement friction in all cases.

Contact forces, both along a line of nodes in the rolling direction and across the full distribution, were compared using statistical moments and kernel density estimation. Results showed that increasing load amplified both the magnitude and spatial spread of the contact forces compared to changes in speed. Specifically, heavier loads led to higher peak values in the vertical and longitudinal directions, along with a broader spatial distribution of these forces over the enlarged contact path. In contrast, variations in slip ratio mainly affected longitudinal contact forces. This underscores the importance of carefully accounting for rolling conditions when evaluating potential pavement damage from HDEVs.

CHAPTER 3: NUMERICAL ANALYSIS OF PAVEMENTS UNDER IC AND HDEV LOADING

INTRODUCTION

Closed-form expressions and semi-analytical solutions are inadequate when applied to real-world scenarios because these involve complex, nonlinear, and multiple interacting variables that cannot be represented or solved using simple mathematical expressions. The multilayered elastic theory introduced by Burmister in the 1940s provides analytical solutions for stress, strain, and deflection in pavement structures modeled as linear elastic, homogeneous, and isotropic layers (Burmister, 1943, 1945). Even then, solutions are only valid for simple loading conditions (e.g., circular loads) and assume uniform material properties. Despite being initially formulated for two-layer systems, the theory has been extended over the years for an arbitrary number of layers through the implementation of high-performance numerical methods (Khazanovich & Wang, 2007), and it is widely used for the analysis of flexible pavement structures. In fact, the Mechanistic-Empirical Pavement Design Guide (MEPDG) software, also known as AASHTOWare Pavement ME Design, relies on a layered elastic analysis back-end engine to compute pavement responses. However, pavement structures are continuous physical systems with responses that are influenced by numerous factors, such as traffic, material properties, and environmental conditions. Under these conditions, numerical approximation schemes or open-form solutions such as the finite element (FE) method serve as a reliable approach to overcome the inherent limitations of multilayered linear elastic analysis because they offer greater flexibility in modeling real-world complexities.

The FE method approximates the solution by dividing a continuous system into smaller interconnected components called finite elements. The use of 3D FE flexible pavement models has allowed researchers to investigate the influence of factors otherwise unexplored, such as contact stress distribution, load magnitude, axle configuration, loading time, rest period, layer thickness, dynamic loading, constitutive material model, boundary conditions, layer interaction, and seasonal effects on overall pavement responses (Castillo et al., 2019; Elseifi et al., 2006; Gamez et al., 2018; Gungor et al., 2017; Hernandez et al., 2016; Jiang et al., 2019; Kim et al., 2009; Masad et al., 2006; Mikhail & Mamlouk, 1997; Ramakrishnan & Al-Qadi, 2023; Said & Al-Qadi, 2023; Wang et al., 2013a; Wang & Al-Qadi, 2010; Yoo et al., 2006; Yoo & Al-Qadi, 2007; Zaghloul & White, 1993). This chapter details the FE model used in this project to predict pavement responses to IC and HDEV loading.

MODEL DEVELOPMENT

The modeling framework used in this study is a two-pronged FE approach composed of decoupled models to predict tire contact stress and flexible pavement response. The previous chapter detailed contact stresses, while this chapter deals with the pavement model. Although such FE models integrate several advanced features—including a 3D tire model, realistic contact stress distribution, multi-axle load configuration, nonlinear material characterization, and implicit dynamic analysis—to more accurately represent field conditions, some simplifying assumptions were necessary to ensure computational feasibility. A thorough validation with in situ field data and parameter sensitivity

studies have been conducted over three decades to ensure that the model outcomes accurately reflect actual flexible pavement behavior. More details can be found in Al-Qadi et al. (2016).

Four pavement sections within the Illinois roadway network were selected for FE simulations. The sections were chosen to evaluate pavement responses for roads likely to experience HDEV traffic, particularly in terms of increased load magnitude and greater torque access. The four pavement sections are listed below:

- A typical thick section: a pavement design commonly found in rural and semi-urban areas, such as state route US 24, with an annual average daily traffic (AADT) of 7,750 (Figure 8-a).
- A full-depth section: commonly featured in heavily trafficked corridors, such as state highway IL-83 and known for its higher truck percentages with an AADT of 13,500 (Figure 8-b).
- A low-volume section or county road: often encountered in agricultural and sparsely populated regions, with an AADT of 1,200 (Figure 8-c).
- An SMA overlay on PCC section: found in higher-performance sections, designed to handle heavy traffic volumes, such as state road IL-57, with an AADT of 13,800 (Figure 8-d).

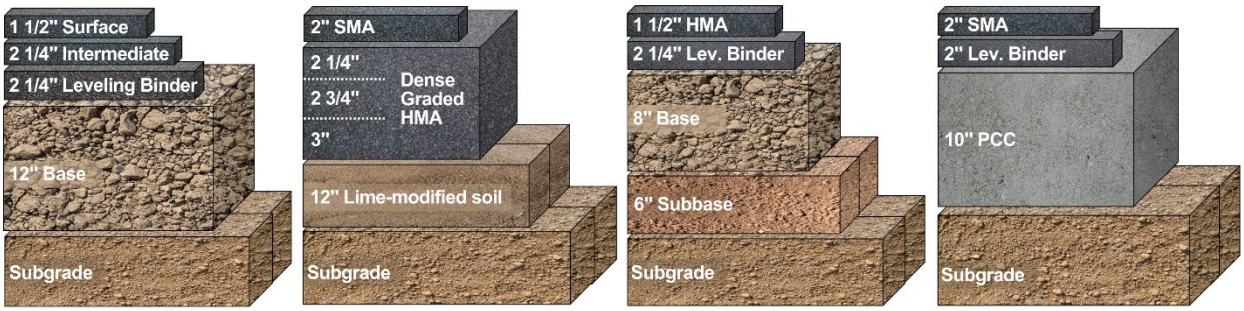

(a) Typical thick (b) Full depth (c) Low volume (d) SMA overlay

Figure 8. Schematic. Selected pavement sections for FE modeling.

This section discusses the formulation of the 3D FE pavement model to simulate the structural behavior of flexible pavement structures under HDEV loading. The pavement model aimed to capture critical factors influencing pavement responses—particularly under varying loading and accelerating conditions. Key steps in the development process include representing the 3D contact stress distribution, selecting appropriate constitutive models for HMA and granular layers, and defining boundary conditions to balance computational efficiency with physical constraints.

Because HMA materials are well represented by viscoelastic constitutive models, a dynamic transient analysis was used as it adequately captures their time and temperature dependencies. The HMA was modeled as viscoelastic materials, as its constitutive behavior inherently accounts for damping. The unbound granular and subgrade layers were modeled as linear elastic for thick pavement and nonlinear stress dependency. Table 4 presents a list of selected HMA mixtures from IDOT projects

along with their Williams-Landel-Ferry (WLF) coefficients (Williams et al., 1955) for a reference temperature of 69.80°F. Mixes T1-80-12.5-0, PG76-28N90, and PG64-22N90 were used for the full-depth section; PG64-22N70 and PG64-22N90 for the typical thick section; PG64-22N70 and PG64-22N50 for the low-volume section; and T1-80-12.5-0 and PG70-22N90 for the SMA-overlay-on-PCC section (García Mainieri & Al-Qadi, 2025; Santos Maia et al., 2024). Note that the WLF coefficients C1 and C2 from the ICT-R39 mix are different in sign and magnitude as this project only included testing at 14°F, 39.2°F and 68F°F, with 68°F as the assumed reference temperature. Additional dynamic modulus testing was conducted to supplement for other mixes considered in the analysis.

Table 4. Williams-Landel-Ferry Coefficients of HMA Mixtures

Label	Source Project	Mix Type	PG	N	NMAS	C1	C2
T1-80-12.5-0	R27-216	SMA	76-28	90	12.50	20.52	186.56
PG70-22N90	R27-216	HMA	70-22	80	9.50	3.23	14.41
PG76-28N90	R27-233	HMA	76-28	90	19.00	3.35	14.89
PG64-22N90	R27-233	HMA	64-22	90	19.00	3.22	14.86
PG64-22N70	ICT-R39	HMA	64-22	70	9.50	−182.52	−1141.04
PG64-22N50	R27-233	HMA	64-22	50	19.00	3.37	14.53

Dynamic modulus E^* master curves were derived by fitting the experimental results to a Prony series, a widely used mathematical representation in viscoelastic material modeling. In practical applications, a Prony series with four to eight terms is generally sufficient to capture the required frequency range with precision while maintaining computational efficiency. The number of terms for each HMA was carefully chosen to ensure an accurate representation of the experimental data while minimizing complexity. This study used the root mean square error of the predicted dynamic modulus as the criterion for selecting the optimal number of Prony terms included. Figure 9 presents a graphical comparison of the master curves for the selected HMA mixes. The dynamic modulus curves were generated using the Prony series coefficients enumerated in Table 5.

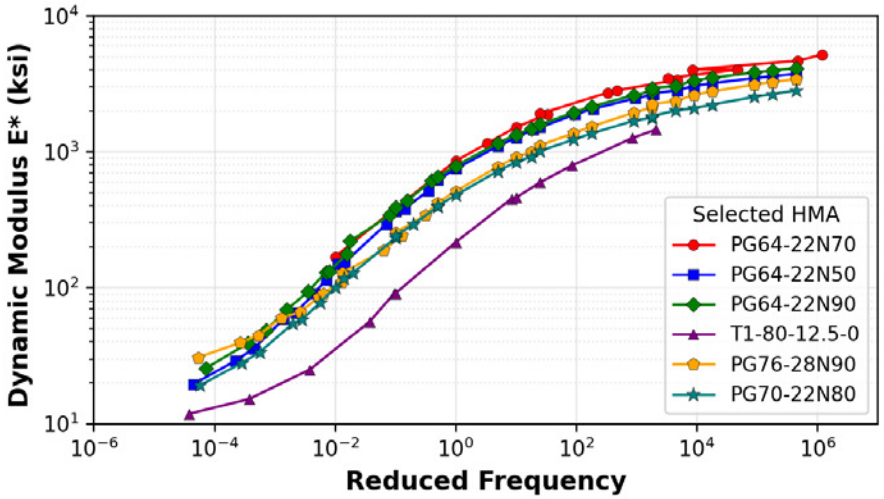

Figure 9. Graph. HMA linear viscoelastic material characterization.

PG64-22N70, used as a surface layer for the typical-thick and low-volume sections, had the highest E^* across all frequencies, which suggested a low potential for rutting and shoving. PG64-22N90, used in the binder layer of the full-depth and typical-thick sections, and PG64-22N50, used in the binder course of the low-volume section, had slightly lower but comparable moduli values. PG76-28N90, used as an intermediate course in the full-depth section, and PG70-22N90, used as a binder course in the SMA overlay section, showed moderate moduli values. As expected, PG76-28N90, a modified binder, showed relatively higher modulus at high frequencies. T1-80-12.5-0, used as a surface course in the SMA overlay and full-depth section, evidenced the lowest modulus, showing significantly lower modulus across the entire frequency range.

Table 5. Prony Series Coefficients for HMA Characterization

PG64-22N70		**PG64-22N50**		**PG64-22N90**	
τ_i	$\overline{g}_i, \overline{k}_i$	τ_i	$\overline{g}_i, \overline{k}_i$	τ_i	$\overline{g}_i, \overline{k}_i$
6.28E+00	2.11E+03	1.00E-05	5.16E+03	1.00E-05	5.84E+03
1.49E-02	6.45E+03	7.36E-05	2.65E+03	7.36E-05	3.03E+03
1.00E-03	6.20E+03	5.41E-04	3.99E+03	5.41E-04	4.77E+03
2.39E-01	5.57E+03	3.98E-03	3.95E+03	3.98E-03	4.06E+03
4.75E-05	7.35E+03	2.93E-02	3.52E+03	2.93E-02	3.65E+03
2.88E-07	1.14E+04	2.15E-01	2.67E+03	2.15E-01	2.68E+03
		1.59E+00	1.58E+03	1.59E+00	1.72E+03
		1.17E+01	6.93E+02	1.17E+01	7.45E+02
		8.58E+01	2.63E+02	8.58E+01	3.10E+02
		6.31E+02	1.04E+02	6.31E+02	1.03E+02
		4.64E+03	4.67E+01	4.64E+03	5.21E+01
		1.00E+08	1.05E+02	1.00E+08	1.33E+02
T1-80-12.5-0		**PG76-28N90**		**PG70-22N90**	
τ_i	$\overline{g}_i, \overline{k}_i$	τ_i	$\overline{g}_i, \overline{k}_i$	τ_i	$\overline{g}_i, \overline{k}_i$
1.00E-05	6.20E+03	1.00E-05	5.97E+03	1.00E-05	4.87E+03
5.40E-05	2.40E+03	7.40E-05	2.93E+03	7.36E-05	1.95E+03
2.93E-04	2.61E+03	5.41E-04	4.07E+03	5.41E-04	3.01E+03
1.59E-03	2.04E+03	3.98E-03	3.06E+03	3.98E-03	2.58E+03
8.58E-03	1.80E+03	2.93E-02	2.70E+03	2.93E-02	2.38E+03
4.64E-02	1.18E+03	2.15E-01	1.68E+03	2.15E-01	1.56E+03
2.51E-01	6.28E+02	1.59E+00	1.01E+03	1.59E+00	1.03E+03
1.36E+00	3.35E+02	1.17E+01	4.14E+02	1.17E+01	4.34E+02
7.36E+00	1.81E+02	8.58E+01	2.05E+02	8.58E+01	2.07E+02
3.98E+01	5.16E+01	6.31E+02	8.46E+01	6.31E+02	6.63E+01
2.15E+02	3.87E+01			4.64E+03	5.81E+01
1.17E+03	1.30E+01			1.00E+08	7.71E+01
6.31E+03	1.13E+01				

The elastic modulus (E_c), Poisson's ratio, and density for concrete materials were determined as 8,000 ksi, 0.20, and 150 lb/ft^3, respectively (Kohler et al., 2002). The stress-dependency of granular layers significantly influenced HMA responses (Wang & Al-Qadi, 2013). Hence, unbound nonlinearity must be considered when thin HMA layers exist. Cross-anisotropy assumed that the material exhibits axisymmetric behavior with different stiffness properties in the vertical and horizontal directions. Empirical formulations have been developed to estimate cross-anisotropic properties from repeated load triaxial tests with only vertical deformation measurements (Tutumluer & Thompson, 1997, 1998). Table 6 summarizes the k-values for the granular materials selected for this study.

Table 6. Assumed k-values of the Stress-Dependent Model for Granular Materials

Label	Granular Layer	Vertical Modulus (MPa)	Horizontal Modulus	Shear Modulus
IS-BS	Base	k_1=k_4=k_7=601.0	k_2=k_5= k_8= 0.106	k_3=k_6= k_9= 0.168
IS-SB	Subbase	k_1=k_4=k_7=545.0	k_2=k_5= k_8= 0.062	k_3=k_6= k_9= 0.110

Subgrade layers were assumed to be linear elastic, as the stresses transmitted to this layer were relatively low (i.e., low stress dependence). The subgrade and stabilized base elastic modulus, Poison's ratio, and density assumed were 10 and 58 psi, 0.40 and 0.43, and 93.6 and 124.9 lb/ft^3, respectively. Moreover, the stick-slip friction model was used at the interface between HMA and other layers (Romanoschi & Metcalf, 2001; Yoo et al., 2006).

Pavement Loading Simulation

The response of pavement systems to traffic and environmental conditions depends heavily on applied loads and distribution over time. Understanding 3D contact stresses, representing continuous moving loads, and imposing adequate temperature profiles across layers are essential steps toward accurately predicting pavement responses. As discussed in Chapter 2, a FE model of a 275/80R22.5 truck tire was developed, which is representative of a single unit in DTA, commonly found on heavy-duty trucks or semitrucks. Rolling simulations were conducted at a constant tire inflation of 100 psi across eight different load conditions. Changes in acceleration and traction forces were induced by adjusting the slip ratio parameter. Through this approach, the contact area and stress distribution varied due to both vertical axle load and acceleration level, providing a better representation of real-world conditions. Detailed information about the formulation, verification, and validation procedures carried out during the development of the model can be found in Chapter 2 of this report and has also been reported in Hernandez et al. (2025).

A key advantage of this modeling strategy is its ability to capture the effect of power trains—including those between ICs and HDEVs—on pavement loading and responses. Because HDEVs can deliver higher torque at a faster rate than ICs, greater in-plane forces on the tire-pavement interface are expected and may not be overlooked. While increased load has a much greater impact on 3D contact stresses than the change in speed for both IC and HDEV, the FE simulations revealed that elevated torque demands significantly affected longitudinal contact forces.

As observed in Figure 10, the longitudinal contact stresses exhibited alternating compression and tension zones. However, under acceleration, larger and more concentrated tension zones are present within the contact patch. Accurately capturing stress distribution changes in each direction is crucial to assess potential distress mechanisms such as increased shoving or top-down fatigue cracking in flexible pavements subjected to HDEV traffic.

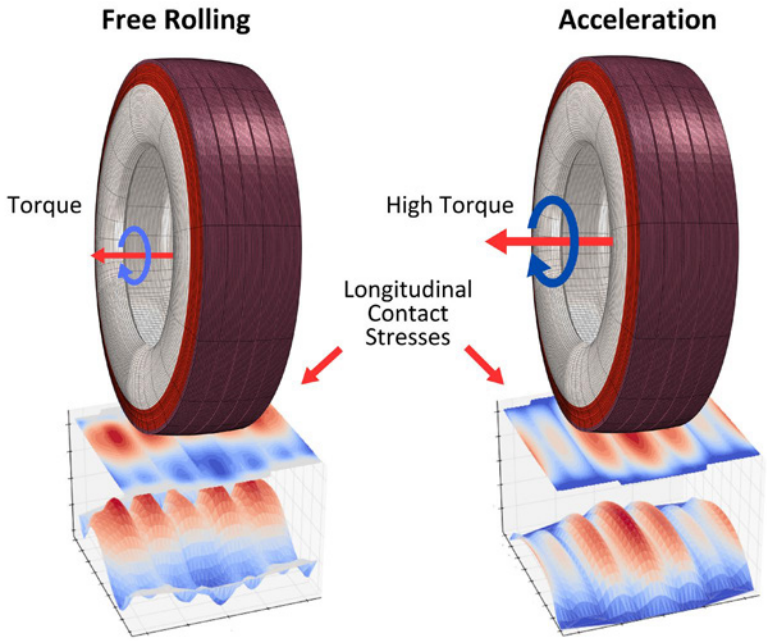

Figure 10. Schematic. Change in longitudinal contact stress distribution due to HDEVs' high torque (contour fill, contour, and 3D surface representation of contact stresses).

To simulate a continuous tire movement along the wheel path of a road at a defined speed, the initial step applied the tire load to the starting segment of the pavement model. This load was then systematically shifted along the longitudinal direction—aligned with the assumed traffic flow—to replicate a full single pass. As depicted in Figure 11, the varying contact stresses imposed by the truck tire were first distributed across the footprint region. Next, these contact stresses were shifted incrementally to adjacent elements of the mesh grid, keeping constant the total number of elements under load. The FE mesh within the wheel path region was designed so that the length of the imprint zone matched a fixed ratio between the tire imprint size and the element size, avoiding undesired gaps or overlaps as the loading zone was shifted.

Following the methodology described by Yoo and Al-Qadi (2007), where the total longitudinal distance over which the tire travels was approximately 39.40 in, a sufficiently large segment to represent the wheel path was ensured so that the complete effect of a moving load could be captured. The wheel path in this study ranged from 50.40 in to 55.12 in. The range of load magnitudes yielded tire imprints from 7.87 in to 12.60 in, leading to an element size of roughly 0.80 in. As each incremental shift in load controlled the stresses within the pavement structure, the number of elements by which the load was shifted was evaluated at various increments. Al-Qadi et al. (2018) demonstrated that shifting the load by three elements per time step proved to be an optimal

strategy. Table 7 summarizes the wheel path length, contact length, and element size used in the FE highway pavement model for each axle load at a slip ratio of 0%. With increasing load magnitude, the contact length increased, but the element size along the traveling direction was kept constant. Although real-world truck loading typically involves multiple-axle load configurations (e.g., tandem, tridem) spaced longitudinally, loads herein were represented using a conventional single-wheel or single-axle approach, as illustrated in Figure 12.

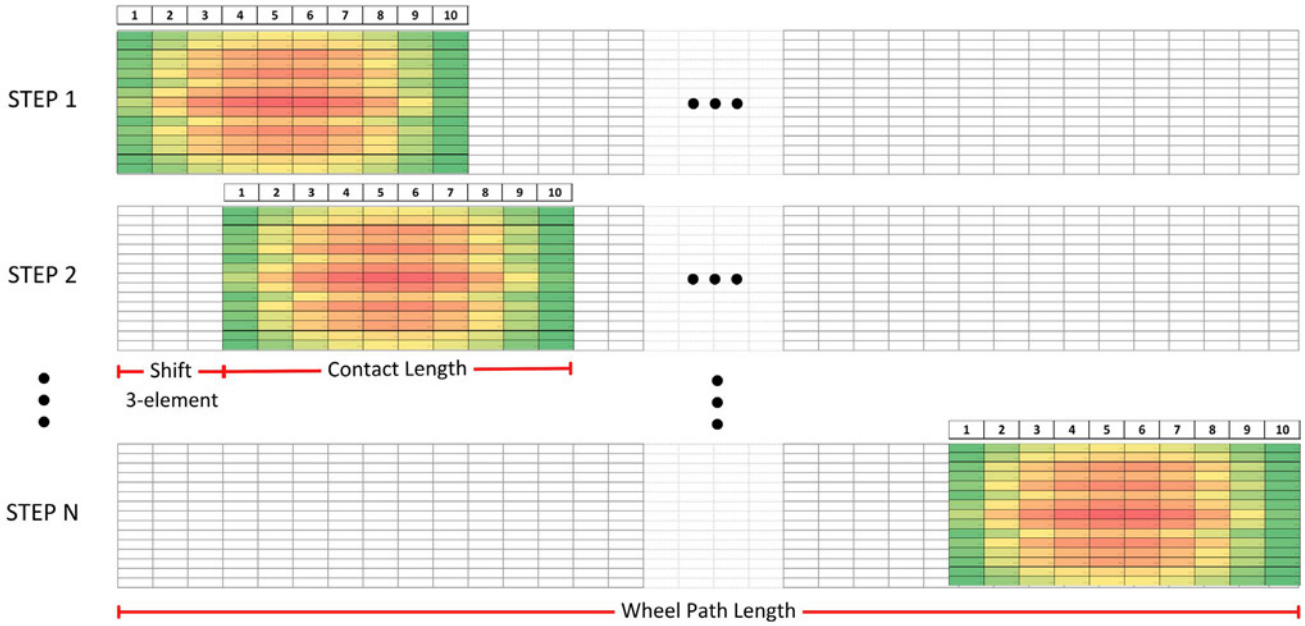

Figure 11. Schematic. Step loading of the tire imprint over the 3D FE model.

Table 7. Loading Area Geometry Configuration

Nomenclature	Tire Type	Load (kips)	Contact Length (in)
P1	Steering	6.00	9.45
P2	DTA	4.20	7.87
P3	Steering	9.50	12.60
P4	DTA	4.70	7.87
P5	Steering	7.00	10.24
P6	DTA	4.20	7.87
P7	DTA	3.60	7.87
P8	Steering	5.00	8.66

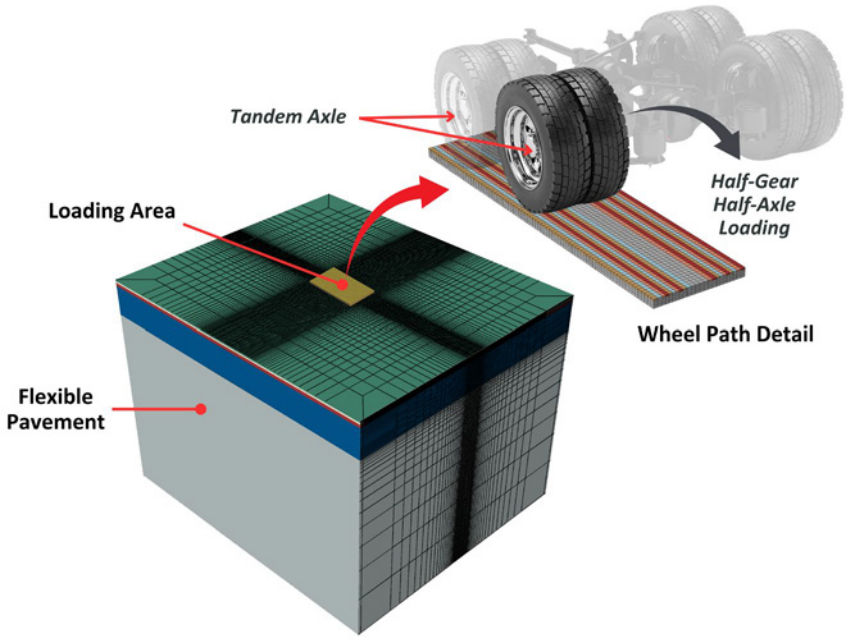

Figure 12. Schematic. Axle load configuration on highway FE pavement model.

Pavement Temperature Profile

The mechanical behavior of an HMA layer is dependent not only on loading conditions and rate, but also on environmental conditions. As temperature reduces, HMA becomes stiffer (more elastic), whereas it softens (more viscous) at higher temperatures, thereby creating significant variations in the modulus and the corresponding stress-strain response of a pavement structure. This study imposed a temperature profile throughout the HMA depth based on the procedure described by Wang et al. (2009) in lieu of a uniform temperature that can lead to inaccurate results. For this study, the thermal conductivities of $\alpha_{AC} = 0.0226$ ft²/h and $\alpha_g = 0.0323$ ft²/h were used, together with thermal diffusivities of $\lambda_{AC} = 1.67$ BTU/h·ft·°F and $\lambda_g = 1.21$ BTU/h·ft·°F. Table 8 summarizes the critical temperature limits: maximum, minimum, and initial.

Table 8. Parameters for Temperature Distribution

Section	T_{max} (°F)	T_{min} (°F)	c (°F)	Shape Parameter
SMA Overlay	69.8	59.0	64.4	6
Typical Thick	69.8	59.0	64.4	6
Low Volume	69.8	59.0	64.4	6
Full Depth	69.8	59.0	64.4	6

Figure 13 displays temperature gradients along the depth for the four pavement structures considered in this study. The gradients illustrate a nonlinear distribution (although the gradient between adjacent elements is linear). Moreover, the temperature across the horizontal direction was assumed constant.

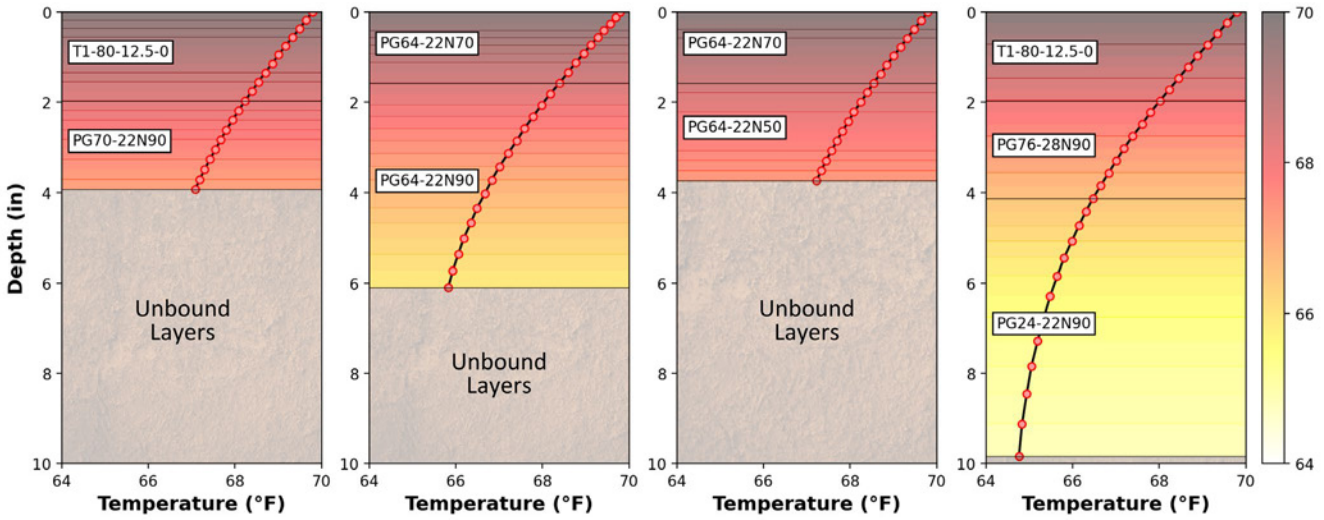

(a) SMA Overlay (b) Typical Thick (c) Low Volume (d) Full Depth

Figure 13. Schematic. Temperature profiles for the pavement sections.

Model Verification

The pavement model was verified by comparing the results of the FE model with the semi-analytical solution coded in WinJulea (a multilayered linear elastic program used in MEPDG). The verification was performed for each pavement structure considered, and the optimized size and type of the finite element in the model were provided. Appendix D provides the details of the calculation and the final mesh configuration in the vertical, longitudinal, and lateral directions.

NUMERICAL MATRIX OF SIMULATED PAVEMENT STRUCTURES

Each of the four selected pavement sections (full depth, typical thick, SMA overlay, and low volume) was simulated under a set of loading conditions. Figure 14 summarizes the combinations of steer tire and DTA loading, as well as slip ratio combinations, reflecting the three battery pack locations (detailed in Chapter 2) illustrated in Figure 2. To assess the independent effect of each variable considered in the numerical matrix, selected cases were grouped into categories. The loading scenarios are labeled based on the tire (S and D for steering and dual-tire assembly, respectively) and vehicle type ($ICEV$ and $HDEV$). In this context, SIC refers to a steering wheel load of the standard $ICEV$ axle weight distribution, while DIC refers to a DTA load. For instance, "DEV, 4.7 kips, 0%" considered a DTA load of the HDEV axle scenario with 4.7 kips (single-tire loading) and a 0% slip ratio. In reference to Figure 2, loads $P1$ and $P2$ represent the steering and drive axle tire loads for an IC, respectively, while $P3$, $P4$, $P5$, $P6$, $P7$ and $P8$ are derived from the three scenarios of the assumed HDEV battery pack locations. To account for different rolling conditions, 2% and 3% slip ratios were used for most cases. Additional cases were added to evaluate slip ratios as high as 6%.

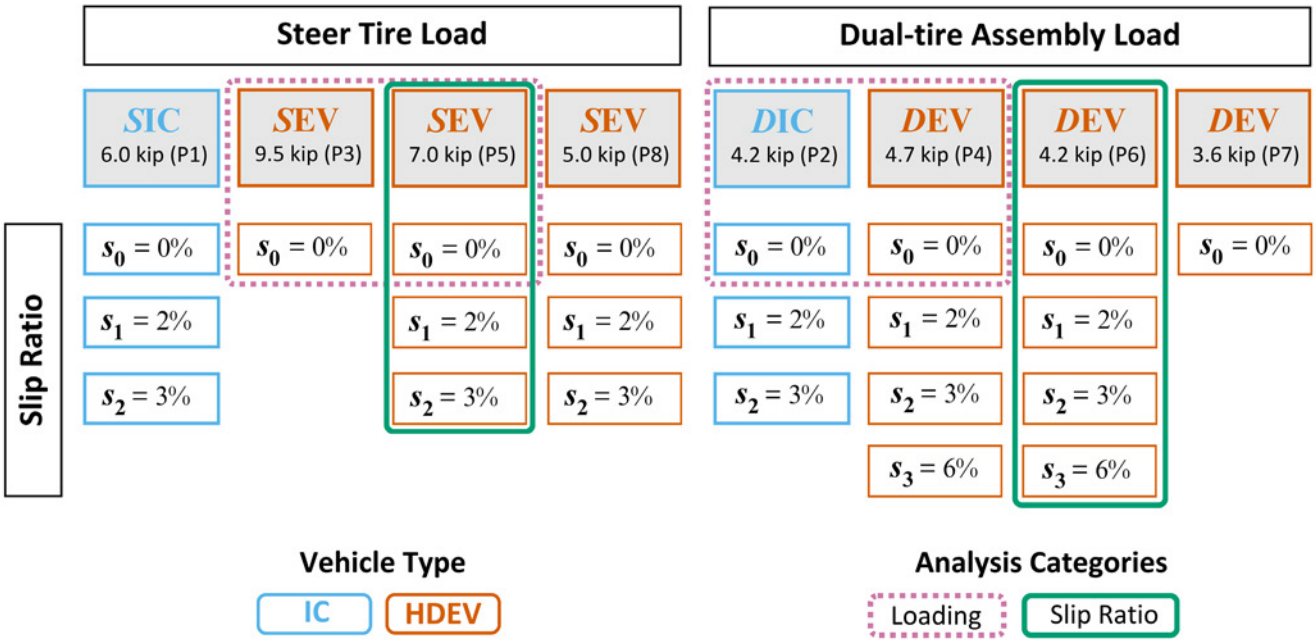

Figure 14. Schematic. Loading and slip ratio combinations for steer tire and DTA.

CRITICAL PAVEMENT STRAIN RESPONSES

The FE model allowed for a detailed computation of pavement responses to predict and quantify critical strains and their corresponding locations under given loading conditions, including the following:

- Tensile strain at the bottom of the HMA layer ($\varepsilon_{HMA_{11}}$ or $\varepsilon_{HMA_{33}}$ in the longitudinal and transverse directions, respectively) for bottom-up fatigue cracking
- Tensile strain at the surface of the HMA layer ($\varepsilon_{surf_{33}}$) for top-down cracking
- Longitudinal shear strain within the HMA layers ($\varepsilon_{HMA_{13}}$) for HMA shoving
- Vertical shear strain within the HMA layer ($\varepsilon_{HMA_{23}}$) for near-surface cracking
- Compressive strain within the HMA layer ($\varepsilon_{HMA_{22}}$) for rutting
- Compressive strain within the unbound layers—base and subbase—($\varepsilon_{B_{22}}$) for rutting
- Vertical shear strain within the unbound layers—base and subbase—($\varepsilon_{B_{23}}$)
- Compressive strain at the top of the subgrade ($\varepsilon_{SG_{22}}$) for rutting

The following section discusses the influence of each parameter included in the numerical matrix (Figure 14) for a sample pavement section for brevity, followed by a summary of the findings for the resulting critical strains. Appendix E provides summary plots of all pavement responses.

Load Magnitude Impact

Two sets of cases were selected to assess the influence of load magnitude on strain distributions: $P1$ and $P5$ for the steering axle and $P2$ and $P4$ for the DTA. Figure 15 depicts the changes in the longitudinal tensile, vertical shear, and compressive strains along the depth of the typical-thick HMA pavement section (Figure 8-a). The strain profiles were extracted along the critical strain $\varepsilon_{HMA_{11}}$ location for each loading scenario. An increase of 1.0 kip between the steering wheel loads $P1$ and $P5$ induced higher strains throughout the pavement depth, reflected in increases of 15%, 16%, and 19% in $\varepsilon_{HMA_{11}}$, $\varepsilon_{HMA_{23}}$, and $\varepsilon_{SG_{22}}$, respectively (Figure 15-a through Figure 15-c). Given that there is only a 0.5-kip increment between the DTA loads $P2$ and $P4$, the impact was lower than that of the steering wheel loads. However, increases of 11%, 11%, and 15% are still reported for $\varepsilon_{HMA_{11}}$, $\varepsilon_{HMA_{23}}$, and $\varepsilon_{SG_{22}}$, respectively (Figure 15-d through Figure 15-f).

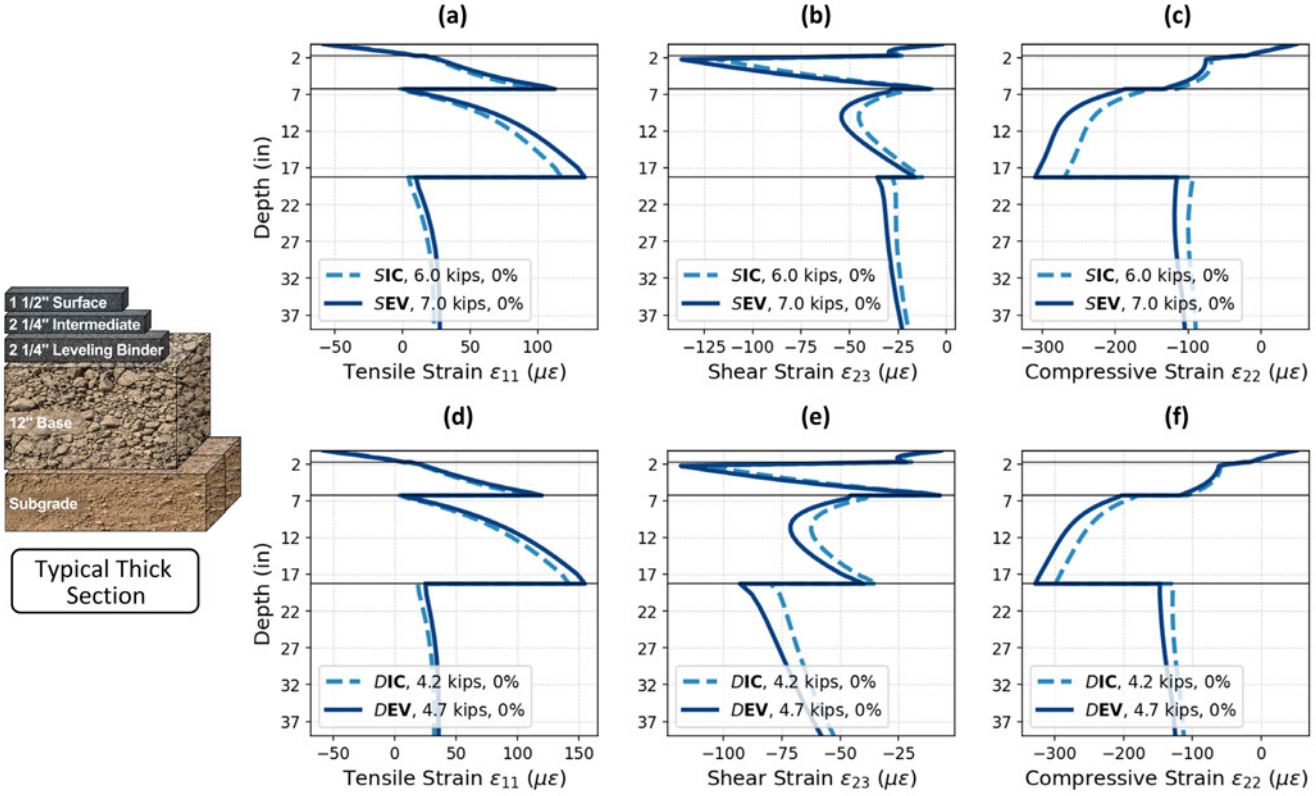

Figure 15. Graph. Effect of load magnitude on pavement response distributions.

Slip Ratio Impact

Similarly, two sets of loads were selected to evaluate the impact of the slip ratio. $P5$ at slip ratios 0% and 3% were selected to compare the steering load at varying acceleration levels. Changes in the longitudinal tensile, vertical shear, and compressive strains along the depth are displayed in Figure 16-a through Figure 16-c, respectively. The slip ratio did not significantly influence the distributions. A change in ε_{HMA23} sign was observed; however, its absolute magnitude changed marginally. The differences between the critical responses $\varepsilon_{HMA_{11}}$, $\varepsilon_{HMA_{23}}$, and $\varepsilon_{SG_{22}}$ were 3%, 4%, and 2%, respectively. The shift in the strain distribution sign was a consequence of the change in the location

of $\varepsilon_{HMA_{23}}$, which was located slightly further away from the tire edge. Due to the nature of shear deformation, the shear strain generally exhibited opposite signs on different sides of the same plane.

When a greater change in the slip ratio was imposed, as represented by the DTA load $P6$ at 0% and 6% (Figure 16-d through Figure 16-f), the same trend was observed as that of the steer load cases. For the DTA cases, the critical responses $\varepsilon_{HMA_{11}}$, $\varepsilon_{HMA_{23}}$, and $\varepsilon_{SG_{22}}$ differed by 3%. These findings aligned with the fact that the impact of the slip ratio was constrained within the near-surface region rather than influencing responses at deeper locations.

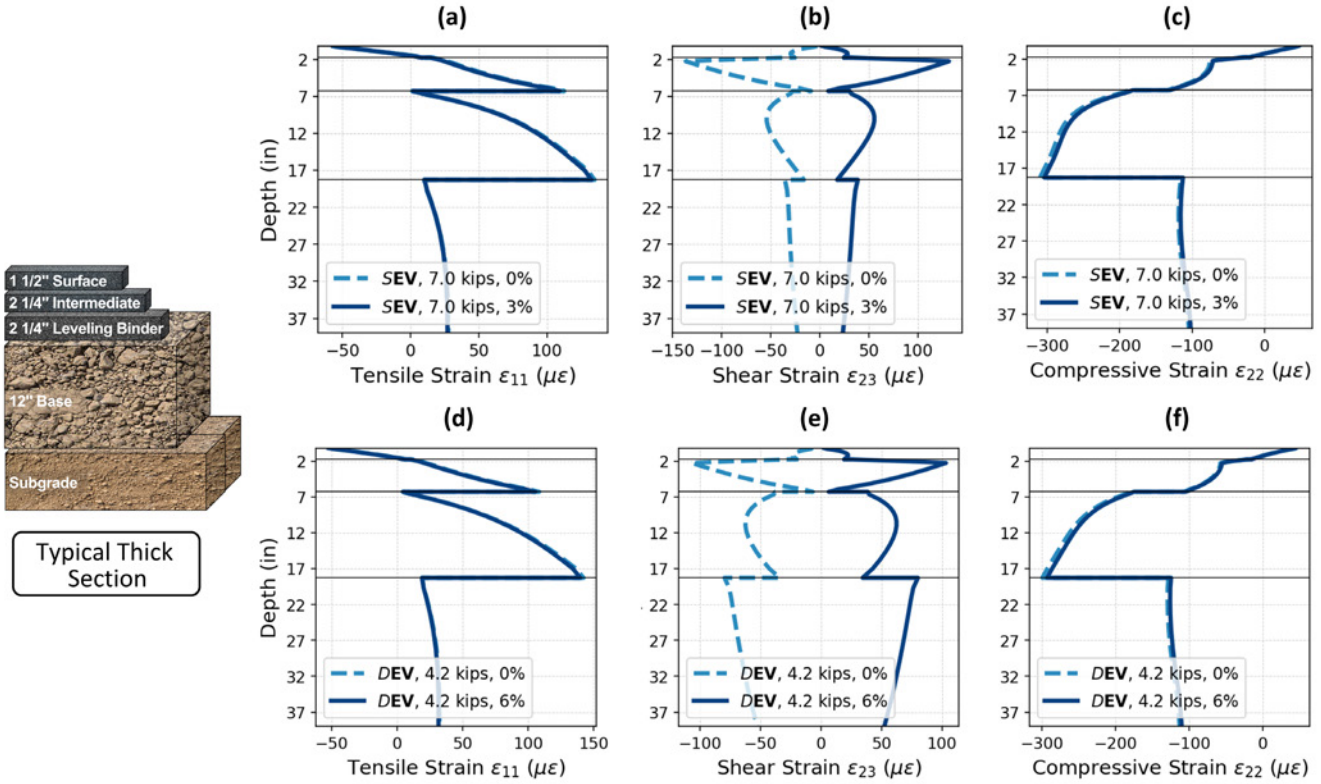

Figure 16. Graph. Effect of slip ratio on pavement response distributions.

To overcome such limitations, the analysis focused on the near-surface region (i.e., 4 in below the HMA surface). Traditionally, only the vertical shear component in the plane parallel to the tire edge ($\varepsilon_{HMA_{23}}$) is analyzed, but shear also includes components in the vertical plane perpendicular to the front of the tire ($\varepsilon_{HMA_{13}}$) and along the horizontal plane parallel to the load application ($\varepsilon_{HMA_{12}}$). The traveling direction of the tire load is along the 1-axis (longitudinal direction).

When focusing on the near-surface strain distribution of the shear components, ε_{HMA23} was barely altered as three different slip ratios were compared for the same DTA load (Figure 17-a). On the other hand, ε_{HMA12} only resulted in a change in sign with a marginal change in magnitude compared to a 0% slip ratio (see Figure 17-c). However, ε_{HMA13} resulted in a shift in the strain distribution in Figure 17-b, as the slip ratio increased from 0% to 6% for the DTA load of 4.2 kips (for both IC and HDEV). When comparing the critical values of $\varepsilon_{HMA_{13}}$ between the cases at 0% and 2% slip ratio, a 22%

difference was observed, while the cases at 0% and 6% slip ratios differed by 26% (Figure 17-b). Hence, the change in $\varepsilon_{HMA_{13}}$ may not be overlooked.

For some pavement configurations, such as the low-volume section (Figure 8-c), the near-surface shear components remained practically unchanged for small changes in the slip ratio between 0% and 2%. However, its influence in shear strain became evident in the supporting layers. Figure 18-b highlights that while ε_{HMA13} showed only a slight increase, it led to a more pronounced effect in the underlying base layer. The shear components ε_{HMA23} and ε_{HMA12} also exhibited noticeable variations as the slip ratio increased (Figure 18-a and Figure 18-c, respectively).

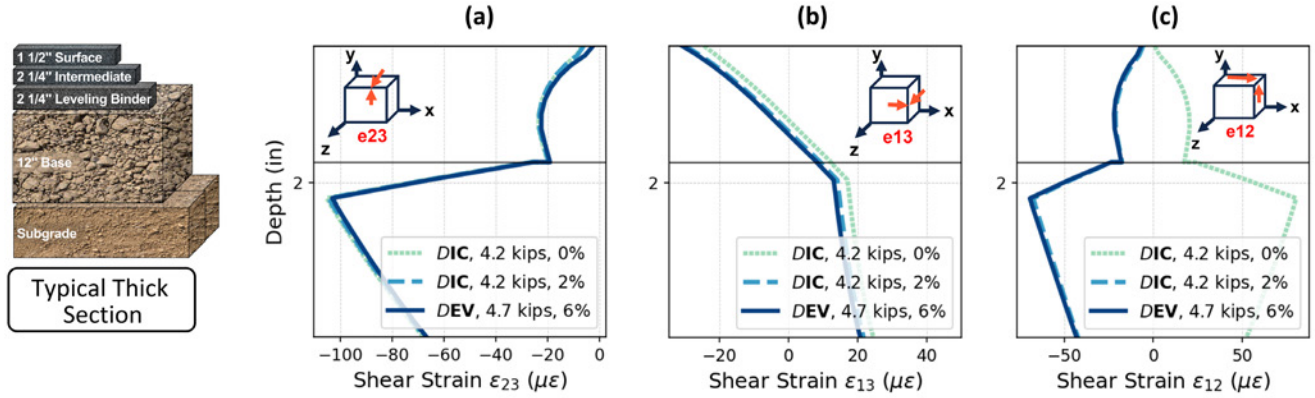

Figure 17. Graph. Effect of slip ratio on near-surface shear components.

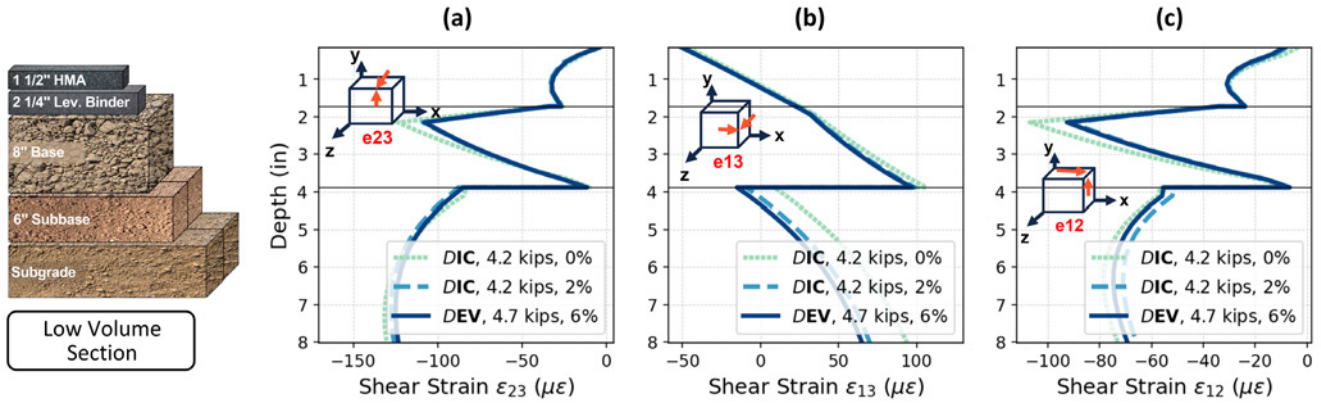

Figure 18. Graph. Effect of slip ratio on base shear.

Although the four pavement structures yielded critical responses at varying magnitudes and strain distributions along the depth, the aforementioned trends were generally maintained. Table 9 provides a high-level summary of the slip ratio and load impacts by IC and HDEV on pavement responses. Relative arrow indicators are used for each critical pavement response (i.e., increase ↑, higher increase ↑↑, reduction ↓, or marginal change ↔.)

The slip ratio influenced sections with relatively thicker HMA layers or those with a supporting layer with high modulus (e.g., PCC). Particularly, the full-depth section and the section with PCC overlaid

with SMA experienced higher ε_{13} at a 0% slip ratio compared to the other structures. However, as the slip ratio increased, these sections experienced a significant rise in ε_{13}, which could be attributed to larger in-plane contact stresses generated under acceleration. This indicated that sections with stiffer sublayers were more sensitive to slip-induced shearing effects, which could potentially accelerate near-surface cracking.

Table 9. Impact of Load Magnitude and Slip Ratio on Select Critical Pavement Responses

	SMA Overlay	Typical Pavement	Full Depth	Low Volume
Slip ratio of 0%, Increased tire load	Tensile strain ε_{HMA11} at HMA bottom			
	↑	↑↑	↑	↑↑
	Shear strain ε_{HMA23} within HMA near-surface			
	↑↑	↑	↑↑	↑
	Shear strain ε_{13} within HMA near-surface			
	↑↑	↑	↑↑	↑
	Compressive strain $\varepsilon_{SG_{22}}$ at the top of SG			
	↑	↑	↑	↑
Constant load, Increased slip ratio	Tensile strain ε_{HMA11} at HMA bottom			
	↔	↔	↔	↔
	Shear strain ε_{HMA23} within HMA near-surface			
	↓	↔	↔	↔
	Shear strain ε_{HMA13} within HMA near-surface			
	↑↑	↑	↑↑	↑
	Compressive strain $\varepsilon_{SG_{22}}$ at the top of SG			
	↔	↔	↔	↔

Figure 19 summarizes the critical responses for the four pavement sections under various loading and slip ratio combinations. A higher load magnitude induced higher pavement responses, wherein the typical-thick and low-volume sections yielded a considerable increase in $\varepsilon_{HMA_{11}}$ (which generally decreased as HMA thickness increased). This trend aligned with expectations, as thicker HMA layers provided greater structural support. The full-depth and SMA overlay sections resulted in higher $\varepsilon_{HMA_{23}}$ and $\varepsilon_{HMA_{13}}$, suggesting these pavement sections experienced more pronounced shear deformations, particularly in near-surface layers. Similarly, $\varepsilon_{SG_{22}}$ was governed by the increase in load magnitude, especially for structures with thinner HMA layers—namely, the low-volume and typical-thick sections. This indicates that the subgrade layer in these sections was more susceptible to vertical compressive strains, which could accelerate permanent deformation.

Moreover, a marginal increase in $\varepsilon_{SG_{22}}$ for the SMA overlay section was expected due to the presence of the PCC layer, which helped distribute and reduce the applied stress more effectively as it transferred to the unbound layers. Overall, the vertical compressive strain at the top of the subgrade is governed by the type and thickness of the upper layer. In contrast, the near-surface vertical shear strain was significantly greater than the other strain components for the full-depth and SMA overlay sections, indicating the impact of contact stresses on near-surface pavement behavior. The

differences in strain responses between pavement sections emphasized the importance of selecting appropriate layer configurations to balance fatigue, rutting, and shear-driven distresses. For instance, while a full-depth section might alleviate potential fatigue and rutting, it might require HMA with modified binder to counteract near-surface shear strains.

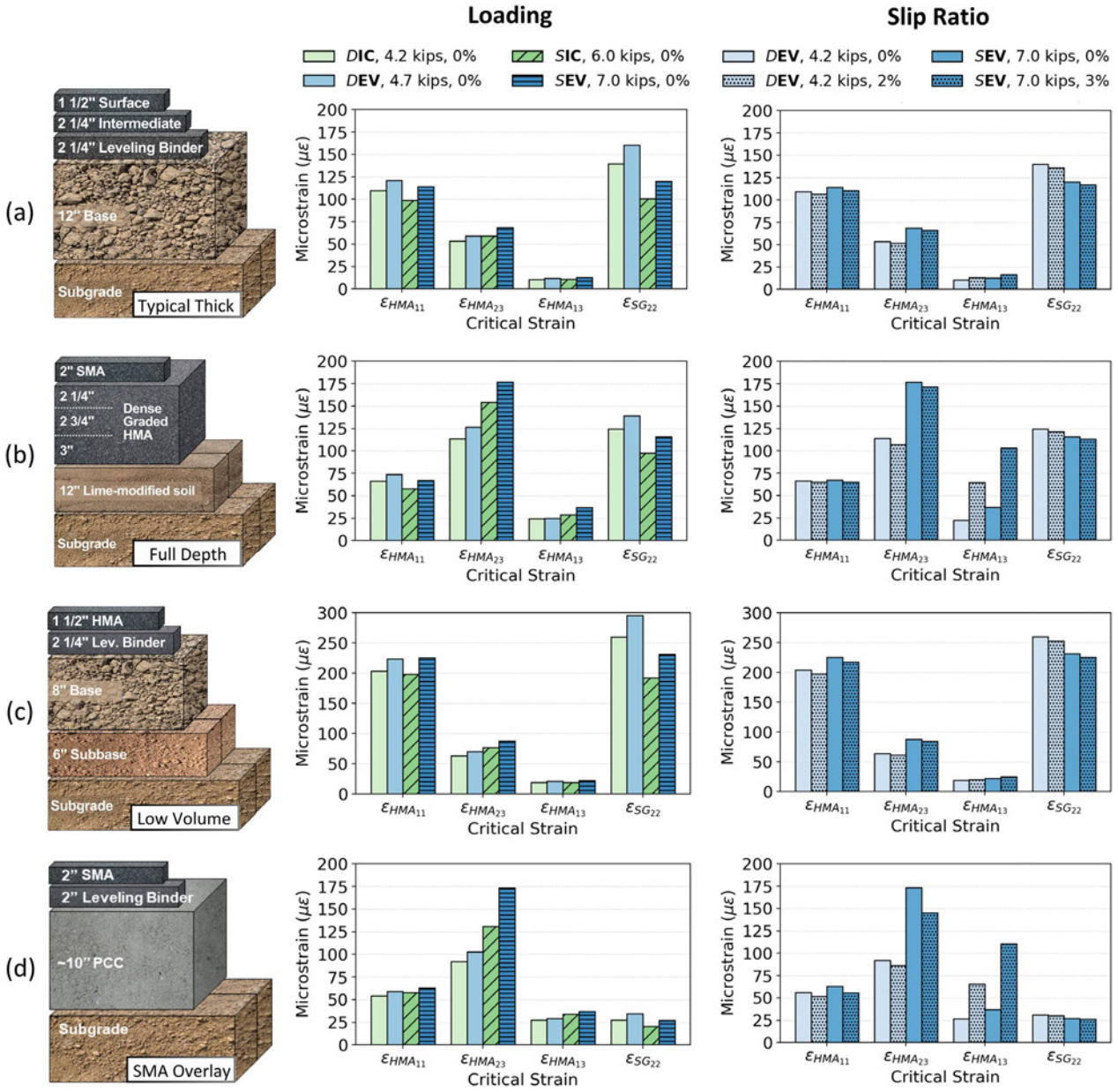

Figure 19. Graph. Summary of critical responses for (a) typical-thick, (b) full-depth, (c) low-volume, and (d) SMA-overlay sections.

PAVEMENT FAILURE CRITERIA

The MEPDG transfer functions were leveraged to evaluate pavement distresses through a quantitative relationship between the associated critical response and resulting service life or distress

threshold value. The resulting metric is the number of load applications (N) a pavement section could endure before a given distress reaches failure. Using AASHTO equations (2020), the calculated allowable axle load applications are presented for HMA fatigue cracking (Figure 20, Figure 21, and Figure 22) and shoving (Figure 23). The MEPDG transfer function for top-down fatigue cracking is presented in Figure 20 and Figure 22, which used the tensile strain at the HMA's surface ($\varepsilon_{surf_{33}}$) as an input. However, because of the importance of shear strain components for the present study, it was deemed appropriate to use the vertical shear component ε_{HMA23} as an input instead, because it is a key pavement response driving near-surface top-down cracking.

$$N_f = k_{f1} \cdot C \cdot C_H \cdot \beta_{f1} \cdot {\varepsilon_t}^{k_{f2} \cdot \beta_{f2}} \cdot {E_{HMA}}^{k_{f3} \cdot \beta_{f3}}$$

$$C = 10^M$$

$$M = 4.84 \cdot \left(\frac{V_{be}}{V_a + V_{be}} - 0.69 \right)$$

Figure 20. Equation. Fatigue cracking transfer function.

where: N_f= number of allowable load applications

ε_t = critical tensile strain

E_{HMA} = HMA dynamic modulus (psi)

k_{f1}, k_{f2}, k_{f3} = global calibration parameters (k_{f1}= 0.007566, k_{f2}= −3.9492, k_{f3}= −1.281)

β_{f1}, β_{f2}, β_{f3} = global calibration parameters (β_{f1}= β_{f2}= β_{f3}= 1.0)

V_{be} = effective asphalt content (% volume)

V_a = percent of air voids in the HMA mixture

C_H = thickness correction term

The thickness correction term C_H depends on the cracking type, and the corresponding expressions for bottom-up and top-down fatigue cracking are presented below:

$$C_H = \frac{1}{0.000398 + \frac{0.003602}{1 + e^{11.02 - 3.49 \cdot H_{HMA}}}}$$

Figure 21. Equation. Bottom-up fatigue cracking thickness correction term.

$$C_H = \frac{1}{0.01 + \frac{12.00}{1 + e^{15.676 - 2.816 \cdot H_{HMA}}}}$$

Figure 22. Equation. Top-down fatigue cracking thickness correction term.

where: H_{HMA}= total HMA thickness (in)

$$\Delta_{p\ (HMA)} = \varepsilon_{p(HMA)} \cdot h_{HMA} = \beta_{1r} \cdot k_z \cdot \varepsilon_{r(HMA)} \cdot 10^{k_{1r}} \cdot n^{k_{2r} \cdot \beta_{2r}} \cdot T^{k_{3r} \cdot \beta_{3r}}$$

$$k_z = (C_1 + C_2 \cdot D) \cdot 0.328196^D$$

$$C_1 = -0.1039 \cdot {H_{HMA}}^2 + 2.4868 \cdot H_{HMA} - 17.342$$

$$C_2 = 0.0172 \cdot {H_{HMA}}^2 - 1.7331 \cdot H_{HMA} - 27.428$$

Figure 23. Equation. HMA rutting transfer function.

Where: $\Delta_{p\ (HMA)}$= accumulated or plastic vertical deformation in the HMA layer

$\varepsilon_{p(HMA)}$ = accumulated permanent or plastic axial strain in the HMA layer

$\varepsilon_{r(HMA)}$ = resilient or elastic strain calculated by structural response at mid-depth per sublayer

h_{HMA} = HMA layer thickness (in)

n = number of axle load repetitions

T = pavement temperature (°F)

k_{f1}, k_{f2}, k_{f3} = global calibration parameters (k_{f1}= −3.35412, k_{f2}= 0.4791, k_{f3}= 1.5606)

β_{f1}, β_{f2}, β_{f3} = global calibration parameters (β_{f1}= β_{f2}= β_{f3}= 1.0)

k_z = depth confinement factor

D= depth below the surface (in)

C_1, C_2 = depth correction factors

H_{HMA} = surface course thickness (in)

A transfer function to evaluate shoving in HMA does not exist. Instead, Hajj et al. (2007) provided a regression equation relating shoving that was observed via laboratory experiments in the material domain. For this study, it was not deemed appropriate to extrapolate material scale observations to the structural scale. Instead, the MEPDG transfer function for HMA rutting (Figure 23) was used and was in closest correspondence to shoving. In lieu of the vertical compressive strain, the longitudinal shear strain $\varepsilon_{HMA_{13}}$, which was impacted by HDEV loading conditions and aligned with the direction of shoving distress, was used as an input to the HMA rutting transfer function to evaluate permanent deformation. The research team acknowledges that the MEPDG transfer function was intended for vertical compressive strain. However, it was beyond the scope of this study to develop a shoving transfer function for HMA pavement structures.

Prior to estimating the number of repetitions per distress, the strain inputs obtained for each section are discussed. Figure 24 reveals distinct trends in tensile, vertical shear, and longitudinal shear strains. Noticeably $\varepsilon_{HMA_{11}}$ exhibited the highest magnitudes, particularly in the low-volume section, where values exceeded 200 $\mu\varepsilon$, indicating a greater susceptibility to bottom-up fatigue cracking. In contrast, SMA-overlay and full-depth sections showed significantly lower tensile strains. Vertical shear strains $\varepsilon_{HMA_{23}}$followed a different pattern, wherein full-depth and SMA-overlay sections exhibited the highest range and strain levels, suggesting these sections had concentrated shear forces more than those of the low-volume and typical-thick pavements. Hence, full-depth and SMA-overlay

sections are likely more susceptible to shoving and top-down fatigue cracking. Moreover, the longitudinal shear strain $\varepsilon_{HMA_{13}}$ remained the lowest among the three shear strain components, with relatively uniform values across all sections. The presence of the outliers in all strain components evidences sensitivity to loading conditions, particularly for the vertical shear strains, where the spread is more pronounced. Overall, the results showcased how strain distribution varied with pavement structure (i.e., thicker sections effectively reduced tensile strains but experienced higher near-surface shear strains). Additionally, pavement sections with higher strain variability might yield greater uncertainty in the predicted pavement life using the MEPDG transfer functions.

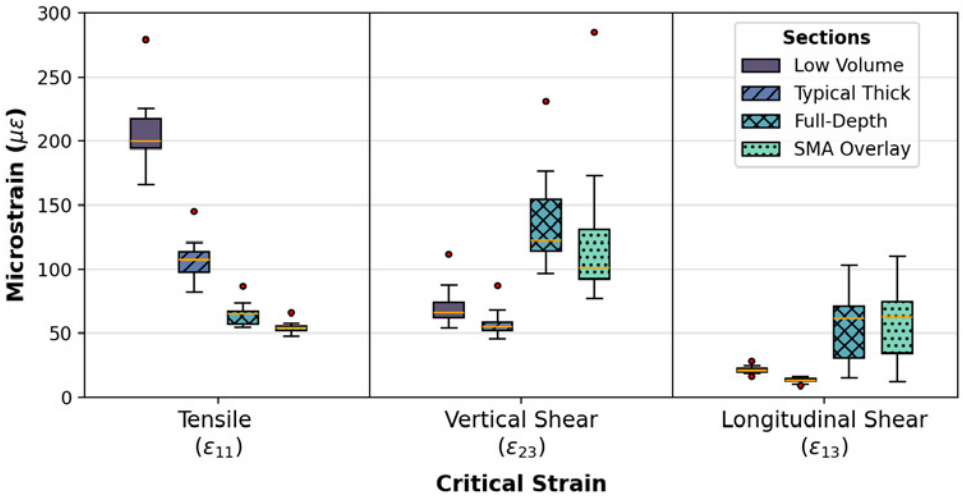

Figure 24. Graph. Spread of critical strains per distress per section.

Given that MEPDG uses an inverse exponential relationship between strain input and the number of repetitions N_f, small increases in strain may cause a drastic reduction in N_f. For instance, if the low-volume section experienced tensile strains more than twice those of the SMA-overlay sections, then the resulting fatigue life could be reduced by more than an order of magnitude (Figure 25).

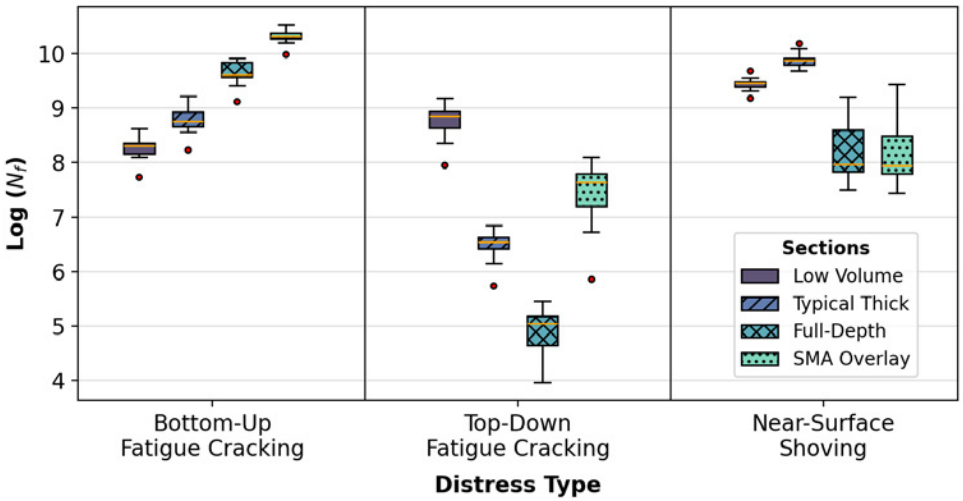

Figure 25. Graph. Spread of the number of repetitions per distress per section.

Moreover, bottom-up fatigue cracking presented the highest N_f, with the SMA section achieving the longest fatigue life, followed by the full-depth, typical-thick, and low-volume sections. In contrast, top-down fatigue cracking showed significantly lower N_f, with values that ranged multiple orders of magnitude from approximately 10^5 to 10^9, which indicated a much higher sensitivity to the inputs. It is worth noting that the full-depth section exhibited the lowest N_f for shear-driven top-down cracking. Near-surface shoving showed the least extreme differences, where SMA-overlay and typical-thick sections endured over 10^9 repetitions, while full-depth and low-volume sections ranged from 10^7 to 10^9. The multi-order magnitudes of difference across distress types led to the conception of the cumulative number of repetitions for a combined damage evaluation.

Cumulative Number of Repetitions and E-Truck Adjustment

To estimate the combined contribution of various distresses into service life, the concept of cumulative number of repetitions until failure (N^e) was introduced. N^e is defined as the weighted linear combination of the number of repetitions per distress N, and can be calculated as shown in Figure 26:

$$N^e = a_1 \cdot N_{BU} + a_2 \cdot N_{TDS} + a_3 \cdot N_{NSS}$$

Figure 26. Equation. Cumulative number of repetitions.

where: a_i = weighing factors

N_{BU} = number of repetitions for bottom-up fatigue cracking

N_{TDS} = number of repetitions for shear-driven top-down fatigue cracking

N_{NSS} = number of repetitions for near-surface shoving

Logarithmic Weights

Different types of distresses may occur simultaneously, but usually one leads to pavement failure. This study considered a weighted average across the relevant types of distress to determine pavement service life. The weighted approach helped to ensure transfer functions associated with lower log-scaled N values (fewer repetitions to failure) received a higher weight to account for a higher likelihood of driving the combined failure (Al-Qadi et al., 2005, 2018). The weighting factors a_i were calculated based on the inverse of the logarithmically scaled number of repetitions (Figure 27).

$$a_i = \frac{\frac{1}{log(N_i)}}{\sum_{j=1}^{m} \frac{1}{log(N_j)}}$$

Figure 27. Equation. Weighting factors.

where: N_i = number of distress-related load repetitions obtained for a specific case

N_j = number of repetitions of each failure mechanism considered

m = number of failure mechanisms considered

Although N^e aimed to establish a metric based on a cumulative number of repetitions from different failure mechanisms, it corresponded to a specific, single-axle loading condition and, therefore, is not sufficient to establish a framework to compare HDEVs and ICs as a full truck configuration.

E-Truck Adjustment

To compare different battery placement scenarios for a full truck, an index to contrast the damage of multi-axle configurations was defined so that the contribution from all axles was incorporated via a single metric. Leveraging Miner's (1945) linear damage rule, the linear cumulative damage D was defined as shown in Figure 28:

$$D = \sum_{i=1}^{k} \frac{n^t}{N_i^e}$$

Figure 28. Equation. Linear cumulative damage.

where: n^t = total number of truck passes
k = total number of axle-load conditions (or number of truck axles)
N_i^e = cumulative number of repetitions until failure for a given truck axle load

According to Miner's linear damage rule, failure occurs when $D \geq 1$. Given that each truck pass represented one loading cycle of each axle load (5 load passes for an 18-wheeler), n^t can be found by using a solver given the constraint that $D = 1$. In contrast to the N^e expression from Figure 26 that represents the combined number of repetitions for a single-axle load only, n^t represents an index for a full truck configuration, allowing a comparison of HDEV scenarios to that of a baseline IC case. By defining n_{ref}^t as the total number of truck passes that the baseline IC scenario could withstand, the ratio number of truck passes to failure of a reference case n_{ref}^t to that of a different scenario n_i^t was used to compute a relative damage index. However, the difference in the effective payload capacity between an HDE and an IC, as discussed in Chapter 2, must also be considered, as it implies a greater number of trips would be required to transport the same freight volume. To account for this, the e-truck adjustment (ETA) factor was introduced to represent these conditions. The ETA parameter can be computed via Figure 29.

$$ETA = \frac{W_{ref}^e}{W_i^e} \cdot \frac{n_{ref}^t}{n_i^t}$$

Figure 29. Equation. E-truck adjustment factor.

where: W_{ref}^e = payload capacity of the reference case (45 kips)
W_i^e = payload capacity of a given scenario (45 and 38 kips for IC and HDEV, respectively)
n_{ref}^t = total number of truck passes for the baseline IC scenario
n_i^t = total number of truck passes for a given scenario

While $n_{ref}^t/n_i^t < 1$ is indicative of an increase in the allowable number of truck cycles until failure (less damaging), and $n_{ref}^t/n_i^t > 1$ corresponds to a decrease in the expected number of truck passes a case can endure (more damaging), notice that the ETA could still be greater than one as long as $n_{ref}^t/n_i^t > 0.85$ when HDEV scenarios are assessed due to the difference in the effective payload. A general overview of the process of estimating the ETA is shown in Figure 30.

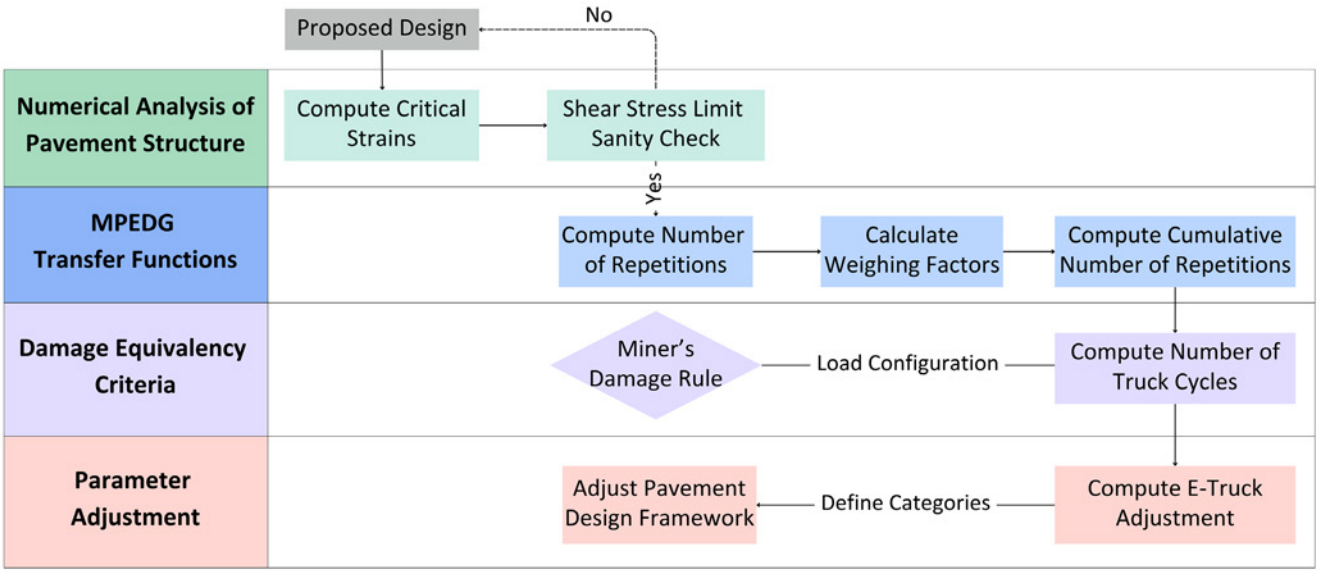

Figure 30. Schematic. E-truck adjustment estimation workflow.

Application of the E-Truck Adjustment

The pavement sections illustrated in Figure 8 served as a case study to demonstrate a detailed calculation of the ETA. Accounting for truck electrification in a forward approach of modifying pavement design input would require updating vehicle classification data, wherein HDEV data are currently not available. A simplified approach could be derived from the use of the calculated ETA values to scale the traffic input accordingly. However, ETA is dependent on loading conditions, axle load configuration, pavement structure, and the effective payload. Therefore, it may be cumbersome to compute ETA values for each specific scenario. Therefore, as part of this study, various ETA values were calculated for a set of qualitative categories based on battery placement alternatives as a preliminary effort at quantifying the impact of HDEVs on flexible pavements due to load redistribution and acceleration.

Full-Depth Section

The ETA factor results presented in Figure 31 highlight the pronounced impact of HDEVs on a full-depth section. The baseline IC scenario remained the least damaging configuration, with ETA values around 1.09 at mild acceleration levels. In contrast, the HDEV scenarios, particularly where the battery is placed on the steering axle, exhibited the highest ETA values at 1.67. Such factor indicated that localizing extra weight on the front axle led to the highest damage. However, it is worth noting that placing the battery on the steering axle is an extreme and unlikely scenario. Placing the battery

pack on the drive axle resulted in a moderate increase at a slip ratio of 0% (ETA = 1.36), but grew more pronounced as the slip ratio increased, wherein ETA was 1.55 and 1.54 for 2% to 3% slip ratios, respectively. This reflects the amplifying impact of higher acceleration levels as additional mass was concentrated on the drive axle. Even distribution of the battery weight across the steering and tractor axles resulted in slightly lower ETA factors (1.33 and 1.44 for 0% and 2% slip ratios, respectively) relative to concentrating the mass on any single axle. However, all HDEV cases resulted in greater ETA than those of the baseline IC.

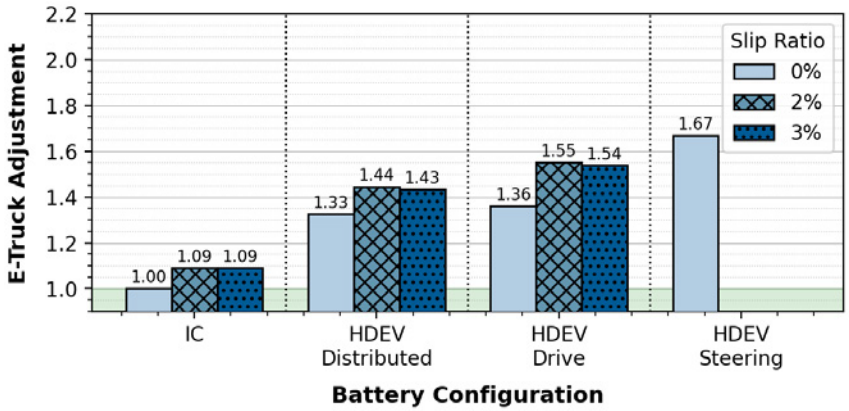

Figure 31. Graph. E-truck adjustment factors for the full-depth section.

Low-Volume Section

For the low-volume section, the ETA variation across slip ratio values was narrower than those of the full-depth section, as illustrated in Figure 32. For instance, evenly distributing the HDEV battery yielded ETA values of 1.30 at 0% slip ratio to 1.46 at 3% slip ratio, which emphasized the impact of a localized front-axle mass on pavement behavior. Shifting the battery mass to the drive axle led to a similar damage profile, with ETA marginally changing as the slip ratio increased from 2% to 3%. This finding is aligned with that of the pavement strains, wherein an increase in slip ratio from 0% to 2% led to more pronounced strain differences, whereas the change in slip ratio from 2% to 3% did not invoke a significant increase in pavement strains (a key input in transfer functions).

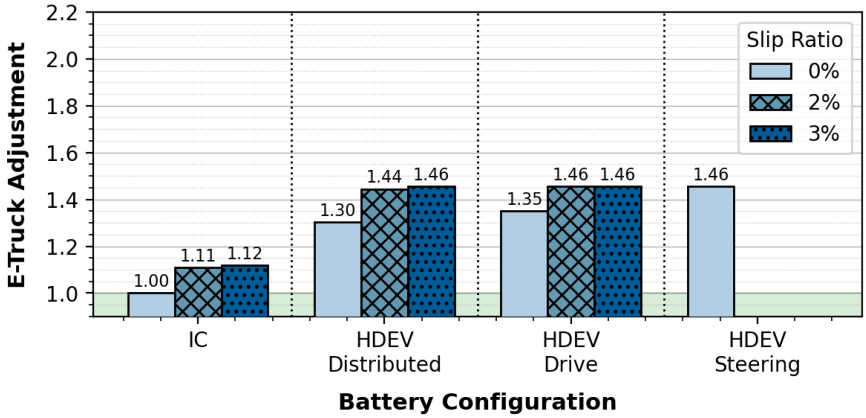

Figure 32. Graph. E-truck adjustment factors for the low-volume section.

Typical Thick Section

The typical thick section results revealed a severe jump from 1.00 to 1.46 at 2% slip ratio and 1.52 at 3% slip ratio for the baseline IC scenario (Figure 33). Compared to the low-volume section, adding the heavier electric battery caused significantly higher ETA values. On the other hand, given an evenly distributed battery weight scenario, the ETA increased from 1.29 at 0% slip ratio to 1.97 at 3% slip ratio. As shown previously (see Figure 19), the typical thick section experienced relatively lower shear strains when compared to other sections, impacting the computed number of repetitions for the failure mechanisms controlled by the longitudinal shear strain (related to near-surface shoving). Moreover, as the battery placement was assumed to be on the drive axle, ETA further increased to 2.04, indicating the influence of loading on a typical-thick HMA section. Interestingly, the steering-axle configuration did not result in the most critical case for this section. As the tensile strain observed in this section was higher than that observed in other sections, such as full depth, the service life to fatigue cracking decreased, which modified the contributions of this failure mechanism to the cumulative number of repetitions. Owing to the change in distributions, the ETA trends may differ with load and acceleration between all four sections.

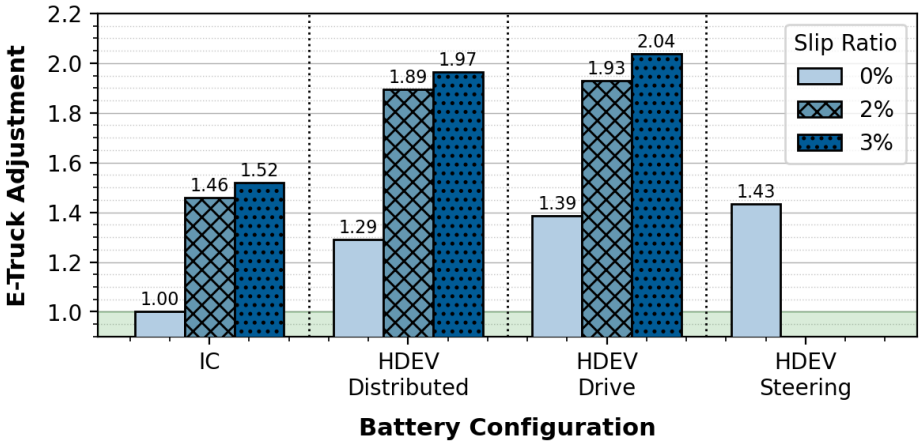

Figure 33. Graph. E-truck adjustment factors for the typical thick section.

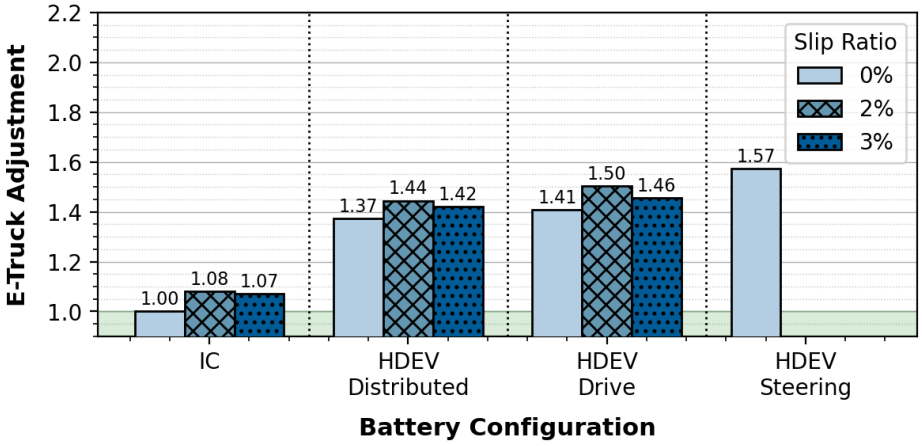

Figure 34. Graph. E-truck adjustment factors for SMA overlay.

SMA Overlay on PCC Section

The trend of the SMA-overlay-on-PCC section was similar to that of the full-depth and typical-thick sections. Distributing the battery weight more evenly reduced the ETA. However, the resulting values remained much greater than that of the baseline IC scenario, increasing up to 44% (Figure 34). Based on previous findings, a small difference in the slip ratio across the simulated cases did not yield a significant difference under the proposed framework compared to the impact of increased axle load (owing to the weight redistribution from the battery pack placement). Therefore, to summarize all e-truck adjustment factors, only a single qualitative category for acceleration was defined based on the values obtained at slip ratio 2%. Figure 35 showcases the final ETA values across all four pavement sections, where "no" and "yes" indicate the absence or inclusion of acceleration, respectively.

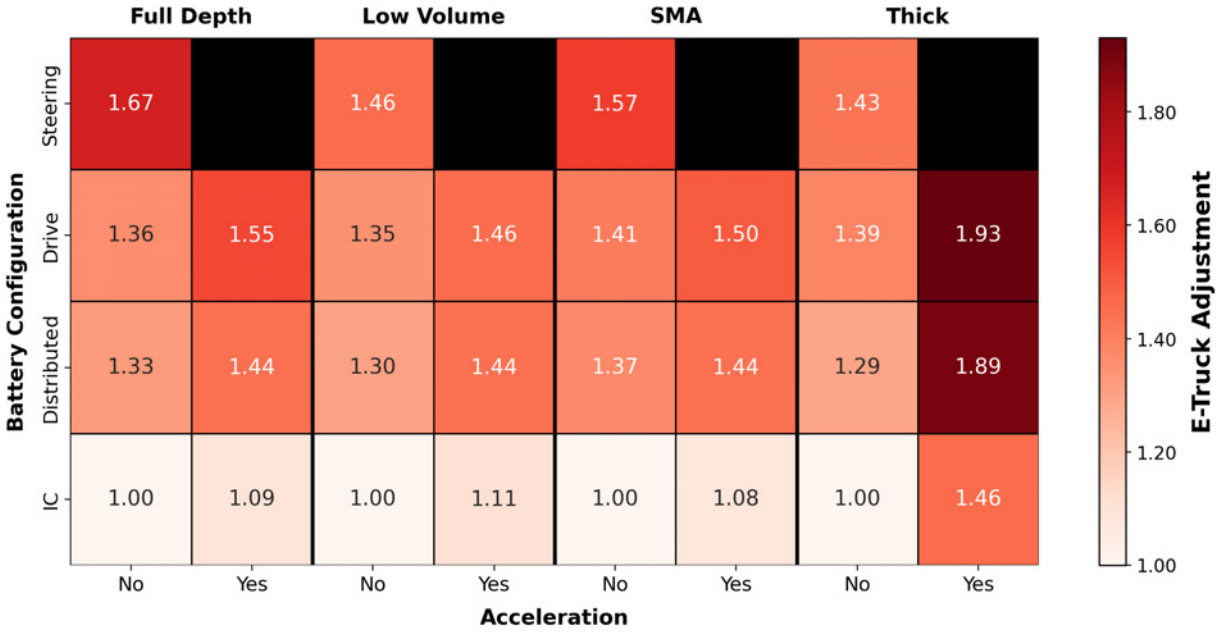

Figure 35. Graph. E-truck adjustment factors for all four Illinois sections.

Although the ETAs only represented two acceleration conditions, further computations could be deduced to extend the results to more specific qualitative categories (e.g., low, medium, high). The importance of adequately characterizing different acceleration levels lies in the fact that pavement sections are subjected to different loading conditions. While intersections, ramps, and exits experience frequent high-level braking and acceleration patterns, such patterns are typically less common on interstate highways under free-flow speed. However, HDEVs' access to high torque or faster braking/acceleration rate does not preclude such conditions on highways if quick braking/acceleration were necessitated, and it may depend on actual driver behavior.

In most pavement design frameworks in Illinois, damage should correspond to increased traffic factors (AASHTO, 2020; IDOT, 2022). However, data for increased axle loading of HDEVs do not exist for a forward-approach modification of traffic factors. Given that the resulting ETAs for HDEVs were greater than 1.0 (relative to the baseline IC scenario), an adjustment to traffic factors should be incorporated in pavement design to account for greater pavement damage induced by HDEVs.

SUMMARY

As transportation agencies prepare for increasing demands associated with truck electrification, adequate pavement design modifications are crucial to support electrified freight transport and long-term infrastructure resilience. This chapter's findings suggest that as HDEVs traverse roadway networks, a shift in pavement design strategies and rehabilitation schedules may be required to mitigate pavement deterioration, particularly in surface layers affected by increased near-surface shear strains from HDEV-induced loads and torque. The presented framework captured the combined effects of tire-pavement contact stresses, pavement responses, distress prediction using mechanistic-empirical transfer functions, and a linear damage rule.

The effects of HDEVs on flexible pavement behavior were evaluated by considering three battery placement scenarios. From a mechanistic analysis perspective, the applied load governed pavement responses throughout the depth, whereas the slip ratio primarily affected near-surface strains. The contact stress inputs accounted for variations in both load magnitude and slip ratio, wherein the latter represented the increased torque of HDEVs compared to ICs. Four distinct pavement structures that represent various functional classes within the Illinois roadway network were considered. As expected, increasing the axle load resulted in higher pavement responses across all pavement sections, wherein the load magnitude governed much more than varying the slip ratio or acceleration level. An increase of 1 kip (from 6 to 7 kips) in the steering axle load led to increases in the critical tensile strain at the bottom of the HMA of 15%, 16%, 13.5%, and 9.3% in the typical-thick, full-depth, low-volume, and SMA-overlay sections, respectively. Slip ratio increases (up to 6%) led to marginal changes in tensile, vertical shear, and vertical compressive strains. However, when acceleration was imposed, a noticeable change in the longitudinal shear strain was observed compared to conditions with 0% slip ratio (no acceleration). An increase of 3% in the slip ratio in the steering axle load (7 kips) led to increases in the critical longitudinal shear strain of 29%, 178%, 16%, and 200% in the typical-thick, full-depth, low-volume, and SMA-overlay sections, respectively. However, note that OEMs are unlikely to place the battery on the steer axle, as it is an extreme condition.

The impact of slip ratio varied depending on pavement type, wherein relatively thicker HMA layers (full-depth HMA) or pavements incorporating a high-modulus supporting layer (e.g., SMA overlay on PCC) experienced more pronounced strains than those of the low-volume and typical-thick pavements. For a typical thick section subjected to a DTA load of 4.2 kips, a 22% increase in longitudinal shear strain was observed at a slip ratio of 2% and was further exacerbated to 26% at a slip ratio of 6%. This finding highlighted an increased risk of near-surface shearing distress or shoving. Moreover, full-depth HMA and SMA-overlay-on-PCC pavements evidenced the highest reductions in allowable repetitions to failure (owing to high near-surface pavement strains), which indicated higher susceptibility to damage compared to other pavement types considered. Although the analysis of shear strains focused only on HMA layers, sections with comparatively lower shear strains in the HMA exhibited correspondingly higher shear responses in the unbound layers.

Using the strain values as inputs into MEPDG transfer functions provided a means to assess the impact of HDEVs on pavement structural capacity, focusing on bottom-up cracking, shear-driven top-down cracking, and shear-driven shoving. A proposed index to quantify the cumulative impact of multi-axle loading configurations and allow an IC to HDEV full-truck comparison was introduced: the

e-truck adjustment (ETA) parameter. The ETA leveraged the results of advanced FE modeling and the estimated cumulative number of repetitions for various distress mechanisms. Increasing load magnitudes consistently led to higher e-truck adjustment factors (i.e., higher damage) across all pavement sections. However, the effect of the slip ratio varied per structure. For typical-thick and low-volume HMA pavements, increasing the slip ratio had a negligible impact on shoving. Although shoving was a critical failure mechanism for full-depth HMA pavements, the e-truck adjustment factor marginally changed with further increases in the slip ratio (from 2% to 3%). For the SMA-overlay section, increasing the slip ratio led to a marginal change in top-down cracking and bottom-up cracking. Shoving was controlled by HMA and was critical for sections with a surface course of relatively lower modulus.

CHAPTER 4: RECOMMENDED MODIFICATIONS TO IDOT PAVEMENT DESIGN

IDOT PAVEMENT DESIGN

The IDOT *Bureau of Design and Environment Manual* (*BDE Manual*) (Chapter 54) outlines the currently employed pavement design procedures, primarily focusing on jointed plain concrete pavement and full-depth HMA pavement. However, as traffic loads continue to evolve—both in magnitude and frequency—refinements to these procedures are warranted to account for current traffic and emerging transportation technology demands.

Within the Illinois mechanistic pavement design framework, traffic factors serve as a critical metric to assess the cumulative damage imposed by repeated traffic loads over the design life of a pavement structure. The current methodology relies on equivalent single-axle loads (ESALs). It was derived using a modified AASHTO approach that accounts for mixed-traffic axle loadings, roadbed soil variations, and extended traffic exposure periods. Historically, weigh-in-motion data and traffic studies have provided the necessary input for determining axle load distributions and developing load equivalency factors. However, as the truck fleet composition may shift toward EVs, these data sources must be revisited to ensure the derived traffic factors remain representative of the conditions present in the state of Illinois.

Existing traffic factor equations do not account for some effects (e.g., higher static axle loads and greater torque access), necessitating an update to pavement design methodologies. The recalibration of load equivalency factors, however, would require integrating HDEV-specific weigh-in-motion data, conducting controlled-loading tests, and validating predictions through mechanistic-empirical modeling approaches. Given the complexity and extensive data requirements of this process, a simplified approach could involve a phased implementation, beginning with a baseline framework to incorporate HDEV effects via adjustment factors that are directly applied to the aforementioned traffic equations. This would allow IDOT and other transportation agencies to apply interim adjustments to traffic factors while more detailed studies are conducted using a forward approach to update HDEV-based traffic factors. Eventually, probabilistic design methodologies—accounting for variations in vehicle weights, acceleration patterns, platoon, and load spectra—could be developed to help ensure that pavement design remains robust despite current uncertainties in HDEV adoption rates. As IDOT continues to refine its pavement design framework, adapting to electrified freight is essential to ensure long-term infrastructure resiliency and to develop rehabilitation strategies.

IDOT's pavement design framework has evolved over decades, integrating both empirical and mechanistic principles to design cost-effective pavements. Rooted in the findings of the AASHO Road Test of the late 1950s (Highway Research Board, 1961), Illinois initially relied on AASHTO design equations (AASHTO, 1961, 1972), which correlated pavement performance with axle load applications and structural capacity. Later, as traffic patterns, materials, and construction practices evolved, IDOT tailored the methodology to Illinois-specific conditions. The AASHTO guide itself had been updated to include an extension of load equivalency values and a method for calculating ESALs

with higher reliability (AASHTO, 1986). In the late 1980s and early 1990s, mechanistic design concepts were first introduced, leveraging stress-strain analysis, field monitoring, and computer modeling to better predict pavement responses and performance (AASHTO, 1993, 1998). This shift led to the adoption of mechanistic pavement design guidelines, which later became the foundation of pavement design in the *BDE Manual*.

Design Considerations

The pavement design in the *BDE Manual* integrates material properties, traffic loading, subgrade support, and environmental conditions to provide a robust pavement design approach. Flexible pavement structures are designed to control fatigue cracking by limiting tensile strains at the bottom of the HMA layer over the design period. Hence, IDOT primarily relies on a thickness-oriented pavement design approach, meaning that as anticipated traffic loads increase, pavement layers are designed to be thicker to accommodate higher traffic levels. Although this method effectively enhances pavement performance against structural failures, it does not necessarily mitigate near-surface distresses, such as shoving, which may be alleviated by changing HMA composition and material properties rather than the structural thickness alone.

A critical aspect of the BDE pavement design is the selection of asphalt binder and mixture quality so that pavements can withstand temperature fluctuations, loading conditions, and long-term traffic. The performance-grade (PG) binder system is central to the selection process, as it tailors binder selection to regional climate conditions and expected pavement performance. Binder grades are determined based on high and low pavement temperatures a road is likely to experience, with modifications made to improve resistance to rutting, fatigue cracking, and thermal cracking.

In high-traffic corridors and truck routes, IDOT specifies polymer-modified asphalt binder to control deformation. This is also important at intersections, ramps, and high-stress locations, where shear forces can accelerate shoving and rutting failures. The binder selection also helps to address top-down cracking, as this initiates at the surface because of high in-plane contact stresses, unlike bottom-up (traditional) fatigue cracking, which occurs due to bending under repeated load cycles. Beyond binder selection, the asphalt mixture type is another variable that affects pavement behavior. The *BDE Manual* allows the use of a range of asphalt concrete materials, including dense and gap graded mixes. For instance, stone-matrix asphalt (SMA), a gap-graded mix, is encouraged for areas with heavy truck traffic because of its better aggregate interlock and resistance to rutting. Alternatives, such as highly modified gap-graded mixtures, could also provide improved fatigue cracking and rutting resistance.

Traffic factors (TF) define the cumulative effects of axle loads over time, which influence thickness design. The *BDE Manual* provides equivalency factors for passenger vehicles (*PV*), single-unit trucks (*SU*), and multi-unit trucks (*MU*), as presented in Table 10, which could be converted into ESALs. The equivalency factors vary according to facility class. Class I encompasses highways and interstates that experience the highest traffic loads. Class II includes facilities that experience moderate truck traffic, and Class III and IV are local roads and collectors that generally carry fewer heavy vehicles. Despite the practical application of the concept of ESALs, mechanistic-empirical procedures have already replaced it with the concept of load spectra (AASHTO, 2008).

Table 10. Equivalency Factors (IDOT, 2022)

Facility Class	PV*	SU*	MU*
Class I	0.0004	0.363	1.322
Class II	0.0004	0.307	1.056
Class III and IV	0.0004	0.299	1.053

*18-kip ESAL applications per vehicle

Table 11 summarizes IDOT's traffic factor (TF) equations. The equations incorporate traffic distribution percentages (P, S, and M) for PVs, SUs, and MUs, respectively, as well as their corresponding traffic volumes. They also incorporate equivalency factors from Table 10 (multiplied by 365 days a year), and the design period (DP) expressed in number of years. The TF typically ranges between 0.5 and 100, expressed in millions of ESALS or MESALs, representing the projected total of load repetitions in the design lane during the design period.

Table 11. Traffic Factor (IDOT, 2022)

Facility Class	Traffic Factor Equation
Class I	$TF = DP \cdot \left(\frac{(0.15 \cdot P \cdot PV) + (132.50 \cdot S \cdot SU) + (482.53 \cdot M \cdot MU)}{1 \cdot 10^6} \right)$
Class II	$TF = DP \cdot \left(\frac{(0.15 \cdot P \cdot PV) + (112.06 \cdot S \cdot SU) + (385.44 \cdot M \cdot MU)}{1 \cdot 10^6} \right)$
Class III and IV	$TF = DP \cdot \left(\frac{(0.15 \cdot P \cdot PV) + (109.14 \cdot S \cdot SU) + (384.35 \cdot M \cdot MU)}{1 \cdot 10^6} \right)$

The full-depth HMA thickness design is bound as follows:

- The lower bound is determined by a minimum traffic factor of 0.5 MESALs so that even low-volume roadways meet a baseline level.
- The upper bound is governed by the *limiting strain criterion*, which determines the tensile strain levels under which pavements are unlikely to experience damage, thereby setting a threshold on the maximum allowed pavement thickness.

Fatigue failure is thought to occur because of repeated tensile strains. Under cyclic loading, the material would eventually exceed its endurance limit, leading to microcracks that propagate through HMA layers. While increasing pavement thickness reduces the tensile strain, as discussed in Chapter 3, the limiting strain criterion prevents excessively thick pavement designs, which would be inefficient and costly.

Moreover, subgrade support is another key design element, classified into three subgrade support ratings (SSR): poor, fair, and granular. The mechanistic pavement design assumes a stable subgrade,

often requiring subgrade improvements such as lime or cement stabilization to achieve a stable working platform. The full-depth mechanistic design process, per the *BDE Manual*, is summarized in Figure 36.

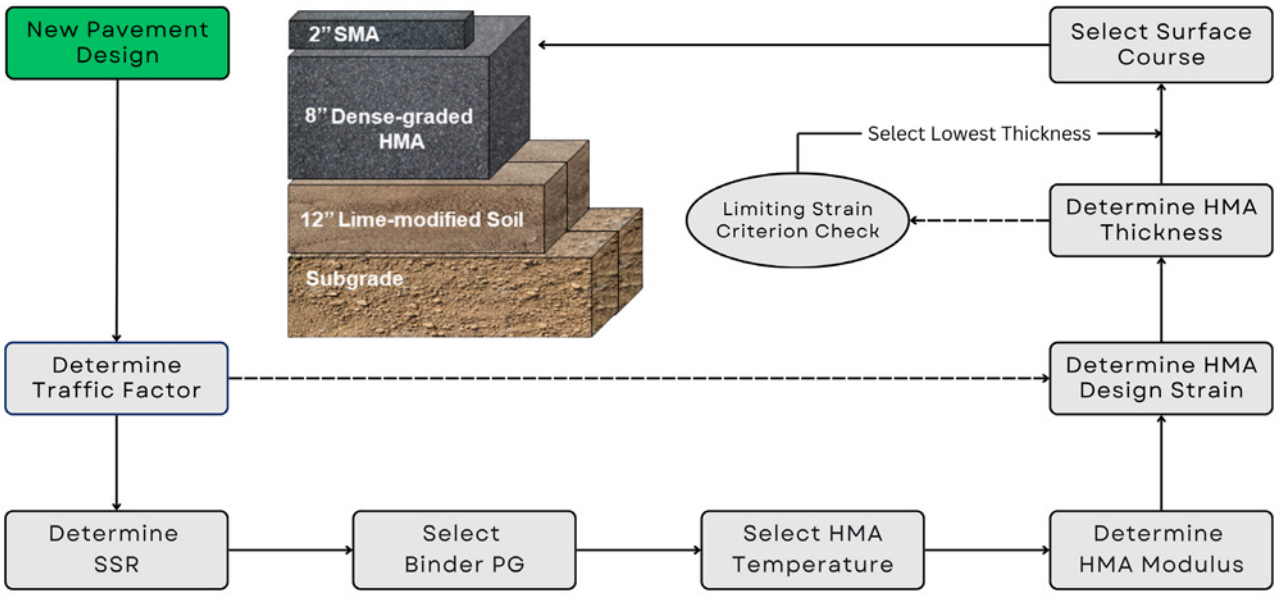

Figure 36. Schematic. Thickness design process for full-depth HMA.

This report focuses primarily on the traffic factor (TF), as no additional material testing beyond dynamic modulus characterization was conducted. Without extensive testing of other critical material parameters—such as binder performance grading, mixture temperature susceptibility, and subgrade soil characterization—additional recommendations could not be made regarding mix performance, rutting control, or fatigue behavior under repeated loading. The proposed TF-targeted approach prioritizes the impact of HDEV traffic-demand changes, increased axle loads, and evolving acceleration patterns on expected pavement performance. By focusing solely on the traffic factor, the study proposes a simple, preliminary approach to refine ESAL estimations when HDEVs are introduced to the Illinois roadway network. The research team acknowledges that further investigation into HMA design and material selection may be needed to evaluate possible mitigation of shear-drive near-surface distresses.

ADJUSTMENT FACTOR FRAMEWORK

As outlined in Chapter 3, the ETA calculation process uses critical strains as input. Traffic factors were scaled accordingly via the ETA, which integrates mechanistic analysis outcomes to better capture the effects of evolving loading conditions from IC to HDEV. Unlike the traditional approach, which primarily relies on ESALs and ESAL-based traffic projections, the proposed framework incorporates mechanistic pavement analysis to assess HDEV-induced damage. While the *BDE Manual* uses tensile strain as the main input during the thickness design process, the incorporation of mechanistic analysis allows the use of MEPDG transfer functions to assess the combined impact of bottom-up fatigue,

shear-driven top-down cracking, and shear-driven shoving. Figure 37 illustrates the suggested modifications to the existing full-depth mechanistic design framework.

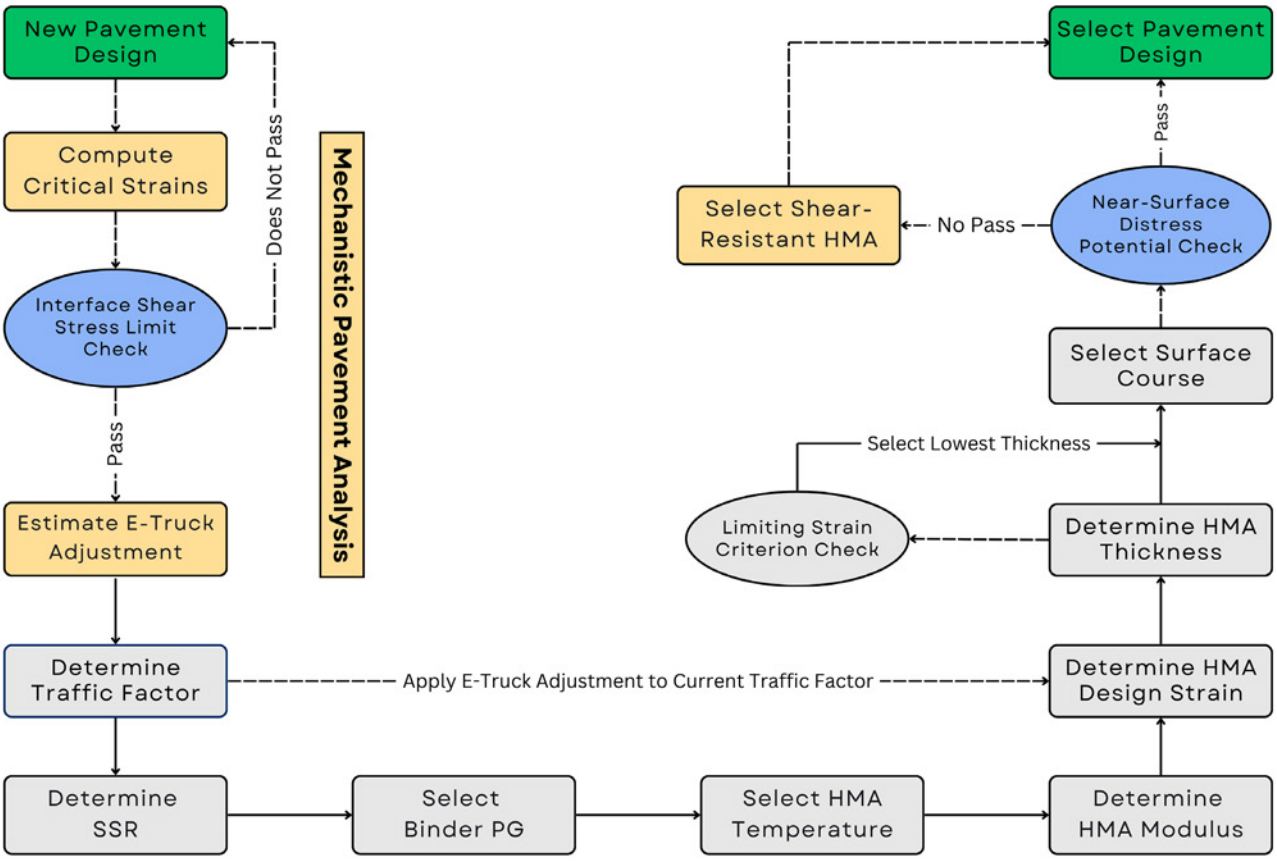

Figure 37. Schematic. Modified mechanistic design process for a full-depth HMA pavement.

FE-based critical strain outputs were leveraged and directly linked to a pavement section's structural response to any loading condition in lieu of traffic load equivalency factors. Instead of treating all truck traffic as a uniform load input, the ETA could be estimated based on any axle configuration, axle weight, or acceleration pattern for HDEVs. A modified traffic factor (TF^*) is then applied to the design process to determine any change in pavement thickness per IDOT's full-depth mechanistic design. This step ensured the limiting strain criterion was checked after accounting for realistic HDEV-induced loading conditions, making the current thickness estimation more traffic-responsive. It is noteworthy that the proposed framework also checks for interface shear stresses to ensure the tack coat strength is not exceeded.

Given that increasing thickness alone is not sufficient to mitigate near-surface failures, the framework suggests a final distress check to assess whether shear-driven top-down cracking or interface shearing might still be a concern. This decision could be made based on the actual traffic distribution. If HDEVs are expected, then shear-resistance HMA may be considered. The surface course material could be adjusted independently of the structural thickness to avoid overdesigning a section while maintaining structural performance.

Qualitative Classification

The computation of the ETA was sensitive to changes in the distinct input parameters during the two-pronged FE approach. The introduction of qualitative categories for the calculation of ETA aimed to facilitate the practical implementation of the recommendations given herein. Categorical battery configuration and acceleration levels were defined, and the precalculated ETAs were obtained for a full-depth section (Figure 38). This is the only section among the pavement structures evaluated that could be subject to the pavement design framework in the *BDE Manual*.

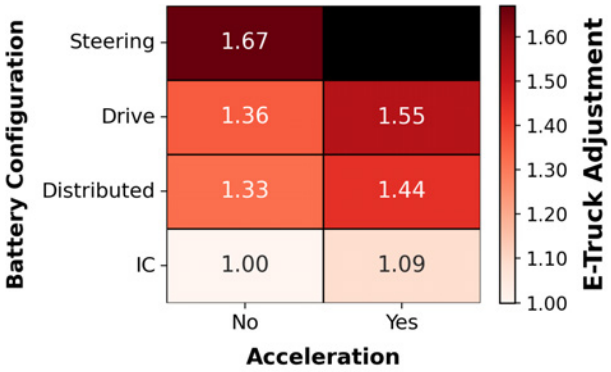

Figure 38. Graph. E-truck adjustment factors for full-depth section.

Load Distribution

As explained in detail in Chapter 2, HDEV battery placement affected the axle load distribution and corresponding pavement responses (Chapter 3). The reference IC scenario represented a conventional truck with standard axle load distribution with a ETA of 1.00. When the battery pack weight was concentrated on the steering axle, the ETA reached a value of 1.67 for the full-depth section. The optimal HDEV scenario is represented by the evenly distributed battery configuration, wherein each axle experienced the least perturbation because of the uniform distribution of the added weight across the vehicle chassis. Compared to the baseline IC, an HDEV with evenly distributed battery weight across the steering and drive axles did not alter the resulting pavement responses. Higher than the IC baseline, the ETA increased by 33%. On the other hand, assuming the placement of the battery only on the drive axles resulted in lower values than those of the steering-axle-dominant configuration (an extreme battery-placement assumption).

Acceleration Rates

A key aspect of the numerical simulation framework was the incorporation of the slip ratio as a means to represent acceleration. Although three slip ratio values were used (2%, 3%, and 6%), representing different levels of tire slip, beyond a certain threshold, additional slip did not lead to a further increase in the ETA computation. The observed plateau trend suggested that while acceleration-induced pavement loads were significant, the difference between the responses yielded under two different slip ratios did not lead to significant differences (compared to load impact). As a result, a categorical classification was implemented, assigning *Yes* to cases where a slip ratio was present and *No* to 0% slip ratio (nonaccelerating) conditions. The proposed approach streamlines the framework while ensuring that the influence of acceleration is captured without additional

complexity. In general, higher acceleration levels contributed to an increase in the ETA. Because the load governed the results of the steering-axle scenario, acceleration-induced responses were not expected to alter the ETA significantly.

Traffic Input Adjustment

While, in theory, ETA values primarily affected a subset of multi-unit trucks (MUs), specifically heavy-duty freight vehicles, the research team considered that for high-traffic sections, the influence of heavy-duty freight is disproportionately large, as the per-vehicle pavement damage is greater. Although the traffic factor equation accounted for different vehicle classifications, the term $482.53 \cdot M \cdot MU$ becomes dominant in the overall computation, as the percentage of heavy-duty freight is assumed to increase. This dominance occurred not only in numerical magnitude, but also in its practical implications for pavement performance. For low-traffic sections, the total ESAL accumulation derived from light traffic is relatively low, indicating mechanistic pavement design methodologies often default to the lower bound of thickness. Because of the lack of detailed HDEV traffic classification data (for a forward approach change in the traffic factor), a practical assumption was deemed appropriate to showcase the implementation of the ETA concept and propose modified traffic factors, TF^*, in the full-depth HMA mechanistic design accordingly, as presented in Table 12. After the traffic factor modification, the design procedure follows the existing IDOT protocol. Higher traffic factors led to lower HMA design strain, which, in turn, resulted in higher design requirements for HMA layer thickness.

Table 12. Modified Traffic Factor

Facility Class	Traffic Factor Equation
Class I	$TF^* = ETA \cdot DP \cdot \left(\frac{(0.15 \cdot P \cdot PV) + (132.50 \cdot S \cdot SU) + (482.53 \cdot M \cdot MU)}{1 \cdot 10^6}\right)$
Class II	$TF^* = ETA \cdot DP \cdot \left(\frac{(0.15 \cdot P \cdot PV) + (112.06 \cdot S \cdot SU) + (385.44 \cdot M \cdot MU)}{1 \cdot 10^6}\right)$
Class III and IV	$TF^* = ETA \cdot DP \cdot \left(\frac{(0.15 \cdot P \cdot PV) + (109.14 \cdot S \cdot SU) + (384.35 \cdot M \cdot MU)}{1 \cdot 10^6}\right)$

IRI Progression Adjustment

A market penetration of 100% may realistically take decades before pavement performance data could be available to properly assess pavement deterioration appropriately during its service life. The International Roughness Index (IRI) is one of the accepted performance indicators, and its progression over time is generally collected for pavement management decision-making. Traditional IRI models, whether derived from field data or mechanistic-empirical predictions, are calibrated based on standard axle loads and loading conditions. With an increase in pavement deterioration rates due to higher axle loads and acceleration levels, a direct adjustment to the IRI progression was deemed necessary to ensure that pavement life estimates reflect HDEV impacts.

Rather than modifying the shape of the IRI progression curve, this study adopted an alternative approach. Typically, IRI progression data are provided as *X* and *Y* data pairs, where *X* represents pavement service life (years) and *Y* represents the IRI values at a given *X* value. In the proposed approach to adjust IRI progression, the *X*-axis values were scaled based on the e-truck adjustment factor, ETA, which encapsulated a combination of critical pavement distresses. In this implementation, the functional form of the IRI curve remains unchanged. However, the ETA values accounted for the service life adjustment of pavement under HDEV loading. Deterioration occurred rapidly because of the increased damage induced by HDEVs (i.e., earlier trigger for rehabilitation).

The presented approach allows for a rapid assessment of the reduction of pavement service life without requiring significant recalibration of existing IRI models. Given that most pavement management systems (PMS) and mechanistic-empirical design tools rely on precalibrated IRI progression equations, implementing the ETA-based scaling ensures that HDEV impacts could be incorporated seamlessly into existing methodologies. Because transportation agencies rely on IRI thresholds to schedule maintenance and rehabilitation (M&R) interventions, planners could anticipate earlier intervention with the scaled IRI progression curves or earlier M&R triggers.

This approach implicitly assumes all deterioration mechanisms that contribute to the IRI progression scale proportionally to increased axle load and acceleration levels, which may not always be the case. While fatigue cracking, subgrade deformation, and HMA rutting may indicate strong correlations with load-induced deterioration, top-down cracking, near-surface shear failures, and moisture-related damage may follow nonlinear progression patterns, which may not be adequately captured by a simple time-scaling adjustment. Furthermore, in extreme loading scenarios, the IRI curve does not maintain a smooth progression, as it exhibits abrupt jumps in roughness when surface distresses appear.

To illustrate the application of the IRI-scaling approach, Figure 39 presents the IRI progression curve of the full-depth pavement section soon after construction (with an initial IRI of 60 in/mi) until it reaches a poor-condition threshold and rehabilitation is needed. According to the Federal Highway Administration (FHWA, 2020), this condition occurs when an IRI reaches 170 in/mi.

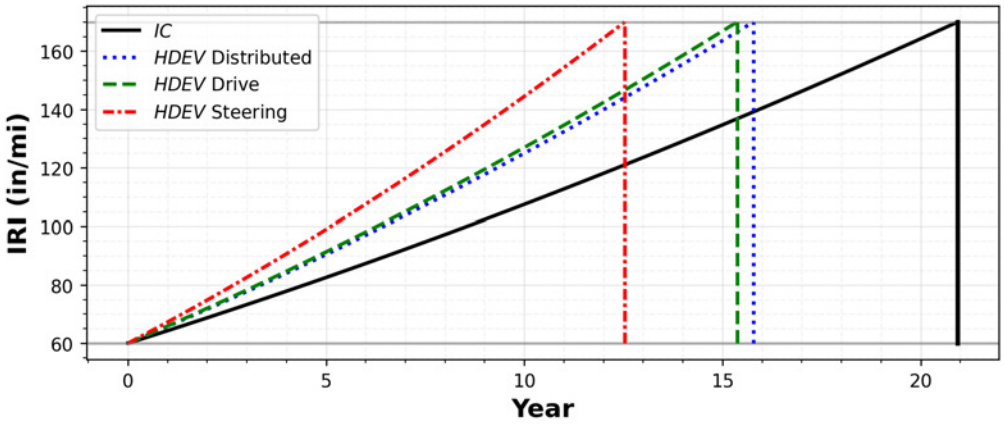

Figure 39. Graph. IRI progression curves under different loading scenarios.

In the baseline IC case, the IRI progression followed a standard trend, which reached a terminal roughness level at approximately 21 years, consistent with conventional empirical and mechanistic-empirical pavement deterioration models. However, for HDEVs with various battery placements, the service life was significantly reduced—driven by the reduced allowable number of repetitions of various distress mechanisms. The HDEV steering axle scenario (S1) resulted in the highest life reduction of 13 years, which is 38% lower than that of IC. The HDEV drive axle scenario (S2) resulted in faster deterioration than that of the evenly distributed HDEV battery pack, which reduced the service life to 15 years. The HDEV with an evenly distributed load (S3) resulted in an IRI progression reaching the threshold nearly 24% earlier than the IC, thereby shortening the expected service life to approximately 16 years. The trigger-time differences compounded throughout the analysis period. Given that pavements were subjected to rehabilitation after reaching the IRI threshold, differences became more noticeable in the IRI progression after rehabilitation occurred. Figure 40 presents IRI progression curves for all loading scenarios over a 50-year analysis period.

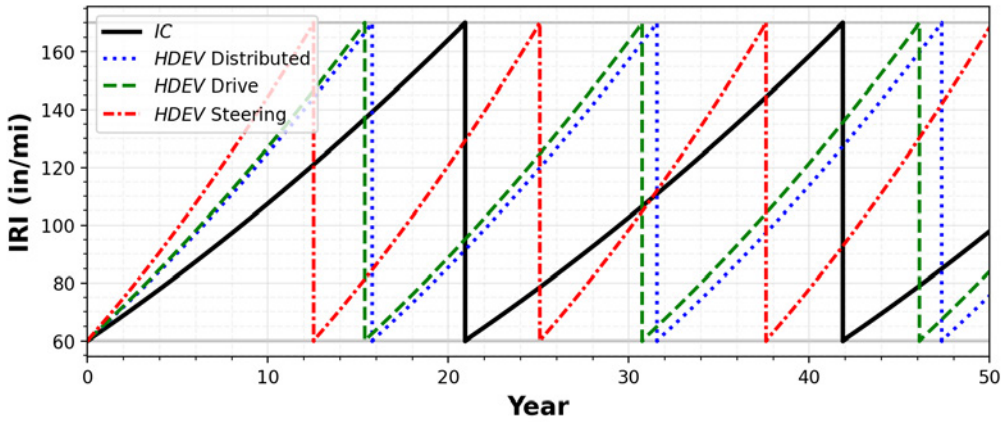

Figure 40. Graph. IRI progression curves over an analysis period of 50 years.

IMPLEMENTATION POTENTIAL: CASE STUDY

The full-depth pavement section served as a practical case study to demonstrate a detailed application of the proposed framework. The *BDE Manual* design uses HMA tensile strain, which is a function of the traffic factor. The design HMA tensile strain graph in the *BDE Manual* is computed based on a transfer function (Figure 41), where sections with higher traffic factors require lower design HMA tensile strains to guarantee their service life and can be directly obtained from the use of the Illinois mechanistic transfer function (Thompson & Cation, 1986).

$$N_f = \frac{8.78 * 10^{-8}}{(\varepsilon_t)^{3.5}}$$

Figure 41. Equation. Illinois mechanistic transfer function.

where: N_f = number of repetitions to failure, and ε_t = critical tensile strain at the bottom of the HMA.

As noted, the ETA captured the combined effect of three distresses (bottom-up cracking, shear-driven top-down cracking, and shear-driven shoving). On the other hand, TF^* only impacted what is relevant to the *BDE Manual*. To showcase this application, the following information was assumed:

- New four-lane state highway (Facility Class I)
- Design period = 20 years
- $P = 32\%, S = 45\%, M = 45\%$ (see Figure 54-2.B of the *BDE Manual*)
- $PV = 9450, SU = 2300, MU = 1750$
- Subgrade Support Rating (SSR) = Poor
- Asphalt binder type = PG 76-28, HMA modulus = 600 ksi

Using the traffic factor equation presented in Table 11 for a Facility Class I:

$$TF = 20 \cdot \left(\frac{(0.15 \cdot 0.32 \cdot 9450) + (132.50 \cdot 0.45 \cdot 2300) + (482.53 \cdot 0.45 \cdot 1750)}{1 \cdot 10^6} \right) = 10.35$$

A traffic factor of 10.35 MESALs was calculated for the IC baseline scenario. Using the Illinois mechanistic transfer function, an HMA design strain ε_t of 64.2 $\mu\varepsilon$ could be obtained. (Recall that the number of repetitions N_f is multiplied by ~0.25 to account for the design reliability of 95%.)

$$TF = N_f * 0.25$$

$$N_f = 41.40 * 10^6$$

$$\varepsilon_t = \sqrt[3.5]{\frac{8.78 * 10^{-8}}{N_f}} = 64.2 * 10^{-6}$$

The corresponding ETA for the HDEV case with evenly distributed, drive axle, and steering axle configurations were 1.33, 1.36, and 1.67 (Figure 38), respectively, for the no acceleration condition. When acceleration was considered, the ETA was 1.09, 1.44, and 1.55, respectively. Table 13 presents the estimated changes in the traffic factor and HMA design tensile strain.

Figure 42 illustrates the variability in the computed design HMA tensile strain for free-rolling conditions. Although there is a difference of 67% between the computed traffic factor for the IC and the HDEV-steering axle scenario, the design HMA tensile strain decreased by 13.63%, from 64.20 $\mu\varepsilon$ to 55.45 $\mu\varepsilon$. As expected, damage should increase as the traffic factor increased per Figure 42.

After obtaining the design HMA strain, the next step was to estimate HMA thickness for various HDEV battery placement locations (no acceleration). For this purpose, an HMA modulus at traffic conditions

of 600 ksi and a reference temperature of 64.4°F were assumed in this sample implementation. Figure 43 showcases how the HMA thickness is obtained from the estimated HMA strain (see Figure 42), and the selected HMA modulus.

Table 13. Adjusted Traffic Factors and HMA Design Strain

Battery Configuration (Accel)	E-Truck Adjustment	Traffic Factor (MESALs)	HMA Design Strain ($\mu\varepsilon$)
IC (No)	1.00	10.35	64.20
IC (Yes)	1.09	11.28	62.64
HDEV Distributed (No)	1.33	13.73	59.22
HDEV Distributed (Yes)	1.44	14.96	57.79
HDEV Drive (No)	1.36	14.10	58.78
HDEV Drive (Yes)	1.55	16.06	56.63
HDEV Steering (No)	1.67	17.29	55.45

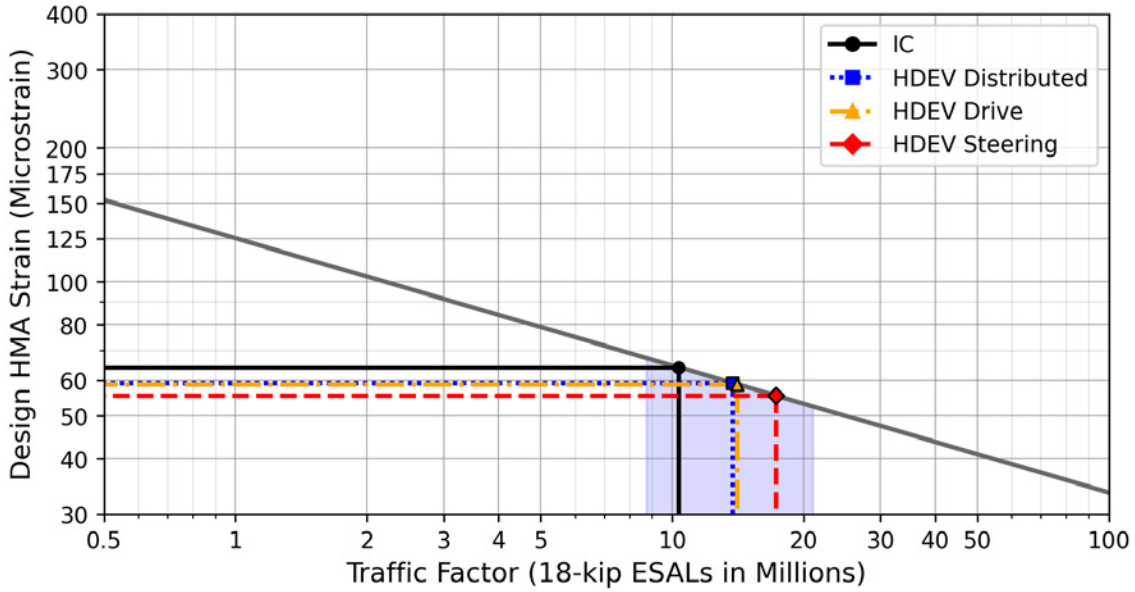

Figure 42. Graph. Design HMA strain computation for IC and HDEV scenarios.

Given that the HMA thickness design curve depends on SSR, the design chart for a poor subgrade was used as it was listed as an assumption because it is a common condition in Illinois. As expected, higher ETAs resulted in increased design HMA thicknesses. Table 14 summarizes the differences in HMA thickness designs based on the proposed ETAs. The most critical case yielded an overall thickness of 14.0 in for the HMA layer for the HDEV with the battery placed on the steering axle (an extreme and unlikely scenario), which was 1.00 in thicker than the value obtained for the reference IC case. On the other hand, for the two other HDEV scenarios, an increase in thickness up to 0.75 in was observed.

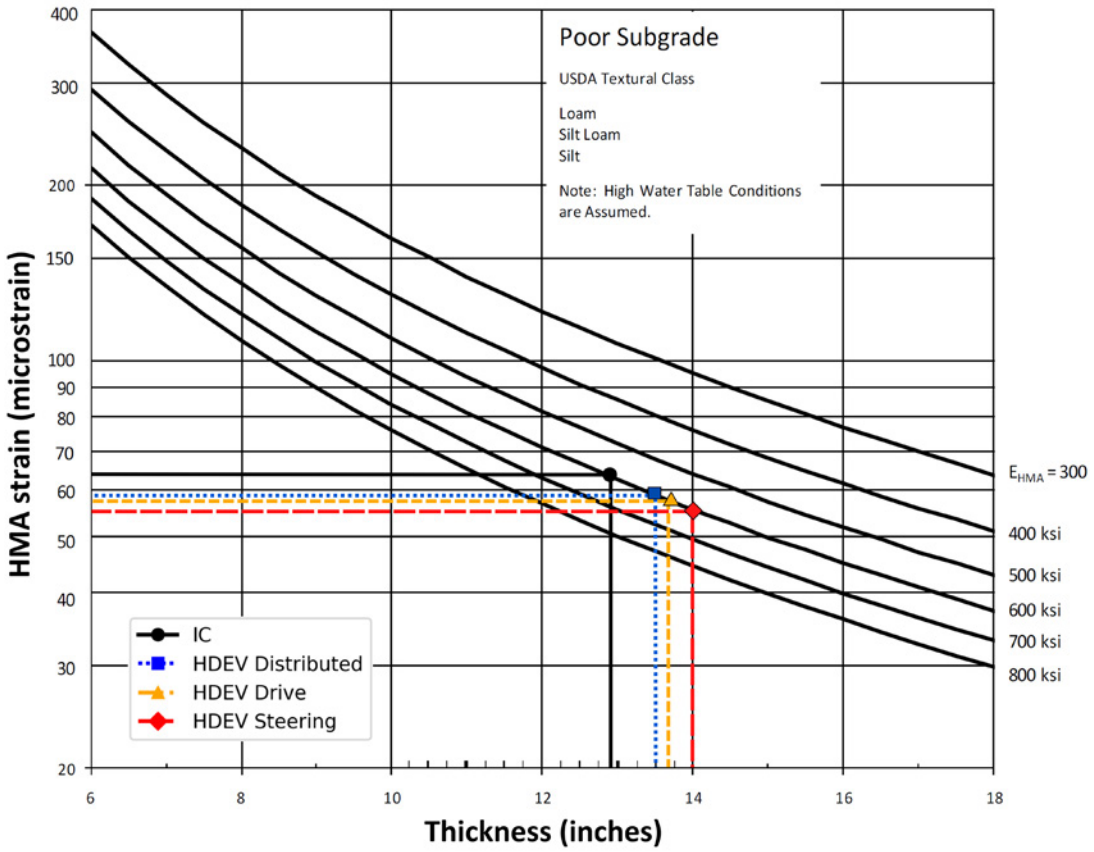

Figure 43. Graph. HMA thickness estimation.

Table 14. Computed Thickness for Different E-Truck Adjustment Factors

Battery Configuration (Accel)	ETA	HMA Thickness (in)
IC (None)	1.00	13.00
HDEV Evenly Distributed (None)	1.33	13.50
HDEV Drive Axle (None)	1.36	13.75
HDEV Steering Axle (None)	1.67	14.00

In the current IDOT full-depth HMA mechanistic design framework, the ETA could only impose an increase in HMA layer thickness to compensate for higher traffic loading. While this method is effective in addressing structural fatigue failure, it has several inherent limitations, particularly when considering HDEVs. The provided implementation focused on HMA thickness under the no acceleration scenario. Increased HMA thickness does not necessarily address acceleration effects. Mitigating near-surface distresses (e.g., ones induced by in-plane contact stresses), such as shear-driven shoving and top-down cracking, may be better addressed by changing HMA materials. Therefore, suggesting only increased thickness may not be an appropriate or cost-effective solution.

SUMMARY

The IDOT *BDE Manual* provides a structured approach to a full-depth HMA mechanistic pavement design. However, the anticipated presence of HDEVs may require modifications to existing design methodologies, particularly the computation of traffic factors and load equivalency factors. The unique axle load distributions of HDEVs—resulting from increased battery weight and greater torque access—call for a recalibration of load equivalency factors to ensure that mechanistic pavement design reflects evolving traffic conditions and emerging transportation technologies. Given the complexity of these modifications, a simplified approach is proposed by integrating adjustments to existing traffic factor equations. The e-truck adjustment factor, ETA, framework is proposed for implementation. Its application scales standard traffic factors to account for HDEV-induced pavement loading.

While IDOT's design methodology is effective in preventing fatigue cracking, it does not adequately address near-surface distresses such as shear-driven shoving and top-down cracking. Therefore, while ETA-based traffic factor adjustments may justify higher pavement thickness, additional considerations for material selection and optimization may be needed. Incorporating HDEVs led to increased HMA design thicknesses, a maximum increase of 0.75 in for HDEVs with batteries placed on drive axles or evenly distributed on the tractor compared to that of ICs for the full-depth HMA section.

Although IDOT does not rely on specific IRI thresholds or directly correlate them with Illinois Condition Rating Survey (CRS) thresholds as formal triggers for rehabilitation, CRS and IRI can be correlated. IRI is widely used as a relative indicator of pavement performance in pavement management across the U.S. By scaling the IRI progression timeline using ETA values, this study demonstrated that pavement structures under loading conditions associated with higher ETAs reached rehabilitation triggers earlier because of reduced pavement life. Specifically, the HDEV steering axle configuration shortened the expected service life of a full-depth section by approximately 38%, which showcased the importance of incorporating HDEV-specific load considerations into long-term pavement performance models.

CHAPTER 5: ECONOMIC AND ENVIRONMENTAL IMPLICATIONS OF HDEV ON PAVEMENTS

Life cycle assessment (LCA) and life cycle cost analysis (LCCA) are critical tools for evaluating long-term impacts on pavements, especially when considering the adoption of new technologies like HDEVs. These methodologies provide a thorough evaluation of the environmental and economic implications, respectively, of HDEV traffic on pavement performance. By analyzing the entire life cycle of pavements under HDEV loading, LCA identifies environmental consequences. On the other hand, LCCA evaluates long-term costs associated with different stages of a pavement's life cycle. This approach is essential for understanding the sustainability and economic feasibility of pavements as HDEV market penetration increases. The environmental and economic impacts of HDEVs were assessed across multiple market penetration scenarios, guided by McKinsey's projected sales trajectory (McKinsey, 2024). Market penetration (MP) levels were evaluated at 0%, 2.5%, 5%, 10%, 25%, 50%, and 100% to capture a broad range of adoption levels. This approach allowed for a detailed analysis of how increasing HDEV adoption affects costs, emissions, and pavement performance under various scenarios.

LIFE CYCLE ASSESSMENT

LCA is a cradle-to-grave evaluation technique that assesses environmental impacts of products or processes from raw material extraction to manufacturing, production, and construction, followed by operation, maintenance, and eventual disposal (Aryan et al., 2023). LCA provides a holistic view of the environmental impacts at each stage of a product's life cycle. The standard outlines four distinct phases to complete an assessment: goal definition and scope, life cycle inventory analysis, impact assessment, and interpretation (Pscherer & Krommes, 2025). This study conducted an LCA for a full-depth pavement section in accordance with the ISO 14044:2006 standard.

Goal and Scope Definition

This study evaluated the environmental impacts of IC and HDEV loading on a full-depth HMA pavement section. To achieve this, the IL 83 pavement section in Lake County was selected as the study site. Seven scenarios were analyzed:

- IC (with no acceleration and acceleration)
- HDEV with the battery placed on the steering axle, S1 (with no acceleration)
- HDEV with the battery placed on the drive axle, S2 (with no acceleration and acceleration)
- HDEV with battery evenly distributed across the steer and drive axles, S3 (with no acceleration and acceleration)

Although lane-mile-vehicle is the ideal functional unit, the functional unit for this study was defined as one lane-mile because only one section is considered for the same total vehicles (Ziyadi & Al-Qadi, 2017). Figure 44 illustrates the system boundary and associated processes for each stage of the LCA.

End-of-life impacts were assumed to be the same across all loading scenarios, so this stage was excluded from the analysis. A 50-year analysis period was selected to capture the long-term environmental effects of pavement performance under different truck-loading scenarios. The IC and HDEV manufacturing were not considered.

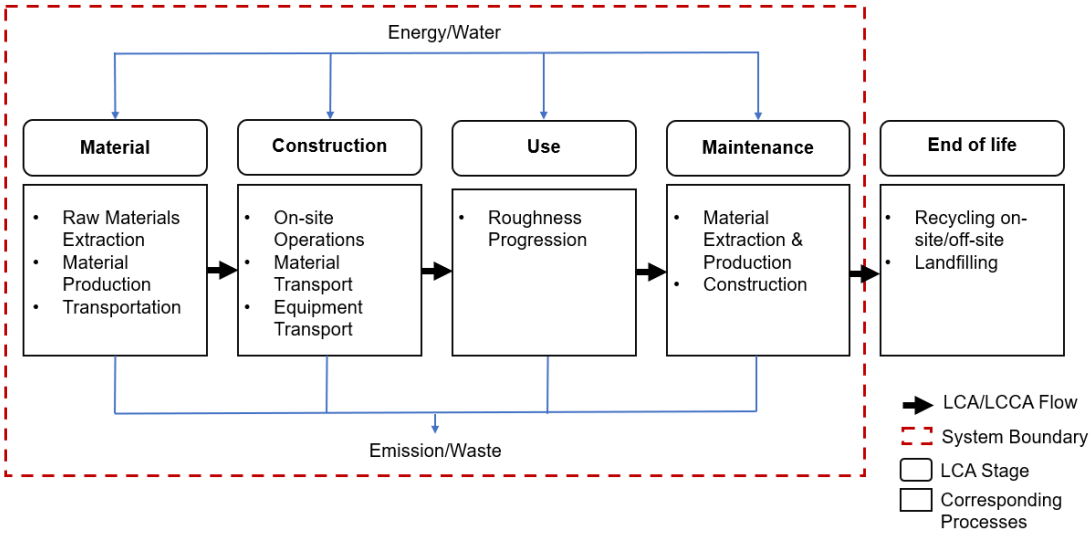

Figure 44. Schematic. LCA processes and system boundary.

Materials and Construction Stage

The full-depth HMA pavement section consisted of a 2-in-thick SMA surface layer using PG 76-28 (N80, NMAS 12.5 mm), 2.25-in-thick HMA PG 76-28 (N90, NMAS 19 mm, 15% RAP) intermediate layer, and 5.75-in-thick HMA PG 64-22 (N90, NMAS 19 mm, 15% RAP) binder course. A 12-in lime-modified base (1% lime treatment) was assumed. The environmental impacts of these materials were modeled using the US ecoinvent commercial database accessed through the SimaPro software. The environmental impacts were quantified by per pay-item (ton of material).

Use Stage

For the use stage, a mechanistic pavement rolling resistance model considering dynamic loading (Liu & Al-Qadi, 2022a) was employed to estimate the excess fuel consumption from pavement roughness. To compare energy usage between the IC and HDEV scenarios, a diesel gallon equivalent (DGE) value of 0.027 was assumed to convert diesel consumption to electricity (kWh) in accordance with US Department of Energy recommendations (DOE, 2025).

The analysis solely focused on truck traffic, with a traffic growth rate of 0.8%, per FHWA recommendations. It was assumed that trucks accounted for 50% of the AADT for the analyzed section. The AADT for the section was 13,500, with 6,750 designated as truck traffic for the analysis. A posted speed limit of 40 mph was assumed for all calculations. Electricity impacts were assessed based on Illinois' electricity grid composition (EIA, 2024). The carbon footprint of 1 kWh of electricity in Illinois was determined at 0.284 kg CO_2-eq. The assumed electricity grid mix for Illinois was presented in Chapter 1 (see Figure 1).

Maintenance Stage

The rehabilitation strategy was determined based on IDOT's *BDE Manual* (IDOT, 2022). The flowchart in Figure 45 depicts the decision-making process for pavement rehabilitation.

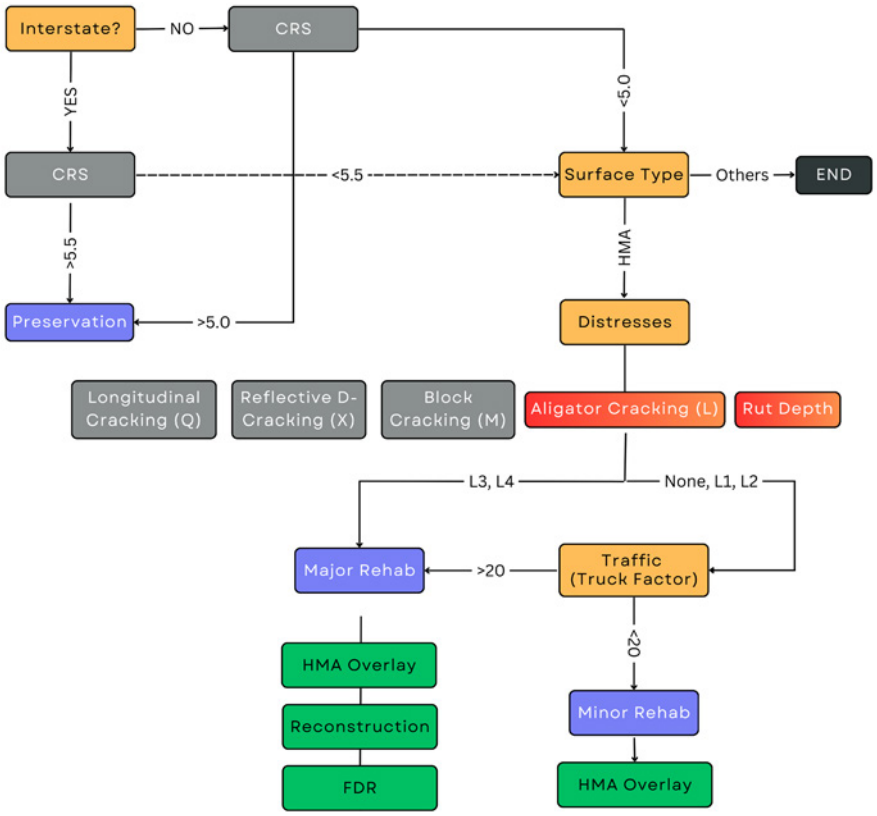

Figure 45. Schematic. Pavement rehab decision-making process.

Given that the roadway is a state highway, the evaluation utilizes the Condition Rating Survey (CRS). Following the IDOT standard, a CRS value below 5.0 requires further assessment of the pavement surface type and distresses. With a truck factor above 20, major rehabilitation was required. According to IDOT guidelines, interstates require two HMA lifts with a total thickness of 3.00 to 4.25 in. Therefore, for a state highway, as the IRI reached 170 in/mi (Figure 39 and Figure 40 from Chapter 4), a 3 in HMA overlay was selected as the appropriate rehabilitation treatment. Table 15 summarizes the rehabilitation timeline and activity for all loading scenarios on the full-depth pavement.

Table 15. Rehabilitation Schedule

Scenarios (Vehicle Type [Acceleration])	**Year of Rehab Activity**		
	Rehab 1	**Rehab 2**	**Rehab 3**
IC (No)	21	42	–
HDEV steering (No)	13	25	38
HDEV drive (No)	16	32	47
HDEV evenly distributed (No)	16	32	48

Scenarios (Vehicle Type [Acceleration])	Year of Rehab Activity		
	Rehab 1	Rehab 2	Rehab 3
IC (Yes)	20	39	–-
HDEV drive (Yes)	14	27	41
HDEV evenly distributed (Yes)	15	29	44

LCA RESULTS

The LCA results are divided into two parts: four scenarios where acceleration effects are not included (Figure 46) and three scenarios where acceleration is included (Figure 47). Both figures show results for 0% HDEVs (100% ICs) and 100% HDEVs. The emissions from the materials and construction stages remained consistent across all scenarios, as all considered the same full-depth pavement structure.

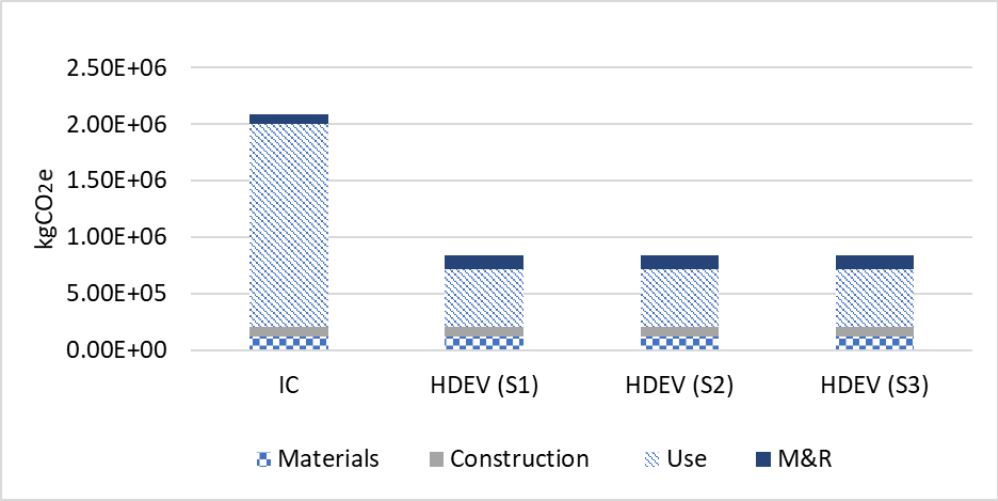

Figure 46. Graph. Greenhouse gas results for all load scenarios for 0% vs 100% MP (no acceleration)

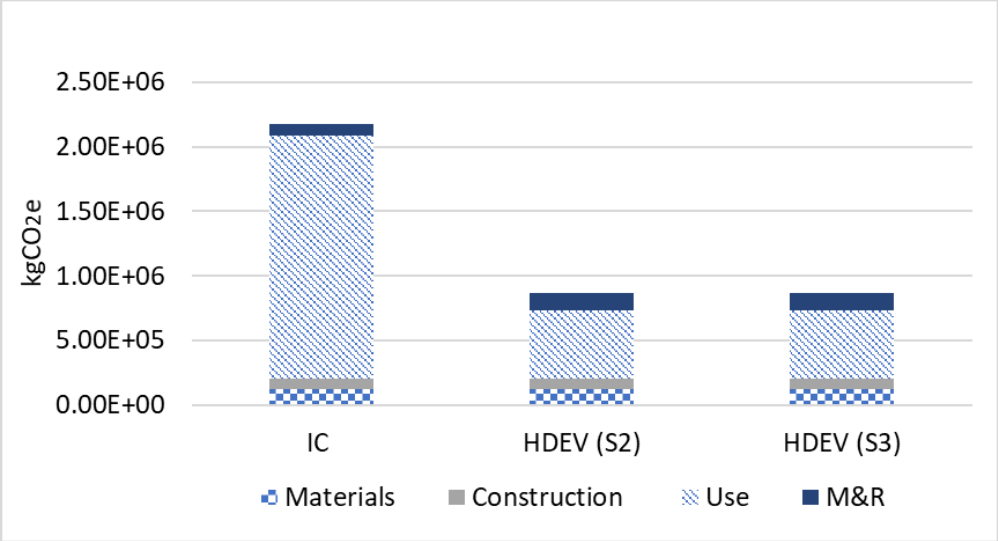

Figure 47. Graph. Greenhouse gas results for all load scenarios for 0% vs 100% MP (acceleration)

The LCA results indicate a significant reduction in emissions when transitioning from IC trucks to HDEVs. The fuel consumption of ICs was measured in gallons, while the energy consumption of HDEVs was quantified in kilowatt-hours (kWh). Without acceleration impacts, the total emissions for the IC scenario amount to 2,090,301 $kgCO_2eq$, whereas the HDEV scenarios (S1, S2, S3) yield an average of 840,492 $kgCO_2eq$, representing a 60% reduction. The most substantial decrease is observed in the use stage, where emissions dropped from 1,795,478 $kgCO_2eq$ for IC vehicles to 502,698 $kgCO_2eq$ for HDEVs, a 72% reduction. However, emissions from maintenance and rehabilitation (M&R) increased from 85,900 $kgCO_2eq$ to 129,000 $kgCO_2eq$. This 50% rise is due to the increased pavement wear associated with HDEVs.

When acceleration effects are included, the total emissions for IC vehicles increase slightly to 2,173,432 $kgCO_2eq$, while HDEVs (S2, S3) show an increase to 863,767 $kgCO_2eq$, reflecting a similar 60% reduction in emissions compared to IC vehicles. The use-stage emissions for IC vehicles increase slightly to 1,878,609 $kgCO_2eq$, while for HDEVs, they rise to 525,973 $kgCO_2eq$, maintaining the 72% reduction trend. The M&R emissions remain 50% higher for HDEVs compared to IC vehicles. Overall, the acceleration effect leads to a 4% increase in emissions for IC vehicles and a 2.8% increase for HDEVs. The results also indicate that use stage emissions constitute the largest portion of total life cycle emissions for all scenarios. In the case of ICs, the use stage accounts for 86.1% of the total emissions. Similarly, with acceleration effects, use-stage emissions are making up 86.5% of the total. In general, the total emissions from HDEVs are significantly less than those from ICs.

For HDEVs, use stage emissions are significantly lower due to the relatively cleaner electricity grid in Illinois, where approximately 55% of energy is produced by nuclear power. For HDEVs without acceleration, the use stage contributes 59.8% of total emissions (503,000 $kgCO_2eq$ out of 840,492 $kgCO_2eq$), and with acceleration, it remains dominant at 60.9% (526,000$kgCO_2eq$ out of 863,767 $kgCO_2eq$). Despite the increase in M&R emissions, the substantial reductions in use-stage emissions highlight the potential environmental benefits of adopting HDEVs in freight transportation. However, these results are highly dependent on the energy mix of the electricity grid. In states with higher reliance on fossil fuels for electricity generation, the emissions reduction potential of HDEVs may be lower, altering the overall life cycle impact.

LIFE CYCLE COST ANALYSIS

Life cycle cost analysis is an economic evaluation method used to compare investment alternatives based on their long-term costs (Li et al., 2019). It accounts for initial costs as well as future agency costs and user costs. By applying discounting principles, LCCA ensures that future costs are properly considered in present-value terms. Agency costs refer to the expenses obligated to the owner agency. It includes initial construction, maintenance, and rehabilitation costs. These costs include expenditures on materials, labor, and equipment, all of which directly impact the agency's budget. Given that agency costs are typically documented in contracts as pay items with specified prices, their estimation is relatively straightforward. However, uncertainties may arise in projecting future maintenance and rehabilitation costs.

User costs are expenses incurred by the traveling public on roadways maintained by the owner agency. User costs generally account for expenses related to vehicle operation, crashes, and user delays. The analysis considers only the vehicle operating cost (VOC) associated with fuel/energy consumption. Other user cost factors may also include user comfort, local economic impacts, and noise. These tend to be difficult to quantify and are therefore excluded in the analysis. The performance life of the initial pavement and rehabilitation triggers significantly impact LCCA results. It determines agency intervention frequencies, which influences both agency and user costs.

Analysis Period

FHWA (2025b) guidelines recommend an analysis period longer than the pavement design life to capture long-term costs. Moreover, FHWA suggests at least one rehabilitation activity is considered. Based on these guidelines, a 50-year analysis period was chosen for this study, and all scenarios invoked more than one rehabilitation trigger.

Discount Rate

FHWA (2025a) recommends using a real discount rate between 3% and 5%. For this study, a 3% discount rate was applied to calculate the net present value (NPV), aligned with the value used for Illinois.

Agency Costs

Agency costs were determined by calculating the initial construction cost of the pavement section and the rehabilitation costs for each scenario. The initial construction cost, based on pay items #40701876 and #30300112 from IDOT Contract 60N11, was calculated specifically for 1 lane-mile of pavement. The total estimated initial construction cost for this section amounted to $504,416 per mile-lane.

Table 16. Rehabilitation Costs (2025$)

Scenarios Vehicle Type (Acceleration)	**Rehab 1**	**Rehab 2**	**Rehab 3**	**Remaining Life**	**Total** *(R1+R2+R3-RL)*
IC (No)	$72,489.16	$38,966.50	–	$14,354.91	$97,100.76
HDEV steering (No)	$91,827.11	$64,405.68	$43,857.14	$6,152.10	$193,937.82
HDEV drive (No)	$84,034.81	$52,367.72	$33,612.84	$24,608.41	$145,406.96
HDEV evenly distributed (No)	$84,034.81	$52,367.72	$32,633.83	$26,659.11	$142,377.24
IC (Yes)	$74,663.84	$42,579.74	–	$8,202.80	$109,040.78
HDEV drive (Yes)	$89,152.53	$60,708.53	$40,135.49	$12,304.21	$177,692.35
HDEV evenly distributed (Yes)	$86,555.85	$57,223.62	$36,729.66	$18,456.31	$162,052.82

The cost of the rehabilitation activity was estimated using pay items #AR401650 and #40604060, totaling $134,851 for 1 lane-mile of pavement, which is the functional unit used in this analysis. For all scenarios, the NPV of a rehabilitation activity was calculated based on the year of occurrence, using a discount rate of 3%. Table 16 summarizes the NPV of each rehabilitation activity for all 100%

IC and 100% HDEV scenarios for a full-depth pavement. When acceleration was considered, the rehabilitation costs for ICs increased from $97,101 to $109,041, reflecting a 12.3% increase compared to the IC scenario at a 0% slip ratio (no acceleration). This increase was observed due to earlier rehab intervention when acceleration was imposed. Among HDEVs, the steering scenario (S1) resulted in the highest total rehabilitation cost of $193,938, which is approximately twice the cost in the IC scenario. This was due to the additional costs associated with the third rehabilitation phase ($43,857).

User Costs

User costs were estimated based on additional fuel/energy consumption resulting from pavement roughness. Manufacturing, purchasing, and maintenance costs of trucks were not included in the analysis. The price of diesel was obtained from the US Energy Information Administration (2025) with a recorded value of $3.697 per gallon. The electricity cost for Illinois was $0.1154/kWh. To account for the time value of money, the costs were converted to the net present value using 2025 as the base year. Table 17 enumerates the user costs for each scenario all calculated per 1 lane-mile of pavement. Under no acceleration conditions, ICs incurred a user cost of $232,733, serving as the baseline for comparison. Among HDEV scenarios, the steering (S1), drive (S2), and evenly distributed (S3) scenarios each had a user cost of $101,878, indicating significantly lower costs compared to ICs. When acceleration was considered, IC user costs increased to $243,509, reflecting a 4.63% rise compared to the no-acceleration condition. Similarly, for HDEVs, the drive (S2) and evenly distributed (S3) scenarios experienced an increase to $106,595, marking a 4.63% increase (see Table 17).

Table 17. User Costs (2025$)

Scenarios (Vehicle Type [Acceleration])	**User Cost (2025$)**
IC (No)	232,733
HDEV steering (No)	101,878
HDEV drive (No)	101,878
HDEV evenly distributed (No)	101,878
IC (Yes)	243,509
HDEV drive (Yes)	106,595
HDEV evenly distributed (Yes)	106,595

LCCA RESULTS

The LCCA results are divided into two parts: four scenarios where acceleration is not considered (Figure 48) and three scenarios where acceleration effects are accounted for (Figure 49). Both figures show results for 0% HDEVs (or 100% ICs) and 100% HDEVs. The materials and construction costs were the highest among all life cycle stages for all load scenarios, which remained constant at $504,416, as the same pavement structure was considered.

Rehabilitation costs varied across scenarios, with the HDEV steering scenario (S1) exhibiting the highest maintenance and rehabilitation (M&R) costs at $193,938 when acceleration was neglected.

This was due to more frequent rehabilitation activities compared to other HDEV configurations, where batteries were either placed on the drive axles (S2) or evenly distributed between the steer and drive axles (S3). The lowest M&R costs were observed in the IC scenario without acceleration at $97,101. When acceleration was considered, M&R costs increased across all scenarios, with the highest observed in the HDEV drive scenario (S2) at $177,692.

The use-stage analysis revealed that including acceleration resulted in higher pavement damage, leading to higher IRI values. This increased roughness led to higher fuel/energy consumption, exacerbating use-stage costs for scenarios with acceleration conditions. However, use-stage costs for HDEVs remained lower than ICs across all cases. Materials and construction costs remained the dominant component, accounting for an average of 62.4% of total costs across all scenarios. Rehabilitation costs made up approximately 19.7%, while use-stage costs constituted around 17.9%. The use-stage costs appear relatively low because only truck traffic was considered in the analyses; whereas, including passenger vehicle traffic would likely result in a higher proportion of use-stage costs. The use-stage cost reflects only the additional fuel consumption resulting from pavement roughness, and not the total fuel cost.

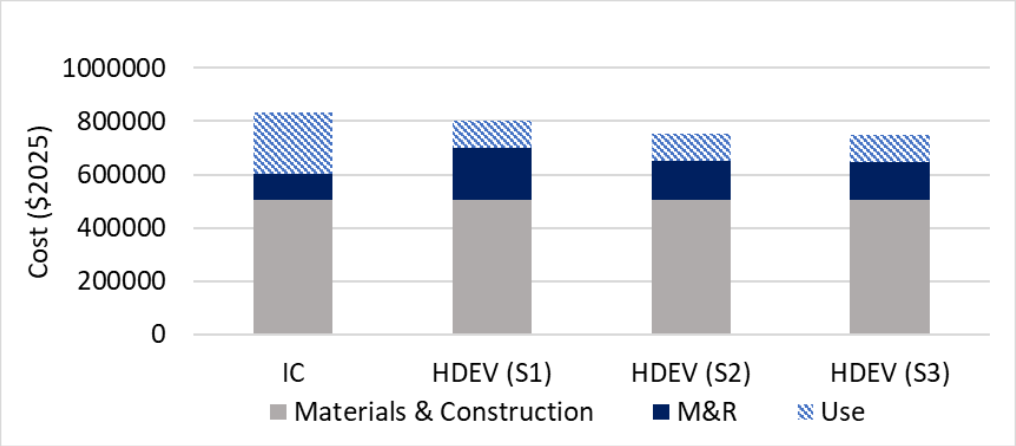

Figure 48. Graph. Economic costs for IC and HDEV scenarios (no acceleration).

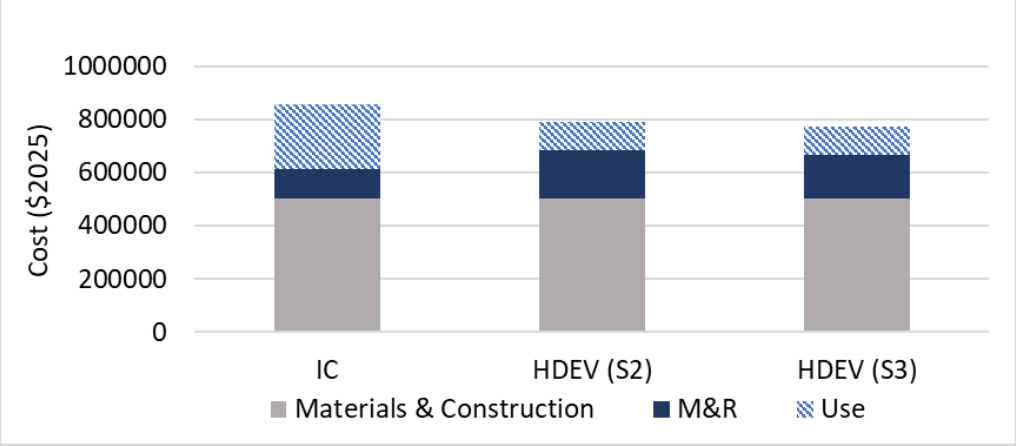

Figure 49. Graph. Economic costs for IC and HDEV scenarios (acceleration).

HDEV AT VARYING MARKET PENETRATION LEVELS: LCA AND LCCA IMPLICATIONS

Market penetration levels of 0% to 100% HDEVs showcased traffic mix conditions. In this section, varying penetration levels are presented to represent the assumed gradual transition of truck traffic from all ICs to all HDEVs, alongside their implications on environmental and economic costs. Figure 50 presents emissions from the M&R and use stages across varying HDEV market penetration levels without acceleration, while Figure 51 shows the corresponding results assuming the influence of HDEV acceleration. The GHG emissions and economic costs for the material and construction stage were excluded as the analysis considered the same full-depth pavement structure.

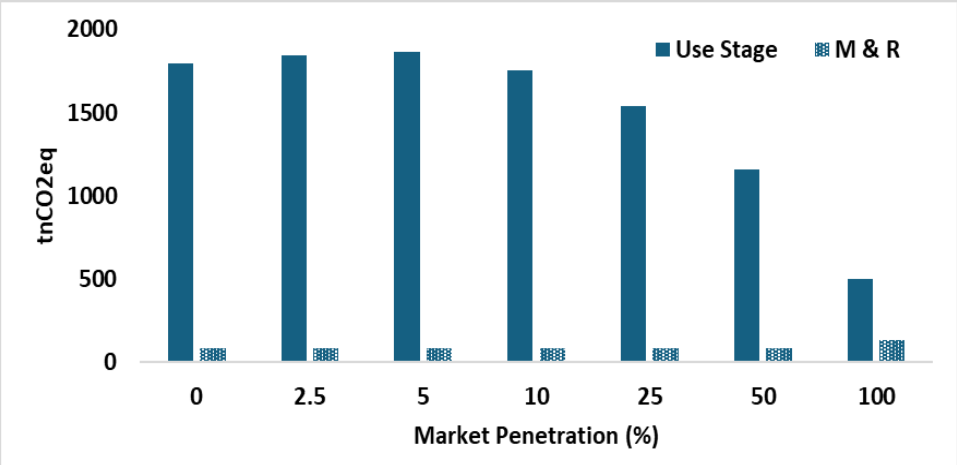

Figure 50. Graph. Emissions across varying HDEV market penetration rates (no acceleration).

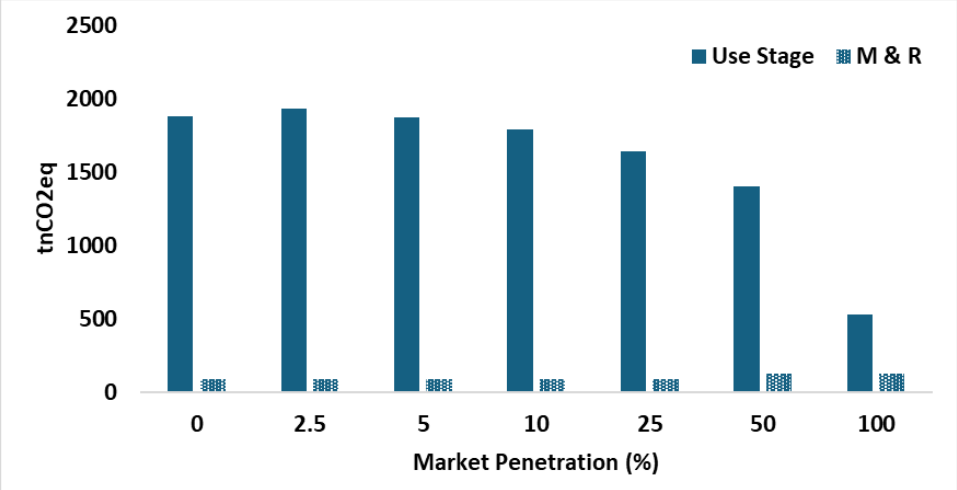

Figure 51. Graph. Emissions across varying HDEV market penetration rates (acceleration).

The results indicate that as HDEV market penetration increased, use-stage emissions decreased significantly. Without acceleration, use-stage emissions increased from 1,795 $tnCO_2eq$ at 0% MP to 1,847 $tnCO_2eq$ at 2.5% and to 1864 $tnCO_2eq$ at 5%, then declined slightly 1,755 $tnCO_2eq$ at 10%, 1,540 $tnCO_2eq$ at 25%, 1,156 $tnCO_2eq$ at 50% MP, and finally dropped significantly to 503 $tnCO_2eq$ at

100% MP. A similar pattern was observed under acceleration conditions, where use-stage emissions started at 1,879 $tnCO_2eq$ at 0% penetration, peaked slightly at 1,931 $tnCO_2eq$ at 2.5%, then dropped to 1,872 $tnCO_2eq$ at 5%, 1,788 $tnCO_2eq$ at 10%, 1,643 $tnCO_2eq$ at 25%, 1,405 $tnCO_2eq$ at 50%, and 526 $tnCO_2eq$ at 100%. These reductions indicate that greater adoption of HDEVs leads to lower use-stage emissions, primarily due to their higher energy efficiency and the relatively cleaner energy mix in Illinois.

In contrast, maintenance and rehabilitation (M&R) emissions remained constant at 86 $tnCO_2eq$ across all market penetration levels up to 50%, regardless of acceleration conditions. However, at 100% penetration, M&R emissions increased to 129 $tnCO_2eq$ in both cases. This suggests that while HDEVs substantially lowered operational emissions, their higher weight led to increased pavement wear, necessitating more frequent rehabilitation activities at full market penetration. Figure 52 illustrates economic costs from the M&R and use stages across at varying HDEV market penetration levels without acceleration, while Figure 53 shows the results with acceleration.

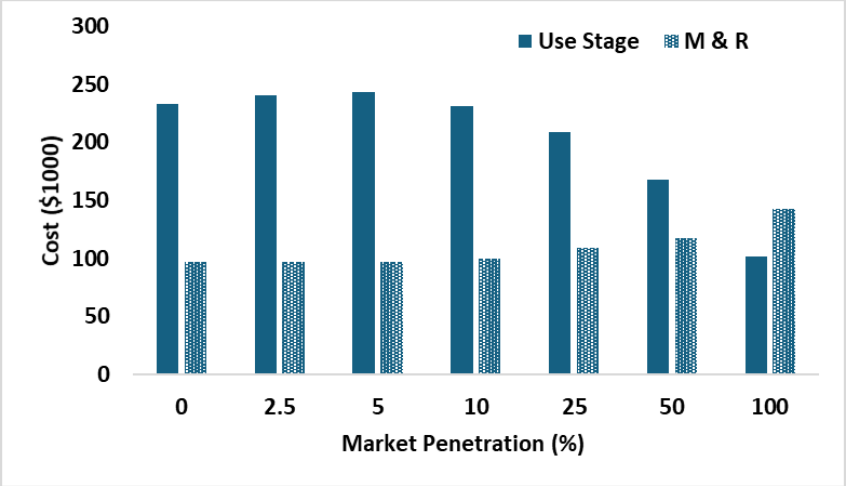

Figure 52. Graph. Cost across varying HDEV market penetration rates (no acceleration).

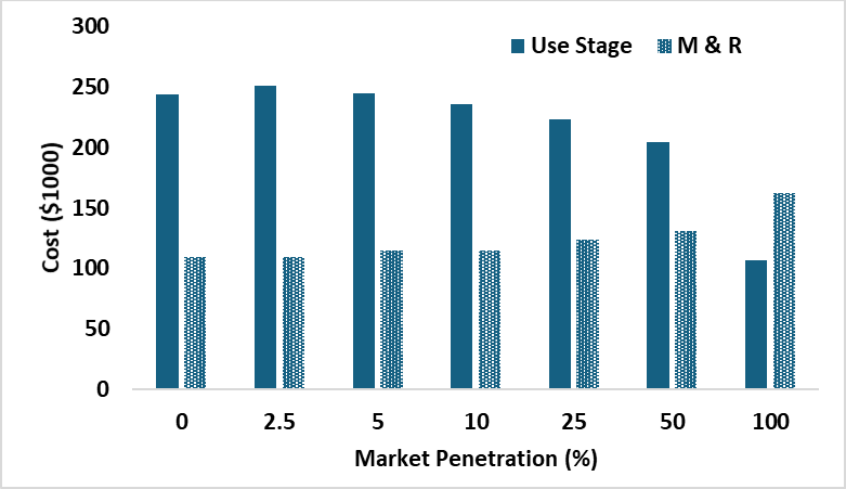

Figure 53. Graph. Cost across varying HDEV market penetration rates (acceleration).

Use-stage costs initially increased at 2.5% MP, rising by 3.3% without acceleration and 3.2% with acceleration, before steadily decreasing by approximately 56% at 100% MP. In contrast, M&R costs remained relatively stable up to 5% MP but increased significantly at rising MP levels, wherein increases of 47% without acceleration and 49% with acceleration at full HDEV adoption were observed. This reflected the impact of heavier axle loads. Acceleration further amplified M&R costs and led to a 14% increase at 100% MP. These results highlight a trade-off, where HDEVs may reduce use-stage costs owing to vehicle design efficiency but may escalate pavement maintenance expenses. Including carbon costs in the analysis can result in significant life cycle savings for pavements. Using the average European carbon-tax rate of $53 per tn$CO_2$-eq (Mengden, 2024), the reduction in use-stage emissions under the acceleration scenario with HDEVs translates to monetary savings of approximately $371, $4,823, $12,508, $25,122, and $71,709 per mile at market-penetration levels of 5%, 10%, 25%, 50%, and 100%, respectively.

SUMMARY

Considering both operational and long-term infrastructure impacts when assessing the sustainability of HDEVs is important. The LCA and LCCA for a full-depth pavement section were completed to compare IC versus HDEV impacts on a full-depth pavement life cycle, including materials and construction, rehabilitation, and use stages. This analysis underscores the importance of conducting LCA and LCCA to evaluate the long-term environmental and economic impacts of pavement performance, respectively, under HDEV loading. The LCA results indicate that IC vehicles have the highest total emissions, primarily driven by the use stage, which contributed to 86% of total emissions. In contrast, HDEVs significantly reduced use-stage emissions by 72%; however, they induced higher M&R emissions by 50%. HDEVs exhibited higher M&R emissions primarily due to increased maintenance and rehabilitation activities. While electricity is often considered a cleaner energy source, frequent rehabilitation requirements for HDEV scenarios contributed significantly to their overall emissions. Moreover, the emissions from the materials and construction stage remained constant across all scenarios as only one pavement structure was evaluated. Considering all LCA stages, the reduction in total emissions as HDEV penetration increases from 0% to 100% is approximated at 60%. The LCCA results indicated that materials and construction costs remained the dominant expense across all scenarios, averaging approximately 63% of total costs. Rehabilitation costs varied significantly based on the scenario, accounting for 11% to 24% of the total cost. The use stage contributed less (because only truck traffic was considered), ranging from 13% to 28%, with lower values for HDEV scenarios due to reduced fuel consumption. In this study, the cost associated with the use stage only accounts for excess fuel consumption due to pavement roughness.

CHAPTER 6: SUMMARY, KEY FINDINGS, AND CONCLUSIONS

SUMMARY

Emerging technologies, including heavy-duty electric vehicles, pose new challenges to flexible pavement design and analysis. The combined impact of load redistribution due to battery placement and access to higher torque warrants a holistic evaluation of existing Illinois pavement sections (i.e., the capacity of current flexible pavements in Illinois to carry HDEV loading). This study evaluated four common pavement structures across Illinois—representative of interstate highways, arterial roads, and rural routes—to quantify HDEV impacts on pavement performance. Compounding factors included increased axle load and acceleration, which governed the contact stress inputs for the pavement structure simulations. The resulting critical strains were assessed, alongside the corresponding number of repetitions to failure for various distresses: bottom-up cracking, shear-driven top-down cracking, and shear-driven shoving. A proposed framework was presented, which includes a new metric—e-truck adjustment factor—that enables a full truck comparison of an internal combustion engine vehicle conventional semitruck with an HDEV, alongside the proposed modification of the truck factor in the IDOT full-depth HMA pavement design methodology. Moreover, environmental and economic impacts of the scenarios considered were evaluated, further enriching the evaluation of HDEV presence on HMA roadways. Key findings are presented as follows.

FINDINGS

- *Increased impact on pavement due to HDEV load and acceleration.* This study utilized and further developed a validated dual-tire assembly (DTA) model to generate a 3D contact stress database for HDEVs and ICs. As expected, the increase in axle load alone (no acceleration) induced higher vertical and longitudinal forces up to 56.4% and 99.7%, respectively, over an enlarged tire-pavement contact area (i.e., longer contact length). Moreover, an increase in acceleration level resulted in a shift in distribution and peak values of the longitudinal forces, which was in line with the increased tractive force that the tire applied during an accelerating scenario. The combined impact of the increased load and the highest slip ratio of 6% resulted in an increase in longitudinal contact force (i.e., the relative difference is high but is a magnitude lower than vertical contact force). Longitudinal contact stresses were a magnitude lower than those of the vertical contact stresses, while transverse forces were marginally influenced.

- *A 1-kip tire load would result in a significant increase in pavement critical strains.* Using the numerically generated contact stress inputs, pavement structure simulations revealed an increase up to 15%, 16%, and 19% at the bottom of hot-mix asphalt (HMA) tensile strain, in HMA-near-surface vertical shear strain, and subgrade compressive strain, respectively, for a given increase of 1 kip on the steer axle (with one tire) for a typical thick pavement section. This contrasts with the drive axles, equipped with a DTA, wherein increases up to 11%, 11%, and 15% were observed for the same respective critical strains, respectively, due to a 0.5-kip increase in DTA loading for a typical-thick HMA pavement structure.

- *Acceleration rate impacts traditional critical strains at a minimum*. As the acceleration level is increased (from 0% to 3% slip ratio) for the steer tire, the bottom HMA tensile strain, HMA-near-surface vertical shear strain, and subgrade compressive strain increased up to 3%, 4%, and 2%, respectively, for a typical-thick HMA pavement. This finding indicates a reduced impact of acceleration on critical pavement strains compared to the effect of the applied load. Further increase of the acceleration level (up to a 6% slip ratio) for the DTA resulted in a 3% difference in strains conventionally used in pavement design.

- *Acceleration affects the near-surface horizontal shear strain.* An increase in acceleration (from a slip ratio value of 0% to 6%) resulted in a 22% difference in the horizontal shear strain, a direct manifestation of an increase in longitudinal forces.

- *Resulting critical strains are pavement-structure dependent.* As expected, the typical thick and low-volume pavements of the four representative Illinois pavement structures revealed a considerable increase in the HMA bottom tensile strain due to increased tire load and acceleration. On the other hand, for similar loading conditions, full-depth and stone-matrix asphalt (SMA)-overlaid-on-Portland Cement Concrete (PCC) pavement sections resulted in higher near-surface vertical and horizontal shear strains, indicating more pronounced shear deformations closer to the tire-pavement contact.

- *E-truck adjustment (ETA)* revealed the following multipliers to the number of repetitions to failure for a full truck for the four pavement sections, relative to the baseline IC scenario of each pavement structure:

    - Full depth: 1.22, 1.31, and 1.41 for HDEV batteries that were evenly distributed, placed on the drive axle only, and steering axle only, respectively.

    - Low volume: 1.23, 1.23, and 1.23 for HDEV batteries that were evenly distributed, placed on the drive axle only, and steering axle only, respectively.

    - Typical thick: 1.66, 1.72, and 1.21 for HDEV batteries that were evenly distributed, placed on the drive axle only, and steering axle only, respectively.

    - SMA overlay: 1.22, 1.27, and 1.33 for HDEV batteries that were evenly distributed, placed on the drive axle only, and steering axle only, respectively.

- *The ETA values can be used as a modification for the traffic factor used in the IDOT full-depth mechanistic design.* For ICs, the corresponding ETA is 1.0 (baseline, no acceleration) and 1.09 (with acceleration). On the other hand, HDEVs with the battery placed on the steer axle (which is an extreme and unlikely scenario) resulted in an e-truck adjustment factor of 1.41, the highest among all HDEV scenarios. As an HDEV battery is placed on the drive axle, the resulting ETA is 1.15 and 1.31 for scenarios with no acceleration and acceleration, respectively. The resulting ETA are 1.12 and 1.22 for no acceleration and with acceleration scenarios, respectively, under the HDEV evenly distributed battery assumption.

- *HDEVs could reduce pavement life cycle.* For the full-depth section, the pavement service life of 21 years under IC loading could be reduced to 14, 18, and 19 years for the HDEV steer, drive-axle, and evenly distributed scenarios, respectively, based on an International Roughness Index (IRI) of 170 in/mi trigger (per FHWA recommendation). In addition to increased impacts on pavement, increased roughness would exacerbate energy use and corresponding emissions.

- *Use of HDEV may require an increase in pavement design thickness using the IDOT approach.* Modifying the traffic factor for a 12 in HMA full-depth design would result in thickness increases of 0.25, 0.50, and 0.75 in for the HDEV evenly distributed, drive-axle, and steer scenarios (without acceleration), respectively.

- *HDEV uses more energy*. Based on the life cycle assessment (LCA), increasing IC acceleration by 2% led to a 3% increase in energy consumption due to pavement roughness. Focusing on realistic scenarios and at 2% acceleration, the HDEV drive axle and evenly distributed scenarios consumed up to 72% less than that of the IC.

- *Acceleration increases the cost for pavements under HDEV loading*. Given that the acceleration effect is more pronounced for HDEV on full-depth pavement, it increased costs by $68,262 per lane-mile for the entire analysis period for the HDEV drive with acceleration scenario (compared to IC with acceleration) due to an increased rehabilitation frequency.

- *Emissions decreased with greater HDEV penetration*. Under the no-acceleration scenario, use-stage emissions decreased by 35.6% when the HDEV market penetration increased from 0% to 50% and by 56.5% when further increased from 50% to 100%. Similarly, under the acceleration scenario, use-stage emissions decreased by 25.2% and 62.6% for the same levels of HDEV market penetration, respectively.

CONCLUSIONS

This study underscores the importance of holistically evaluating flexible pavements subjected to new technologies, such as HDEV—from pavement response/damage, LCA, and LCCA. The impact of HDEVs not only factors load increase from battery placement and higher acceleration, but also pavement structural configuration, which further defines the governing distress. The following conclusions are drawn:

1. Avoid placing the HDEV's battery on the steering axle. It leads to the highest combined distress of bottom-up fatigue cracking, shear-induced top-down cracking, and shear-induced shoving. This extreme scenario is unlikely to be a choice for original equipment manufacturers. The HDEV evenly distributed scenario may impost the lowest costs incurred.

2. Consider nontraditional critical strains in assessing HDEV impact on flexible pavement to control cracking and shoving, including horizontal and vertical shear strains within HMA

layers. A modification for the traffic factor in IDOT pavement design using ETA is recommended to account for such impacts.

3. Increasing HDEV penetration would increase pavement rehabilitation frequency and corresponding cost but would reduce overall energy use and corresponding emissions. The associated costs and emissions are pavement-structure dependent and must be analyzed for each pavement project.

4. Because of the reduced hauling capacity of HDEVs compared to ICs, additional trips may be required to transport the same amount of freight—leading to increased traffic and required pavement maintenance and rehabilitation. Hence, the traffic level must be modified based on potential HDEV penetration.

REFERENCES

AASHTO. (1961). *Interim Guide for Design of Flexible Pavement Structures 1961*. American Association of State Highway and Transportation Officials (AASHTO), National Academy of Science, National Research Council.

AASHTO. (1972). *Interim Guide for Design of Pavement Structures 1972*. American Association of State Highway and Transportation Officials (AASHTO), National Academy of Science, National Research Council.

AASHTO. (1986). *Guide for Design of Pavement Structures*. American Association of State Highway and Transportation Officials (AASHTO).

AASHTO. (1993). *Guide for Design of Pavement Structures*. American Association of State Highway and Transportation Officials (AASHTO).

AASHTO. (1998). *Guide for Design of Pavement Structures, Supplement*. American Association of State Highway and Transportation Officials (AASHTO).

AASHTO. (2008). *Mechanistic-Empirical Pavement Design Guide—A Manual of Practice*. American Association of State Highway and Transportation Officials (AASHTO).

AASHTO. (2020). *Mechanistic-Empirical Pavement Design Guide: A Manual of Practice*. American Association of Highway and Transportation Officials.

Adeleke, O. P., Li, Y., Chen, Q., Zhou, W., Xu, X., & Cui, X. (2022). Torque distribution based on dynamic programming algorithm for four in-wheel motor drive electric vehicle considering energy efficiency optimization. *World Electric Vehicle Journal*, *13*(10), 181. https://doi.org/10.3390/wevj13100181

AFDC. (2023a). *Alternative Fuels Data Center: Commercial Electric Vehicle (EV) and Fuel Cell Electric Vehicle (FCEV) Tax Credit*. Alternative Fuels Data Center. https://afdc.energy.gov/laws/13039

AFDC. (2023b). *Alternative Fuels Data Center: Illinois Transportation Data for Alternative Fuels and Vehicles*. Alternative Fuels Data Center. https://afdc.energy.gov/states/il

Al-Qadi, I. L., Hernandez, J. A., Gamez, A., Ziyadi, M., Gungor, O. E., & Kang, S. (2018). Impact of wide-base tires on pavements: A national study. *Transportation Research Record: Journal of the Transportation Research Board*, *2672*(40), 186–196. https://doi.org/10.1177/0361198118757969

Al-Qadi, I. L., Hernandez, J. A., Gamez, A., Ziyadi, M., Gungor, O. E., Kang, S., Harvey, J., Wu, R., Green, J., Choubane, B., De Beer, M., & Scarpas, T. (2016). *The impact of wide-base tires on pavement—A national study* (Report No. ICT-15-UILU-ENG-2015). Illinois Center for Transportation.

Al-Qadi, I. L., Wang, H., Yoo, P. J., & Dessouky, S. H. (2008). Dynamic analysis and in situ validation of perpetual pavement response to vehicular loading. *Transportation Research Record: Journal of the Transportation Research Board*, *2087*(1), 29–39. https://doi.org/10.3141/2087-04

Al-Qadi, I. L., Yoo, P. J., Elseifi, M. A., Janajreh, I., Chehab, G., & Collop. (2005). Effects of tire configurations on pavement damage. *Asphalt Paving Technology: Association of Asphalt Paving Technologists-Proceedings of the Technical Sessions*, *74*, 921–961.

https://experts.illinois.edu/en/publications/effects-of-tire-configurations-on-pavement-damage

Ameri-Gaznon, M., Button, J. W., Perdomo, D., Little, D. N., & Zollinger, D. G. (1989). *Avoiding Early Failure of Intersection Pavements* (Nos. 1172-1F). Texas A&M Transportation Institute. https://tti.tamu.edu/tti-publication/avoiding-early-failure-of-intersection-pavements/

Arora, S., Abkenar, A. T., Jayasinghe, S. G., & Tammi, K. (2021). *Heavy-duty electric vehicles*. Elsevier. https://doi.org/10.1016/C2018-0-02433-0

Aryan, Y., Dikshit, A. K., & Shinde, A. M. (2023). A critical review of the life cycle assessment studies on road pavements and road infrastructures. *Journal of Environmental Management*, *336*, 117697. https://doi.org/10.1016/j.jenvman.2023.117697

Aschenbrener, T., & Shuller, S. (1995). *High performance hot mix asphalt pavement for intersections* (Technical Report No. CDOT-DTD-R-95-10). Colorado Department of Transportation.

Battle Motors. (2023). *Battle motors low entry Tilt II—Electric: Specifications and performance*. https://battlemotors.com/

Botshekan, M., Tootkaboni, M. P., & Louhghalam, A. (2019). Global sensitivity of roughness-induced fuel consumption to road surface parameters and car dynamic characteristics. *Transportation Research Record: Journal of the Transportation Research Board*, *2673*(2), 183–193. https://doi.org/10.1177/0361198118821318

BTS. (2025). *US vehicle-miles.* Bureau of Transportation Statistics. https://www.bts.gov/content/us-vehicle-miles

Burmister, D. M. (1943). Theory of stresses and displacements in layered systems and application to the design of airport runways. *Proceedings 23rd Annual Meeting of the Highway Research Board*.

Burmister, D. M. (1945). The General Theory of Stresses and Displacements in Layered Systems. I. *Journal of Applied Physics*, *16*(2), 89–94. https://doi.org/10.1063/1.1707558

BYD. (2023). *Model: All-electric BYD 8TT tandem axle*. https://en.byd.com/Truck/Class-8-Day-Cab/

Castillo, D., & Al-Qadi, I. L. (2018). Importance of heterogeneity in asphalt pavement modeling. *Journal of Engineering Mechanics*, *144*(8), 04018060. https://doi.org/10.1061/(ASCE)EM.1943-7889.0001488

Congress. (2022a). *H.R.3684—Infrastructure Investment and Jobs Act*. Congress.Gov. https://www.congress.gov/bill/117th-congress/house-bill/3684/text

Congress. (2022b). *H.R.5376—Inflation Reduction Act of 2022*. Congress.Gov. https://www.congress.gov/bill/117th-congress/house-bill/5376/text

Continental. (2020a). *Prototypes tires for electric buses tested at the Contidrom [Press release]*. Continental: The Future in Motion. https://www.continental.com/en/press/press-releases/2020-07-20-vehicles-with-electric-drive-need-special-tires/?ref=3844890&navigationPath=transport-en-us/fleetsolutions

Continental. (2020b). *Vehicles with electric drive need special tires [Press release]*. Continental: The Future in Motion. https://www.continental.com/en/press/press-releases/2020-07-20-vehicles-with-electric-drive-need-special-tires/?ref=3844890&navigationPath=transport-en-

us/fleetsolutions

Continental. (2024). *Continental to present highly efficient and sustainable tire solutions at IAA transportation [Press release]*. Continental: The Future in Motion. https://www.continental.com/en/press/press-releases/20240905-truck-bus-tires/

Costa, R. (2021). *Balanced mix design of asphalt mixtures for intersections* [Master's Thesis, University of Nevada, Reno]. https://scholarwolf.unr.edu/server/api/core/bitstreams/59894229-333e-49ee-a841-c28aab6cb500/content

Cunanan, C., Tran, M.-K., Lee, Y., Kwok, S., Leung, V., & Fowler, M. (2021). A review of heavy-duty vehicle powertrain technologies: diesel engine vehicles, battery electric vehicles, and hydrogen fuel cell electric vehicles. *Clean Technologies*, *3*(2), 474–489. https://doi.org/10.3390/cleantechnol3020028

Daimler Trucks North America LLC (2024). eCascadia® Specification Sheet [PDF]. *Freightliner*. https://dtnacontent-dtna.prd.freightliner.com/content/dam/enterprise/documents/eCascadia%20Spec%20Sheet_2023.pdf

Dizqah, A. M., Lenzo, B., Sorniotti, A., Gruber, P., Fallah, S., & De Smet, J. (2016). A fast and parametric torque distribution strategy for four-wheel-drive energy-efficient electric vehicles. *IEEE Transactions on Industrial Electronics*, *63*(7), 4367–4376. https://doi.org/10.1109/TIE.2016.2540584

DOE. (2022). *The Inflation Reduction Act Drives Significant Emissions Reductions and Positions America to Reach Our Climate Goal*. Department of Energy. https://www.energy.gov/sites/default/files/2022-08/8.18%20InflationReductionAct_Factsheet_Final.pdf

DOE. (2025). *Alternative Fuels Data Center: Fuel Properties Comparison*. https://afdc.energy.gov/fuels/properties?fuels=GS

EIA. (2024). *US Energy Information Administration—EIA - Independent Statistics and Analysis*. https://www.eia.gov/state/?sid=IL

EIA. (2025). *Gasoline and Diesel Fuel Update*. https://www.eia.gov/petroleum/gasdiesel/index.php

Elseifi, M. A., Al-Qadi, I. L., & Yoo, P. J. (2006). Viscoelastic modeling and field validation of flexible pavements. *Journal of Engineering Mechanics*, *132*(2), 172–178. https://doi.org/10.1061/(ASCE)0733-9399(2006)132:2(172)

EPA. (2024). *Fast Facts on Transportation Greenhouse Gas Emissions*. Environmental Protection Agency. https://www.epa.gov/greenvehicles/fast-facts-transportation-greenhouse-gas-emissions

FHWA. (2025a). *FHWA Emergency Relief Program: Understanding Betterment Eligibility and Approval*. https://flh.fhwa.dot.gov/programs/erfo/training/life_cycle_cost_analysis/select_discount_rate.php

FHWA. (2025b). *Key Issues in Life-Cycle Cost Analysis for Pavements—References—Sustainable Pavement Program—Sustainability—Pavements—Federal Highway Administration*. https://www.fhwa.dot.gov/pavement/sustainability/articles/key_issues.cfm

Fleming, K. L., Brown, A. L., Fulton, L., & Miller, M. (2021). Electrification of medium- and heavy-duty

ground transportation: Status report. *Current Sustainable/Renewable Energy Reports*, *8*(3), 180–188. https://doi.org/10.1007/s40518-021-00187-3

Forrest, K., Mac Kinnon, M., Tarroja, B., & Samuelsen, S. (2020). Estimating the technical feasibility of fuel cell and battery electric vehicles for the medium and heavy duty sectors in California. *Applied Energy*, *276*, 115439. https://doi.org/10.1016/j.apenergy.2020.115439

Freightliner Trucks. (2023). *Freightliner eCasadia(R) specs*. Freightliner. https://www.freightliner.com/Trucks/Ecascadia/Specifications/#tab-1

Gamez, A., Hernandez, J. A., Ozer, H., & Al-Qadi, I. L. (2018). Development of domain analysis for determining potential pavement damage. *Journal of Transportation Engineering, Part B: Pavements*, *144*(3), 04018030. https://doi.org/10.1061/JPEODX.0000059

Gao, Z., Lin, Z., & Franzese, O. (2017). Energy consumption and cost savings of truck electrification for heavy-duty vehicle applications. *Transportation Research Record: Journal of the Transportation Research Board*, *2628*(1), 99–109. https://doi.org/10.3141/2628-11

García Mainieri, J. J., & Al-Qadi, I. L. (2025). Designing stone-matrix asphalt to optimize sustainability using limestone, dolomite, and crushed gravel aggregates. *Journal of Transportation Engineering, Part B: Pavements*, *151*(1), 04024061. https://doi.org/10.1061/JPEODX.PVENG-1614

Goodyear. (2023). *Goodyear Introduces First EV Tire for Regional Fleets [Press release]*. Goodyear Corporate. https://news.goodyear.com/goodyear-introduces-first-ev-tire-for-regional-fleets?

Gungor, O. E., Al-Qadi, I. L., Gamez, A., & Hernandez, J. A. (2017). Development of adjustment factors for MEPDG pavement responses utilizing finite-element analysis. *Journal of Transportation Engineering, Part A: Systems*, *143*(7), 04017022. https://doi.org/10.1061/JTEPBS.0000040

Hajj, E. Y., Sebaaly, P. E., & Siddharthan, R. V. (2006). Response of asphalt pavement mixture under a slow moving truck. *Geotechnical Special Publication*, *146*, 134–146.

Hajj, E. Y., Siddharthan, R. V., Sebaaly, P. E., & Weitzel, D. (2007). Hot-mix asphalt mixtures for Nevada's intersections. *Transportation Research Record: Journal of the Transportation Research Board*, *2001*(1), 73–83. https://doi.org/10.3141/2001-09

Hajj, E. Y., Tannoury, G., & Sebaaly, P. E. (2011). Evaluation of rut resistant asphalt mixtures for intersection. *Road Materials and Pavement Design*, *12*(2), 263–292. https://doi.org/10.1080/14680629.2011.9695246

Hajj, E. Y., Thushanthan, P., Sebaaly, P. E., & Siddharthan, R. V. (2012). Influence of tire–pavement stress distribution, shape, and braking on performance predictions for asphalt pavement. *Transportation Research Record: Journal of the Transportation Research Board*, *2306*(1), 73–85. https://doi.org/10.3141/2306-09

Harvey, J., Saboori, A., Miller, M., Kim, C., Jaller, M., Lea, J., Kendall, A., & Saboori, A. (2020). *Effects of increased weights of alternative fuel trucks on pavements and bridges* (No. UC-ITS-202-19; ITS Reports). UC Office of the President: University of California Institute of Transportation Studies. https://doi.org/10.7922/G27M066V

Hernandez, J. A., & Al-Qadi, I. L. (2016a). Contact phenomenon of free-rolling wide-base tires: effect

of speed and temperature. *Journal of Transportation Engineering*, *142*(12), 04016060. https://doi.org/10.1061/(ASCE)TE.1943-5436.0000893

Hernandez, J. A., & Al-Qadi, I. L. (2016b). Hyperelastic modeling of wide-base tire and prediction of its contact stresses. *Journal of Engineering Mechanics*, *142*(2), 04015084. https://doi.org/10.1061/(ASCE)EM.1943-7889.0001007

Hernandez, J. A., & Al-Qadi, I. L. (2017a). Semicoupled modeling of interaction between deformable tires and pavements. *Journal of Transportation Engineering, Part A: Systems*, *143*(4), 04016015. https://doi.org/10.1061/JTEPBS.0000007

Hernandez, J. A., & Al-Qadi, I. L. (2017b). Tire–pavement interaction modelling: Hyperelastic tire and elastic pavement. *Road Materials and Pavement Design*, *18*(5), 1067–1083. https://doi.org/10.1080/14680629.2016.1206485

Hernandez, J. A., Gamez, A., & Al-Qadi, I. L. (2016). Effect of wide-base tires on nationwide flexible pavement systems: Numerical modeling. *Transportation Research Record: Journal of the Transportation Research Board*, *2590*(1), 104–112. https://doi.org/10.3141/2590-12

Hernandez, J. A., Gamez, A., Shakiba, M., & Al-Qadi, I. L. (2015). *Numerical prediction of three-dimensional tire-pavement contact stresses* (Report No. ICT-17-004). Illinois Center for Transportation. https://www.ideals.illinois.edu/items/98236

Hernandez, J. A., Jayme, A., Cardenas Huaman, J. J., & Al-Qadi, I. L. (2025). Effect of heavy-duty electric vehicles on tire–pavement contact forces. *Journal of Engineering Mechanics*, *151*(1), 04024104. https://doi.org/10.1061/JENMDT.EMENG-7835

Highway Research Board. (1961). *The AASHO Road Test. Report 5: Pavement Research* (No. HRB SR 61E). National Academy of Sciences - National Research Council.

Hjelmstad, K. D., Zuo, Q., & Kim, J. (1997). Elastic pavement analysis using infinite elements. *Transportation Research Record: Journal of the Transportation Research Board*, *1568*(1), 72–76. https://doi.org/10.3141/1568-09

IDOT. (2022). *Bureau of Design and Environmental Manual*. Illinois Department of Transportation, Bureau of Design and Environment. https://public.powerdms.com/IDOT/documents/1881647

Jayme, A., & Al-Qadi, I. L. (2021). Thermomechanical coupling of a hyper-viscoelastic truck tire and a pavement layer and its impact on three-dimensional contact stresses. *Transportation Research Record: Journal of the Transportation Research Board*, *2675*(11), 359–372. https://doi.org/10.1177/03611981211017140

Jayme, A., & Al-Qadi, I. L. (2022). Contact stress and rolling loss estimation via thermomechanical interaction modeling of a truck tire on a pavement layer. *Journal of Engineering Mechanics*, *148*(12), 04022071. https://doi.org/10.1061/(ASCE)EM.1943-7889.0002154

Jiang, X., Zeng, C., Gao, X., Liu, Z., & Qiu, Y. (2019). 3D FEM analysis of flexible base asphalt pavement structure under non-uniform tyre contact pressure. *International Journal of Pavement Engineering*, *20*(9), 999–1011. https://doi.org/10.1080/10298436.2017.1380803

Kandhal, P. S., Mallick, R. B., & Brown, E. R. (1998). *Hot mix asphalt for intersections in hot climates*

(No. NCAT Report 98-06). National Center for Asphalt Technology, Auburn University. https://eng.auburn.edu/research/centers/ncat/files/technical-reports/rep98-06.pdf

Khazanovich, L., & Wang, Q. (2007). MnLayer: High-performance layered elastic analysis program. *Transportation Research Record: Journal of the Transportation Research Board*, *2037*(1), 63–75. https://doi.org/10.3141/2037-06

Kim, B. S., Chi, C. H., & Lee, T. K. (2007). A study on radial directional natural frequency and damping ratio in a vehicle tire. *Applied Acoustics*, *68*(5), 538–556. https://doi.org/10.1016/j.apacoust.2006.07.009

Kim, M., Tutumluer, E., & Kwon, J. (2009). Nonlinear pavement foundation modeling for three-dimensional finite-element analysis of flexible pavements. *International Journal of Geomechanics*, *9*(5), 195–208. https://doi.org/10.1061/(ASCE)1532-3641(2009)9:5(195)

Kluschke, P., Gnann, T., Plötz, P., & Wietschel, M. (2019). Market diffusion of alternative fuels and powertrains in heavy-duty vehicles: A literature review. *Energy Reports*, *5*, 1010–1024. https://doi.org/10.1016/j.egyr.2019.07.017

Kohler, E., Long, G., & Roesler, J. (2002). *Construction of extended life continuously reinforced concrete pavements at ATREL* (Report No. FHWA-IL-UI-282). University of Illinois Urbana-Champaign. https://apps.ict.illinois.edu/projects/getfile.asp?id=2928

Kubo, P., Paiva, C., Larocca, A., & Dawson, J. (2016). Quantification of the vertical load applied to the pavement during braking maneuver of a commercial vehicle. *Journal of Transportation Engineering*, *142*(4), 06016001. https://doi.org/10.1061/(ASCE)TE.1943-5436.0000834

Lambert, F. (2022). *Tesla Semi completes first 500-mile trip with a full load*. Electrek. https://electrek.co/2022/11/27/tesla-semi-completes-first-500-mile-trip-full-load/

Li, J., Xiao, F., Zhang, L., & Amirkhanian, S. N. (2019). Life cycle assessment and life cycle cost analysis of recycled solid waste materials in highway pavement: A review. *Journal of Cleaner Production*, *233*, 1182–1206. https://doi.org/10.1016/j.jclepro.2019.06.061

Liu, X., & Al-Qadi, I. L. (2021). Development of a simulated three-dimensional truck model to predict excess fuel consumption resulting from pavement roughness. *Transportation Research Record: Journal of the Transportation Research Board*, *2675*(9), 1444–1456. https://doi.org/10.1177/03611981211007849

Liu, X., & Al-Qadi, I. L. (2022a). Integrated vehicle–tire–pavement approach for determining pavement structure–induced rolling resistance under dynamic loading. *Transportation Research Record*, *2676*(5), 398–409. https://doi.org/10.1177/03611981211067797

Liu, X., & Al-Qadi, I. L. (2022b). Three-dimensional tire-pavement contact stresses prediction by deep learning approach. *International Journal of Pavement Engineering*, *23*(14), 4991–5002. https://doi.org/10.1080/10298436.2021.1990288

Liu, X., Jayme, A., & Al-Qadi, I. L. (2023). ContactGAN development—prediction of tire-pavement contact stresses using a generative and transfer learning model. *International Journal of Pavement Engineering*, *24*(2), 2138876. https://doi.org/10.1080/10298436.2022.2138876

Lopez Arteaga, I. (2010). Influence of material damping on the prediction of road texture and tread pattern related rolling resistance. *24th International Conference on Noise and Vibration Engineering*, 4029–4052.

Louhghalam, A., Tootkaboni, M., & Ulm, F.-J. (2015). Roughness-induced vehicle energy dissipation: statistical analysis and scaling. *Journal of Engineering Mechanics*, *141*(11), 04015046. https://doi.org/10.1061/(ASCE)EM.1943-7889.0000944

Mareev, I., Becker, J., & Sauer, D. (2017). Battery dimensioning and life cycle costs analysis for a heavy-duty truck considering the requirements of long-haul transportation. *Energies*, *11*(1), 55. https://doi.org/10.3390/en11010055

Masad, S., Little, D., & Masad, E. (2006). Analysis of flexible pavement response and performance using isotropic and anisotropic material properties. *Journal of Transportation Engineering*, *132*(4), 342–349. https://doi.org/10.1061/(ASCE)0733-947X(2006)132:4(342)

McKinsey. (2024). *Decarbonizing trucks: A bumpy road ahead | McKinsey*. https://www.mckinsey.com/industries/automotive-and-assembly/our-insights/the-bumpy-road-to-zero-emission-trucks

Michelin. (2023). *Shop EV Tires*. Michelin. https://www.michelinman.com/auto/shop-ev-tires

Mikhail, M. Y., & Mamlouk, M. S. (1997). Effect of vehicle-pavement interaction on pavement response. *Transportation Research Record: Journal of the Transportation Research Board*, *1570*(1), 78–88. https://doi.org/10.3141/1570-10

Moultak, M., Lutsey, N., & Hall, D. (2017). *Transitioning to zero-emission heavy-duty freight vehicles* [White Paper]. The International Council on Clean Transportation. https://theicct.org/sites/default/files/publications/Zero-emission-freight-trucks_ICCT-white-paper_26092017_vF.pdf

Pscherer, T., & Krommes, S. (2025). LCA standards for environmental product assessments in the bioeconomy with a focus on biogenic carbon: A systematic review. *The International Journal of Life Cycle Assessment*, *30*(2), 371–393. https://doi.org/10.1007/s11367-024-02387-7

Ramakrishnan, A., & Al-Qadi, I. L. (2023). Axle weight limits for single and tandem axles. *Journal of Transportation Engineering, Part B: Pavements*, *149*(3), 04023016. https://doi.org/10.1061/JPEODX.PVENG-1211

Rohlwing, K (2023). Steer-axle specs must be followed—or safety is put at risk. *FleetOwner Magazine*. https://www.fleetowner.com/fleet-owner-magazine/article/21260062/must-follow-steer-axle-regulations

Romanoschi, S. A., & Metcalf, J. B. (2001). Characterization of asphalt concrete layer interfaces. *Transportation Research Record: Journal of the Transportation Research Board*, *1778*(1), 132–139. https://doi.org/10.3141/1778-16

Said, I. M., & Al-Qadi, I. L. (2023). Incorporation of pavement dynamic loading in mechanistic–empirical design frameworks. *Transportation Research Record: Journal of the Transportation Research Board*, *2677*(12), 14–28. https://doi.org/10.1177/03611981231166943

Santos Maia, R., Asadi, B., Vyas, A., Thompson, M., & Hajj, R. (2024). Dynamic modulus prediction models for Illinois' full-depth asphalt pavement M-E design considering modern materials. *14th*

International Conference on Asphalt Pavements ISAP2024 Montreal, 261–265.

Song, S., & Yeom, C. (2021). Reduction of plastic deformation in heavy traffic intersections in urban areas. *Sustainability*, *13*(7), 4002. https://doi.org/10.3390/su13074002

Sripad, S., & Viswanathan, V. (2019). Quantifying the economic case for electric semi-trucks. *ACS Energy Letters*, *4*(1), 149–155. https://doi.org/10.1021/acsenergylett.8b02146

Suriyamoorthy, S., Gupta, S., Kumar, D. P., & Subramanian, S. C. (2019). Analysis of hub motor configuration and battery placement on ride comfort of electric trucks. *2019 IEEE Vehicle Power and Propulsion Conference (VPPC)*, 1–6. https://doi.org/10.1109/VPPC46532.2019.8952254

Thompson, M. R., & Cation, K. (1986). *A proposed full-depth asphalt concrete thickness design procedure* (No. FHWA-IL-UI-213). University of Illinois Urbana-Champaign.

Tutumluer, E., & Thompson, M. R. (1997). Anisotropic modeling of granular bases in flexible pavements. *Transportation Research Record: Journal of the Transportation Research Board*, *1577*(1), 18–26. https://doi.org/10.3141/1577-03

Tutumluer, E., & Thompson, M. R. (1998). *Anisotropic behavior of unbound aggregate bases* (Final Report. Center of Excellence for Airport Pavements No. II). University of Illinois Urbana-Champaign.

Verbruggen, F. J. R., Silvas, E., & Hofman, T. (2020). Electric powertrain topology analysis and design for heavy-duty trucks. *Energies*, *13*(10), 2434. https://doi.org/10.3390/en13102434

VOLVO. (2023). *Volvo VNR electric specifications: VNR electric 6x2 tractor*. https://www.volvotrucks.us/trucks/vnr-electric/

Wang, D., Roesler, J. R., & Guo, D.-Z. (2009). Analytical approach to predicting temperature fields in multilayered pavement systems. *Journal of Engineering Mechanics*, *135*(4), 334–344. https://doi.org/10.1061/(ASCE)0733-9399(2009)135:4(334)

Wang, H., & Al-Qadi, I. L. (2010). Evaluation of surface-related pavement damage due to tire braking. *Road Materials and Pavement Design*, *11*(1), 101–121. https://doi.org/10.1080/14680629.2010.9690262

Wang, H., & Al-Qadi, I. L. (2013). Importance of nonlinear anisotropic modeling of granular base for predicting maximum viscoelastic pavement responses under moving vehicular loading. *Journal of Engineering Mechanics*, *139*(1), 29–38. https://doi.org/10.1061/(ASCE)EM.1943-7889.0000465

Wang, H., Al-Qadi, I. L., Portas, S., & Coni, M. (2013a). Three-dimensional finite element modeling of instrumented airport runway pavement responses. *Transportation Research Record: Journal of the Transportation Research Board*, *2367*(1), 76–83. https://doi.org/10.3141/2367-08

Wang, H., Al-Qadi, I. L., & Stanciulescu, I. (2012). Simulation of tyre–pavement interaction for predicting contact stresses at static and various rolling conditions. *International Journal of Pavement Engineering*, *13*(4), 310–321. https://doi.org/10.1080/10298436.2011.565767

Wang, H., Al-Qadi, I. L., & Stanciulescu, I. (2014). Effect of surface friction on tire–pavement contact stresses during vehicle maneuvering. *Journal of Engineering Mechanics*, *140*(4), 04014001. https://doi.org/10.1061/(ASCE)EM.1943-7889.0000691

Wang, H., Ozer, H., Al-Qadi, I. L., & Duarte, C. A. (2013b). Analysis of near-surface cracking under critical loading conditions using uncracked and cracked pavement models. *Journal of Transportation Engineering*, *139*(10), 992–1000. https://doi.org/10.1061/(ASCE)TE.1943-5436.0000562

Williams, M. L., Landel, R. F., & Ferry, J. D. (1955). The temperature dependence of relaxation mechanisms in amorphous polymers and other glass-forming liquids. *Journal of the American Chemical Society*, *77*(14), 3701–3707. https://doi.org/10.1021/ja01619a008

XOS. (2023). *XOS HDXTTM 100% battery-electric tractor*. https://www.xostrucks.com/hdxt/

Yoo, P. J., & Al-Qadi, I. L. (2007). Effect of transient dynamic loading on flexible pavements. *Transportation Research Record: Journal of the Transportation Research Board*, *1990*(1), 129–140. https://doi.org/10.3141/1990-15

Yoo, P. J., Al-Qadi, I. L., Elseifi, M. A., & Janajreh, I. (2006). Flexible pavement responses to different loading amplitudes considering layer interface condition and lateral shear forces. *International Journal of Pavement Engineering*, *7*(1), 73–86. https://doi.org/10.1080/10298430500516074

Zaghloul, S., & White, T. (1993). *Use of a Three-Dimensional, Dynamic Finite Element Program for Analysis of Flexible Pavement*. https://onlinepubs.trb.org/Onlinepubs/trr/1993/1388/1388-008.pdf

Zhou, Q., Ramakrishnan, A., Fakhreddine, M., Okte, E., & Al-Qadi, I. L. (2024). Impacts of heavy-duty electric trucks on flexible pavements. *International Journal of Pavement Engineering*, *25*(1), 2361087. https://doi.org/10.1080/10298436.2024.2361087

Ziyadi, M., & Al-Qadi, H. O. & I. L. (2017). Functional unit choice for comparative pavement LCA involving use-stage with pavement roughness Uncertainty Quantification (UQ). In *Pavement Life-Cycle Assessment*. CRC Press.

APPENDICES

APPENDIX A: LITERATURE REVIEW

Beginning January 1, 2023, purchase of commercial electric vehicles (EV) and fuel cell EV (FCEV) enables businesses to access a tax credit (AFDC, 2023a). Particularly, the cutoff criteria are vehicles with a gross vehicle weight rating (GVWR) below 14,000 lb and at least 7 kWh capacity or GVWR above 14,000 lb and battery capacity of at least 15 kWh, with the allowable tax credit of up to $40,000. Figure 54 illustrates a clear increase in the number of laws and incentives related to EVs since 2002, with a significant scaling up in 2018.

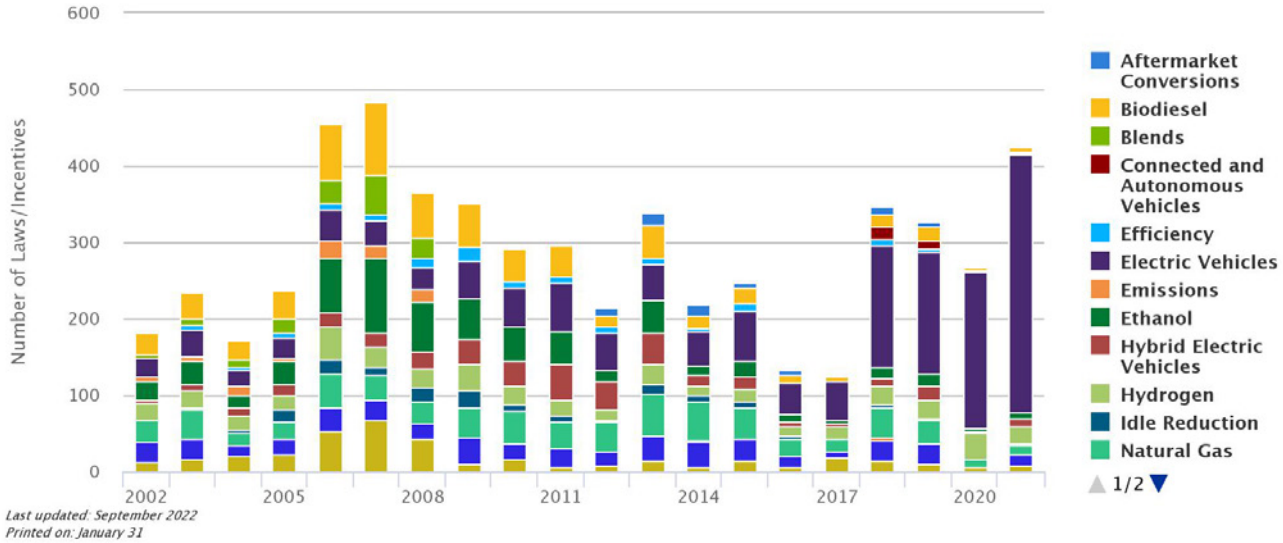

Figure 54. Graph. Summary of the laws and incentives related to alternative fuels and advanced vehicles, enacted in all 50 states and the District of Columbia, from 2002 to 2021 (AFDC, 2023a).

In addition to the electricity sources in Illinois presented in Chapter 1 of this report, historical trends in electricity fuel consumption in Illinois are presented in Figure 55, with an increasing trend since mid-1980s.

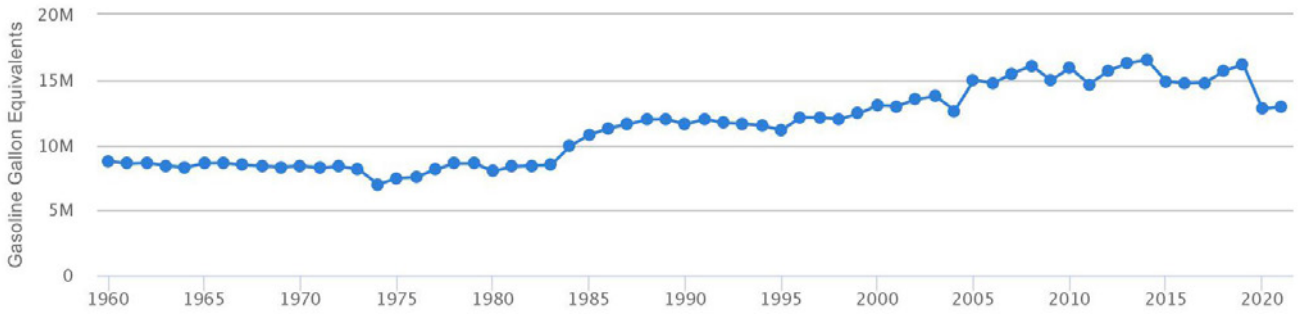

Figure 55. Graph. Historical trend of electricity consumption in Illinois (AFDC, 2023b).

In anticipation of electric MD and HD vehicles, additional weight of the battery pack and instant access to electric-motor torque imposes high levels of forthcoming demands on the already strained, aging road infrastructure. Such demands also implicate changes in the economy and implementation feasibility of EVs. There are some aspects that must be considered when studying HDEVs. Additional information (from the one in Chapter 1) for each aspect is presented below.

Feasibility of Heavy-Duty Electric Vehicles

Some pertinent issues in preventing the transition to zero-emission HD freight vehicles include limited availability of technology, limited travel range, constraints about payload and volume, the limited economy of scale, and insufficient charging stations (Moultak et al., 2017).

Greenhouse gas emissions were also estimated comparing scenarios of increased efficiency in diesel engines, fuel-cell intensive (majority fuel cell use, supplemented by overhead catenary), and electric-intensive (majority electric, supplemented by fuel cell use). Relative to the base scenario of conventional diesel engines, the reduction in emissions ranged between 40% to 70% with the highest saving given the electric-intensive scenario (Moultak et al., 2017). Kluschke et al. (2019) also used technical literature to forecast how alternative fuel and power trains (AFPs) aimed to reduce transportation emissions will become widespread. Battery electric vehicles were one of the technologies considered as part of AFPs. Conclusions were (i) AFPs would have significant relevance in CO2 emission reduction; (ii) substantial uncertainty existed regarding which AFP technology to use to make predictions; and (iii) most studies overlooked infrastructure cost and the impact on the energy system (Kluschke et al., 2019).

Focusing on HD vehicles, Forrest et al. (2020) examined the feasibility of battery and fuel cell electric vehicles in California. The feasibility was quantified as the ability of EVs to meet the requirements of ICE counterparts in terms of vehicle energy efficiency, supply equipment access, access to refueling stations, and charging rates. The feasibility parameter was the percentage of VMT of ICE that the EVs could cover. Challenges lie in the extra weight in HD and the required extended range due to lack of alternative fueling stations in contrast to conventional ones. However, such demands can be mitigated if significant investments are made in charging infrastructure and the electric grid. Moreover, Fleming et al. (2021) identified activities to accelerate the decarbonization of MD and HD vehicles. Regarding long-haul trucking, it is anticipated that vehicle electrification would require multiple charges to support traveling 800 miles in one day that has a direct implication in payload capacity load due to the weight of the batteries. Four strategies were recommended: increase funding for research; extend tax incentives to include MD and HD vehicles and charging infrastructure; establish regulations aimed at phasing out diesel MD and HD vehicles; and pursue state and local policies that would specify corridors to be available only to EVs and electrification of state and local government fleet.

Economic Impact of Heavy-Duty Electric Vehicles

One component in the economic assessment of EVs is the balance between the cost of energy and the batteries. A study in Germany compared the LCCA of electric and diesel trucks and concluded that the payload reduction due to the extra weight of batteries was 20% (Mareev et al., 2017). In addition, in some scenarios, diesel and electric technologies could be equivalent from the cost point of view.

The proposed work provided a battery model to estimate fuel consumption and recommended dimension the battery. The model included GPS routing, driving behavior (acceleration and deceleration patterns), driving resistance (air, rolling, slope, and acceleration resistance), drivetrain, and battery characteristics. The analysis assumed a constant vehicle gross weight (40 t ≈ 88,184 lb.) irrespective of the payload and battery capacity reduction as a function of time. In addition, the LCCA included costs associated with the vehicle, fuel/energy, infrastructure (charging stations), fixed costs (taxes and insurance), and variable costs (service and toll). The weight of components in diesel vehicles that are irrelevant to electric vehicles was assumed to be 3,748 lb, and the energy density reported in the literature was used to determine the weight and volume of the battery. The weight of other components in the drivetrain was assumed to be 1,000 lb, while the gearbox weight was the same for both vehicle types. High-capacity batteries governed the higher cost of EVs, and even though the overall cost can be similar for diesel and EVs in some scenarios, battery lifetime plays a significant role (Mareev et al., 2017).

Some studies have compared the initial investment and operating cost of Class-8 semi-trucks that use diesel engines and electric motors with a 500-mile range (Sripad & Viswanathan, 2019). The comparison included multiple assumptions, such as battery pack weight between 11,000 and 14,600 lb, which leaves a maximum payload capacity between 39,000 and 43,000 lb. Furthermore, the battery pack's price for the 500-mile range was $150,000. The baseline scenario assumed, among others, that the initial price differential between EV and diesel is $100,000 and the electricity cost of 0.15 $/kWh. The average payback period, i.e., the time needed for the savings from the lower operating cost of EVs to be equal to the initial price differential, was 3.2 ± 1.5 years for the baseline scenario. The initial price differential and replacement fraction for the battery showed the highest impact on the payback period. The payback period can be two years if all variables favor EVs. Furthermore, if the price of electricity increases above $0.25/kWh, EVs might not be advantageous compared to diesel. The analysis did not include pavement damage (Sripad & Viswanathan, 2019).

One of the few studies focused on EVs' effects on pavements was performed in California, which allowed a 2,000-lb weight limit increase for near-zero- and zero-emission vehicles (Harvey et al., 2020). The study included three types of alternative fuel vehicles (AFVs): natural gas vehicles (NGVs), EVs, and fuel-cell vehicles (FCVs). Additional weight varied between 500 and 2,000 lb, and three implementation scenarios of AFV were considered. The travel range until 2030 was assumed to be 300 miles, while it increased in year 2050 to 500 miles. In addition, the extra weight for long-haul EVs was 5,328 and 4,267 lb for 2030 and 2050, respectively. Pavement damage calculation was performed using CalME, California's software for mechanistic-empirical flexible pavement design (Harvey et al., 2020). The authors stated that the extra weight led to minimal extra damage to local and state roads. Moreover, additional damage depended on the implementation scenario and pavement structure as the market penetration was assumed to be low until 2030, when EV and FCV batteries are expected to become lighter. Although there was extra gross weight that ranged from 500 to 2000 lb, the maximum axle load remained constant following California's regulated limit. It is worth noting that the extra weight was assumed to be distributed evenly between the steer and trailer axles and that the effect of larger torque and in-plane contact stresses—relevant for near-surface damage evaluation—was omitted in the analysis.

Torque and Pavement Responses

Two factors that may impact pavement damage induced by HD EVs compared to conventional vehicles are extra battery weight and higher wheel torque. A factor that can be more significant is the higher level of wheel torque, which results in higher longitudinal tire-pavement contact stresses. For over two decades, the UIUC team has spearheaded the study of tire-pavement contact stresses, with a focus on HD trucks, along with their impact on pavements.

Moreover, Hajj et al. (2006) calculated pavement responses of two flexible pavements under braking on a downhill grade with a 6% slope considering steering, driving, and trailer axles. The analysis included three speeds (2, 20, and 40 mph) and two HMA thicknesses (4 and 8 in). Braking on slope resulted in a load on the steering axle that was 40% higher than the allowable tire load (8,500 versus 6,100 lb). The authors considered longitudinal contact stresses, which were determined as the product of the vertical contact stresses and a coefficient of friction as opposed to the result of braking torque. On the other hand, vertical contact stresses for a specific wheel load, determined from a vehicle model, were interpolated from experimental measurements of contact stresses. Based on a mechanistic calculation program, 3D-MOVE, the researchers determined that the highest shear strain occurred under braking at low speed. Using a mechanistic-empirical (ME) approach that correlated shear next to the tire with rutting and shear along the traffic direction with shoving, it was found that rutting was more likely to arise under the steering axle, while shoving was more likely under the driving axle. Furthermore, transverse shear under braking was nearly twice the value under free-rolling condition (Hajj et al., 2006). A similar methodology was implemented in 2012, while incorporating transfer functions from AASHTOWare Pavement ME. Braking, which inherently represents a greater torque, resulted in three to four times the rutting values relative to free rolling and the tensile strain at the bottom of the HMA was also more significant (Hajj et al., 2012).

Kubo et al. (2016) measured the magnitude of the change in wheel load under braking in real-life conditions. Based on strain gauges installed in the suspension system, redistribution of the vertical load due to the braking maneuver was observed. Results showed that the braking degree, akin to the level that a driver pressing on the pedal, is the controlling factor rather than the initial speed prior to braking; thereby highlighting the relevance of driving behavior. A fully pressed pedal resulted in a vertical load that was 50% larger than the static load.

Wang and Al-Qadi (2010) used a similar approach to Hajj et al. (2006) to determine tire-pavement contact stresses in the longitudinal direction under braking by multiplying the vertical contact stresses with a friction coefficient of 0.8. A tire manufacturer measured the vertical contact stresses, and the change in vertical contact stresses due to additional vertical load caused by inertia during braking was omitted. The 3D contact stresses were utilized as load inputs in a 3D FE flexible pavement model to compare the impact of free-rolling and braking conditions. Using a similar ME approach as Hajj et al. (2006), the authors reported that braking minimally influenced rutting but significantly affected shoving. Particularly, near-surface cracking potential was evaluated, considering high levels of shear strains induced by braking. Wang and Al-Qadi (2010) determined that vertical shear strain (related to rutting) was not affected by braking; however, longitudinal shear strain (related to shoving) dramatically increased due to braking. Also, the maximum tensile strain location

for the braking condition changed from under tire edges (as observed under free-rolling condition) to under the ribs (Wang & Al-Qadi, 2010).

The work by Wang and Al-Qadi (2010) was later improved by developing a pneumatic tire FE model to predict contact stresses under various rolling conditions, including braking and acceleration (Wang et al., 2012). The material properties were calibrated by comparing predicted and measured load-deflection curves; and the model was validated using measured contact stresses in the vertical and transverse directions. In the model development, the authors controlled the degree of braking and acceleration via the slip ratio parameter. This improved model quantified the importance of braking on longitudinal contact stresses, wherein the stress values increased as the degree of braking increased (Wang et al., 2012). Moreover, Wang et al. (Wang et al., 2013b) completed cracked and uncracked pavement simulations while incorporating contact stresses under the braking condition. In contrast to free rolling, braking induced higher shear stresses and lower compressive stresses, which might increase the likelihood of shear failure. The relevance of shear strain in the analysis was reiterated and confirmed by performing an analysis including pre-existing cracks. In addition, the effect of various tire-pavement surface friction models on the same FE pavement model was assessed (Wang et al., 2014). In lieu of a constant friction coefficient, a sliding-speed-dependent friction model was implemented. The study concluded that using a constant friction coefficient was acceptable for free-rolling and cornering conditions with low slip angle values. On the other hand, assuming a constant value for braking and accelerating scenarios led to an underestimation, wherein the error could be further exacerbated if HD EV were applied on pavements (under the combination of increased axle load and higher torque).

Hot-Mix Asphalt Mix Design for Higher Torque

Currently, the technical literature regarding concrete mixture design modifications aimed at addressing the detrimental effect of HD EVs is scarce. However, some researchers have evaluated the impact of higher in-plane tire-pavement contact stresses in the material design of flexible pavement surface layers, including intersection scenarios.

A study by the Texas Transportation Institute focused on premature intersection failure via site visits, wherein field and laboratory HMA samples were evaluated (Ameri-Gaznon et al., 1989). Site visits at problematic intersections reported distresses such as rutting, shoving, and bleeding. The authors reported that, at an intersection, vehicles applied longitudinal forces of considerable magnitude during braking and acceleration. In addition, while vehicles are stopped, the same pavement section, which experienced high shear stresses from braking, was subjected to a vertical load for a long duration, followed by acceleration. Using volumetric analysis of the field cores, the report determined factors associated with premature rutting failure at intersections: excessive binder content (most common), high percentage of fine aggregate (sand), rounded shape and smooth texture of fine aggregates (sand), and high-density mixes with low voids in the mineral aggregate. The authors also implemented a structural model that relied on octahedral stresses to evaluate the potential of HMA to rut and recommended it as part of a rational design approach to verify mix design (Ameri-Gaznon et al., 1989).

Another two studies addressed additional factors to the already demanding conditions at intersections without accounting for high in-plane contact stress values: very high traffic and high temperature. In Colorado, Aschenbrener and Shuler (1995) detailed a demonstration project to prove that HMA mixtures can handle challenging conditions provided by high torque at intersections with very high traffic. Mix design was performed using Superpave Level I; the mixtures were examined with various tests: French rutting tester, Hamburg wheel-tracking device, and thermal-stress restrained-specimen test. However, the study did not mention the higher magnitudes of longitudinal stresses at intersections (i.e., a high torque of braking and acceleration). In Pennsylvania, Kandhal et al. (1998) attributed the issue of rutting at intersections to slow or standing loads. The forensic investigation extracted cores from five projects (ten cores per section, wherein five cores were tested with rutting and five without rutting) to determine volumetric properties in the laboratory. Particularly, the mixes with very low air voids and voids in the mineral aggregate (VMA) experienced additional compaction induced by slow-moving or standing loads. Kandhal et al. (1998) proposed the use of stone matrix asphalt (SMA) on the surface layer as a solution to take advantage of the stone-to-stone contact. More recently, Song and Yeom (2021) appended to the SMA recommendation, based on the wheel tracking test, and suggested that the mixture should have less than 10% elongated particles, modified binder, and increased use of coarse aggregates.

A study in Nevada combined numerical modeling, forensic investigation, and laboratory testing to recommend HMA mix designs that account for high torque (Hajj et al., 2007). Vehicle acceleration, deceleration, and turning were acknowledged as relevant factors. The forensic investigation of the in-service intersection provided eight cores from sections with minor rutting and three cores from sections with maximum rutting. In particular, the sections with rutting had high asphalt binder content, low air voids, and low VMA—in congruent to findings by Kandhal et al. (1998). This study also indicated densification due to slow/stopped traffic. Additional samples prepared in the laboratory and tested with the asphalt pavement analyzer (APA) were subjected to repeated shear at constant height (RSCH), repeated load triaxial test (RLT), and triaxial compression strength test. The main outcome of the study was to find new criteria for the ME approach to limit rutting at intersections. The mechanistic component was provided by 3D-MOVE, which considered contact stresses of an 18-wheel tractor-trailer, braking at low speed, and braking. Moreover, rutting was estimated using empirical functions, dependent on resilient response. New HMA rutting limits to the HMA mixture testing suite (RSCH, RLT, and APA) were proposed that satisfy rutting criteria at intersections (Hajj et al., 2007). The study was expanded to include cracking for various mixes, while incorporating tests used by AASHTOWare Pavement ME, and recommended aggregate gradation modification for intersections (Hajj et al., 2011).

Follow-up research was completed in 2021 to address durability and cracking issues. Similarly, the study had three components: i) forensic study with 32 field cores from an intersection that was constructed 10 years ago (Hajj et al., 2011); ii) performance thresholds and volumetric requirements from Superpave to propose a balanced mix design (BMD); and iii) a mechanistic approach using 3D-MOVE to evaluate asphalt mixtures for rutting. The proposed BMD utilized IDEAL-CT for cracking and Hamburg wheel track test (HWTT) rutting, and the mechanistic model included an 18-wheel truck traversing a 4% grade downhill section, with and without braking. As in the previous study, the mechanistic model identified lab testing criteria that satisfied the performance criteria. A maximum

HWTT rut depth of 4.8 mm was recommended for intersections and percent passing No. 200 between 3 and 7% (Costa, 2021).

Loading from Heavy-Duty Electric Vehicle

Contact stresses depend not only on the material and structural configurations of the tire and pavement, but also the vehicle drivetrain, in control of the imposed rolling/driving condition. The difference in vertical wheel load between EV and ICE HD vehicles lies in the magnitude and distribution of the battery pack weight. However, the difference between in-plane contact stresses is determined by the torque at the wheel. For EVs, the torque wheel is governed by the electric motor and the characteristics of the power train. The power train constitutes the motor and the drivetrain, wherein the drivetrain is the subsystem used to convert electrical energy from the battery to mechanical wheel torque. Motor torque is then delivered to the wheels and converted via the differential and gearbox, respectively. Particularly, HD electric vehicle drivetrain are grouped in five main configurations: i) central motor + single ratio gearbox + differential (most common); ii) central motor + multiple gearbox + differential; iii) central motor + differential; iv) two by-wheel or hub motors + single ratio gearbox; and v) two in-wheel motors (uncommon) (Arora et al., 2021).

Cunanan et al. (2021) compared the drivetrain of the ICE diesel, fuel-cell electric, and battery-electric HD vehicles. Given that the power train of a battery-electric vehicle (BEV) does include as many moving parts as ICE, its maintenance cost tends to be 20-30% lower than ICE. Furthermore, the study stated that at the current energy densities, a 500-mile range of BEV would require a battery that would weigh 12,000 lb. It is reported that BEV has the highest tank-to-wheel efficiency, on average up to 68%. The losses have been attributed to resistance/friction in the power train during the transfer and conversion of electricity. In addition, the refueling time has been estimated to range between 2.85 to 20 hours—highest for BEVs.

Albeit there are typical power train configurations in HD EVs, its optimization is an active research topic. For instance, Verbruggen et al. (2020) optimized the topology of the electric design to minimize the total cost of ownership and energy consumption by looking at the hardware and the control design. The optimization model included factors, such as, the tractive force the vehicle needs (rolling friction, aerodynamic friction, and gradient resistance), transmission model (multi-speed gearbox with fixed efficiency for each gear), battery model, vehicle mass (mass without power train, mass of trailer, payload, and power train mass), and driving cycles. A total of 44 power train configurations were considered, and the difference between the largest and smallest total cost of ownership (TCO) was estimated as 5.6%. One electric machine and a gearbox provided the lowest TCO of the two driven wheels. The largest TCO was the series configuration of two electric machines and two gearboxes (Verbruggen et al., 2020).

Some assumptions are needed to estimate the wheel torque from the electric-motor torque, in the absence of information regarding the components of the power train configuration. As an example, a summary of NHSTA Vehicle Class 8 HD EVs and their operational characteristics is provided in Table 18.

Table 18. Design Operating Conditions for NHSTA Vehicle Class 8 HDEVs

Manufacturer	Model	Payload (lb)	Energy Capacity (kWh)	*GVWR (lb)		Torque (lb-ft)		**GCWR (lb)		Max Power (HP)	Top Speed (mph)	Range (miles)
				Min	Max	Min	Max	Min	Max			
Battle Motors	LETII EV		540	33000	72000	3500	6000	–	–	310-500	70	175
BYD	8TT	78765	422	–	–	–	664	–	105000	483	65	125
Freightliner	eCascadia	60000	438	–	–	–	23000	**65000**	**82000**	470	–	220
Kenworth	T680E	57500	396	54000	82000	–	1623	–	82000	670	–	–
Lion Electric Co	Lion 8	30000	252	–	54600	–	2507	–	–	470	65	200
Nikola	Tre BEV	40000	753	–	–	–	–	–	82000	645	70	330
Peterbilt	579EV	–	396	–	–	–	–	–	82000	670	–	150
Tesla	Semi	82000	1000	–	–	–	1600	–	82000	–	60	300-500
Volvo	VNR Electric	66000	565	–	–	–	4051	–	82000	455	68	275
XOS	HDXT	56000	**595**	36200	53200	30535	36583	–	**82000**	–	–	230

Electric truck braking systems are anticipated to operate nearly twice as long as traditional braking systems, owed to the regenerative braking feature in EVs—which has a direct and positive implication on maintenance cost related to braking. Given the anticipated increase in weight for HD EVs, new tire designs may be needed for better load durability, while also requiring low rolling resistance to account for farther range of travel and better fuel economy. Currently, EV-specific tires are sold in the market factoring range, durability, performance, and climate season; albeit off-the-shelf EV tires are only available for cars, motorcycles, and bicycles (Michelin, 2023). Additional design factors include safety on wet and dry roads, precision steering, short braking distances, and prevention (Continental, 2020b).

Tire manufacturers have reported that the additional weight is offset by increasing the load-bearing capacity of the tire carcass (sometimes include a special demarcation on the sidewall to indicate higher load index). In addition, low rolling resistance tires has been reported to consider a different tread compound blend, tread pattern, and sidewall construction, while also incorporating low noise properties given that EV is quieter than IC. In 2020, a joint effort by Continental and VDL Bus & Coach to equip an urban electric bus with initial prototype electric bus tires, especially that buses frequently start and stop in any given bus route (Continental, 2020a).

The same problem statement is imposed on freight transportation. In 2021, a Volvo 19-ton truck with a 680 hp and battery capacity of 680 kW (reported to allow a mileage range of up to 472 miles for an empty trailer). Tire design iterations are focused on extending the range, while serving a high load and reducing rolling resistance. In November 2022, the Tesla Semi, a class 8 commercial truck, reported to complete the first 500-mile trip with a full 80,000-lb load (Lambert, 2022). Furthermore, axle weight distribution is often influenced by cargo weight and placement along the trailer, axle configuration, and fuel weight.

The difference in weight distribution can have an impact on the suspension and steering systems, as well as the tires, which may need to be designed to accommodate the additional weight. This can result in changes to the ride quality, handling, and stability of the truck, and may also affect its

braking performance. In addition, the weight distribution of an electric truck is also influenced by the position of other components, such as the electric motor and the drivetrain, which can further affect the overall balance of the vehicle. Zhou et al. (2024) compared a 2-kip battery pack representing a 600-kWh battery with an 8-kip pack to represent an extreme case for 900-kWh battery, while assuming its placement on the tractor. Approximately, 50% of the weight was assumed to be carried by the steering axle, while the remainder by the tandem axle. Currently, manufacturers are determining the design configuration that optimizes the payload and battery weight. Considerations of placing the battery packs on the rear portion of the frame would entail compromising the payload. On the other hand, drive axle weights would not be adversely affected with the increase in weight on the front section. Moreover, the concept of removing the diesel power train allots an available weight to be utilized by the battery packs by 3,000 to 4,000 lb; hence, the general notion in HD EV is to place the extra capacity on the steer axle.

APPENDIX B: NUMERICAL DETAILS OF THE TIRE FEM

Tire Modeling

The 275/80R22.5 truck tire—275 mm (2.1 in.) width, with an aspect ratio of 80%, and mounted on a 22.5-in. rim—typical of dual-tire assemblies on semi-trucks (see Figure 58), was modeled using Abaqus FE software. In North America, the 275/80 R22.5 ranks consistently among the most-popular industry standard fitments alongside the 295/75 R22.5 (Rohlwing, 2023). However, because the latter is only around 0.8 in wider, fleets generally treat them as interchangeable on the same axle. The tire model was developed, verified, and validated by the research team (Hernandez et al., 2015). The dimensions of the tire's cross-section, distribution of rubber components, reinforcement orientation, and material properties (hyperelastic rubber and linear-elastic reinforcement) were obtained from the manufacturer and were verified through laboratory tests.

Most electric semis are expected to retain the same rim diameter and nominal tire sizes as their diesel counterparts. The Freightliner eCascadia specification sheet lists 275/80 R22.5 radial or similar for steer, drive and trailer axles (Daimler Trucks North America LLC, 2024), matching conventional ICs configurations, while the BYD 8TT lists 295/80R 22.5 tires (BYD, 2023). While sizes might stay similar, HDEV tires are engineered to improve durability and reduce rolling resistance by using next-generation compounds, heavier casings, and sustainable sourced materials (Continental, 2024; Goodyear, 2023).

In this study, the research team represented the tire geometry via five ribs: ribs 1 and 5 (the outer ribs) consisted of 11 elements each (12 nodes), whereas ribs 2, 3, and 4 each contained eight elements (9 nodes), as illustrated in Figure 58a. Rayleigh damping was assumed in the model, as presented in Figure 56. Here, β is stiffness-proportional damping, α is mass-proportional damping, and ω is the natural frequency. Truck tires typically exhibited a damping ratio of approximately 0.09 and a natural frequency of 80 Hz (Kim et al., 2007). Meanwhile, dynamic mechanical analysis of a specific tire's rubber material revealed a damping ratio of 0.15. By setting an α coefficient equal to zero in the equation in Figure 56 (Lopez Arteaga, 2010), the mass-proportional damping can be calculated using the equation in Figure 57, where α is equal to 150 when ξ is equal to 0.15.

$$\xi \approx \frac{1}{2}\left(\frac{\alpha}{\omega_r} + \beta\omega_r\right)$$

Figure 56. Equation. Raleigh damping equation.

$$\alpha = 2\omega\xi = 2 \times (2\pi f) \times \xi = 1005\xi$$

Figure 57. Equation. Mass-proportional damping.

The tire model depicted in Figure 58 was comprised of three stages: (i) inflation pressure applied on the axisymmetric model, (ii) static inflation pressure and tire load application on the 3D tire model, and (iii) imposing a rolling condition on the 3D tire model. The rolling simulation began by applying each of the eight load conditions (Table 2) to a static tire model at an inflation pressure of 100 psi.

The tire was rolled 171 ft for the IC and 145.7 ft for the HDEV. This accounted for two different travel speed variations with time (as HDEV could increase its speed up to threefold that of IC due to increased torque access). The research team selected the distances to achieve the target speeds while minimizing computational effort. For the IC case, 171 ft corresponded to a 15-sec acceleration from rest (zero velocity) to 15.5 mph, whereas the HDEV case covered 145.7 ft in 8 sec to accelerate from 0 to 24.9 mph. Figure 59 depicts speed variations over time for both trucks.

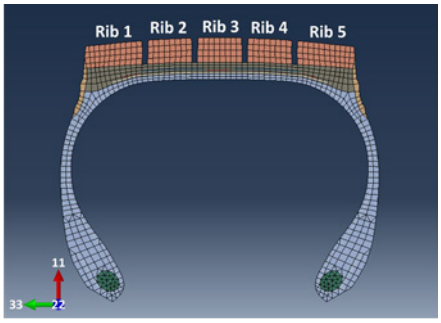

(a) Tire cross section

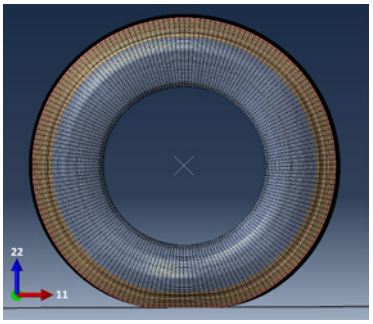

(b) Side View

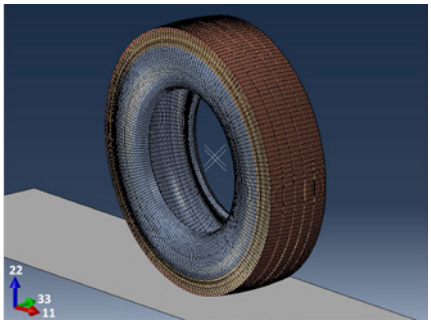

(c) 3D View

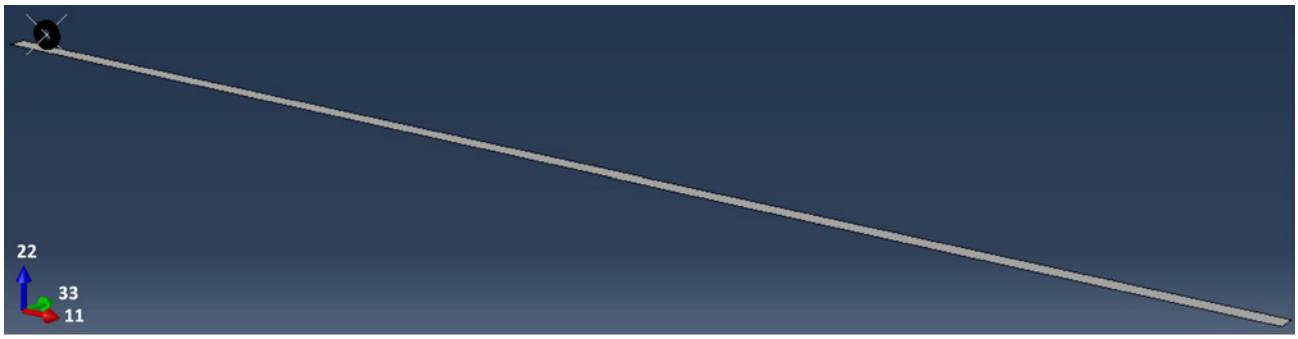

(d) Beginning of travel path in 3D view

Figure 58. FE model: (a) tire cross section; (b) side view; (c) 3D view; (d) beginning of travel path in 3D view.

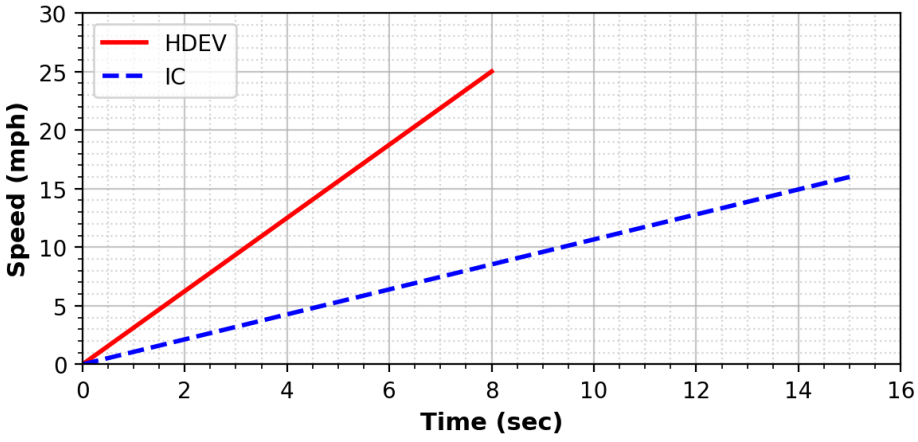

Figure 59. Graph. Speed progression for each truck.

For model boundary conditions, a constraint was imposed at the tire's center, representing the metal wheel hub. A vertical load was applied along the $2-2$ direction, while transverse $(3-3)$ displacement and rotations about the 1 and 2 axes were fully constrained. Friction at the tire-pavement interface was modeled via an exponential decay dependent on slip speed, with a slip tolerance of 0.005 and static and kinetic friction coefficients of 0.30 and 0.17, respectively (Hernandez & Al-Qadi, 2016b). Moreover, a relative penetration tolerance of 0.01 (i.e., allowable penetration divided by the characteristic contact dimension) was enforced. Pavement roughness effects were excluded; they are significant when evaluating dynamic axle load amplification and fuel consumption (Botshekan et al., 2019; Liu & Al-Qadi, 2021; Louhghalam et al., 2015).

The analysis was divided into increments of one 1 sec/step for the HDEV and 3 sec/step for the IC, utilizing the restart feature in Abaqus to manage the overall simulation and supercomputing wall clock limit. An initial time increment of 1×10^{-3} sec was used; however, as speed increased, the time increment was reduced to 2.5×10^{-4} sec to address contact convergence issues. To mitigate the output database file size, displacements, stresses, strains, and contact stresses were saved every 0.05 sec at lower speeds and every 0.025 sec at higher speeds.

Within each step, an amplitude function was applied to gradually increase both translational and angular speeds from the beginning to the end of that step. For instance, when increasing from 3.11 mph to 6.21 mph for the $P6$ case at free rolling (no acceleration or deceleration conditions), a translational speed of 6.21 mph and an angular velocity of 5.5976 rad/s were used. These values were initially scaled by 0.5 at the start of the step (matching $3.11/6.21 \approx 0.5$) and reached 1.0 by the end of the step.

The angular velocities were obtained from a separate steady-state analysis that included inertia, thereby determining the free-rolling condition under zero torque around the tire axis. The free-rolling angular frequency varied linearly with speed. However, during the dynamic implicit analysis, the reaction torque was no longer zero once the tire started accelerating. Table 19 lists the free-rolling angular frequencies for each load and speed included in this study. The final three rows for $P1$ and $P2$ are left blank because they pertain to IC cases traveling only up to 15.5 mph.

Simulations at different slip ratios were performed for each load case to fully capture the effect of various acceleration levels on the contact stresses. $P1$, $P2$, $P4$, $P5$, $P6$, $P7$, and $P8$ at 2% and 3% slip ratios; and $P2$, $P4$, and $P6$ at a 6% slip ratio. The slip ratios were selected based on previous research conducted on FE tire-pavement interaction, where a sensitivity analysis at different slip ratios showed that beyond a slip ratio of 7%, the contact stresses distribution changed marginally, indicating a full slip condition (Hernandez & Al-Qadi, 2016b; Jayme & Al-Qadi, 2021). Therefore, the research team chose 2%, 3%, and 6% slip ratios to represent low, medium, and high acceleration conditions.

Table 19. Free Rolling Angular Frequencies for Each Analysis Case

Speed (mph)	ω (rad/s)							
	P1	***P2***	***P3***	***P4***	***P5***	***P6***	***P7***	***P8***
3.11	2.8077	2.7988	2.8183	2.8016	2.8112	2.7988	2.8014	2.8116
6.21	5.6154	5.5976	5.6365	5.6031	5.6224	5.5976	5.6029	5.6233
9.32	8.4230	8.3936	8.4545	8.4045	8.4334	8.3936	8.4045	8.4351
12.43	11.2300	11.1950	11.2720	11.2060	11.2440	11.1950	11.2060	11.2470
15.53	14.0380	13.9930	14.0900	14.0070	14.0550	13.9930	14.0075	14.0586
18.64			16.9070	16.8080	16.8650	16.7910	16.8090	16.8700
21.75			19.7240	19.6080	19.6750	19.5890	19.6105	19.6821
24.85			22.5400	22.4080	22.4840	22.3860	22.4120	22.4940

APPENDIX C: STATISTICAL MOMENTS AND KERNEL DENSITY ESTIMATE COMPARISON

Statistical Moments Comparison

Statistical moments, namely, mean, variance, skewness, and kurtosis, offer a valuable way of describing contact force/stress distributions in each direction, given the complexity at the tire-pavement interface. The first moment (mean) provides the average force level, while the second moment (variance) represents the distribution wideness/dispersal of the force/stress values around the mean value. The third moment (skewness) indicates whether the force/stress distribution tilts more toward higher or lower values, reflecting any asymmetry relative to the mean. Lastly, the fourth moment (kurtosis) highlights the importance of extreme values (i.e., the tails). Negative kurtosis corresponds to flatter, more spread-out curves, while positive kurtosis implies sharper, more peaked distributions.

Table 20 presents the statistical moments for six loading scenarios, illustrating the impact of axle load and slip ratio on the contact force distributions. Although increasing the slip ratio has a negligible effect on the vertical force distribution—evident in the relatively narrow range of mean values for the DTA cases—it notably alters the mean and variance in the longitudinal direction. This outcome aligned with the influence of slip ratios ranging from 0% to 6% and a 0.49 kips difference in applied load.

Table 20. Longitudinal and Vertical Force Distribution Statistical Moments

Direction	Load	Mean (N)	Variance (N)	Skewness	Kurtosis
Longitudinal	$P2$ 4.2 kips, SL=0%	0.027	3.130	-0.392	0.331
	$P2$ 4.2 kips, SL=2%	6.341	28.918	0.483	-0.759
	$P4$ 4.7 kips, SL=0%	0.261	5.534	-0.196	0.0482
	$P4$ 4.7 kips, SL=2%	9.148	47.304	0.214	-1.146
	$P6$ 4.2 kips, SL=0%	0.095	3.742	-0.264	0.082
	$P6$ 4.2 kips, SL=6%	8.881	44.374	0.302	-0.996
Vertical	$P2$ 4.2 kips, SL=0%	28.413	511.74	0.191	-1.202
	$P2$ 4.2 kips, SL=2%	28.487	513.262	0.239	-1.142
	$P4$ 4.7 kips, SL=0%	31.720	521.474	0.018	-1.272
	$P4$ 4.7 kips, SL=2%	31.693	551.895	0.181	-1.167
	$P6$ 4.2 kips, SL=0%	30.800	480.515	0.084	-1.142
	$P6$ 4.2 kips, SL=6%	30.782	517.289	0.268	-1.022

As the slip ratio increases from 0%, the longitudinal force distribution shifts from left-skewed (negative skewness) to right-skewed (positive skewness), reflecting the presence of additional compressive forces during acceleration (recall the positive net longitudinal finding in the earlier section). Although kurtosis values changed with respect to slip ratio, they remained below 3, suggesting a platykurtic tendency with relatively thin tails. In contrast, increases in axle load primarily raised the mean and variance but had little effect on skewness or kurtosis, both for vertical and longitudinal contact stresses. The statistical moments for the DTA transverse forces are not shown

because the effect on their distribution due to higher loads and/or slip ratios was marginal. Additionally, similar trends were observed for the steering load scenarios.

Kernel Density Estimate Comparison

A helpful tool for examining variations in contact force distributions is the kernel density estimate (KDE), a nonparametric technique that models probability distributions by assessing how observed data points are grouped. The KDE, denoted $\hat{p}_n$, is computed by weighing the distances of each observation against points along a linearly spaced axis, as expressed in the equation presented in Figure 60. In this formulation, X_i is a fixed location, $K(x)$ is the kernel function, and h is the smoothing parameter or bandwidth. A Gaussian kernel, computed with the equation presented in Figure 61 was employed, with bandwidths of 1.0, 0.42, and 0.28 assigned to vertical, longitudinal, and transverse contact stresses, respectively.

$$\hat{p}_n = \frac{1}{nh}\sum_{i=1}^{n} K\left(\frac{X_i - \text{observation}}{h}\right)$$

Figure 60. Equation. Kernel density estimate.

$$K(x) = \frac{1}{2\pi} e^{-\frac{1}{2}x^2}$$

Figure 61. Equation. Gaussian kernel.

Figure 62 displays KDE plots of the contact forces in the three directions—vertical, longitudinal, and transverse—for a 0% slip ratio. The plots appear in the same order from left to right. Under various IC ($P1$, $P2$) and HDEV ($P3$–$P8$) loads at t=3 sec, the vertical component (f_{22}) exhibited the most pronounced response, especially when compared to the horizontal forces. Peaks under 22.48 lb in the f_{22} distribution, shifted horizontally and vertically, mirroring how stress redistributed across the contact path. In particular, the heaviest load case, *P3*, extended the KDE's right tail, reflecting more significant force levels at the tire-road interface. Meanwhile, peaks and ranges in f_{11} (the longitudinal direction) remained roughly an order of magnitude below f_{22}. By contrast, f_{33} (the transverse direction) was only slightly influenced and was approximately twice the maximum f_{11}. The overall magnitudes followed the expected trend of magnitude order: $f_{22} > f_{33} > f_{11}$.

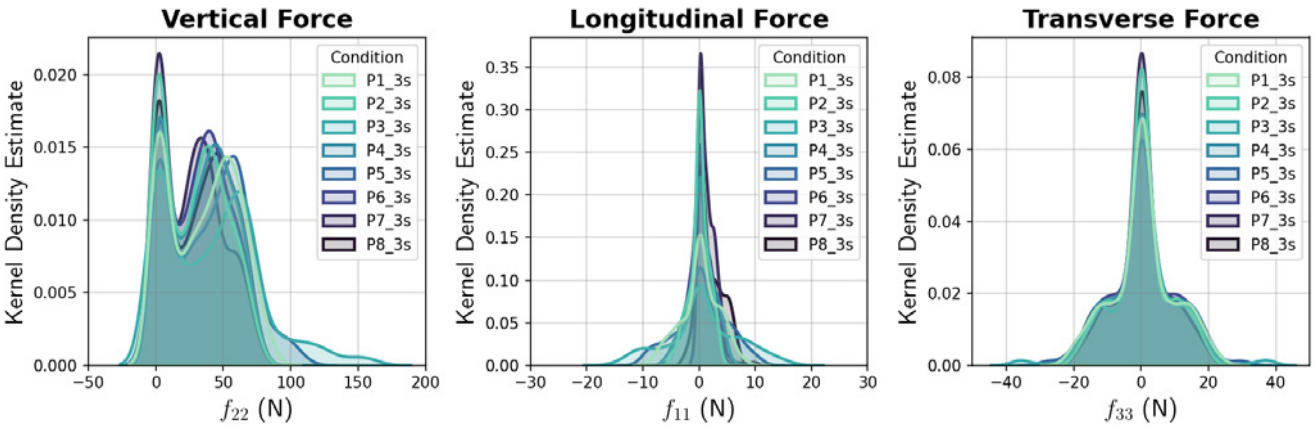

Figure 62. Graph. KDE for all load cases - t=3 sec - 0% slip ratio.

To analyze the impact of varying speeds on contact stress distributions, Figure 63 and Figure 64 illustrate KDEs for $P2$ (IC) and $P6$ (HDEV), respectively, at different timestamps during the simulation. Unlike the results in Figure 62, wherein load strongly influenced the KDE and as speed changed from 0 mph to the final speed, the peaks and distribution spread changed marginally. For f_{22}, only values below 11.24 lb revealed subtle peak shifts. Minor deviations occurred in negative f_{11}, which were less significant than those introduced by load changes. In the transverse direction, f_{33} remained largely unaffected. These KDE outcomes corroborated the trends identified in earlier sections.

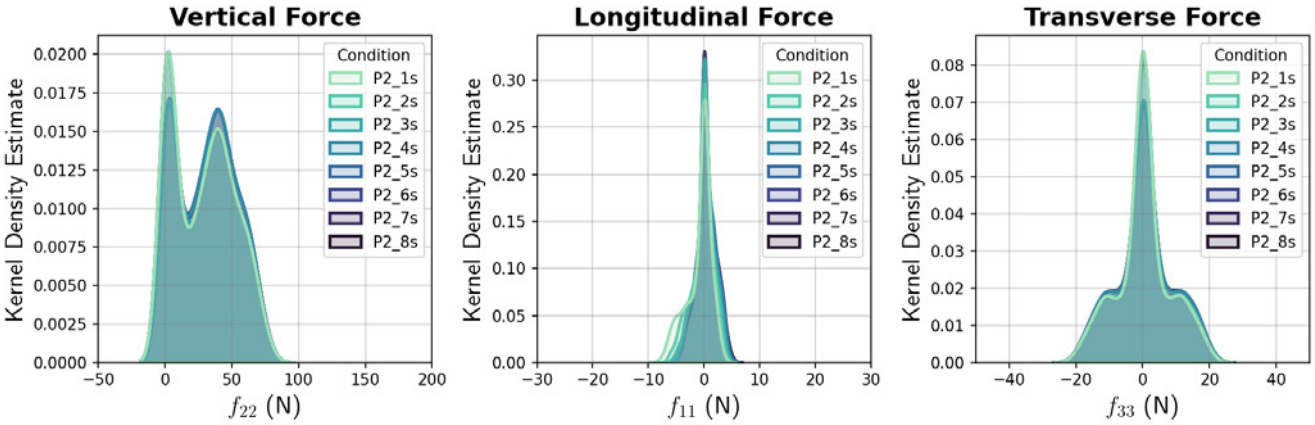

Figure 63. Graph. KDE for $P2$ load case at different times.

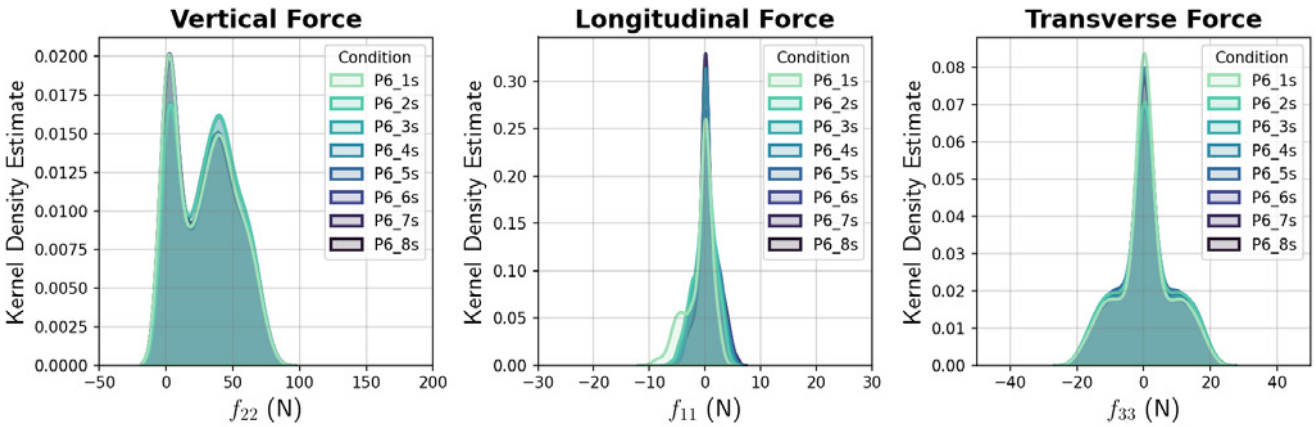

Figure 64. Graph. KDE for $P6$ load case at different times.

Figure 65 illustrates how increasing the slip ratio from 0% to 2%, 3%, and 6% influenced $P2$ (IC) and $P6$ (HDEV) contact force distributions. The vertical force (f_{22}) reconfigured slightly, showing reduced peak values within the 0 to 11.24 lb range. On the other hand, f_{11} experienced considerable redistribution, with most longitudinal forces shifting to positive values because of greater traction/acceleration demands. Simultaneously, f_{33} narrowed considerably, passing from having values between approximately -5.62 lb and 5.62 lb at 0% slip ratio to around -0.9 lb and 0.9 lb at 6% slip ratio. It is evident that slip ratio substantially affected longitudinal in-plane shear forces more than ones in the transverse direction.

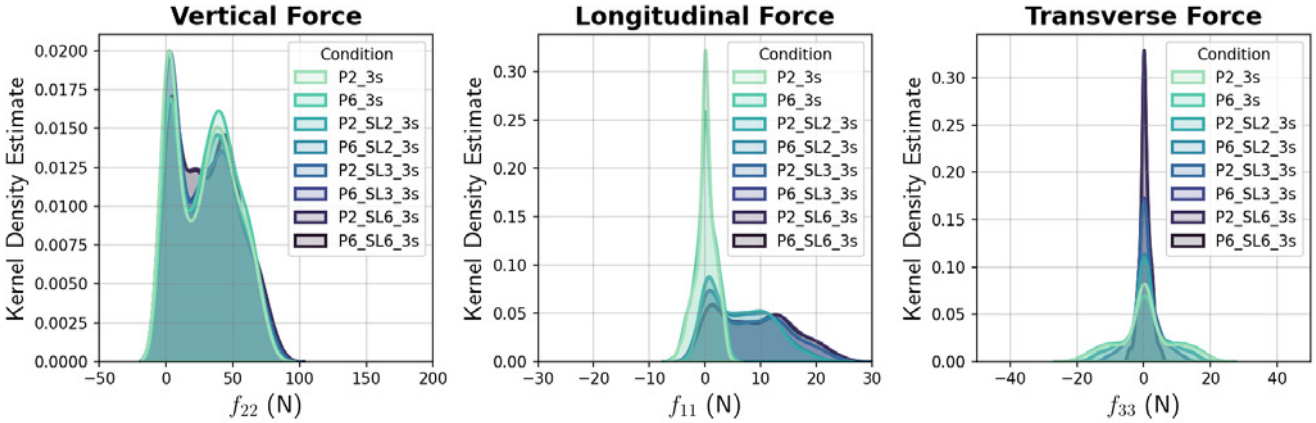

Figure 65. Graph. KDE for $P2$ and $P6$ load cases - slip ratios of 0%, 2%, 3% and 6% - t = 3 sec.

Based on Figure 64 and Figure 65, changes over time have less effect on the KDE distributions than the load or slip ratio; hence, additional descriptive statistical analyses were performed. Figure 66 combines KDE distributions with box plots for the $P6$ HDEV scenario at a 6% slip ratio, taken at two timestamps (t = 3 sec and t = 8 sec). The box plots depict the median, 25th/75th percentiles (the interquartile range), and outliers. An outlier is any point lying beyond 1.5 times the interquartile range. In this study, outliers were mainly observed for f_{33}, presumably due to their overall smaller magnitudes.

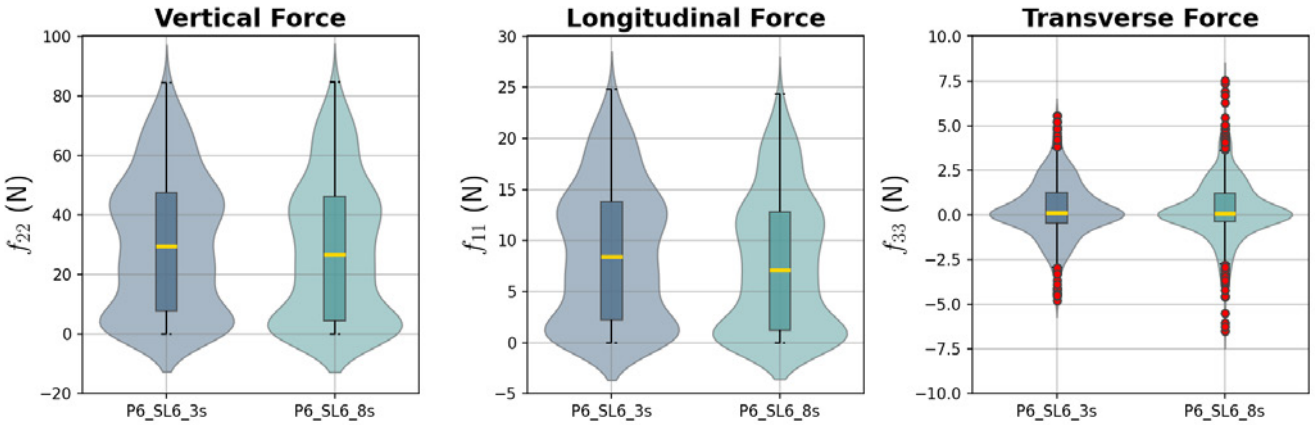

Figure 66. Graph. $P6$ load case violin plot for t = 3 sec and t = 8 sec - 6% slip ratio.

Despite slight changes over time, the distributions in Figure 66 remained broadly comparable. Minor reductions in the median and shifts in the interquartile range across all three force components were consistent with a higher density of nodes at lower force values, which manifested as a broader, lower region in the KDE (often referred to as a *violin* plot).

Recognizing that these time-based KDE changes present only a high-level depiction of global tire-road contact is essential. However, local variations could emerge along the transverse and longitudinal directions (parallel to the tire's meridians). Figure 67 compares the time evolution of f_{11}, f_{33}, and f_{22} along a transverse slice through the mid-section of the contact area. The results showed only marginal shifts in the three principal force components over time. Although f_{33} exhibited some minor variation, its overall magnitude remained relatively small. Figure 68 presents analogous outcomes in the longitudinal direction along the center rib of the tire model, highlighting the minimal differences across time steps. The previous observations suggest that one could extract nodal force data at an earlier moment (e.g., *t* = 3 sec) without compromising accuracy, thereby reducing overall computational expense.

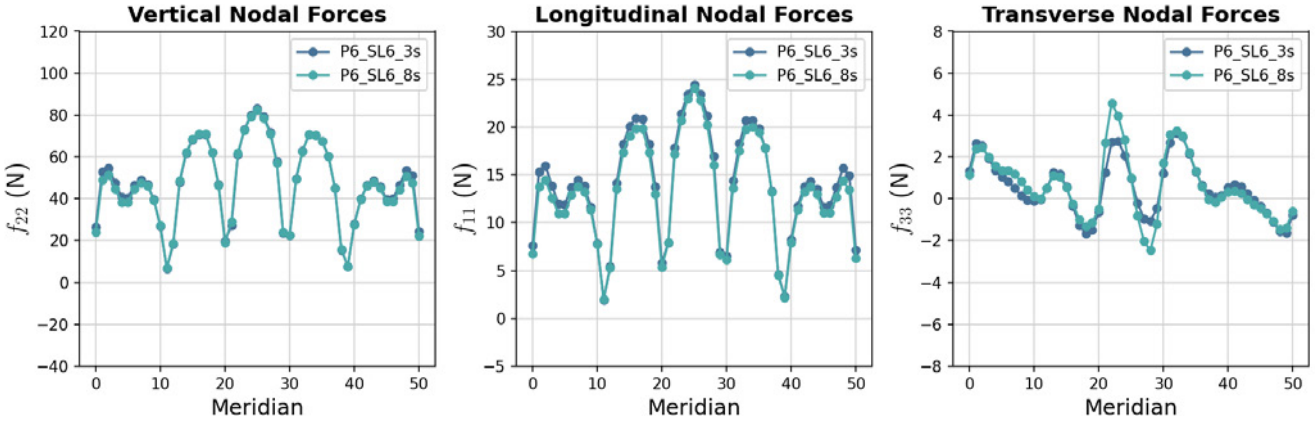

Figure 67. Graph. $P6$ load case contact forces across the middle of the contact length – t = 3 sec and 8 sec – 6% slip ratio.

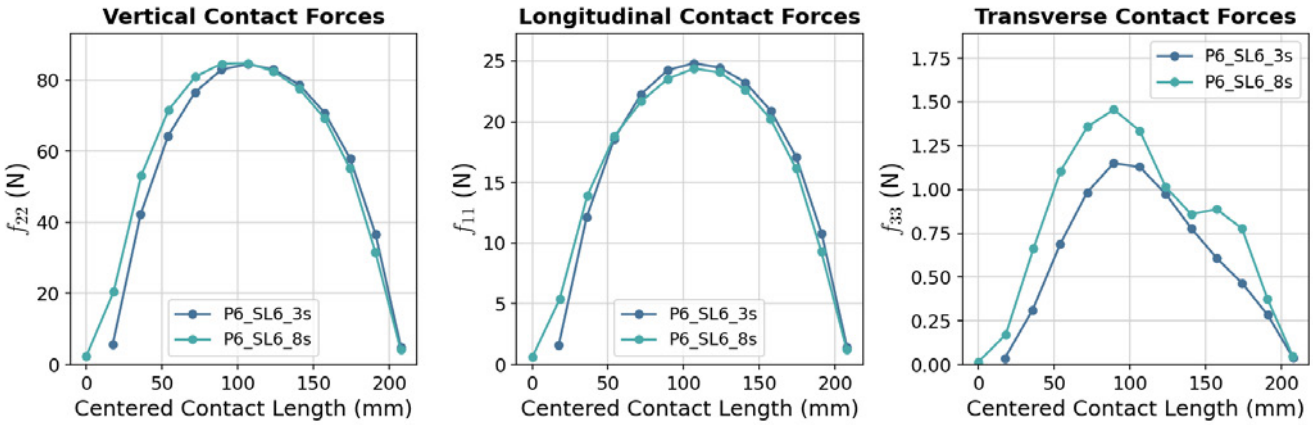

Figure 68. Graph. $P6$ load case contact forces across the central meridian – t = 3 sec and 8 sec – 6% slip ratio.

APPENDIX D: NUMERICAL DETAILS OF PAVEMENT FEM

Model Verification

A key criterion for verifying the accuracy of an FE model is the degree to which its outcomes converge toward an idealized continuum solution. The FE results are deemed acceptable if the stress-strain fields transition smoothly between elements and closely reassemble the predictions obtained from an analytical, semianalytical, or closed-form model. Still, due to the numerical nature of FE methods, perfect agreement with exact solutions is rarely possible. However, small discrepancies are typically acceptable, and thresholds are set to judge whether a solution is sufficiently accurate.

There are two primary strategies to manage and reduce the error in FE solutions: the *h-method* and the *p-method*. In the *h-method,* the polynomial order of the FE shape functions stays fixed, and accuracy is improved by mesh refinement, i.e., subdividing the domain into more, smaller elements. In contrast, the *p-method* maintains the same element density but increases accuracy by using higher-order FE shape functions, allowing each individual element to capture greater detail because of their higher complexity. The *h-method* was selected for relatively lower computational cost and simplicity. Hence, a sensitivity analysis was undertaken to determine the optimal mesh configuration in the vertical, longitudinal, and lateral directions. The acceptable error threshold was set at 3% for this study. Verification was carried out by comparing the results of a simplified FE to a reference analytical model, namely WinJULEA (a multilayer linear elastic analysis software embedded in AASHTOWare).

Mesh Refinement

Based on previous findings, the element size of the first element (from top to bottom) has been suggested to be 0.40 in or thinner, while the top element of the subgrade layer is recommended to be between 1.20 and 2.00 inches (Al-Qadi et al., 2008). An iterative series of mesh refinements was completed until the solution's desired accuracy was reached, at which point differences in the responses between WinJULEA and the FE model became negligible.

To illustrate this iterative process, Figure 69 presents the performance of different vertical mesh configurations for the *SMA overlay* pavement structure, which has two 2-in lifts of SMA and HMA. For each of the six configurations (A, B, C, D, E, and F), a selected load was applied to compute the critical responses using WinJULEA, which provided an axisymmetric analytical benchmark. Then, responses were compared to those yielded by a 2D FE model reflecting the same assumptions: circular tire imprint, uniform vertical pressure, and linear elastic material behavior. As the number of elements increased in the vertical direction, the error prediction for the tensile strain at the bottom of the last HMA layer ($\varepsilon_{HMA_{11}}$) and the maximum vertical shear strain within the HMA layers ($\varepsilon_{HMA_{23}}$) decreased (Figure 69a). Additionally, the number of elements per layer for each of the mesh configurations tested is summarized in Figure 69b. Based on the results, mesh configuration 'E', with a total number of 60 elements along the pavement depth, was selected as optimal.

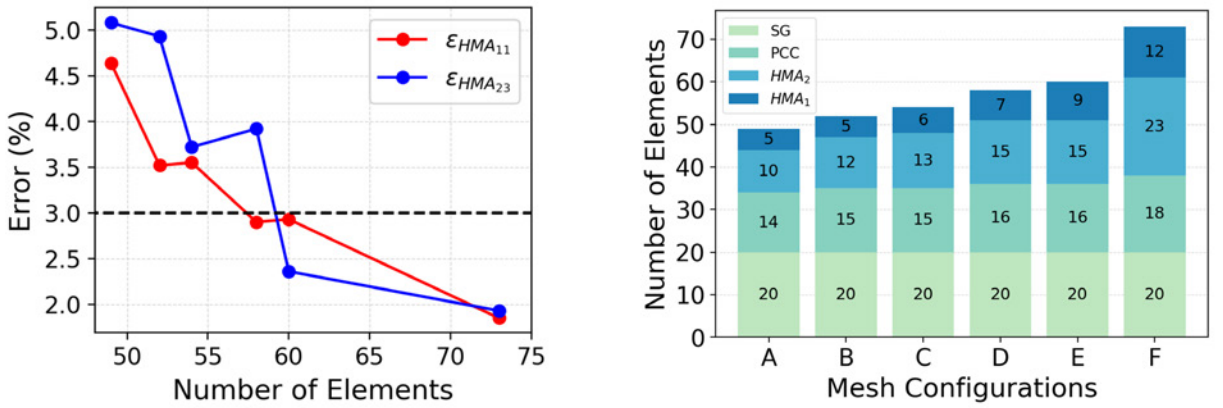

(a) Error progression of mesh configurations (b) Mesh configuration composition

Figure 69. Graph. Mesh refinement of SMA overlay pavement structure.

The mesh sensitivity process to determine the optimal mesh was carried out for all pavement structures in this study. The final vertical mesh configurations are summarized in Table 21**.**

Table 21. Vertical Mesh Configurations per Section

Pavement Structure	Typical Thick	Full Depth	Low Volume	SMA Overlay
Layer Thicknesses	HMA1 = 1 ½ in HMA2 = 2 ¼ in HMA3 = 1 ½ in Base = 12 in	HMA1 = 2 in HMA2 = 2 ¼ in HMA3 = 2 ¾ in HMA4 = 3 in Base = 12 in	HMA1 = 1 ½ in HMA2 = 2 ¼ in Base = 8 in Subbase = 6 in	SMA = 2 in HMA = 2 in PCC = 10 in
	Vertical Mesh Configuration (# elements @ bias)			
Wearing Course	9 @ 1.90	8 @ 1.05	8 @ 1.05	10 @ 1.15
Intermediate Course	15 @ 1.55	8 @ 1.10	–	–
Binder Course		12 @ 2.50	10 @ 1.05	9 @ 1.05
Concrete	–	–	–	21 @ 3.75
Base	16 @ 3.50	12 @ 1.75	20 @ 2.90	–
Subbase	–	–	7 @ 1.60	–
Subgrade	20 @ 19.00	20 @ 20.00	20 @ 28.00	20 @ 36.00

In the longitudinal and lateral directions, special attention was given to the mesh refinement of the tire-pavement contact area. Simulating a full pulse duration — starting and ending at zero while passing through a peak —demanded considerable computational effort. However, capturing the initial post-peak region of the stress pulse is deemed sufficient, as the tail could be predicted by mirroring the curve Al-Qadi et al. (2016)

In this study, the contact length for a single-axle load ranged from 7.87 to 12.60 in based on the load magnitude range. For a wheel path length of 7.87 in, for instance, an element size of 0.79 in allowed 10 elements to represent the tire imprint, resulting in a recommended wheel path length of 50.39 in.

Since the tire contact imprint is dependent on the load magnitude and tire inflation pressure, varying numbers of elements may be needed to represent the imprint for each case. To maintain consistency without jeopardizing the accuracy, the element size in the longitudinal direction of the wheel path was kept at 0.79 in. Table 22 summarizes the longitudinal mesh configurations. It should be noted that within the horizontal plane, the mesh refinement remains the same across the four simulated sections, as they are all subject to the same loading conditions for comparison.

Table 22. Longitudinal Mesh Configuration per Section

Nomenclature	Load (kips)	Model Length (in)	Wheel Path Length (in)	Element Size (in)	Number of Elements
P1	6.00	374.80	51.97	0.79	66
P2	4.20	373.23	50.39	0.79	64
P3	9.50	377.95	55.12	0.79	70
P4	4.70	373.22	50.39	0.79	64
P5	7.00	375.59	52.76	0.79	67
P6	4.20	373.23	50.39	0.79	64
P7	3.60	373.23	50.39	0.79	64
P8	5.00	374.02	51.18	0.79	65

In addition, the lateral mesh refinement within the wheel path was guided by the widths of the tire ribs and grooves at the contact interface. This approach ensures that stress distributions and localized contact pressures resulting from the tire tread pattern are captured. The summary is presented in Table 23. To properly capture the transverse contact stress fluctuations, each rib was subdivided evenly into three elements. In the case of DTA loads, the axle spacing (5.35 in.) was represented by 38 elements.

Table 23. Lateral Mesh Configuration

Component	P1	P2	P3	P4	P5	P6	P7	P8
Rib 1	2.03	2.02	2.04	2.02	2.04	2.02	2.02	2.03
Groove 1-2	0.03	0.07	0.05	0.06	0.03	0.06	0.08	0.06
Rib 2	1.60	1.60	1.61	1.60	1.61	1.60	1.60	1.60
Groove 2-3	0.11	0.12	0.09	0.11	0.10	0.12	0.13	0.12
Rib 3	1.58	1.58	1.59	1.58	1.59	1.58	1.58	1.58
Groove 3-4	0.11	0.12	0.09	0.11	0.10	0.12	0.13	0.12
Rib 4	1.60	1.59	1.61	1.60	1.61	1.59	1.59	1.60
Groove 4-5	0.03	0.07	0.06	0.05	0.03	0.06	0.08	0.05
Rib 5	2.03	2.02	2.04	2.02	2.04	2.02	2.02	2.03
Tire Type	ST	DTA	ST	DTA	ST	DTA	DTA	ST
Elements	19	76	19	76	19	76	76	19

Mesh refinement outside the wheel path region was gradually coarsened and was determined by adjusting the dimension of biased elements surrounding the loading area. Infinite elements were placed at the vertical external edges to simulate far-field boundary conditions and reduce model size. A smooth transition between the FE mesh and the infinite elements was implemented to maintain continuity through two transitional zones. A top view of the FE model is presented in Figure 70**.**

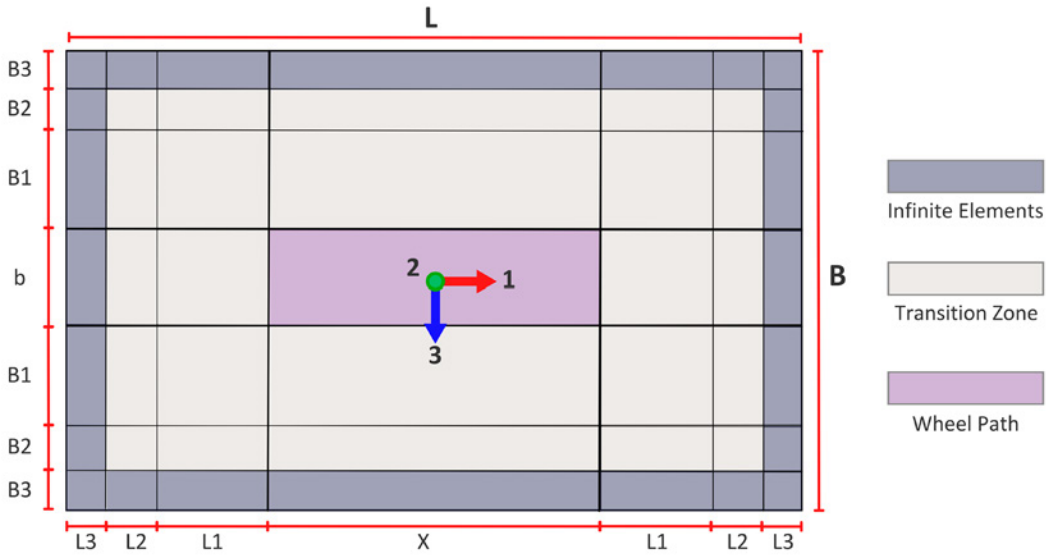

Figure 70. Schematic. Mesh definition in plain view.

APPENDIX E: PAVEMENT RESPONSES

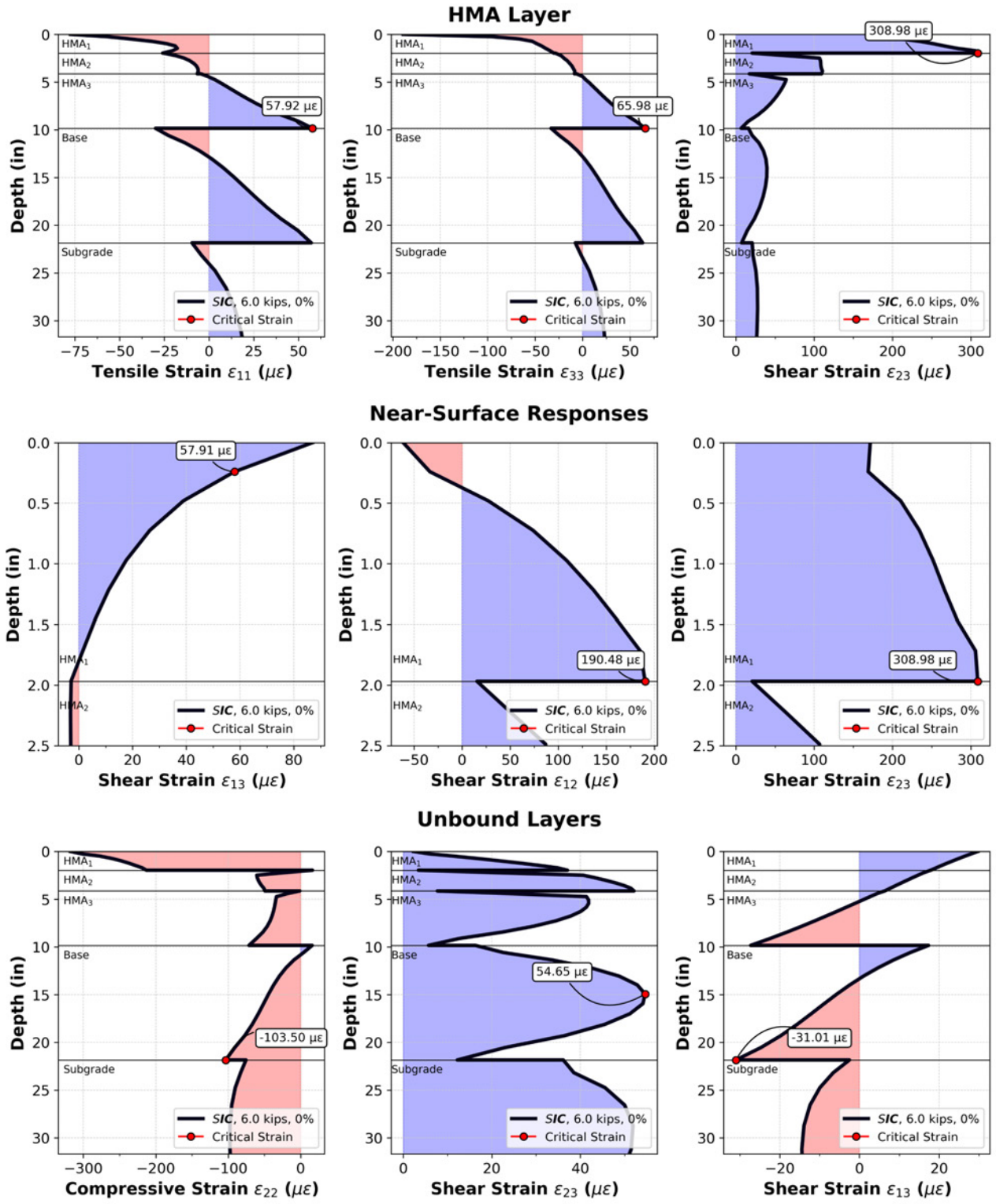

Figure 71. Graph. Summary of pavement responses of full depth section to a 6-kip steering axle load (P1) at 0% slip ratio.

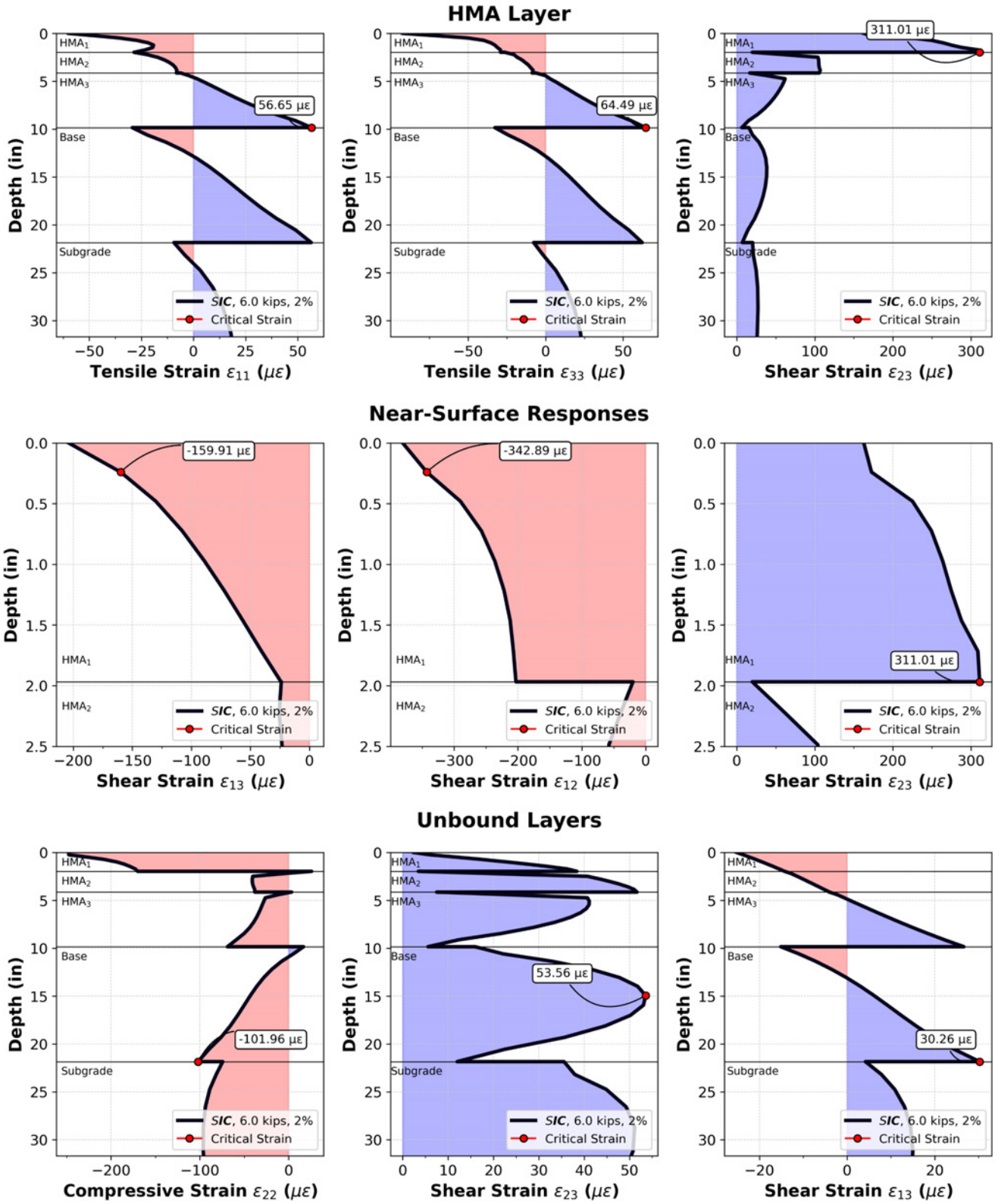

Figure 72. Graph. Summary of pavement responses of full depth section to a 6-kip steering axle load (P1) at 2% slip ratio.

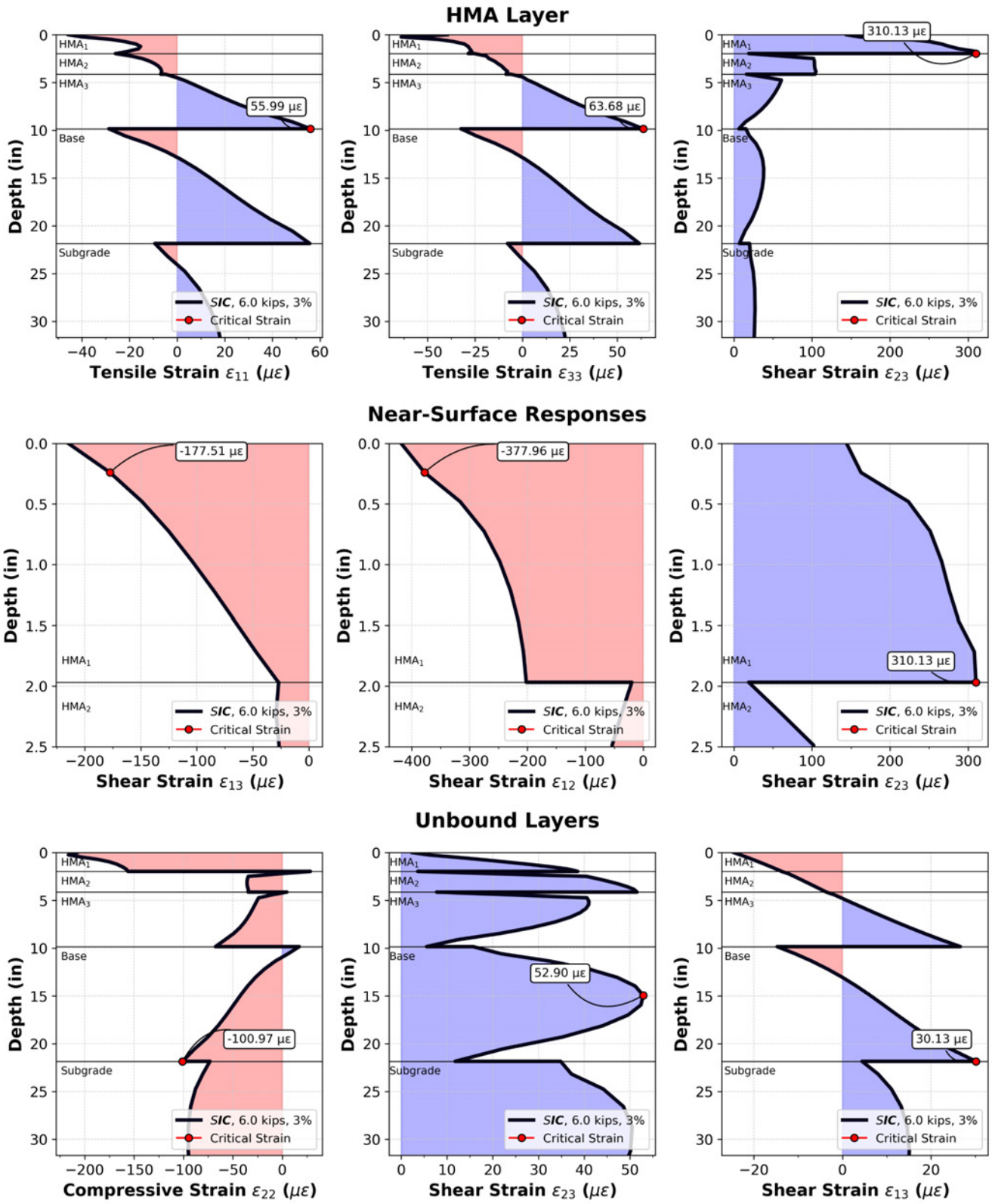

Figure 73. Graph. Summary of pavement responses of full depth section to a 6-kip steering axle load (P1) at 3% slip ratio.

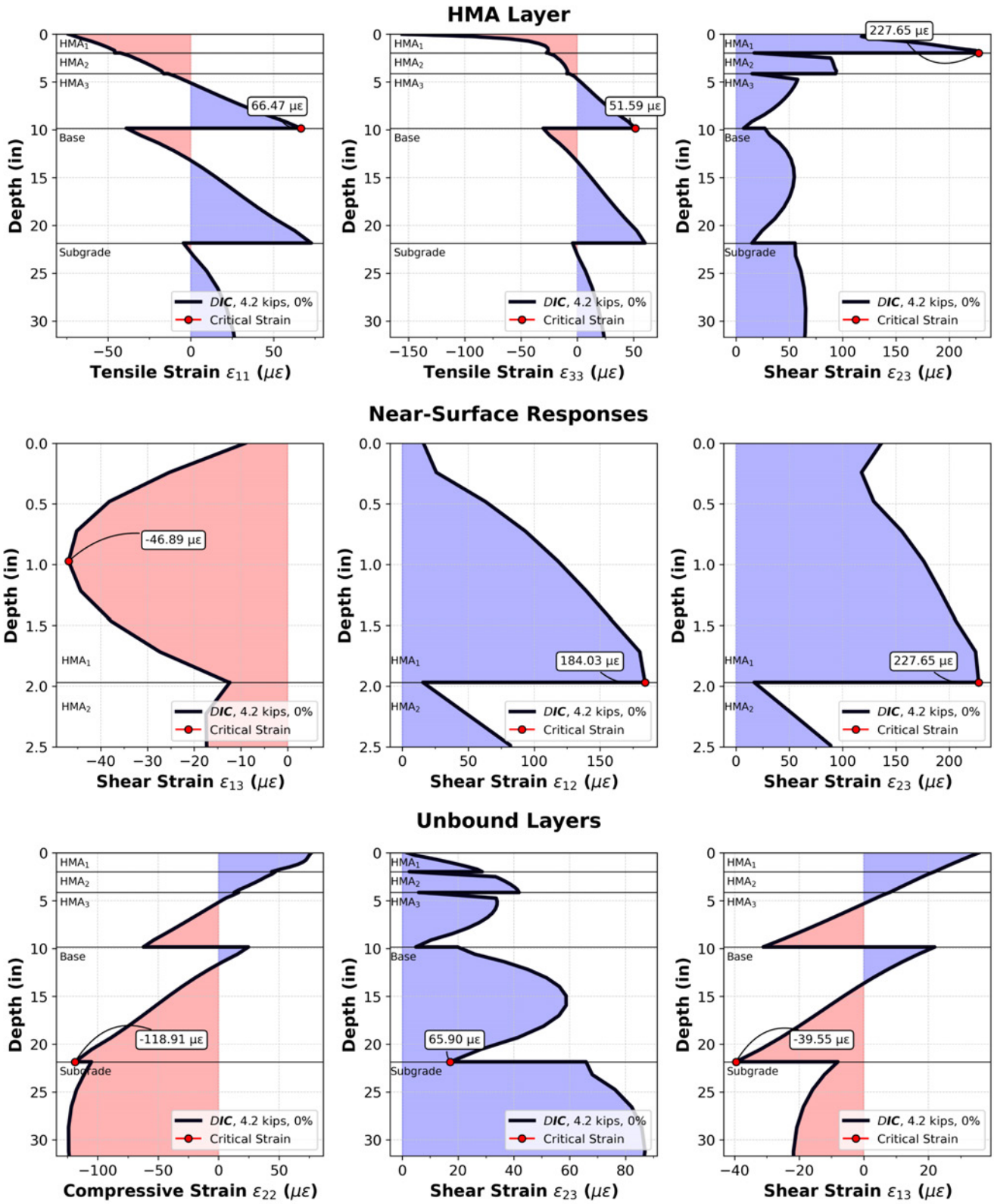

Figure 74. Graph. Summary of pavement responses of full depth section to a 4.2-kip DTA axle load (P2) at 0% slip ratio.

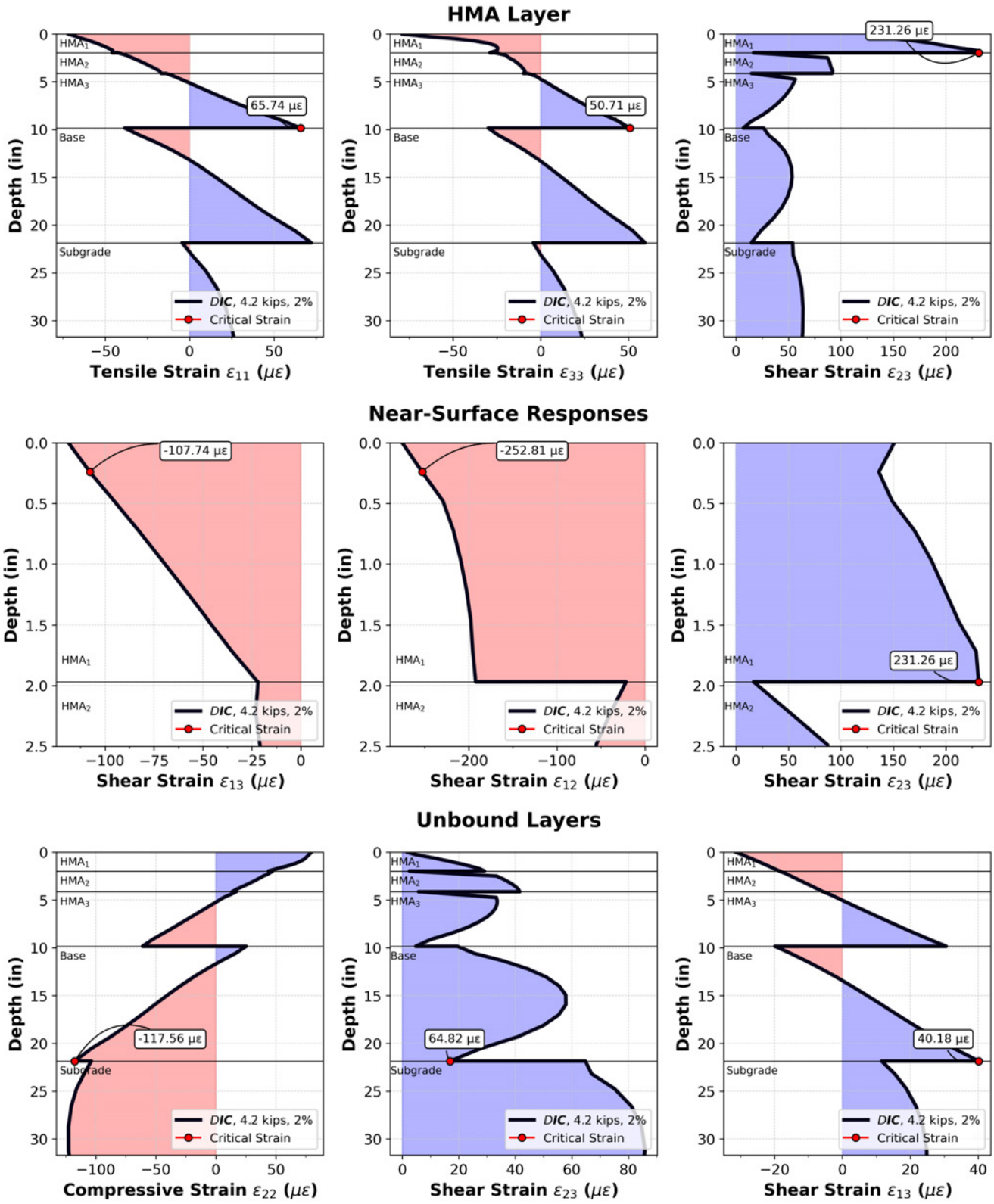

Figure 75. Graph. Summary of pavement responses of full depth section to a 4.2-kip DTA axle load (P2) at 2% slip ratio.

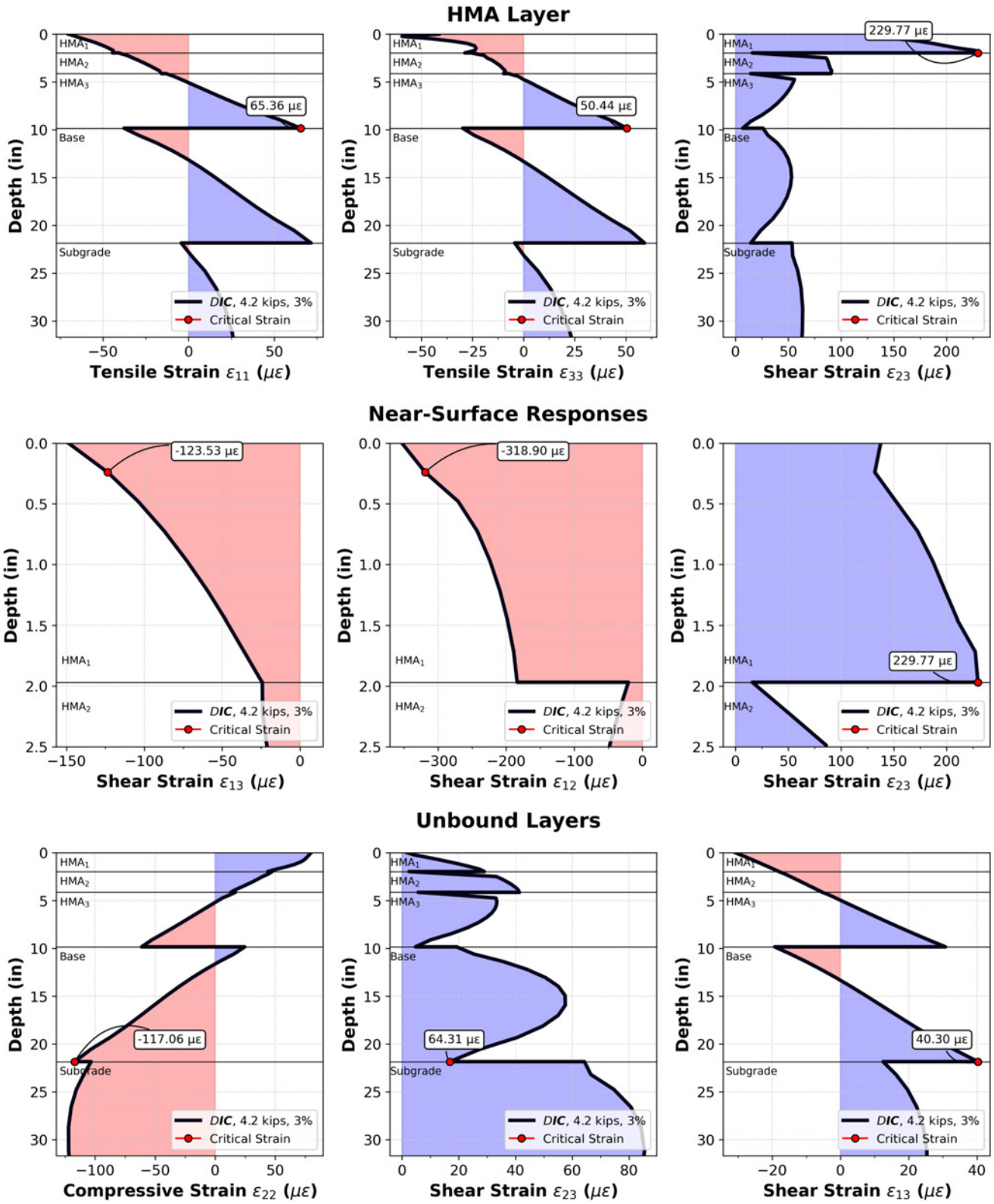

Figure 76. Graph. Summary of pavement responses of full depth section to a 4.2-kip DTA axle load (P2) at 3% slip ratio.

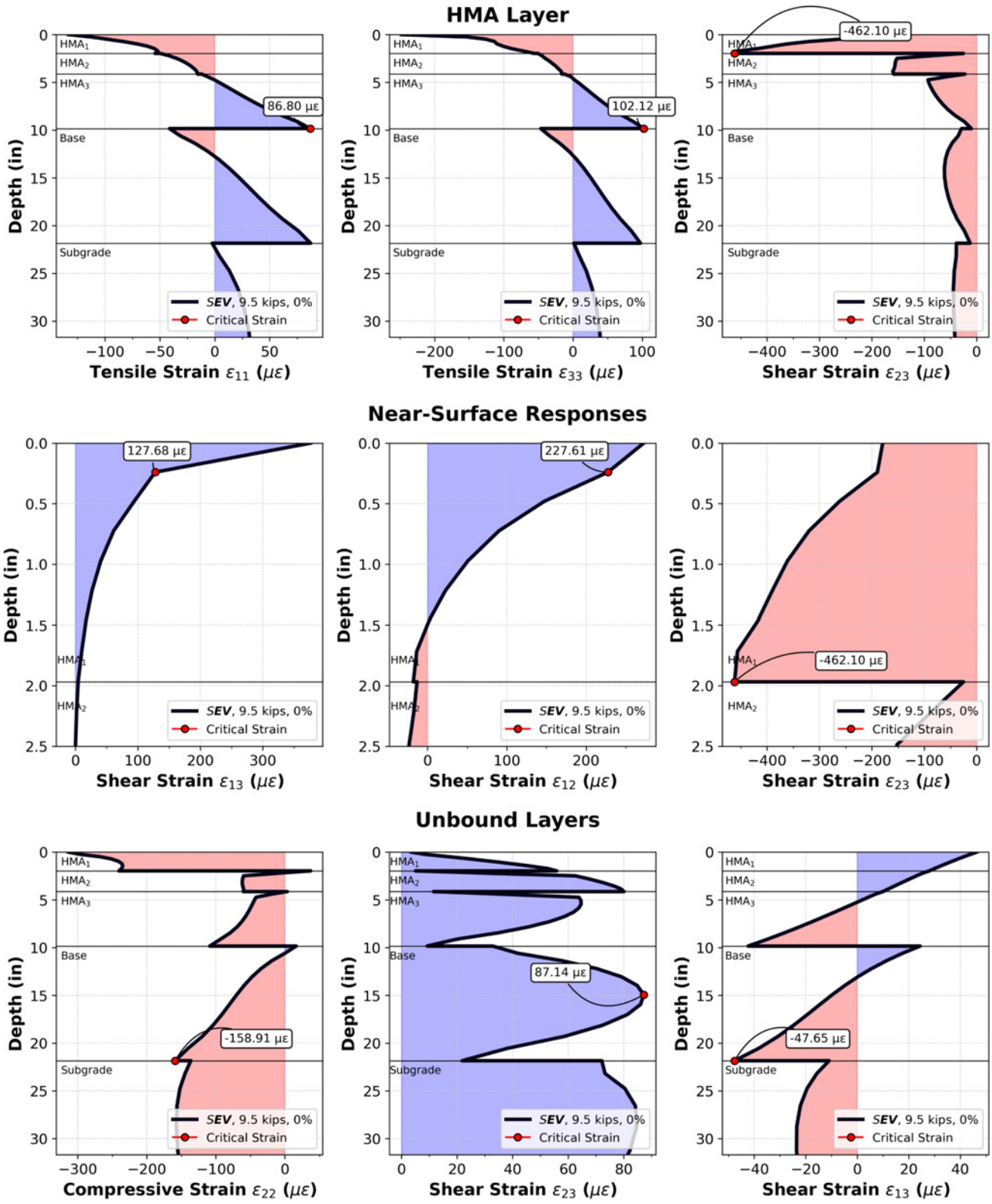

Figure 77. Graph. Summary of pavement responses of full depth section to a 9.5-kip steering axle load (P3) at 0% slip ratio.

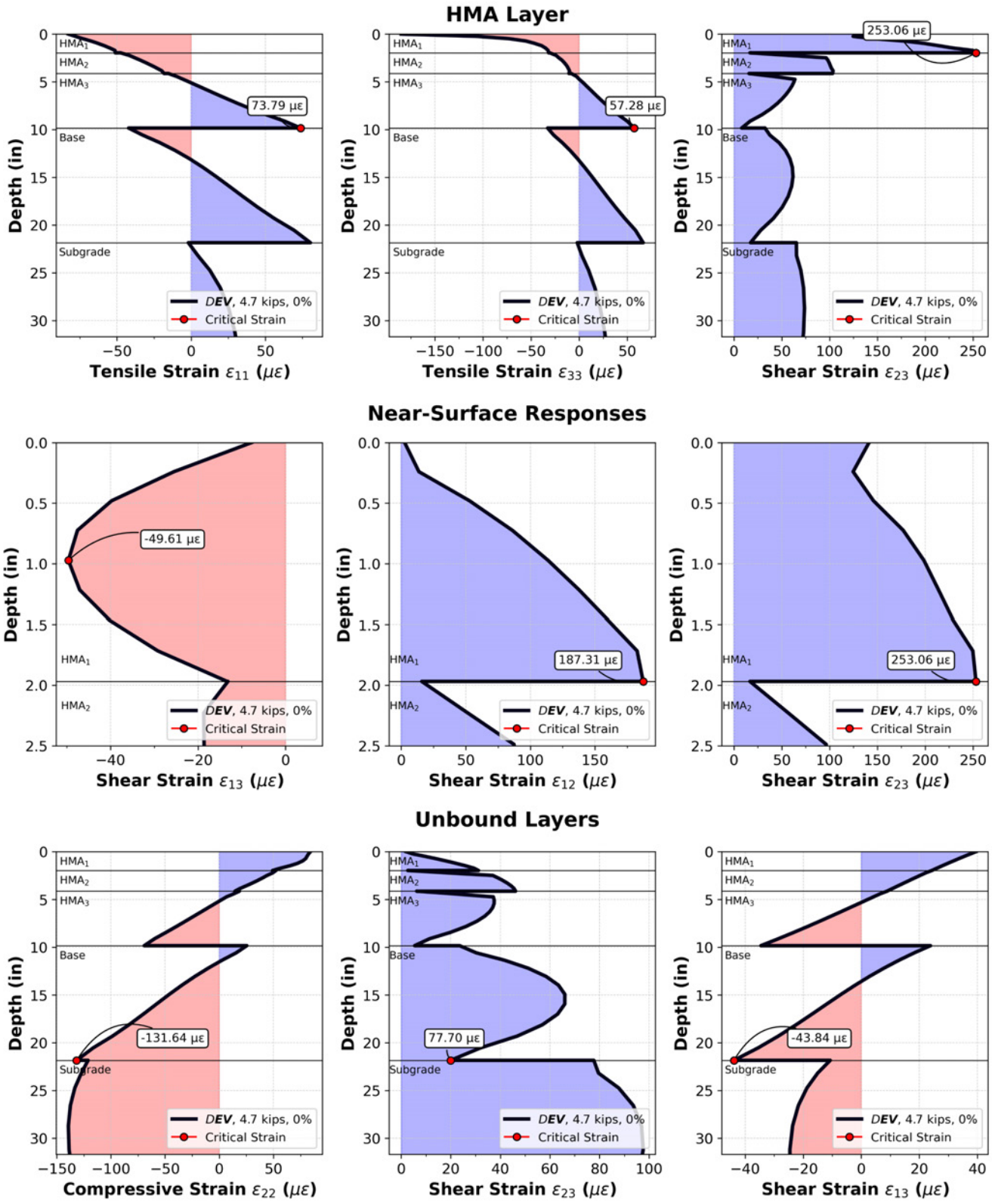

Figure 78. Graph. Summary of pavement responses of full depth section to a 4.7-kip DTA axle load (P4) at 0% slip ratio.

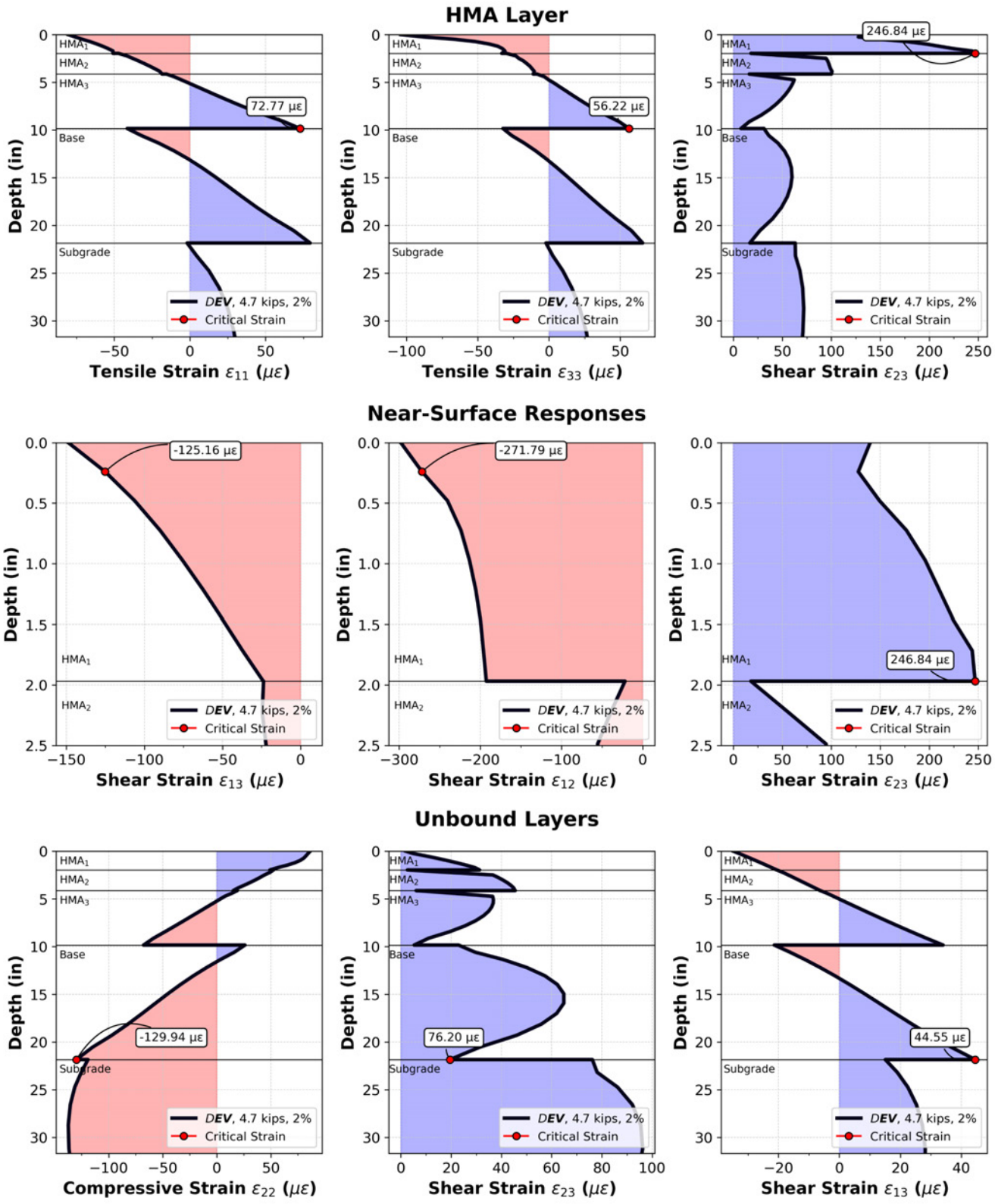

Figure 79. Graph. Summary of pavement responses of full depth section to a 4.7-kip DTA axle load (P4) at 2% slip ratio.

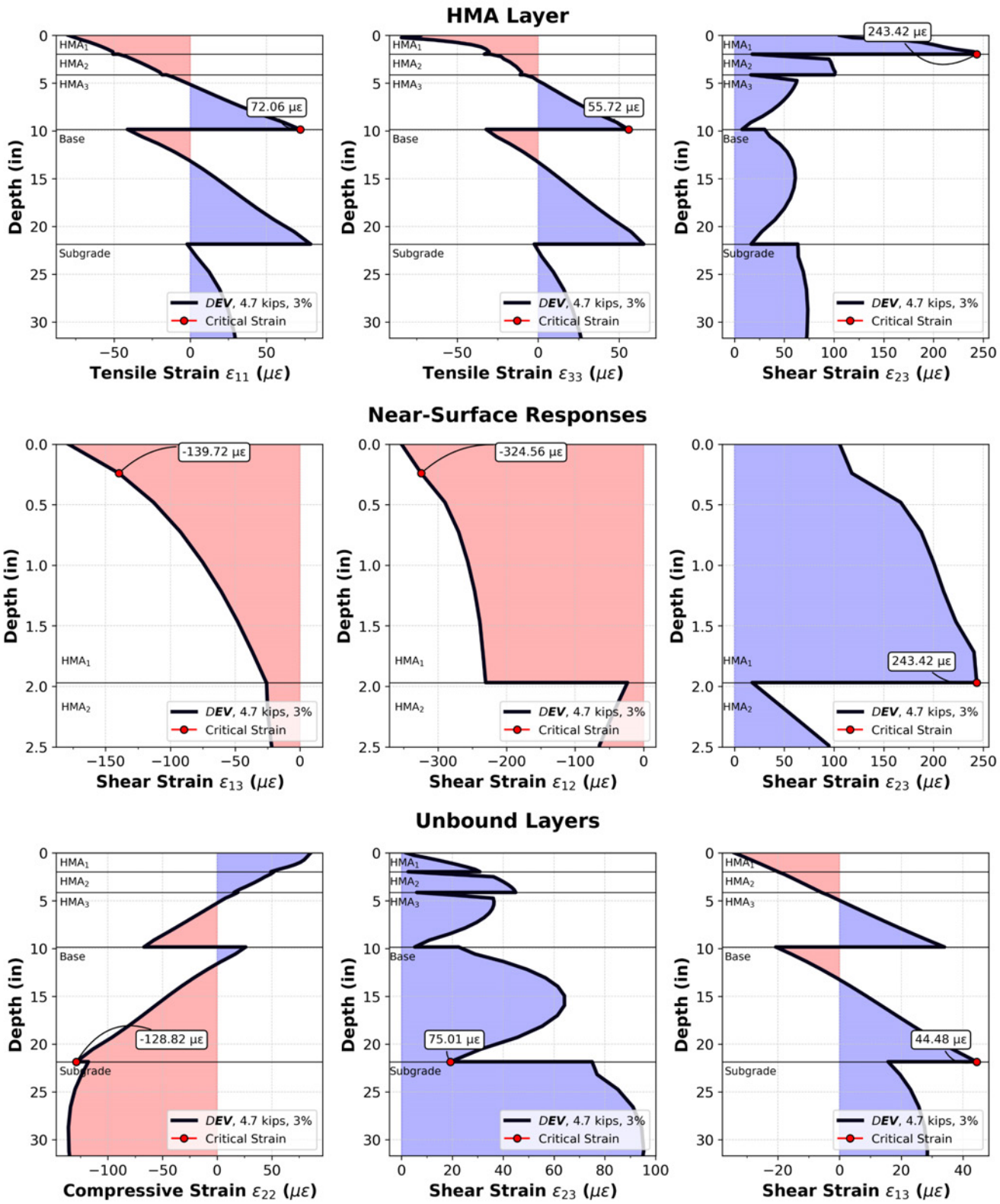

Figure 80. Graph. Summary of pavement responses of full depth section to a 4.7-kip DTA axle load (P4) at 3% slip ratio.

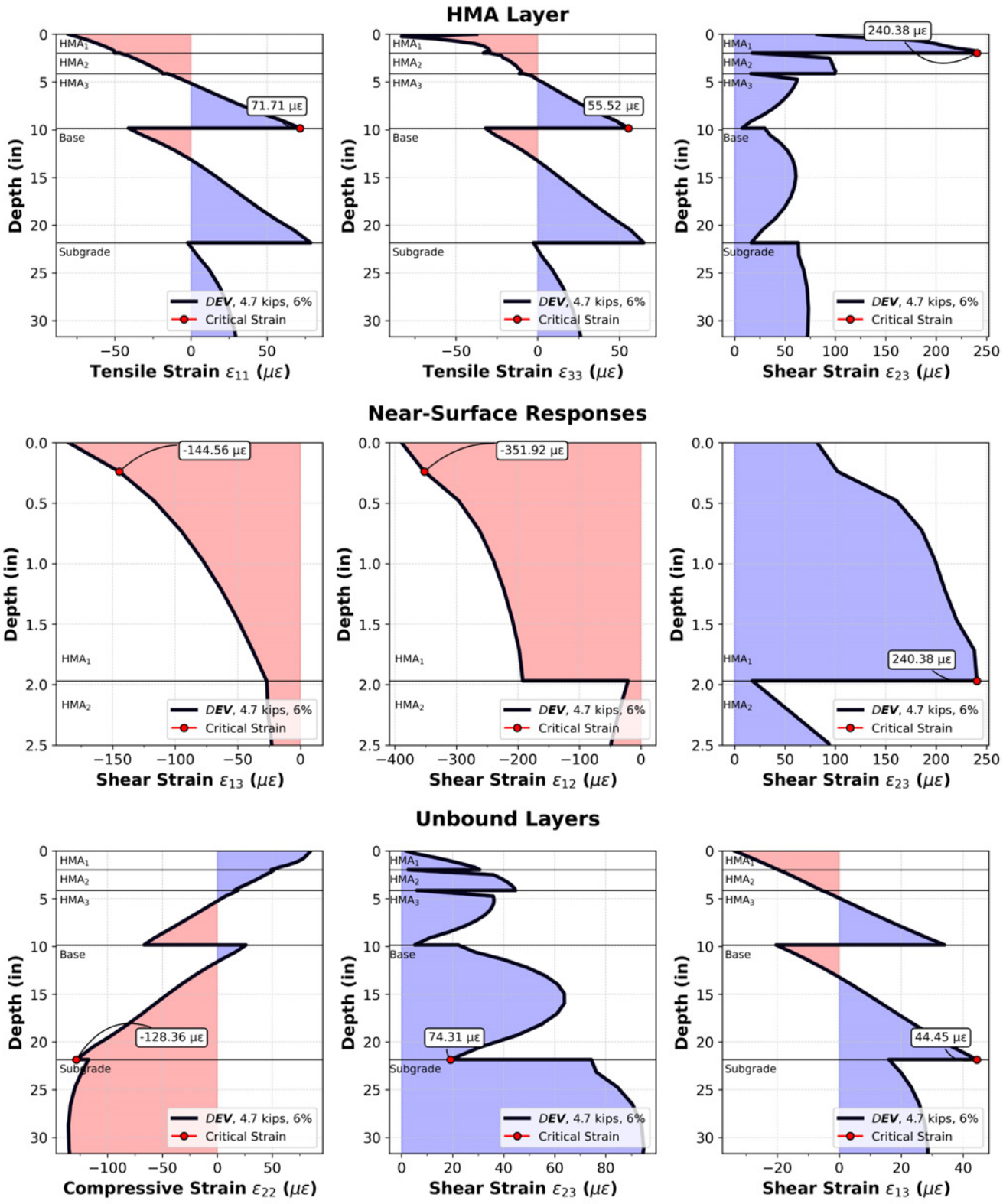

Figure 81. Graph. Summary of pavement responses of full depth section to a 4.7-kip DTA axle load (P4) at 6% slip ratio.

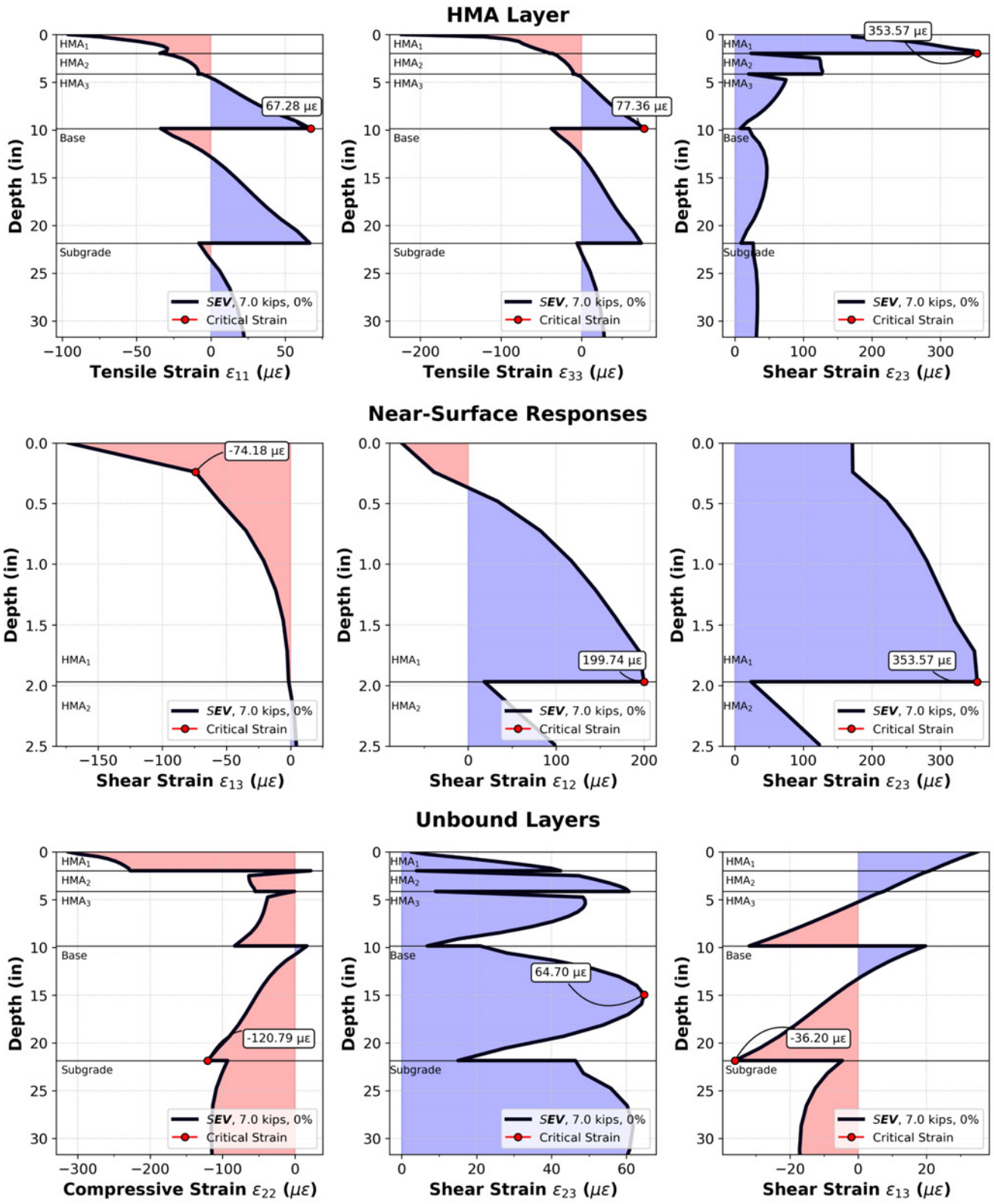

Figure 82. Graph. Summary of pavement responses of full depth section to a 7.0-kip steering axle load (P5) at 0% slip ratio.

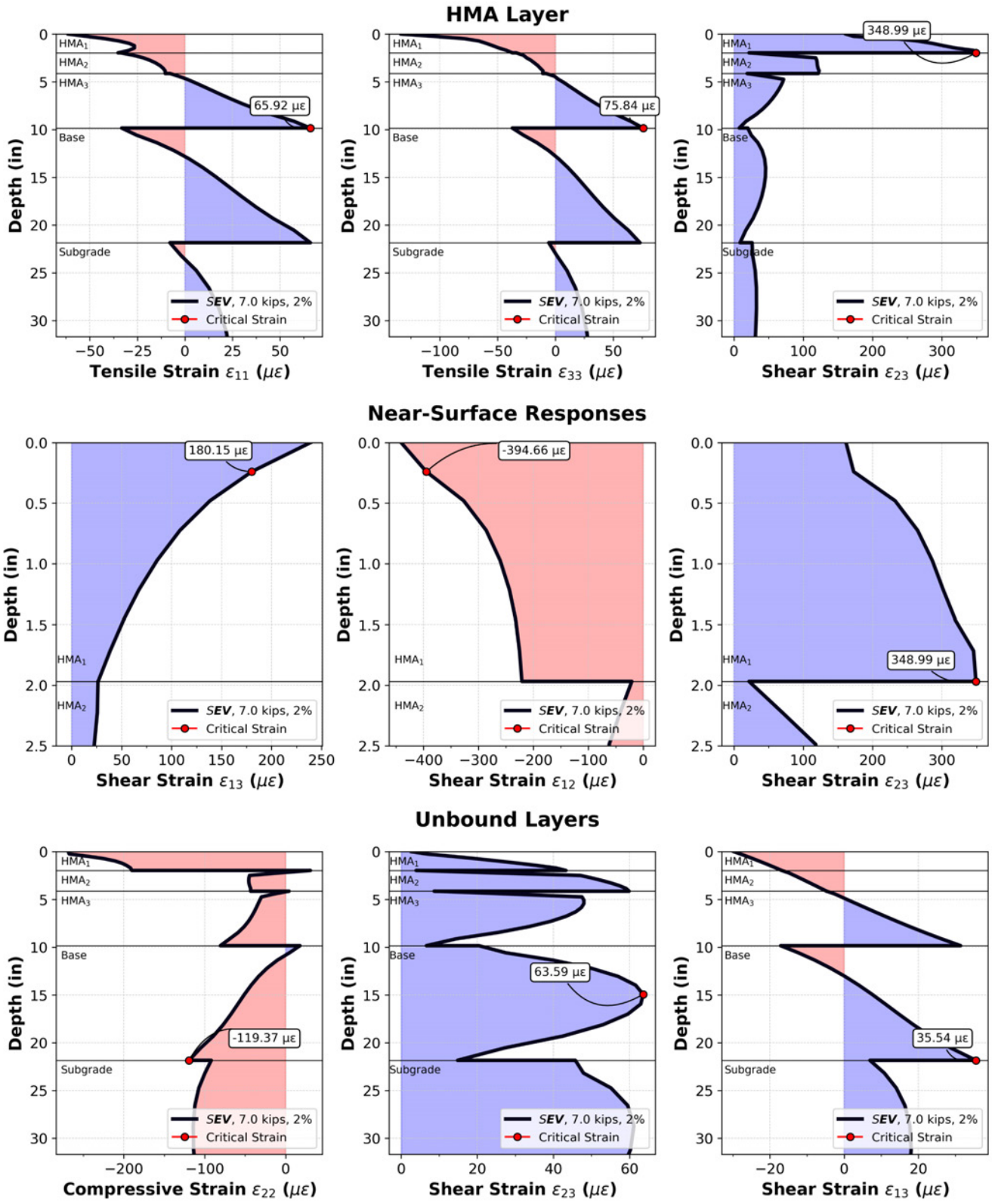

Figure 83. Graph. Summary of pavement responses of full depth section to a 7.0-kip steering axle load (P5) at 2% slip ratio.

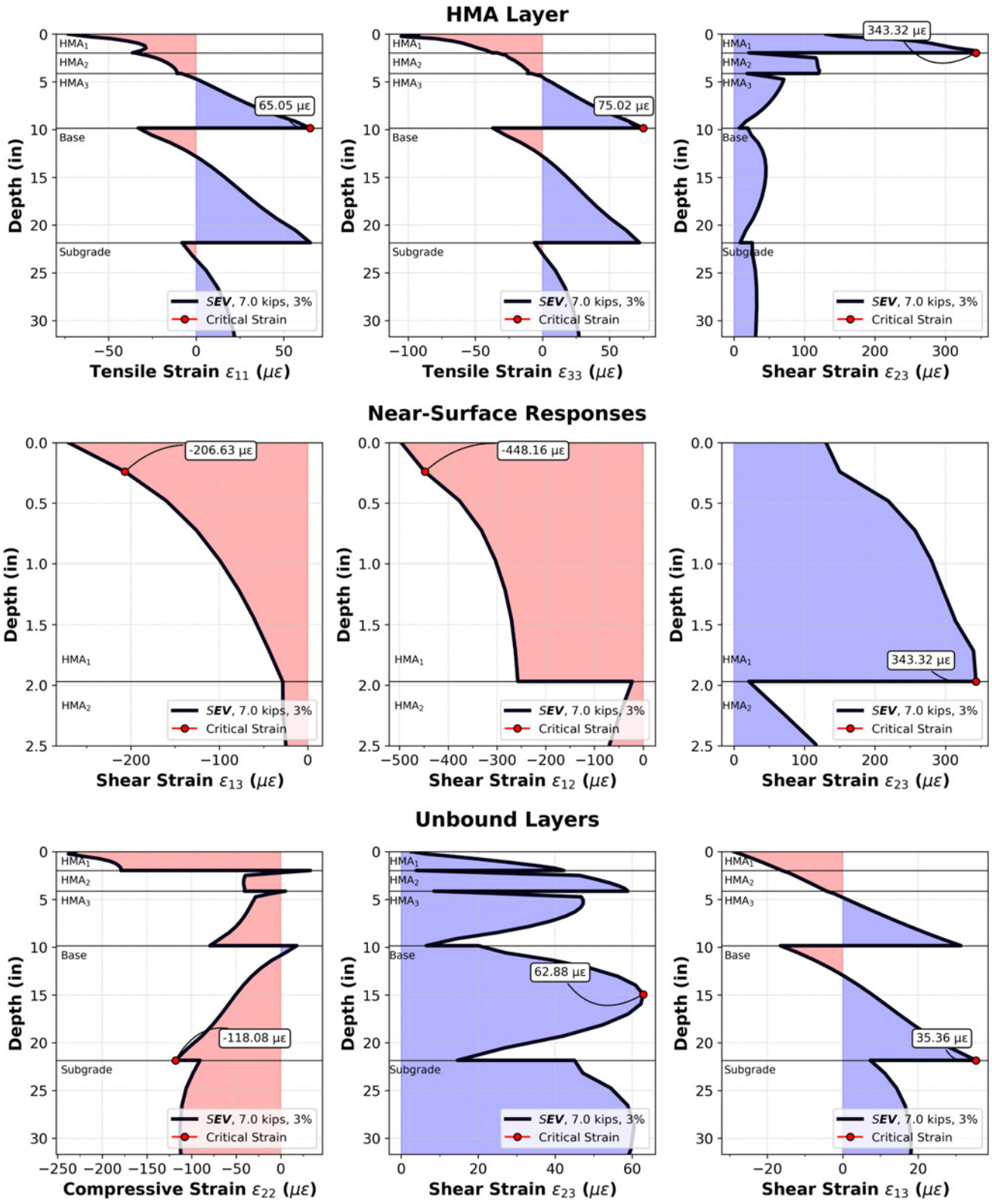

Figure 84. Graph. Summary of pavement responses of full depth section to a 7.0-kip steering axle load (P5) at 3% slip ratio.

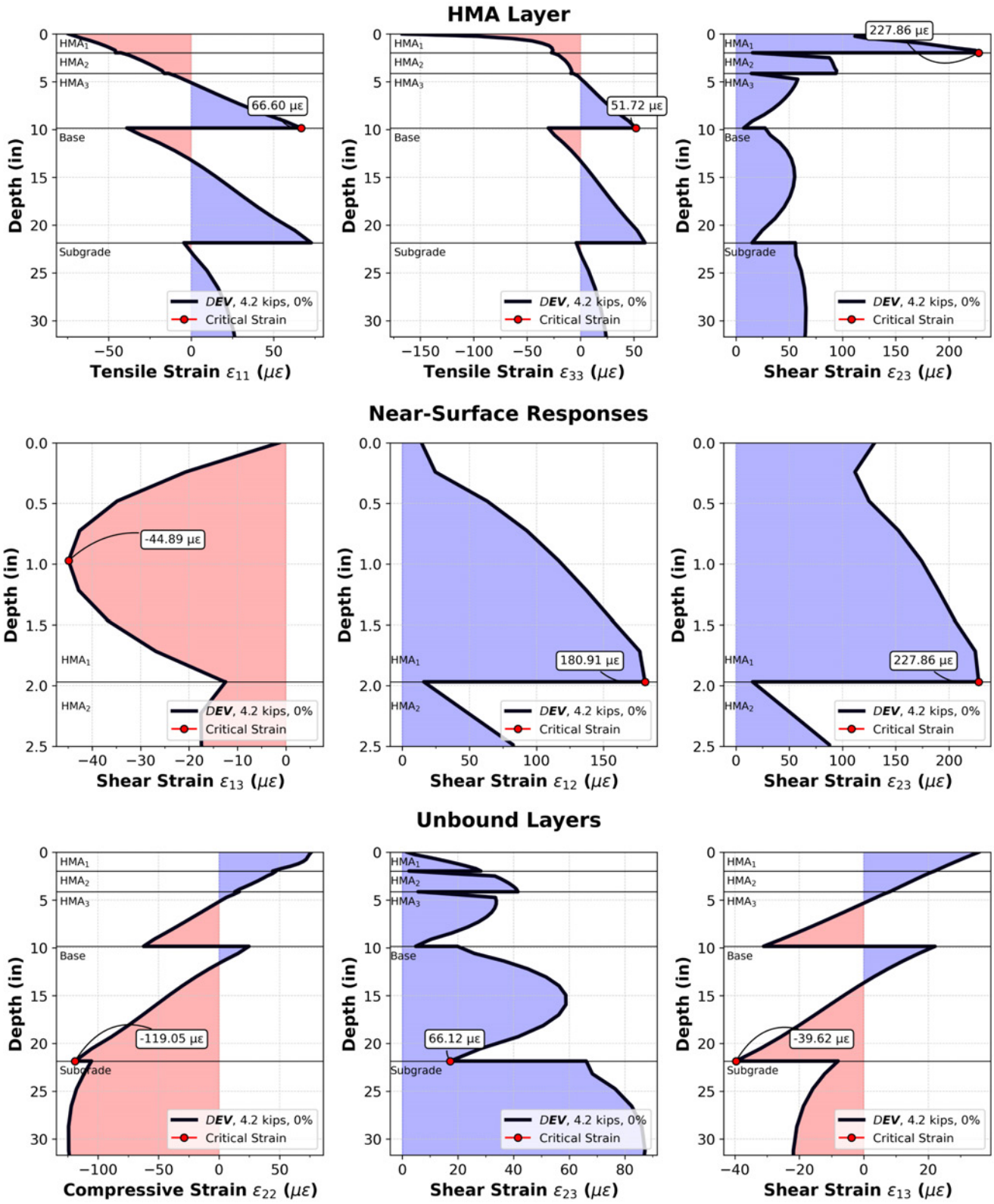

Figure 85. Graph. Summary of pavement responses of full depth section to a 4.2-kip DTA axle load (P6) at 0% slip ratio.

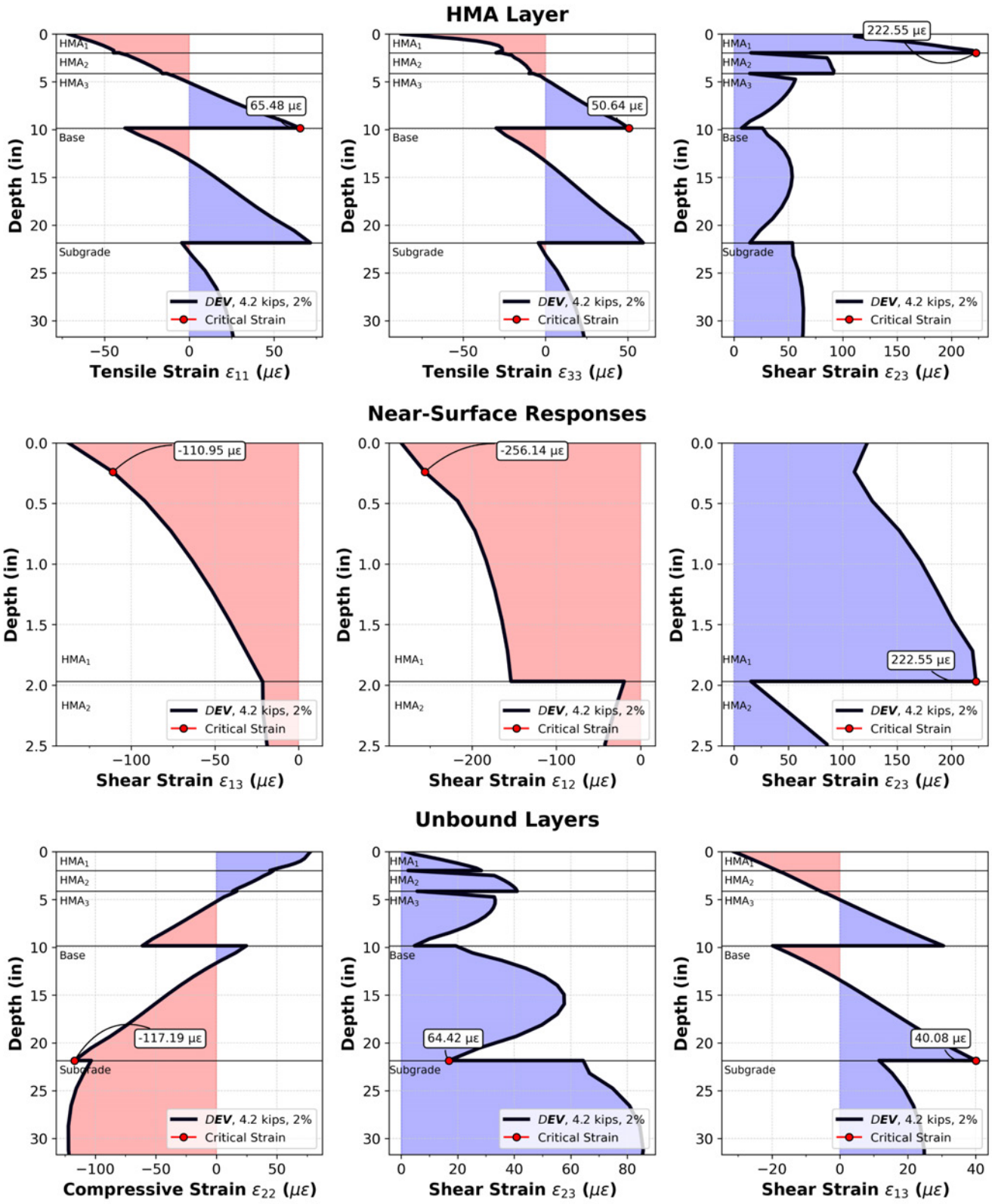

Figure 86. Graph. Summary of pavement responses of full depth section to a 4.2-kip DTA axle load (P6) at 2% slip ratio.

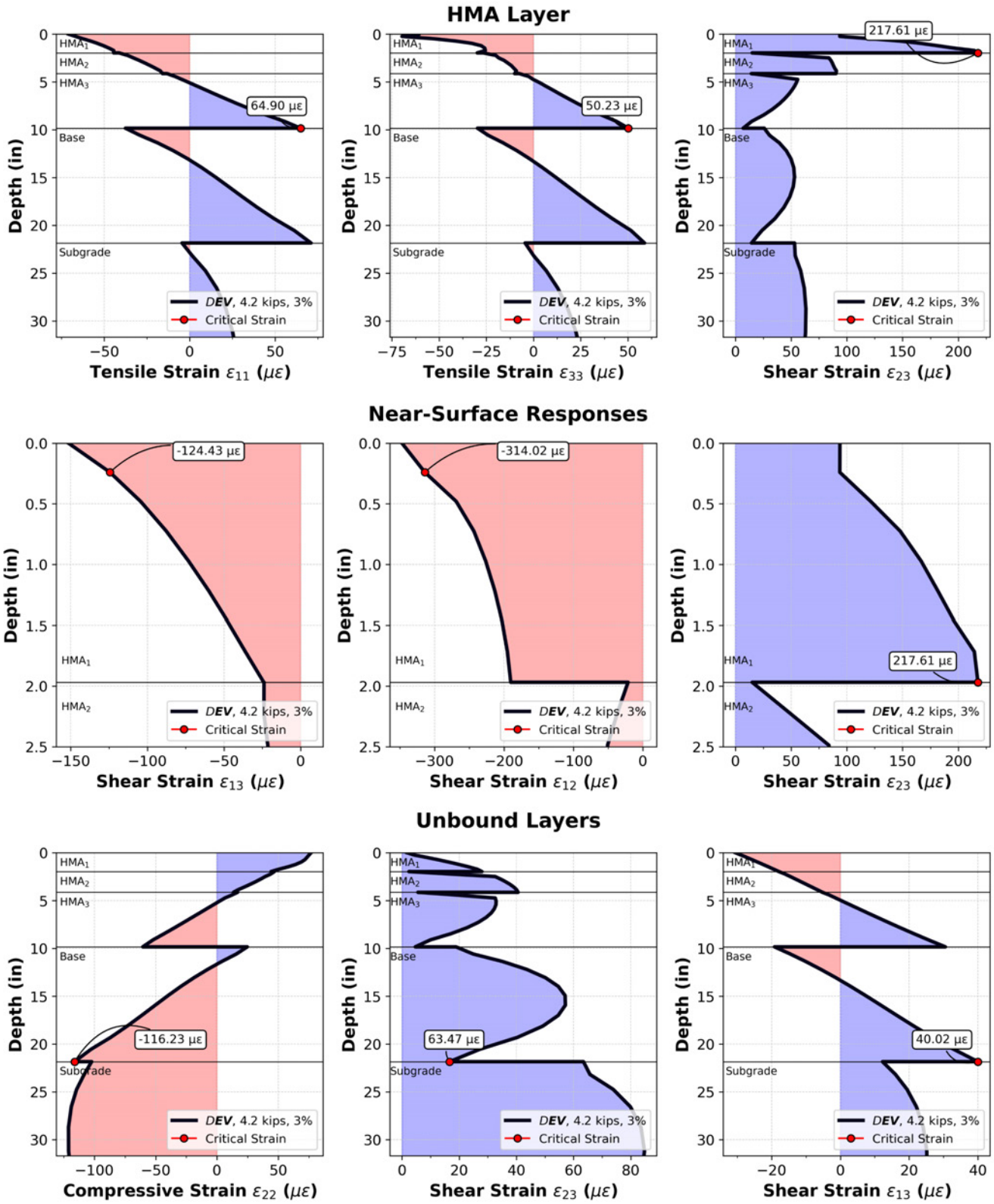

Figure 87. Graph. Summary of pavement responses of full depth section to a 4.2-kip DTA axle load (P6) at 3% slip ratio.

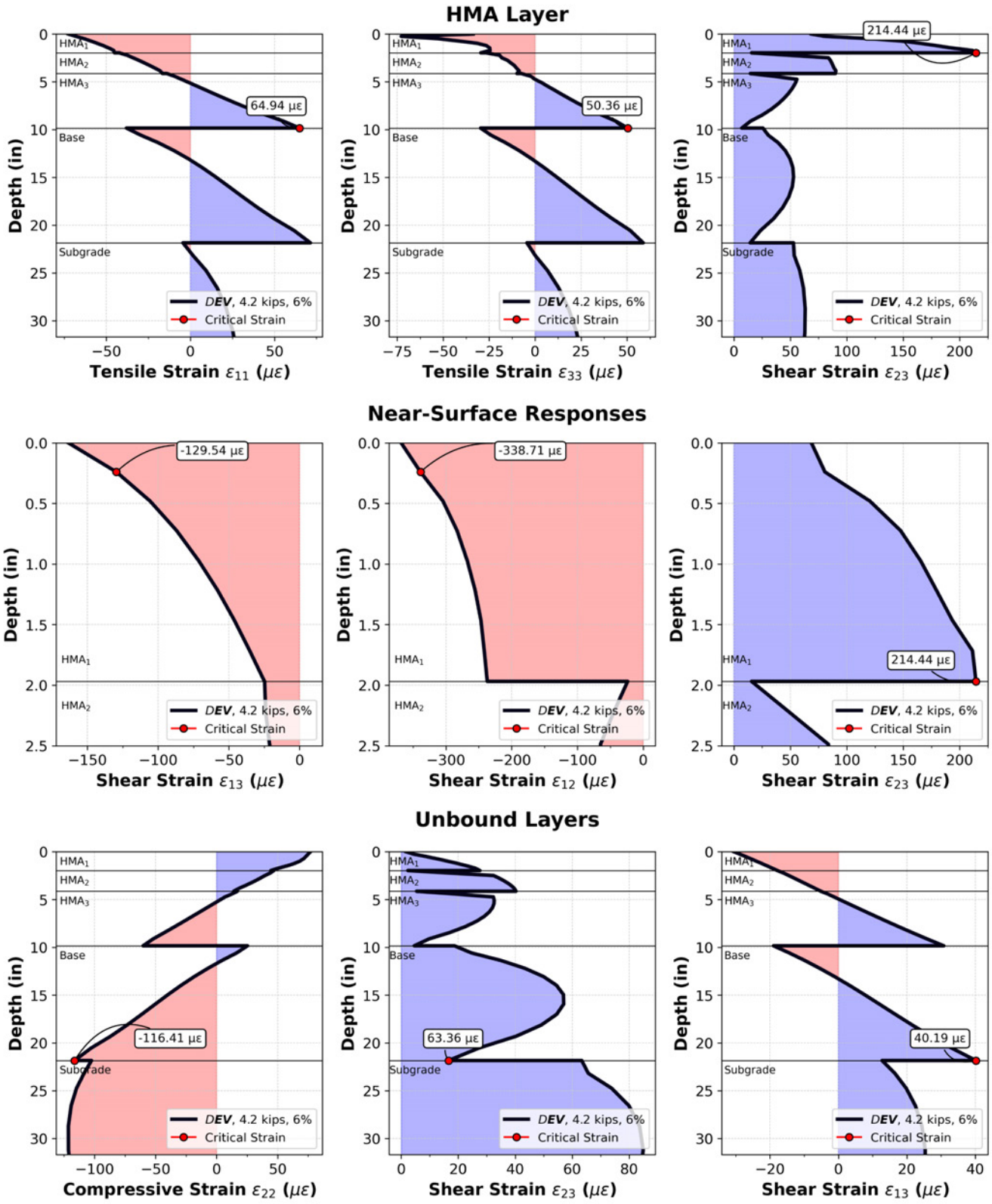

Figure 88. Graph. Summary of pavement responses of full depth section to a 4.2-kip DTA axle load (P6) at 6% slip ratio.

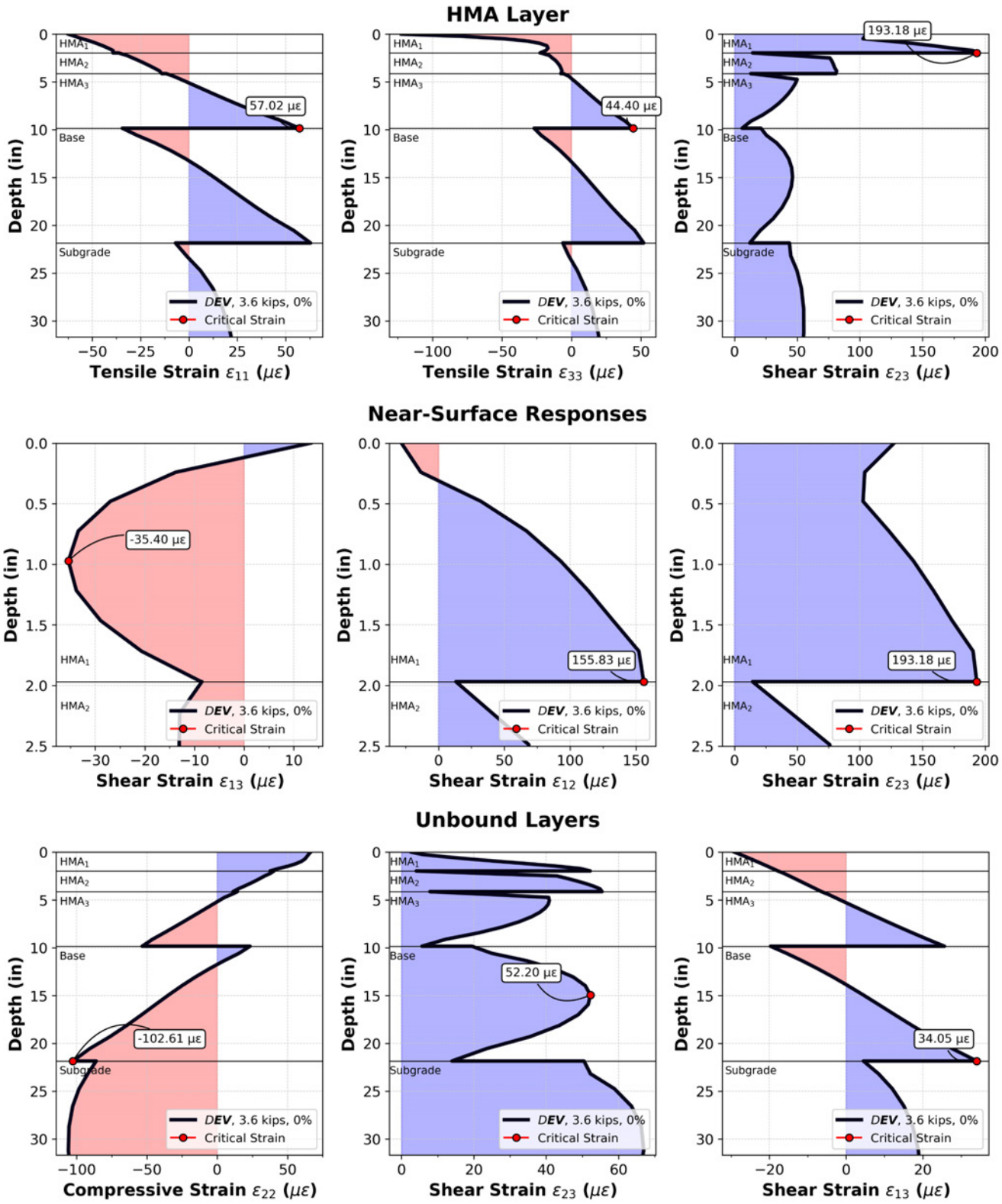

Figure 89. Graph. Summary of pavement responses of full depth section to a 3.6-kip DTA axle load (P7) at 0% slip ratio.

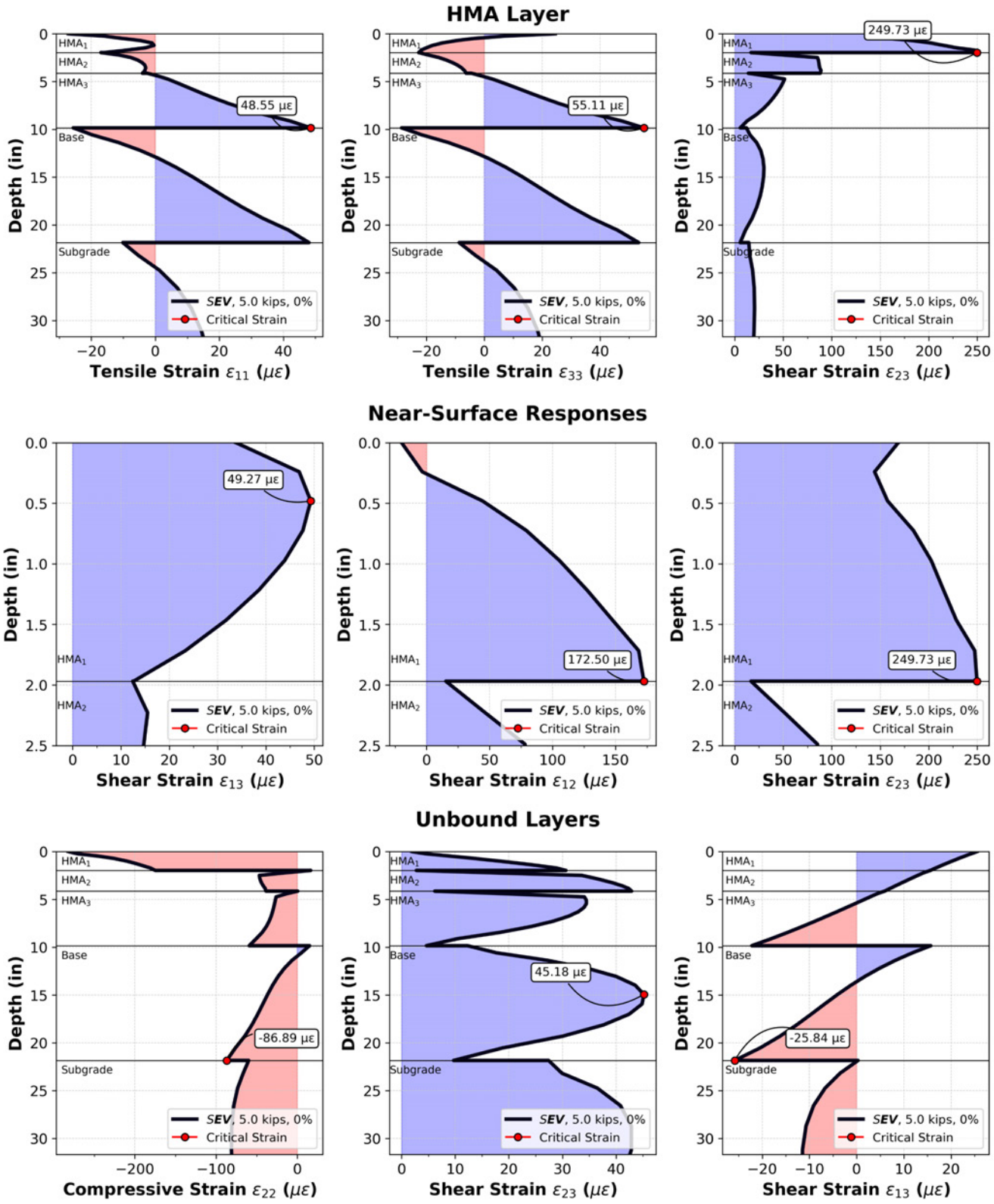

Figure 90. Graph. Summary of pavement responses of full depth section to a 5.0-kip steering axle load (P8) at 0% slip ratio.

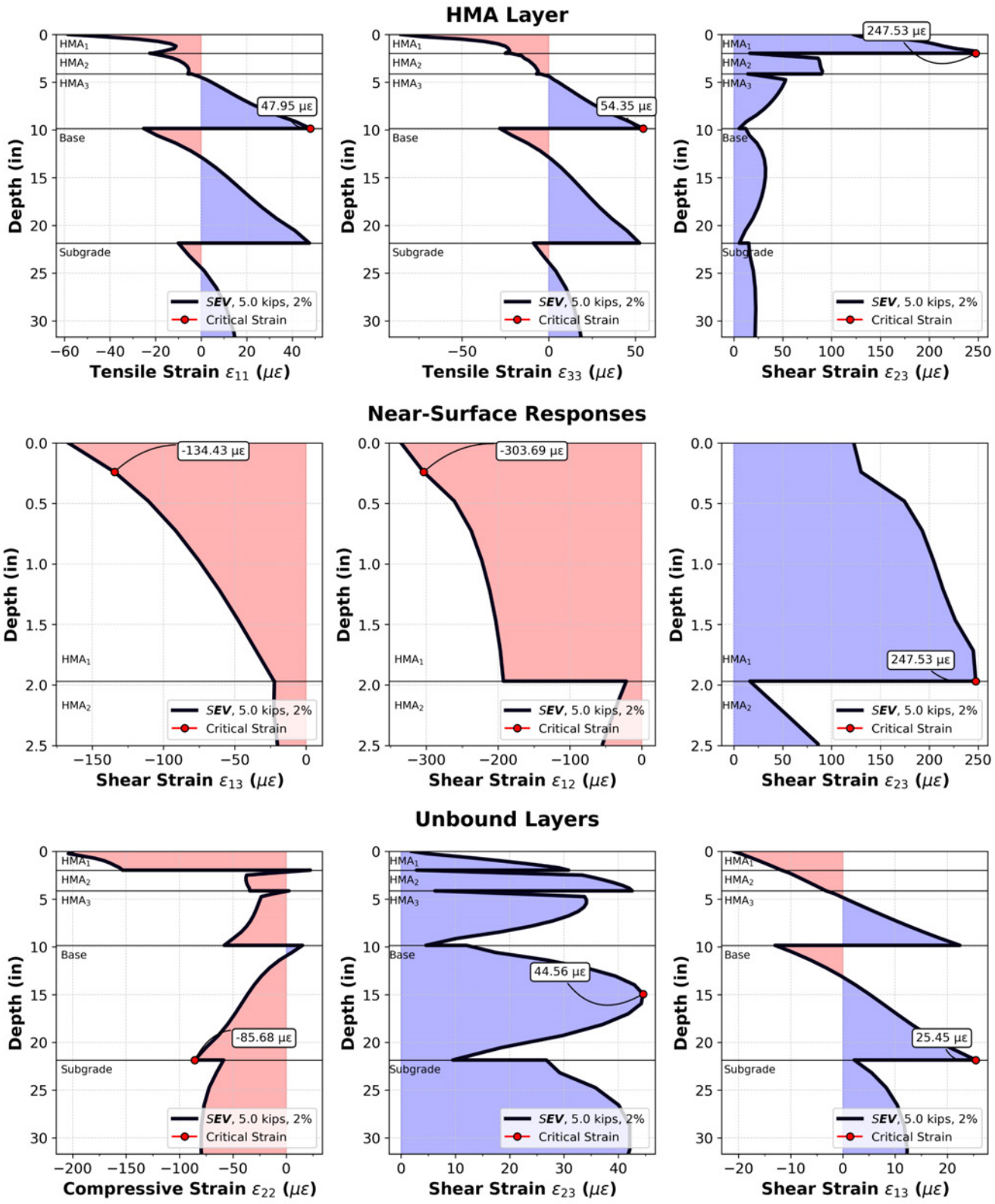

Figure 91. Graph. Summary of pavement responses of full depth section to a 5.0-kip steering axle load (P8) at 2% slip ratio.

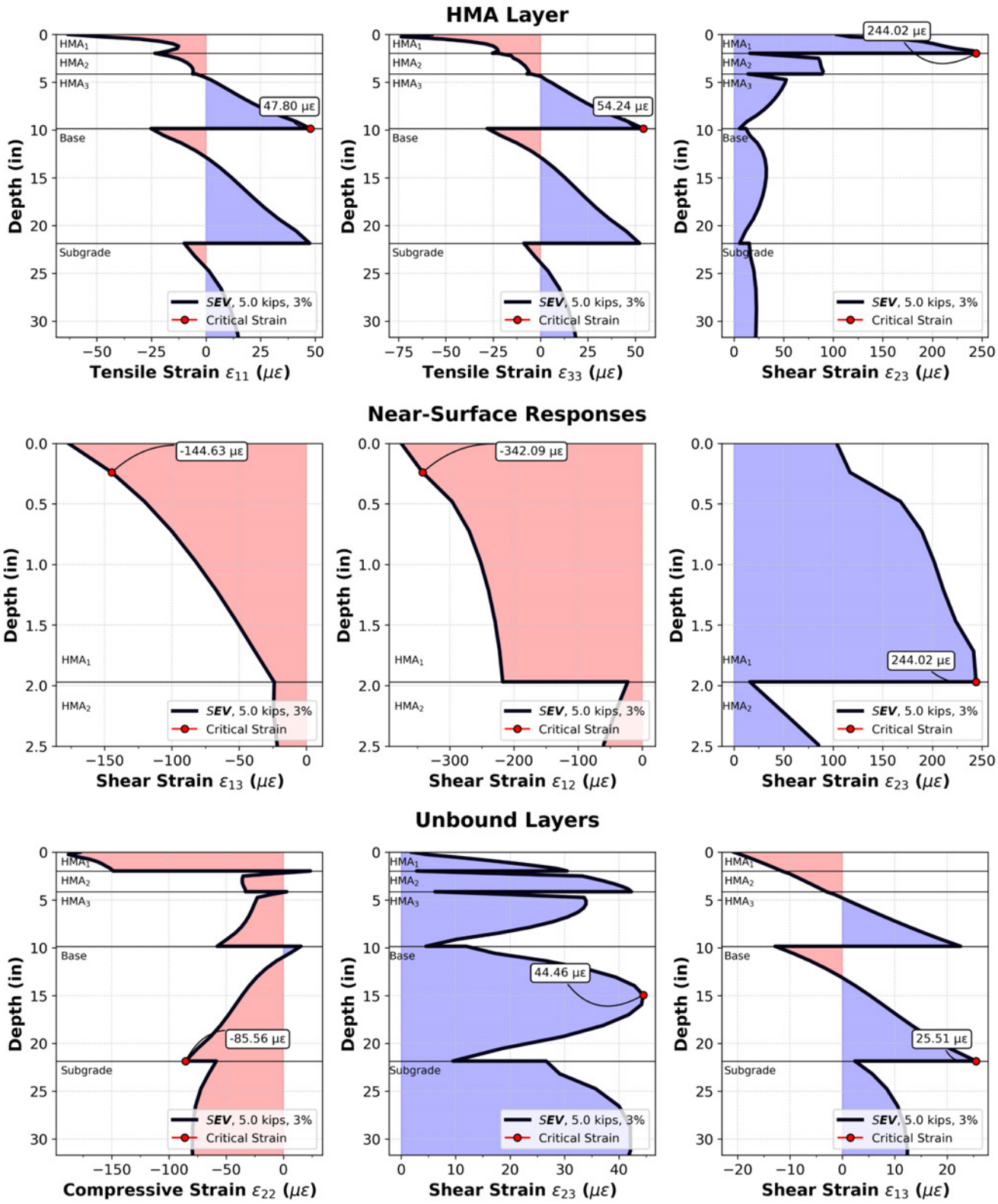

Figure 92. Graph. Summary of pavement responses of full depth section to a 5.0-kip steering axle load (P8) at 3% slip ratio.

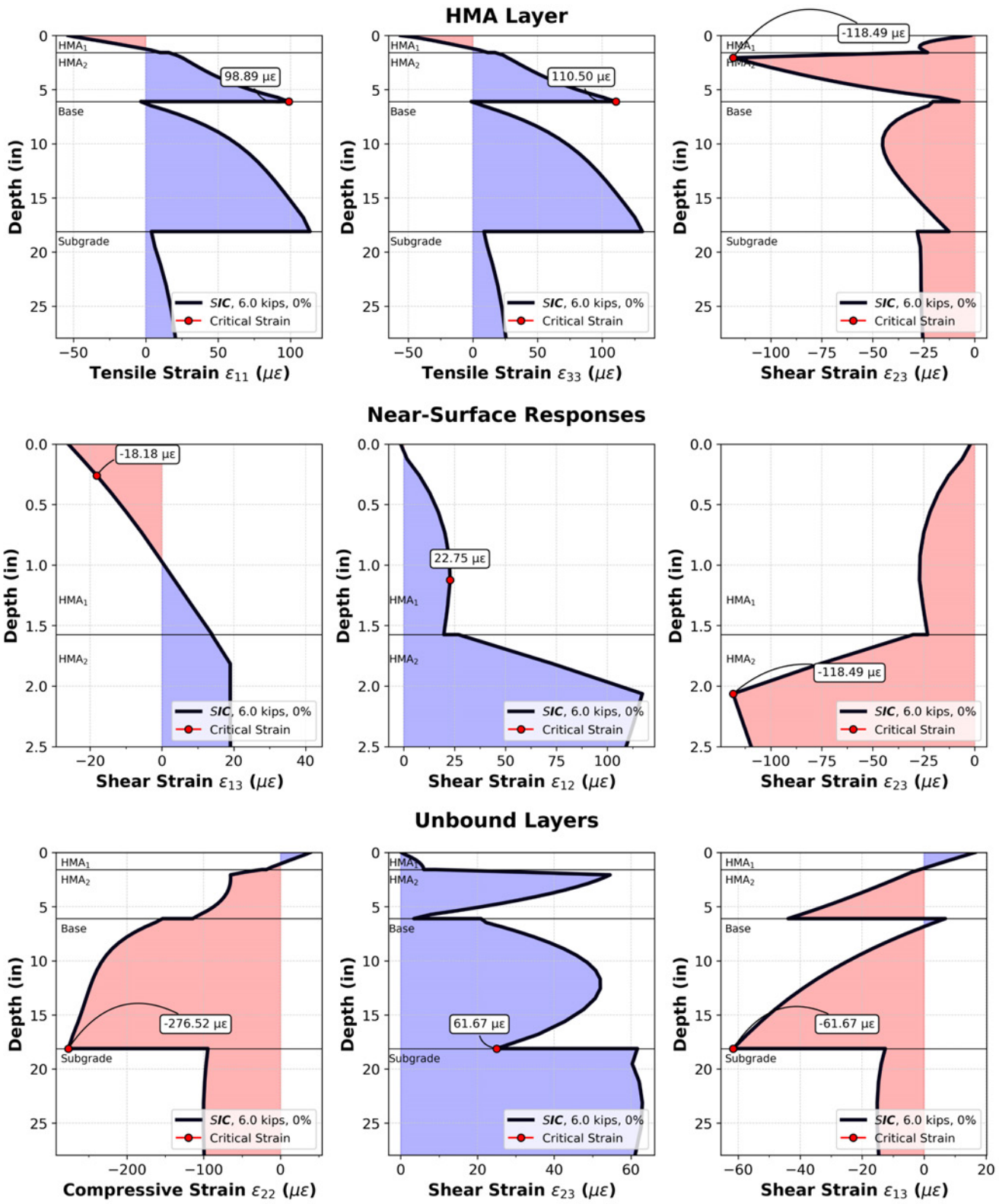

Figure 93. Graph. Summary of pavement responses of typical thick section to a 6-kip steering axle load (P1) at 0% slip ratio.

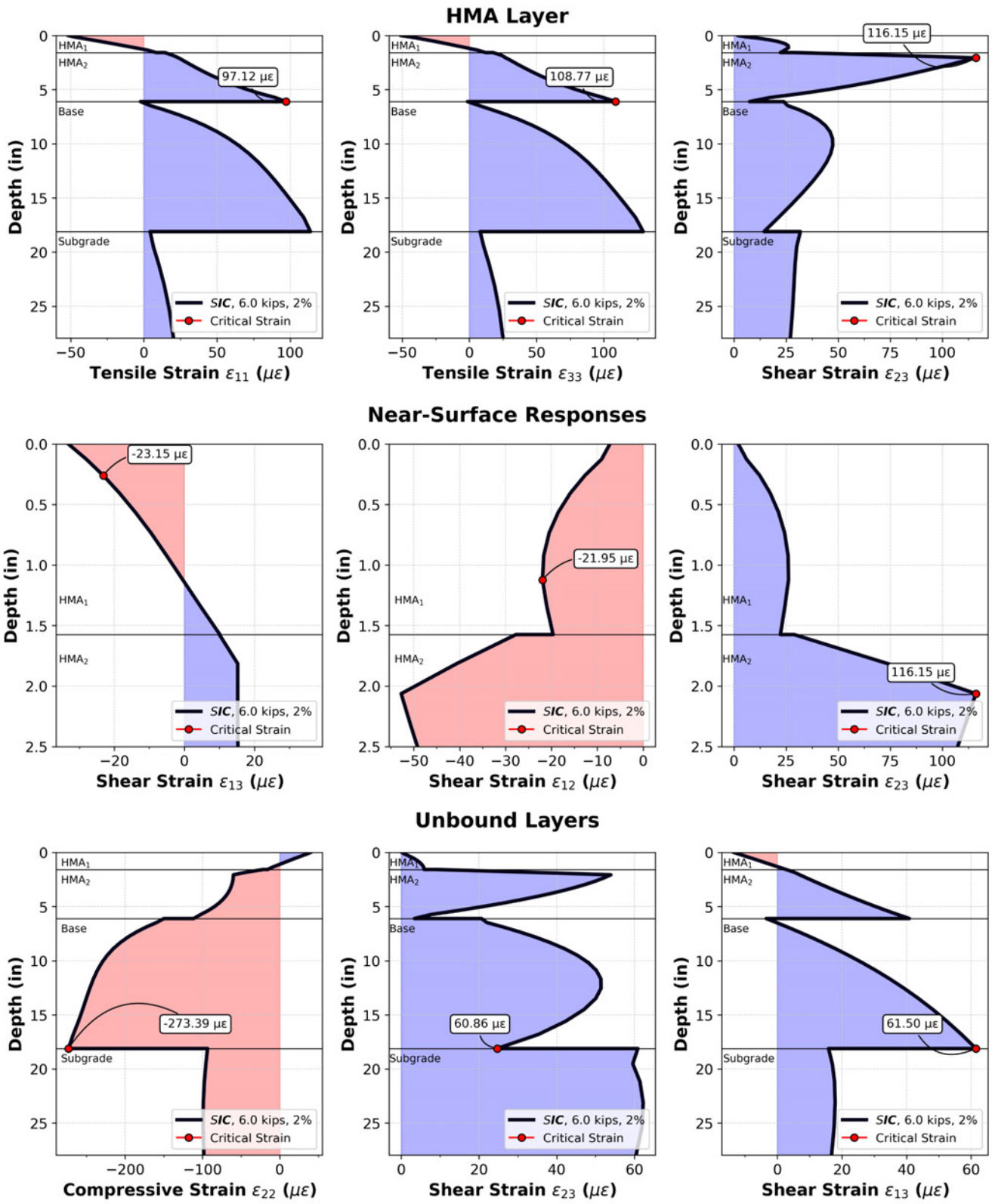

Figure 94. Graph. Summary of pavement responses of typical thick section to a 6-kip steering axle load (P1) at 2% slip ratio.

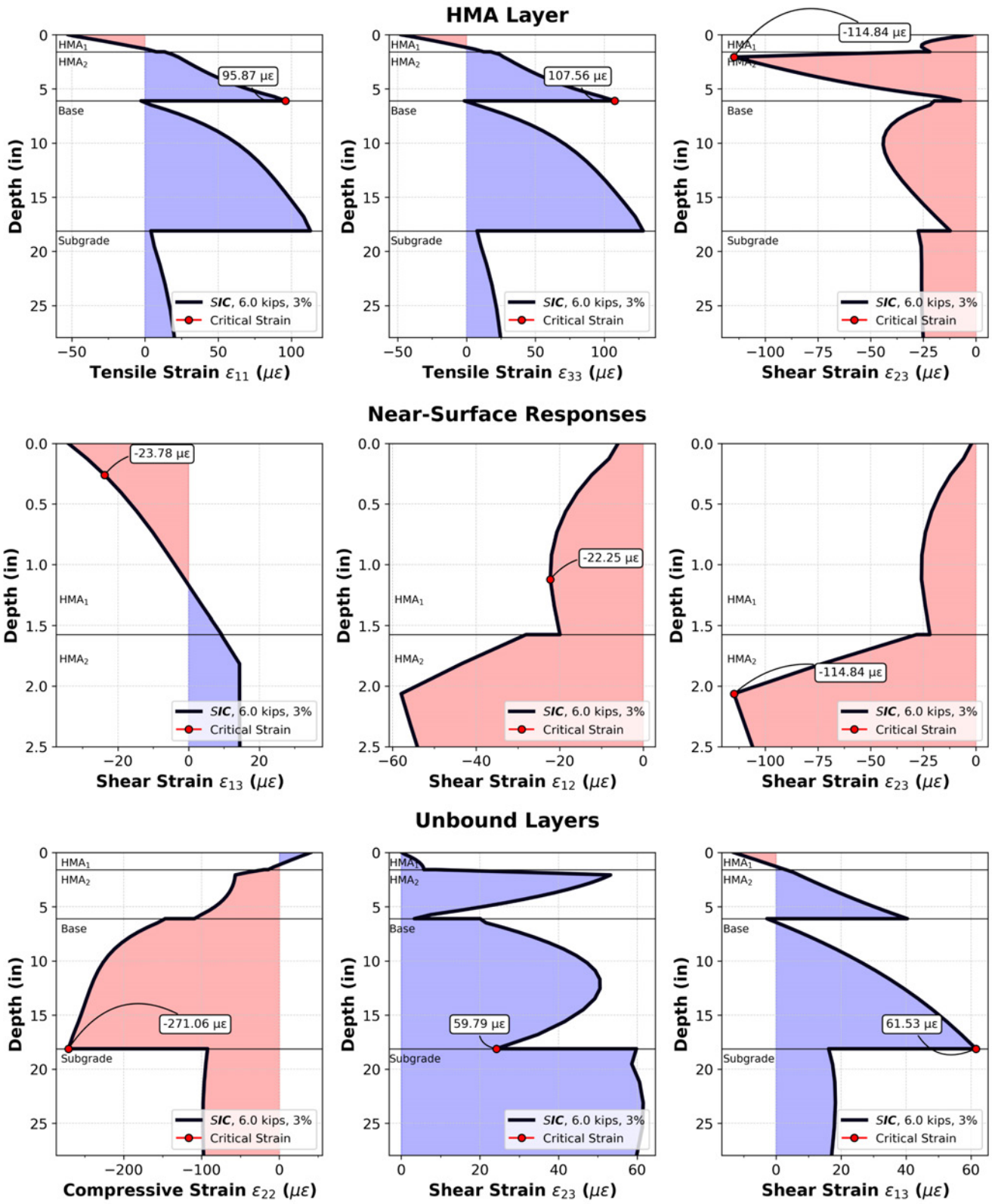

Figure 95. Graph. Summary of pavement responses of typical thick section to a 6-kip steering axle load (P1) at 3% slip ratio.

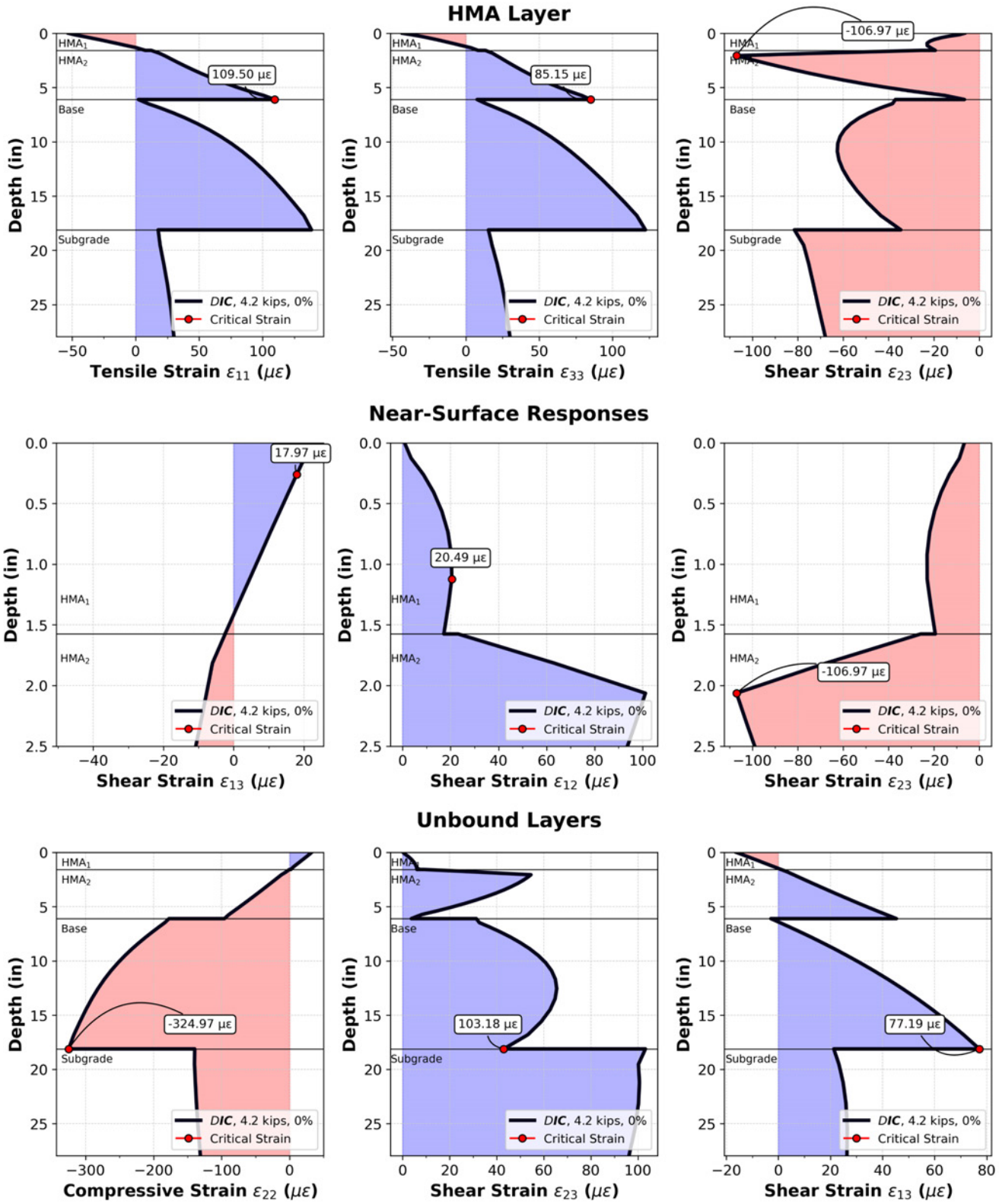

Figure 96. Graph. Summary of pavement responses of typical thick section to a 4.2-kip DTA axle load (P2) at 0% slip ratio.

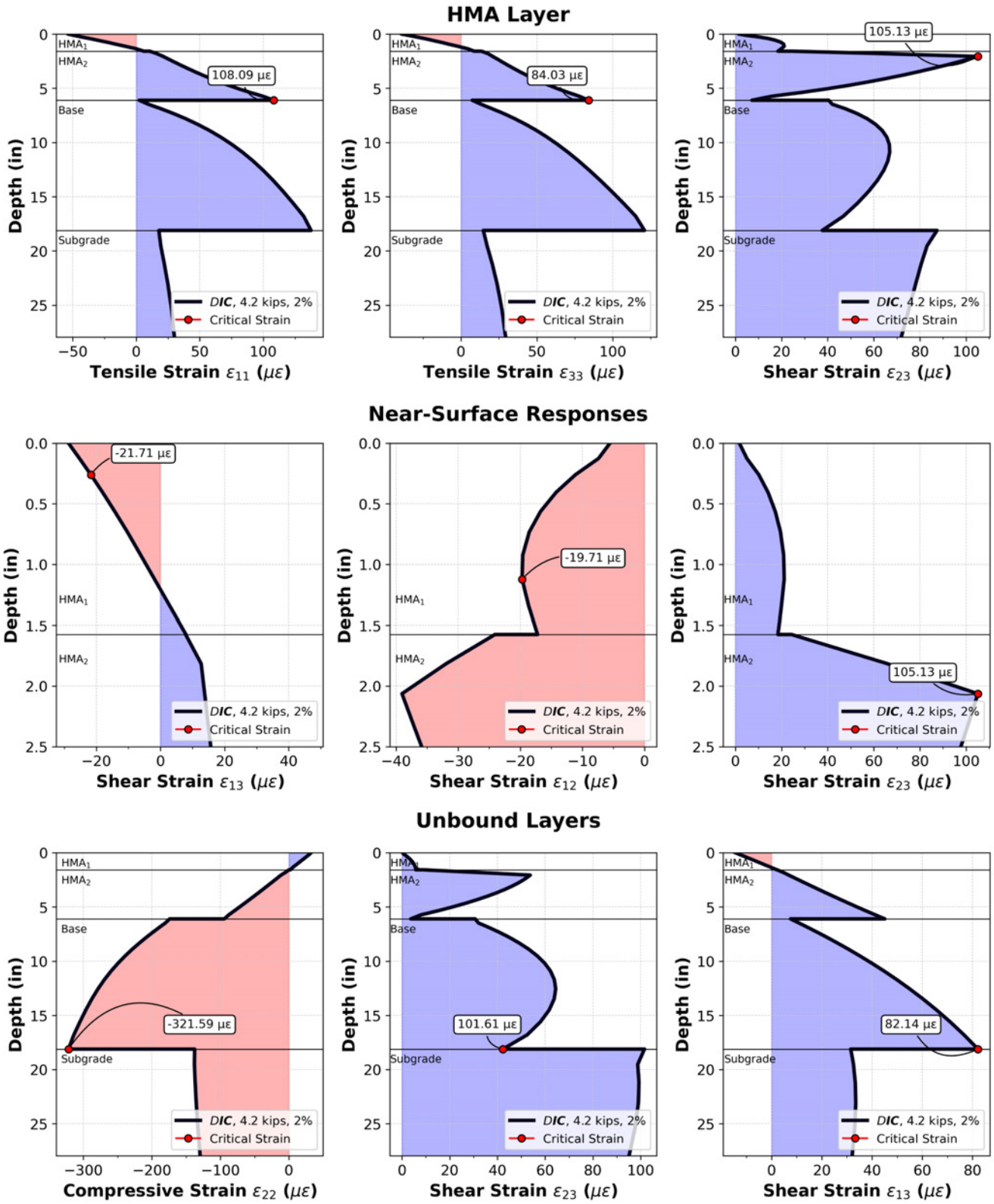

Figure 97. Graph. Summary of pavement responses of full depth section to a 4.2-kip DTA axle load (P2) at 2% slip ratio.

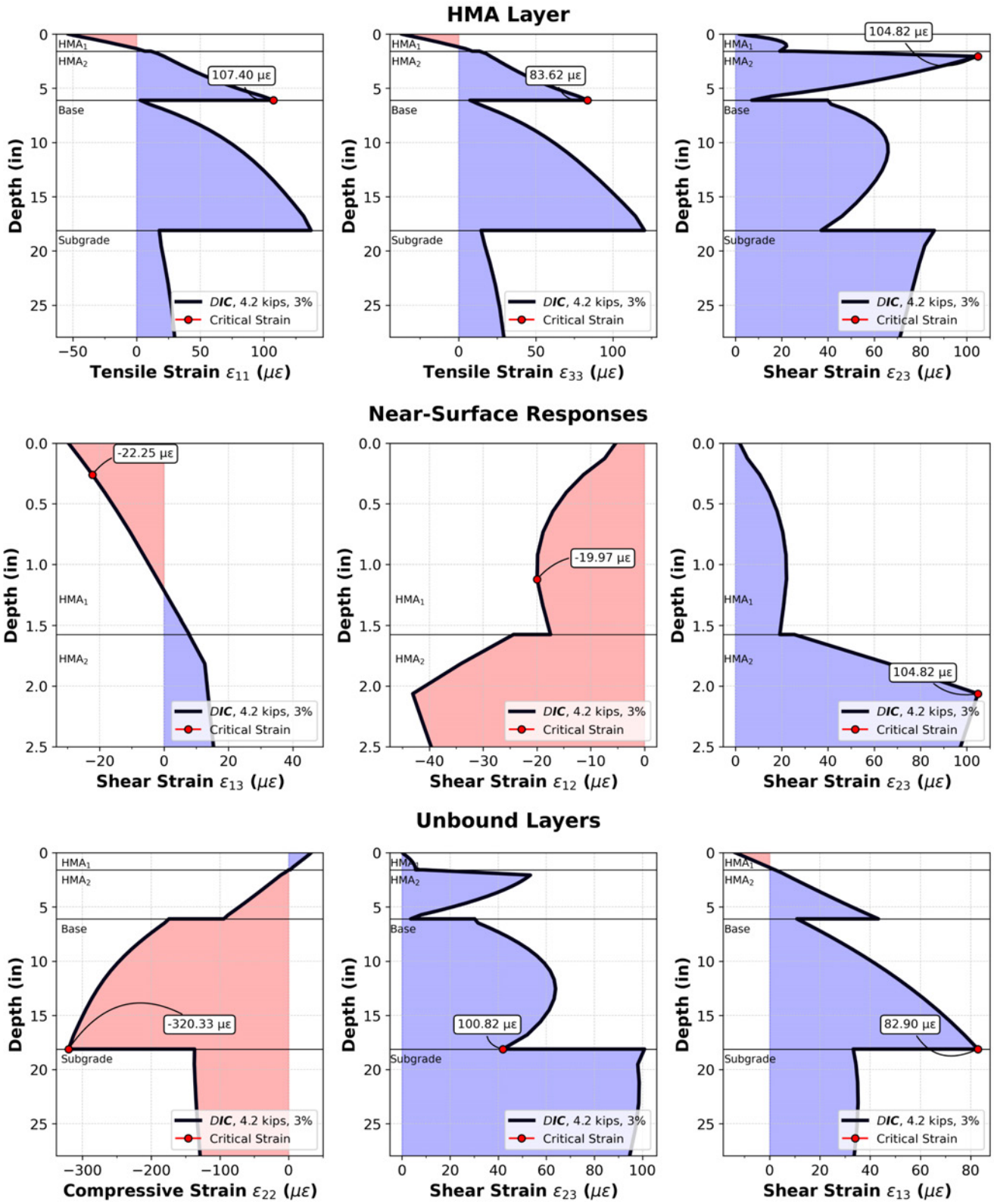

Figure 98. Graph. Summary of pavement responses of typical thick section to a 4.2-kip DTA axle load (P2) at 3% slip ratio.

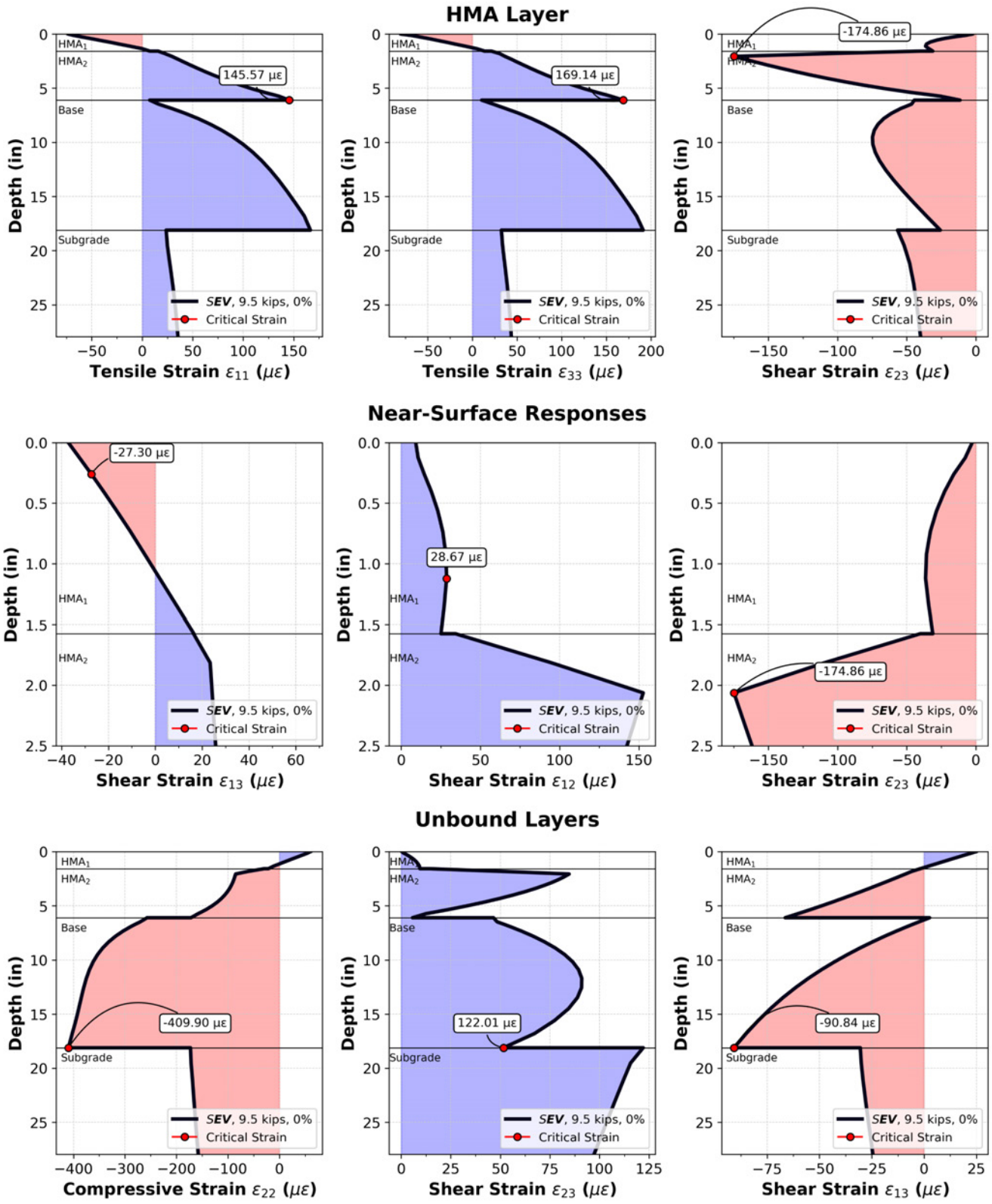

Figure 99. Graph. Summary of pavement responses of typical thick section to a 9.5-kip steering axle load (P3) at 0% slip ratio.

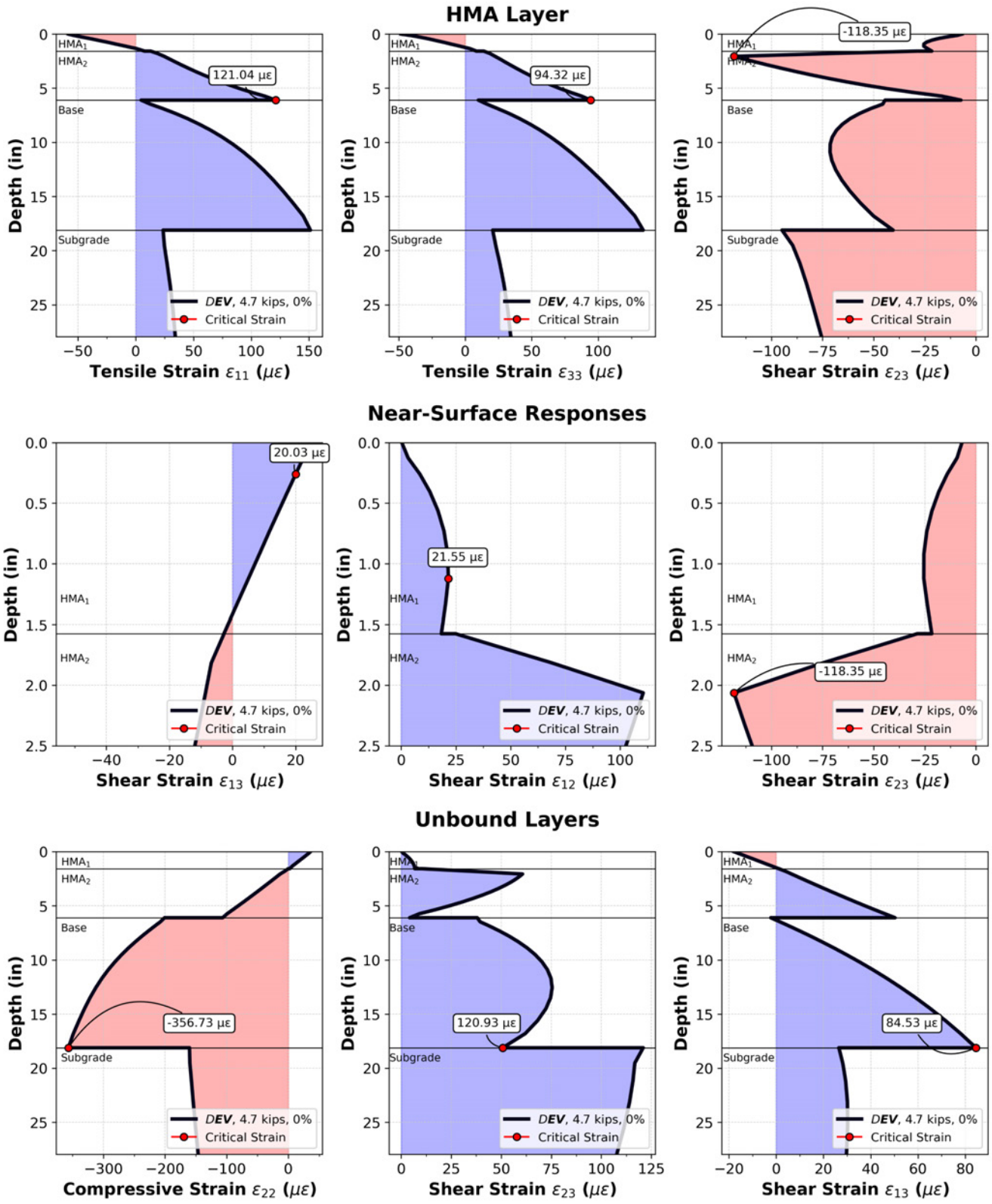

Figure 100. Graph. Summary of pavement responses of typical thick section to a 4.7-kip DTA axle load (P4) at 0% slip ratio.

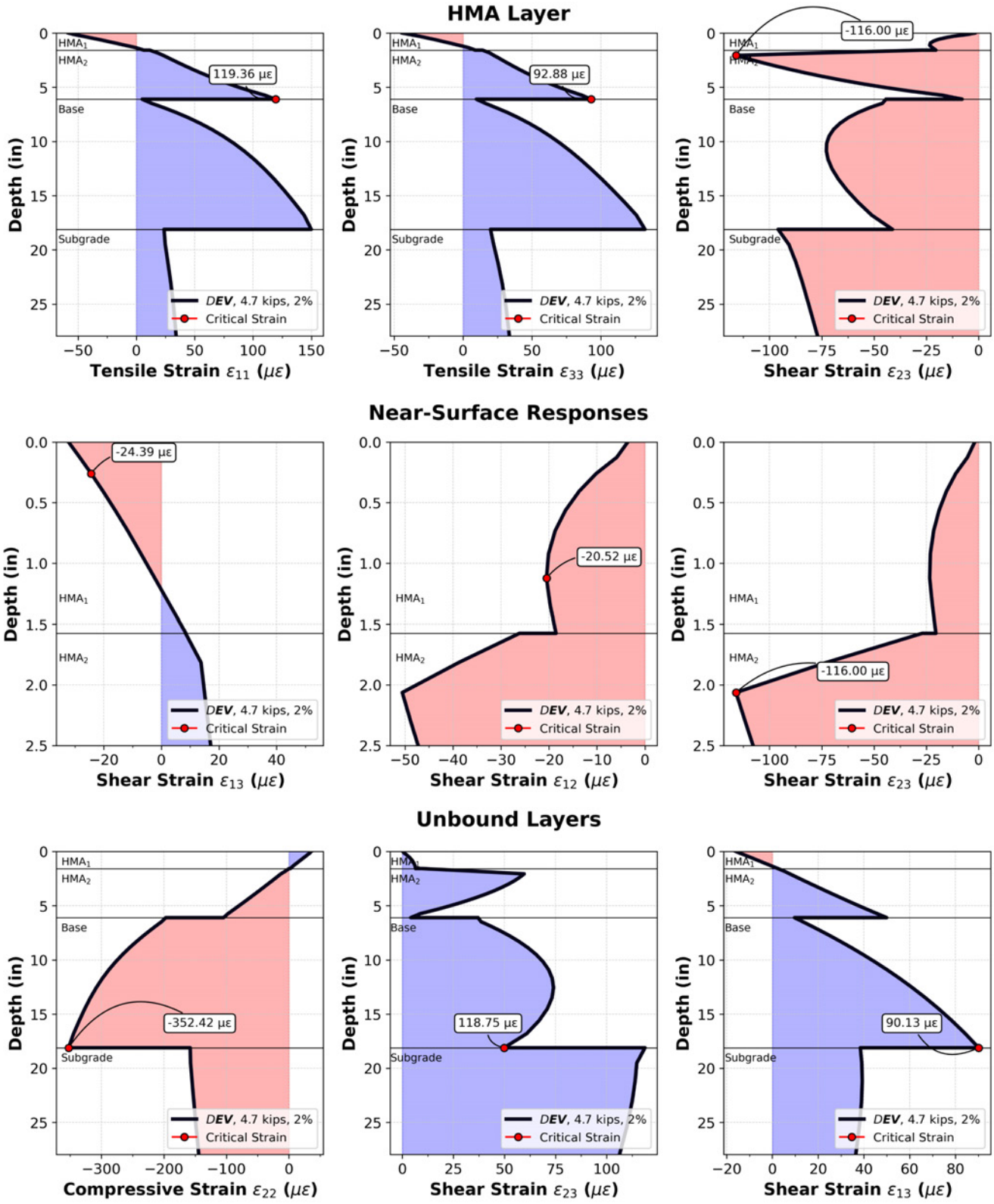

Figure 101. Graph. Summary of pavement responses of typical thick section to a 4.7-kip DTA axle load (P4) at 2% slip ratio.

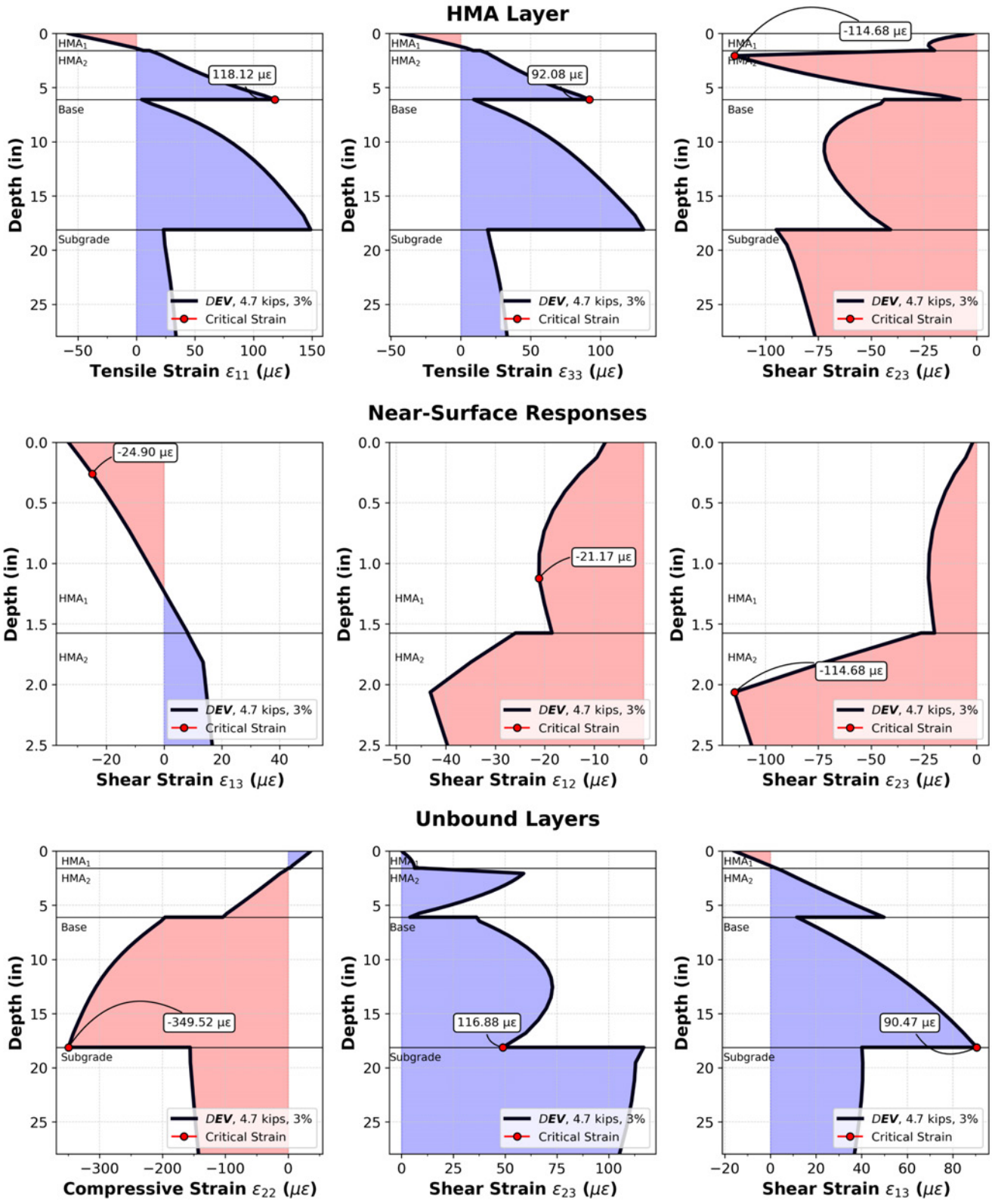

Figure 102. Graph. Summary of pavement responses of typical thick section to a 4.7-kip DTA axle load (P4) at 3% slip ratio.

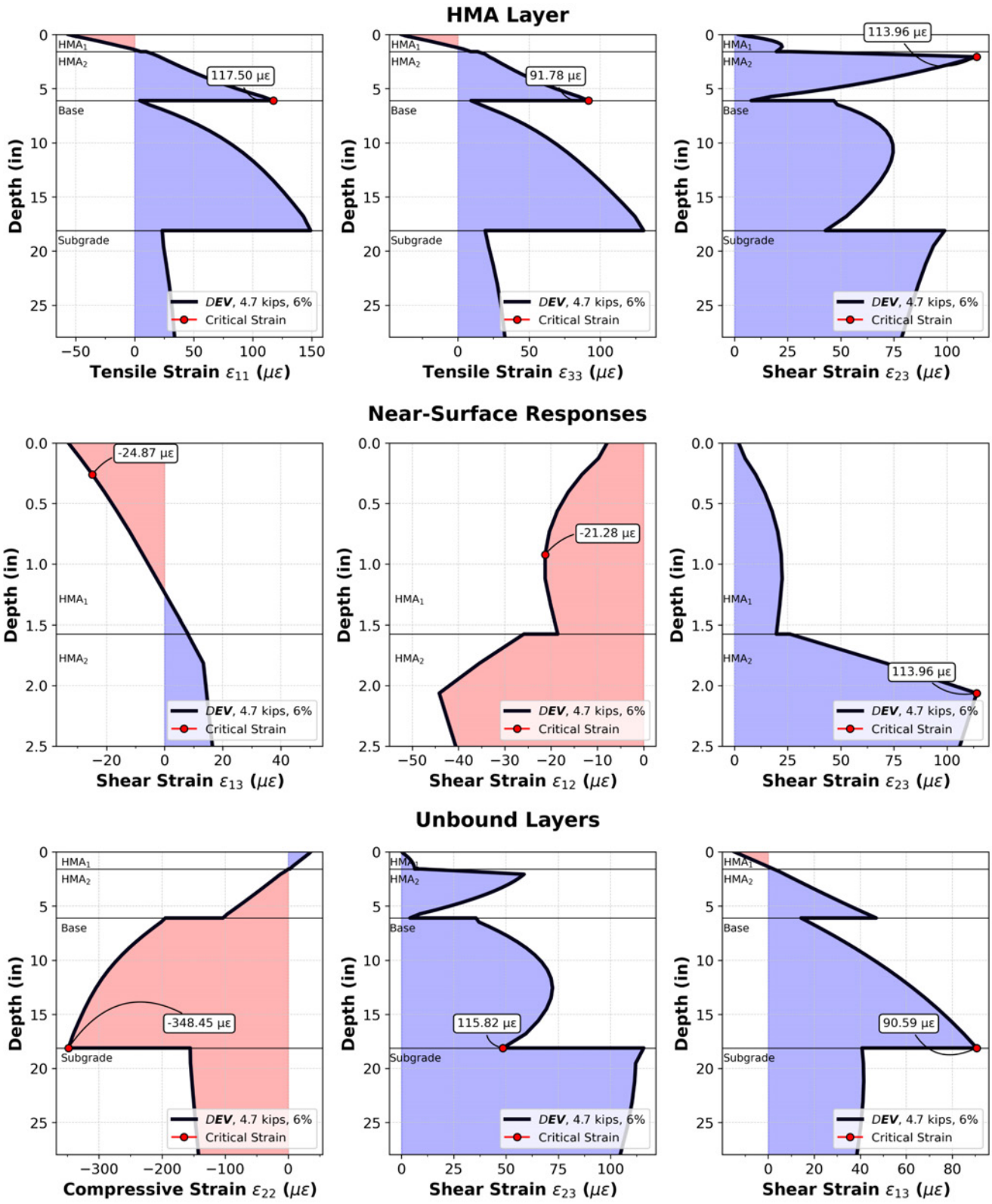

Figure 103. Graph. Summary of pavement responses of typical thick section to a 4.7-kip DTA axle load (P4) at 6% slip ratio.

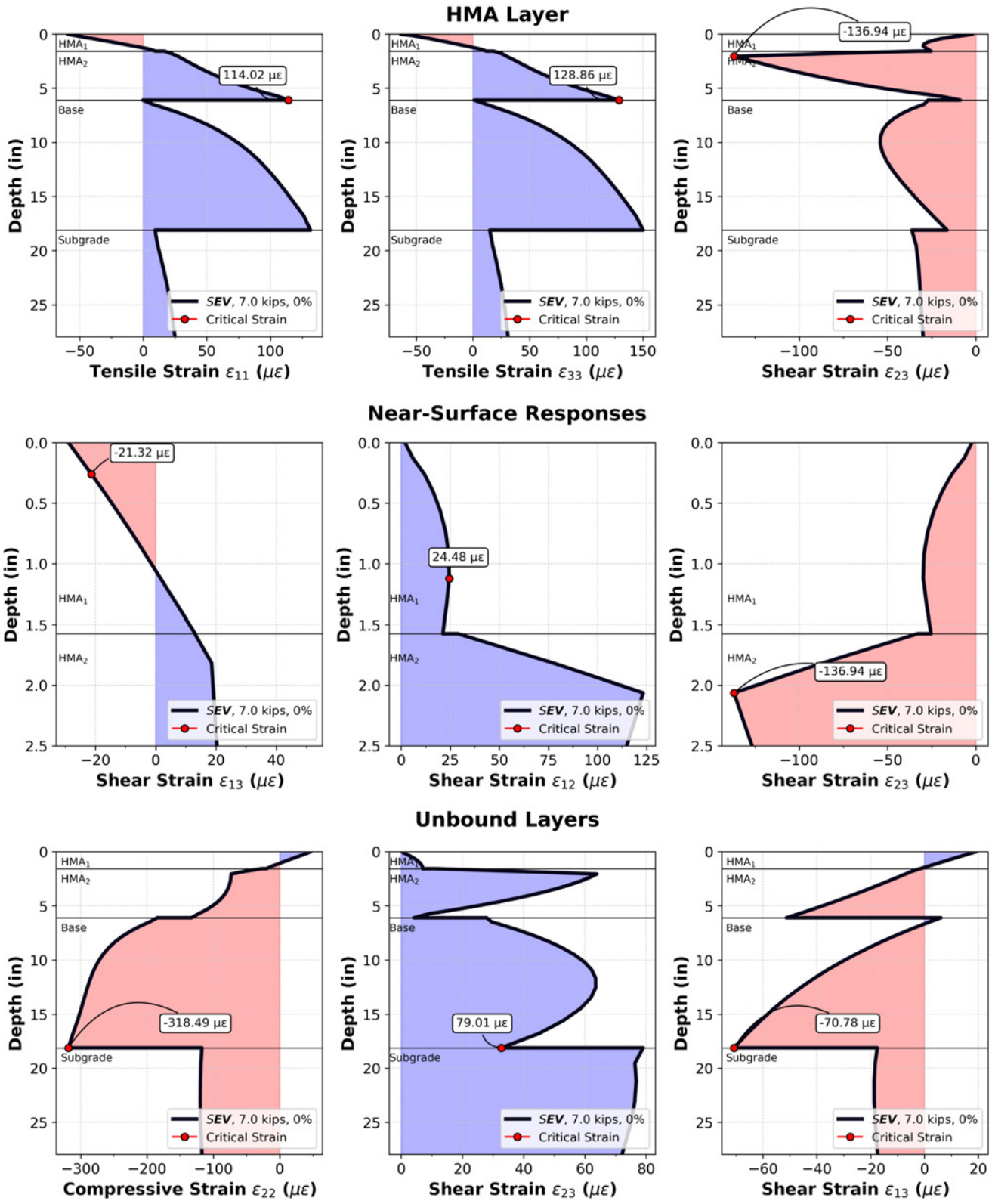

Figure 104. Graph. Summary of pavement responses of typical thick section to a 7.0-kip steering axle load (P5) at 0% slip ratio.

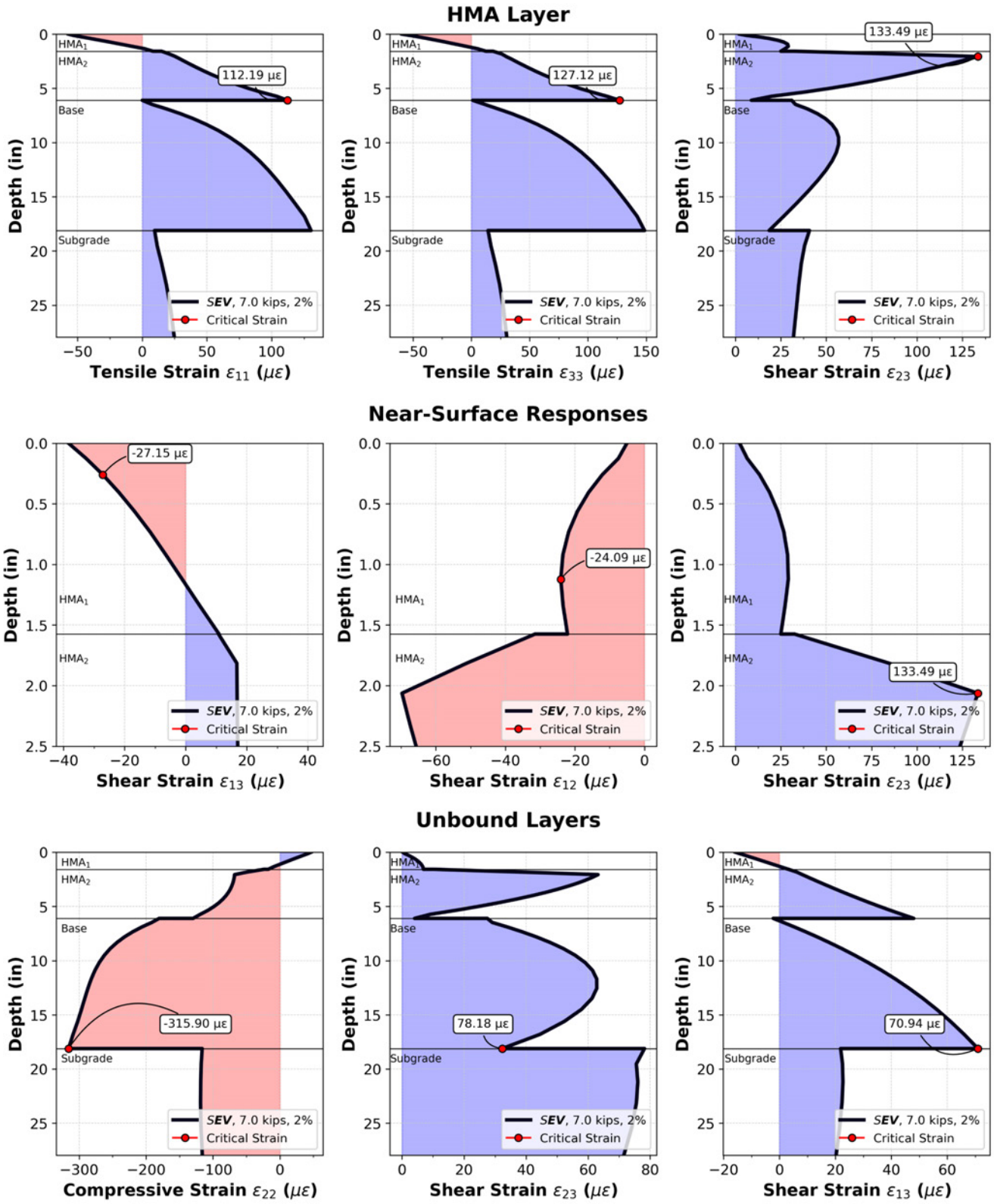

Figure 105. Graph. Summary of pavement responses of typical thick section to a 7.0-kip steering axle load (P5) at 2% slip ratio.

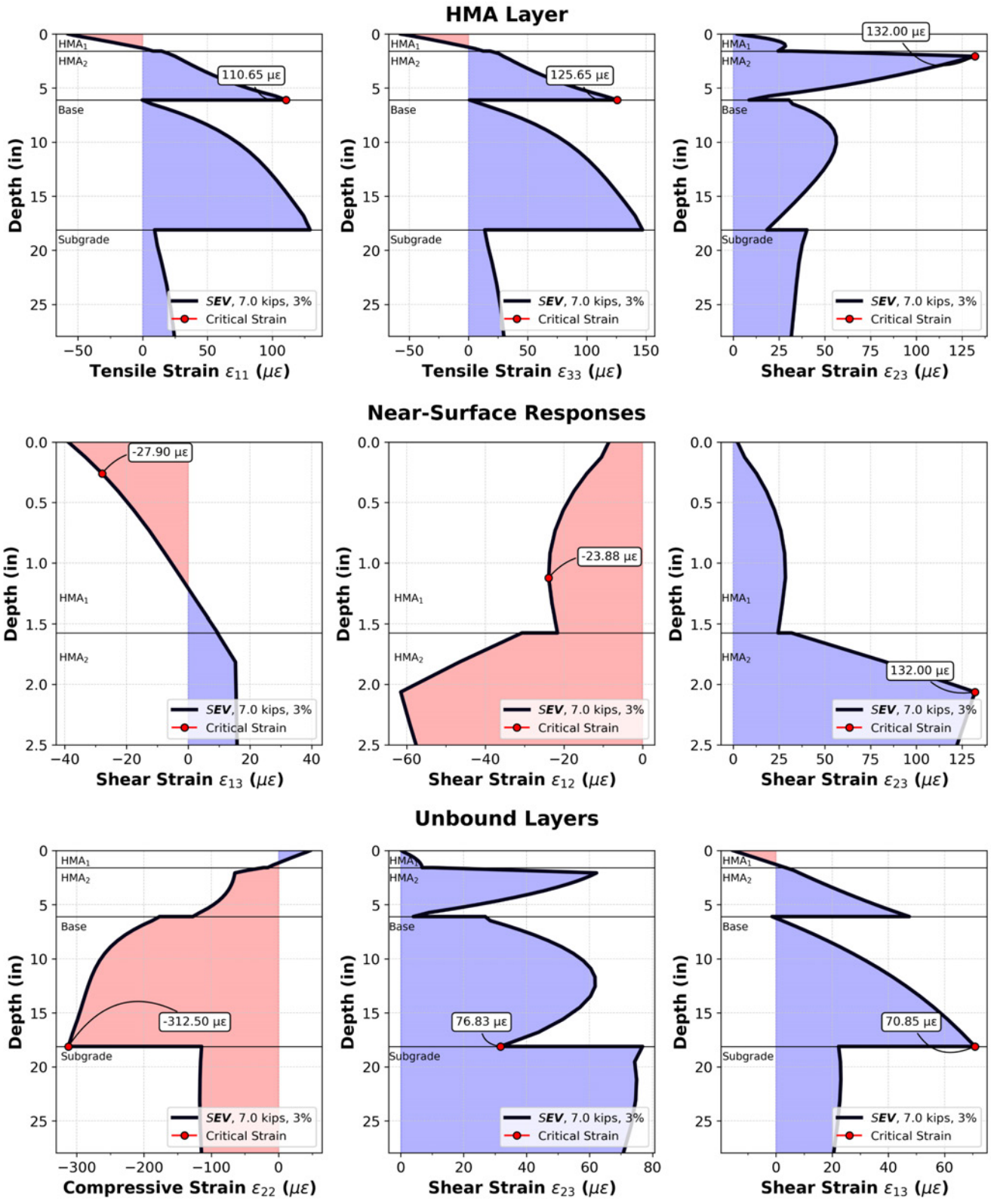

Figure 106. Graph. Summary of pavement responses of typical thick section to a 7.0-kip steering axle load (P5) at 3% slip ratio.

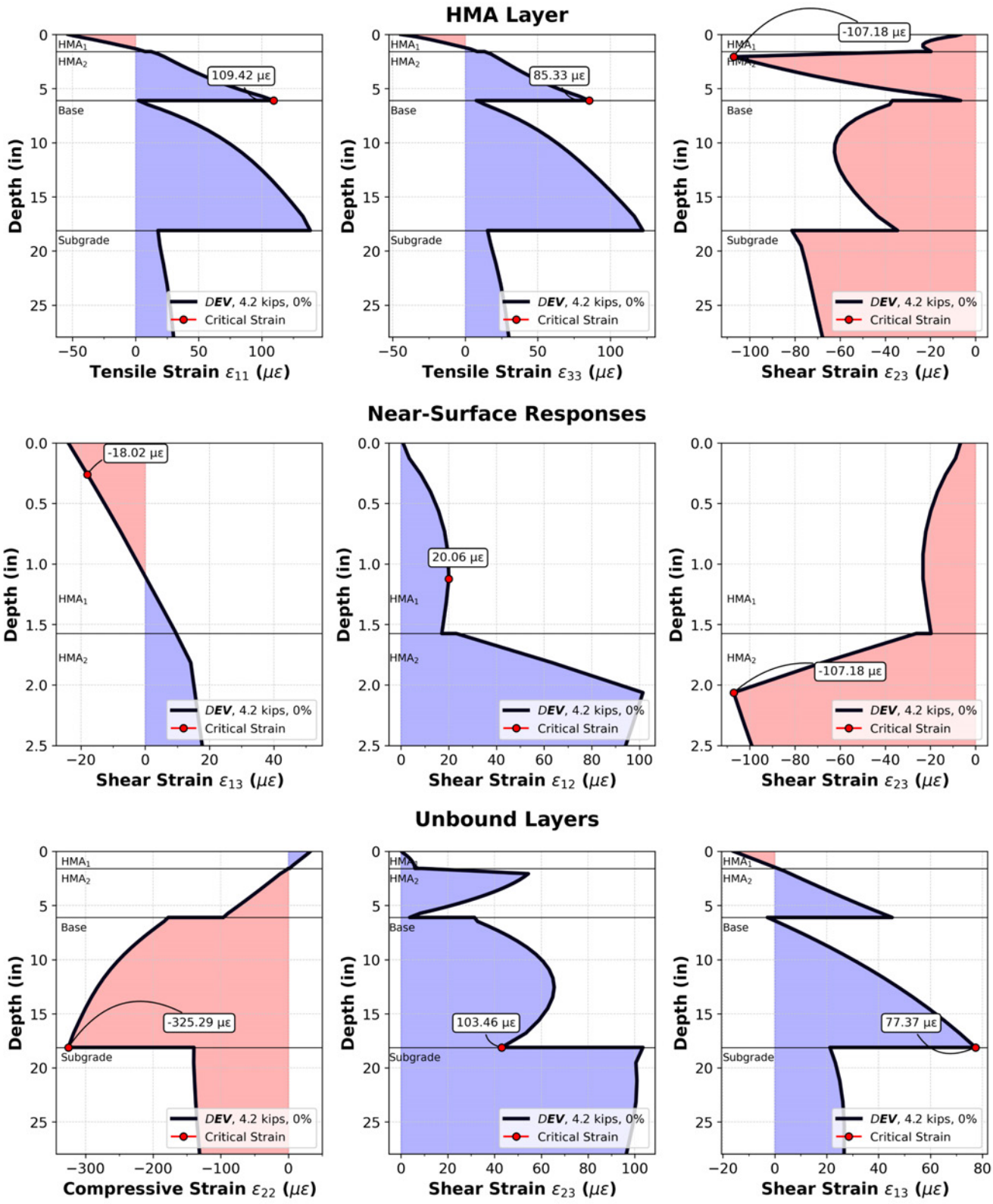

Figure 107. Graph. Summary of pavement responses of typical thick section to a 4.2-kip DTA axle load (P6) at 0% slip ratio.

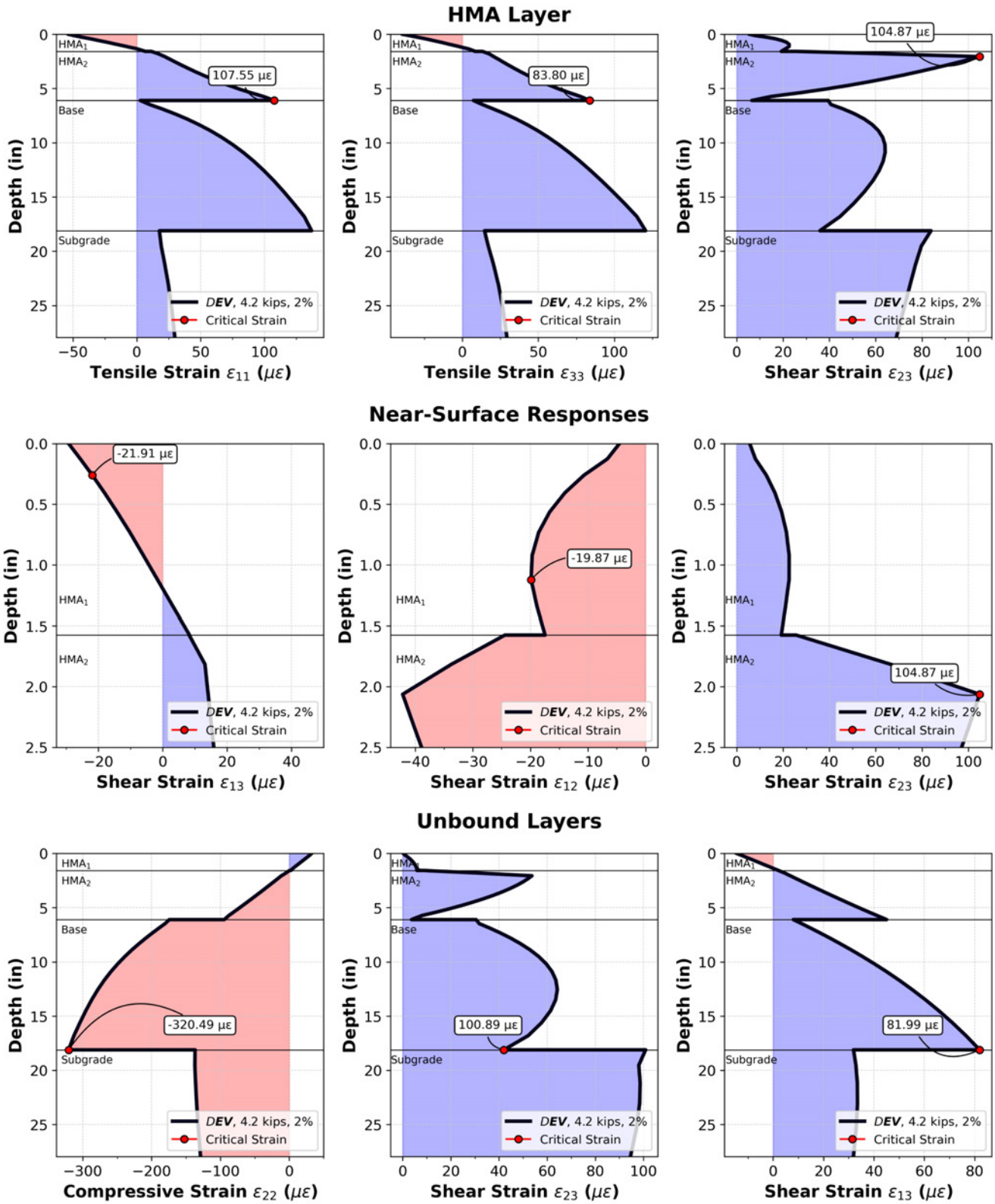

Figure 108. Graph. Summary of pavement responses of typical thick section to a 4.2-kip DTA axle load (P6) at 2% slip ratio.

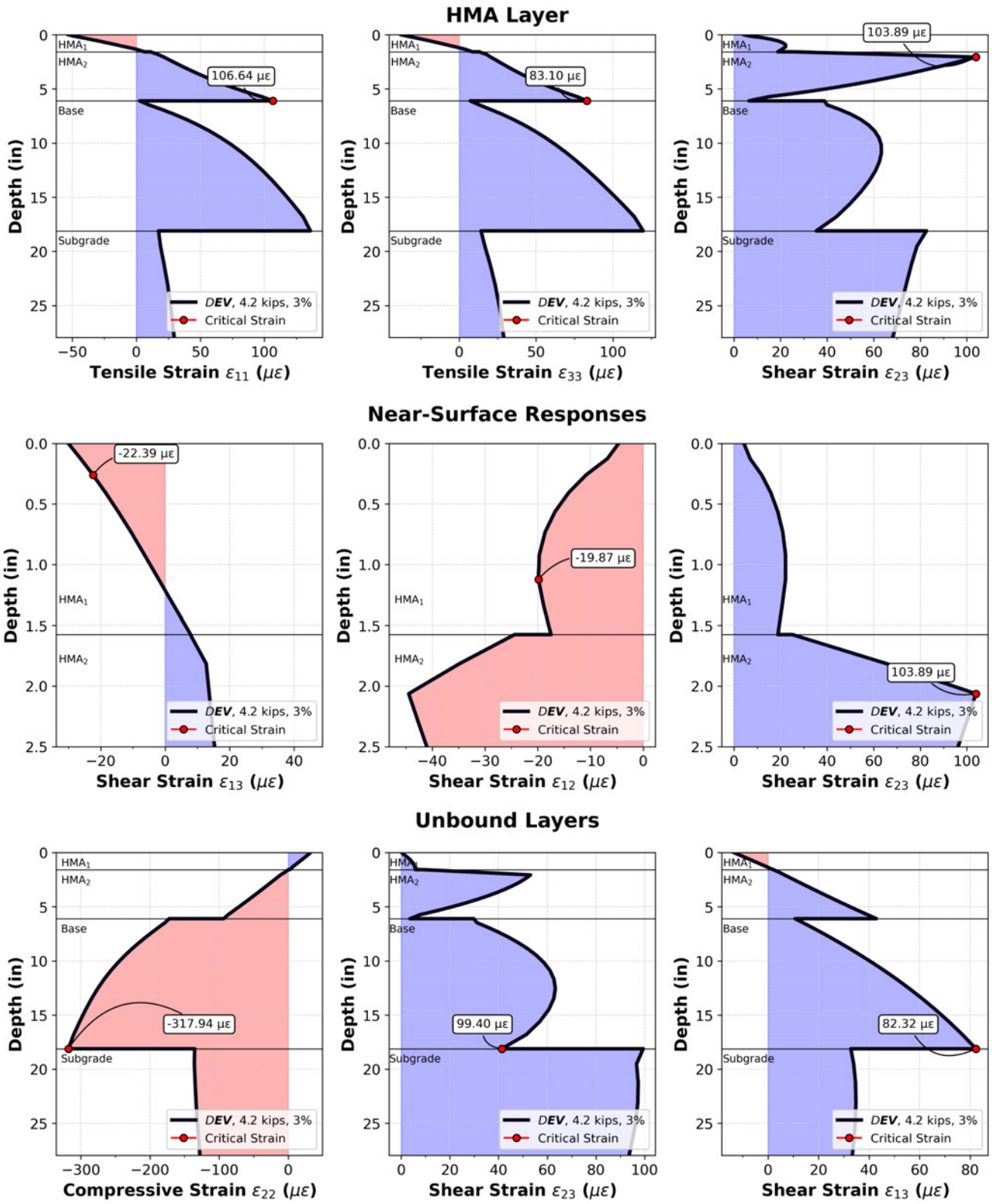

Figure 109. Graph. Summary of pavement responses of typical thick section to a 4.2-kip DTA axle load (P6) at 3% slip ratio.

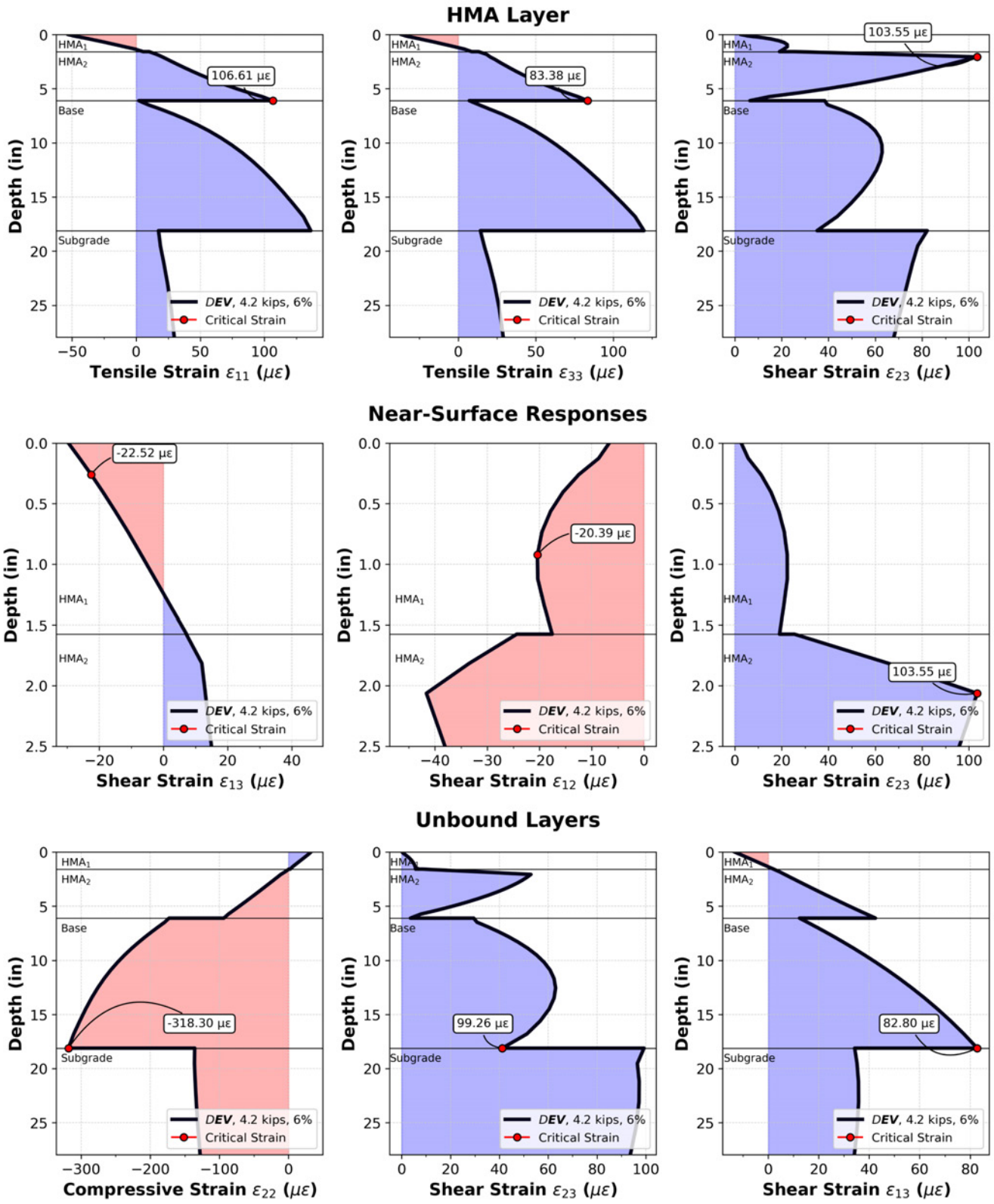

Figure 110. Graph. Summary of pavement responses of typical thick section to a 4.2-kip DTA axle load (P6) at 6% slip ratio.

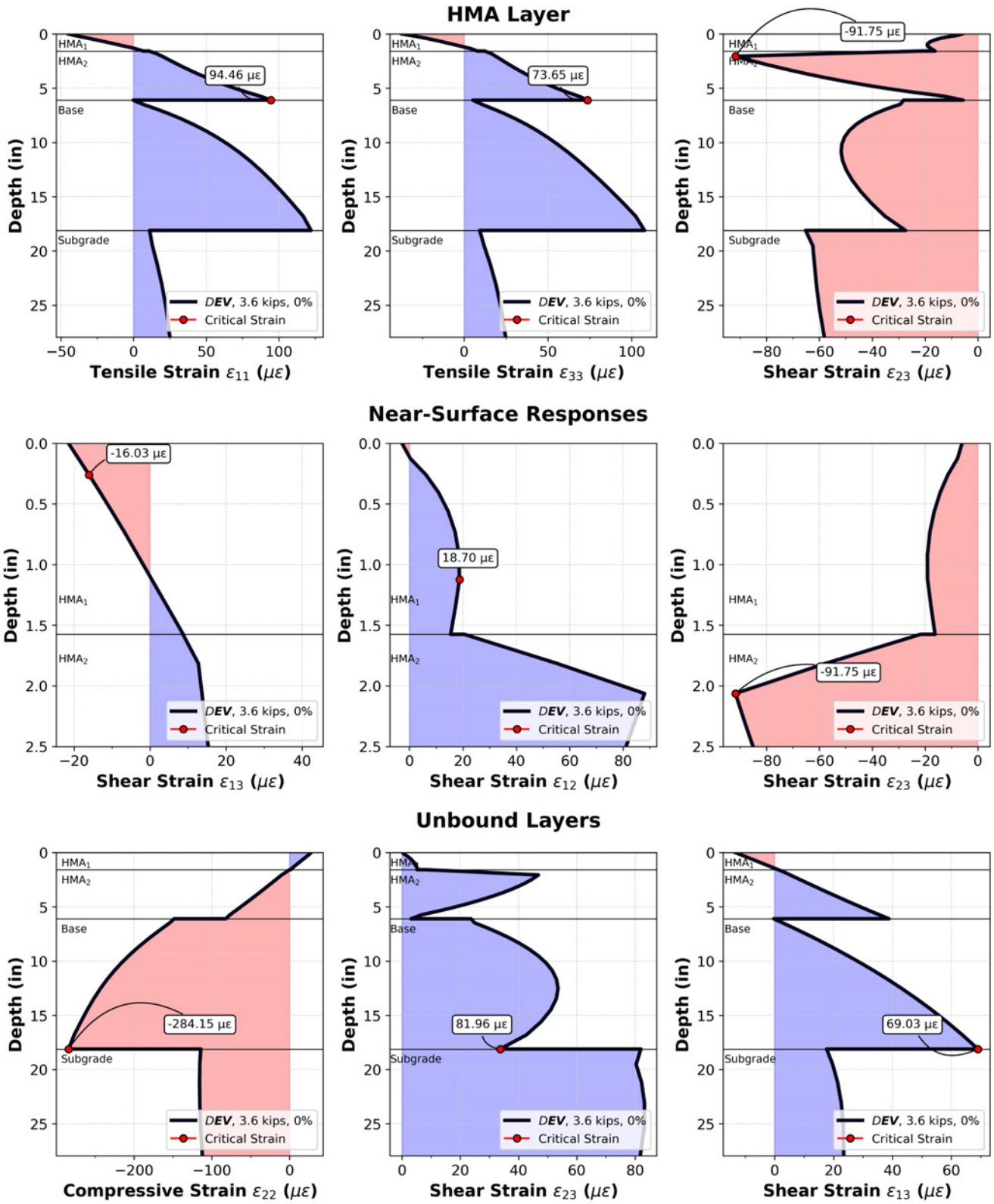

Figure 111. Graph. Summary of pavement responses of typical thick section to a 3.6-kip DTA axle load (P7) at 0% slip ratio.

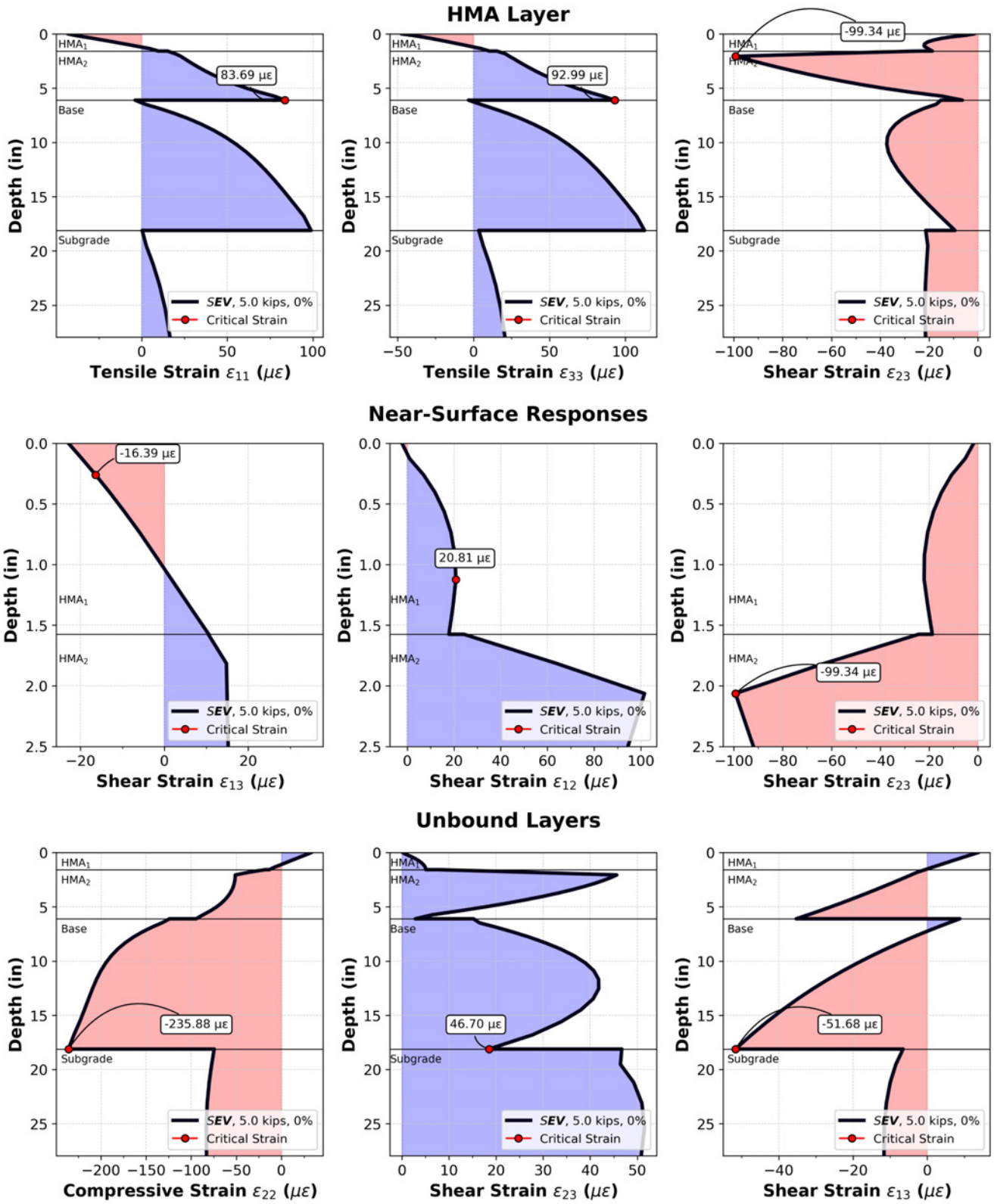

Figure 112. Graph. Summary of pavement responses of typical thick section to a 5.0-kip steering axle load (P8) at 0% slip ratio.

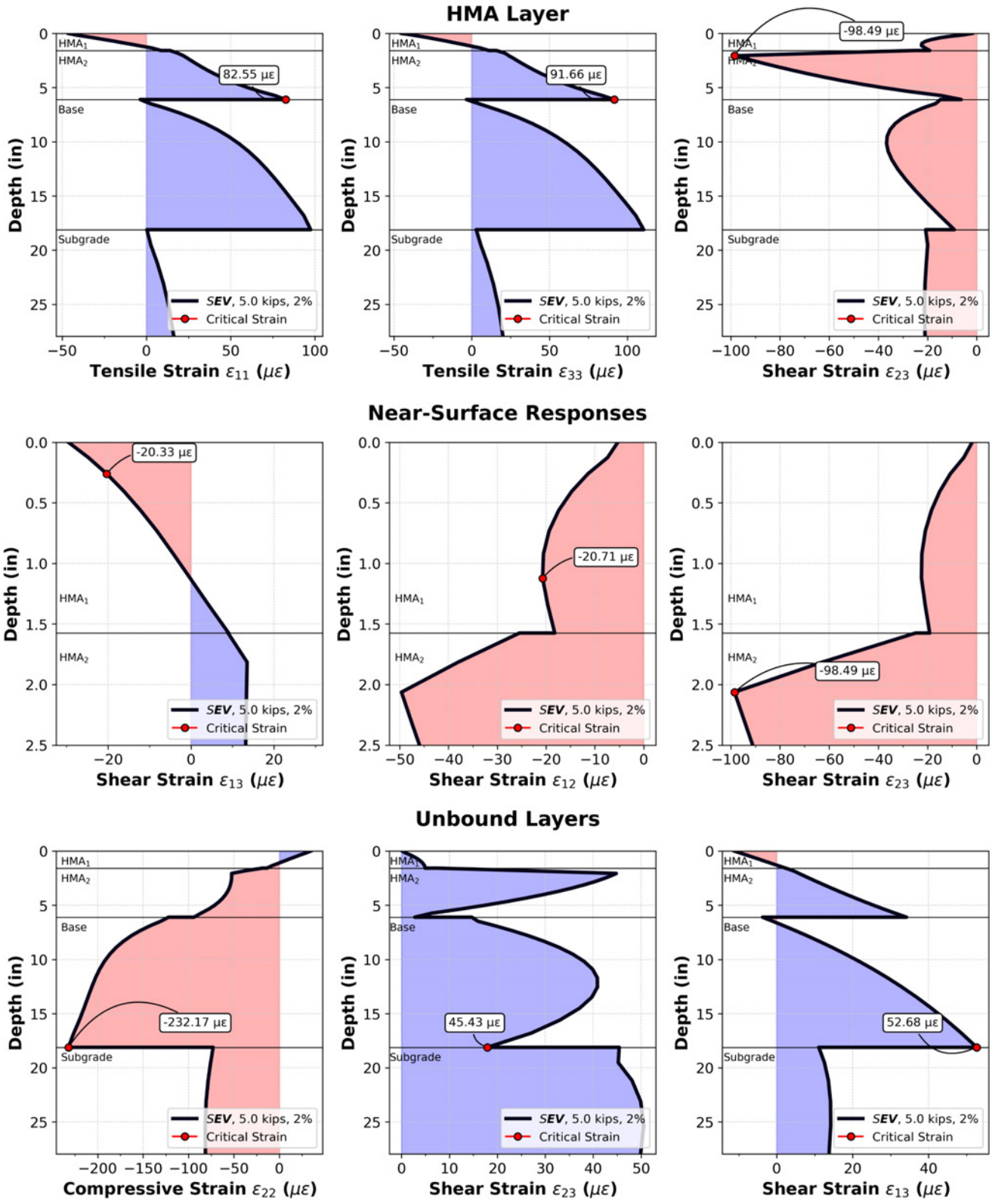

Figure 113. Graph. Summary of pavement responses of typical thick section to a 5.0-kip steering axle load (P8) at 2% slip ratio.

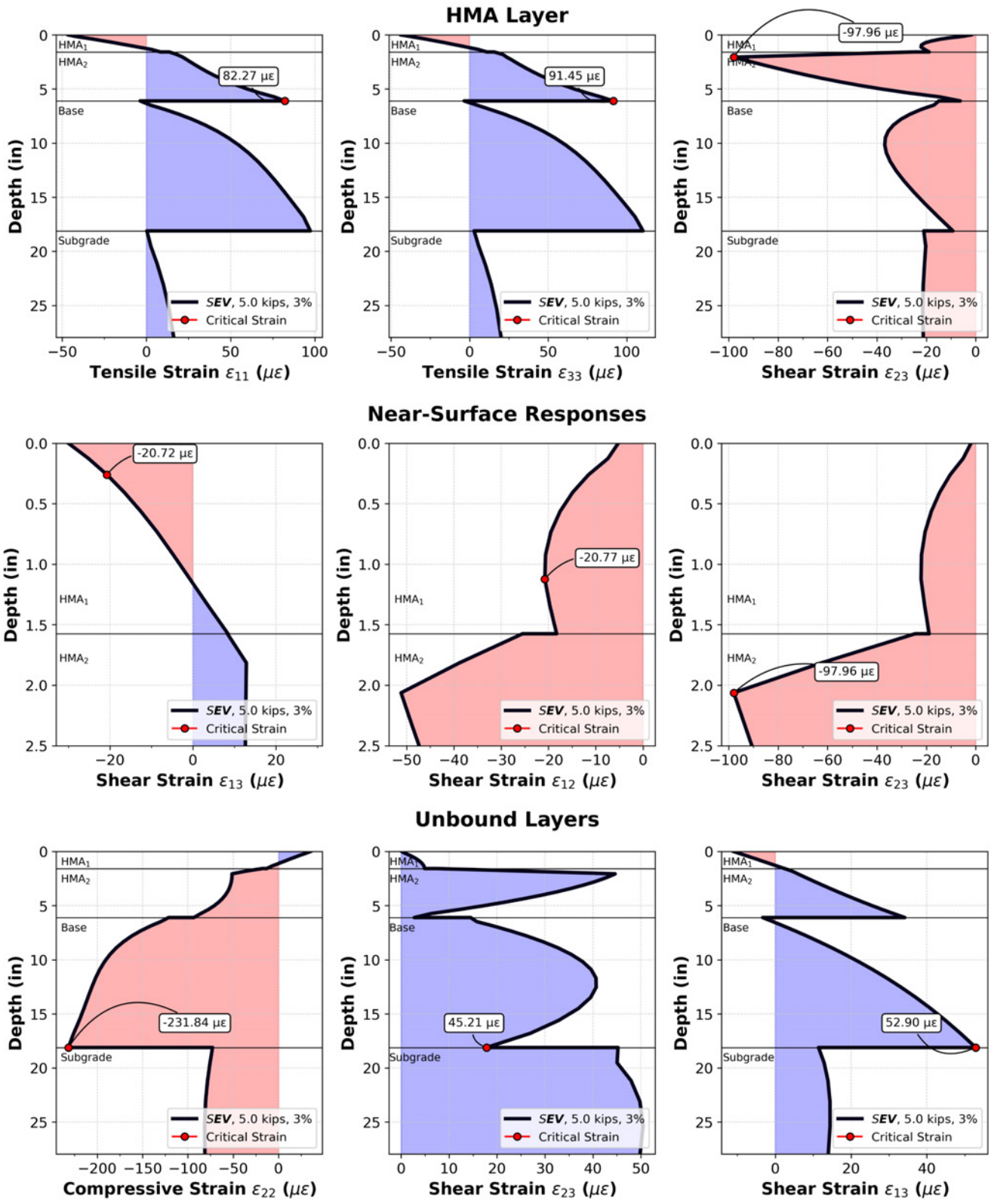

Figure 114. Graph. Summary of pavement responses of typical thick section to a 5.0-kip steering axle load (P8) at 3% slip ratio.

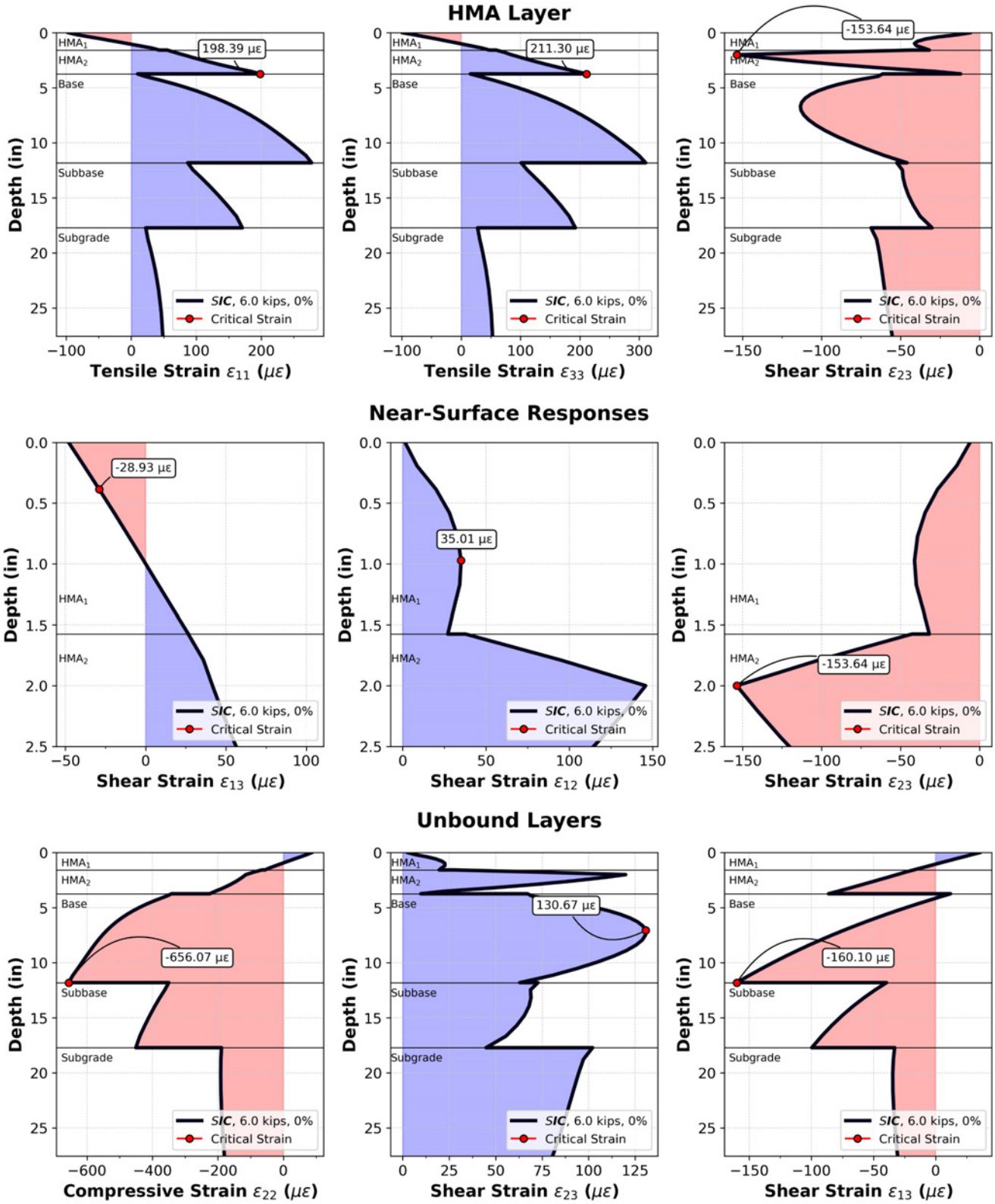

Figure 115. Graph. Summary of pavement responses of low volume section to a 6-kip steering axle load (P1) at 0% slip ratio.

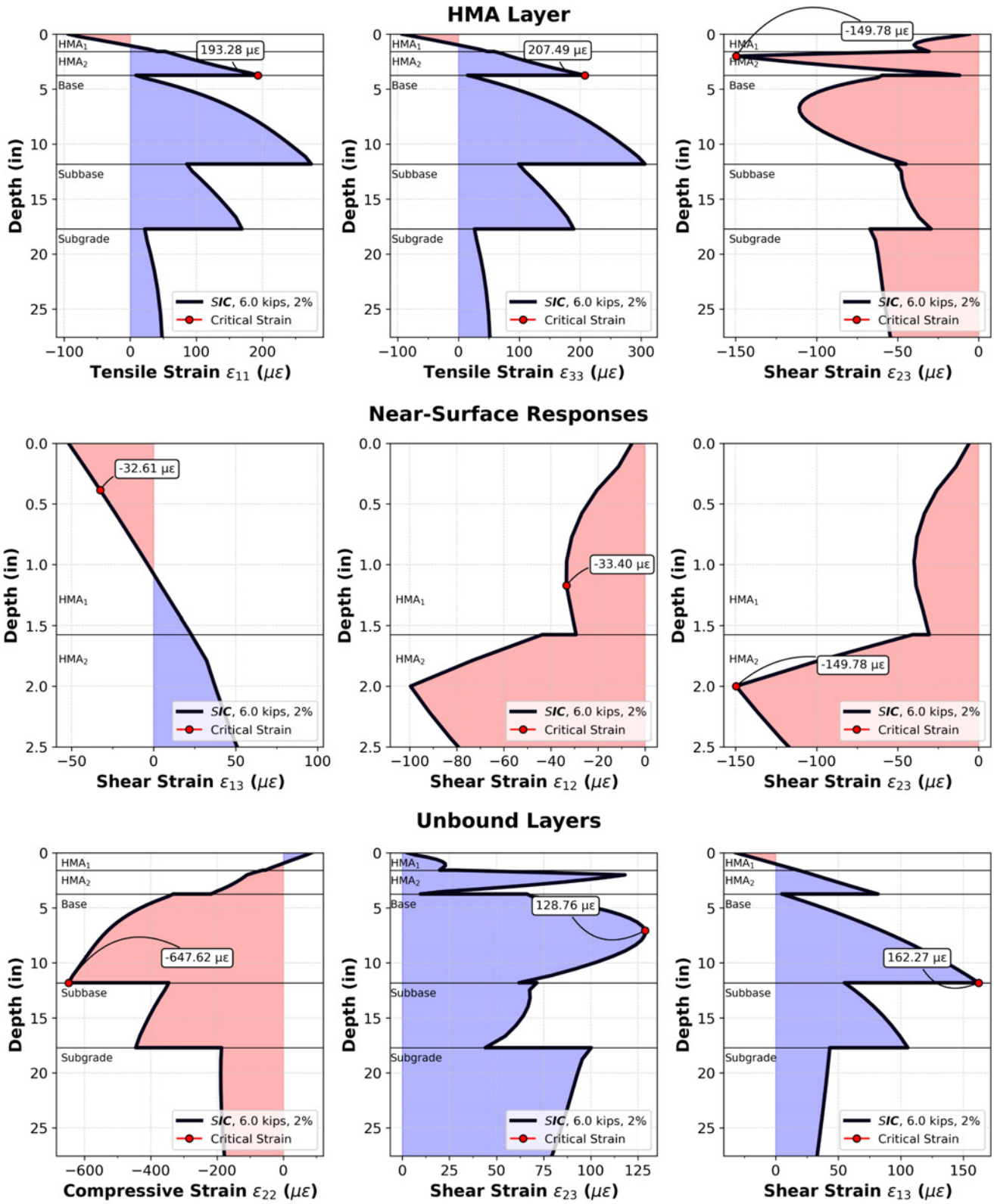

Figure 116. Graph. Summary of pavement responses of low volume section to a 6-kip steering axle load (P1) at 2% slip ratio.

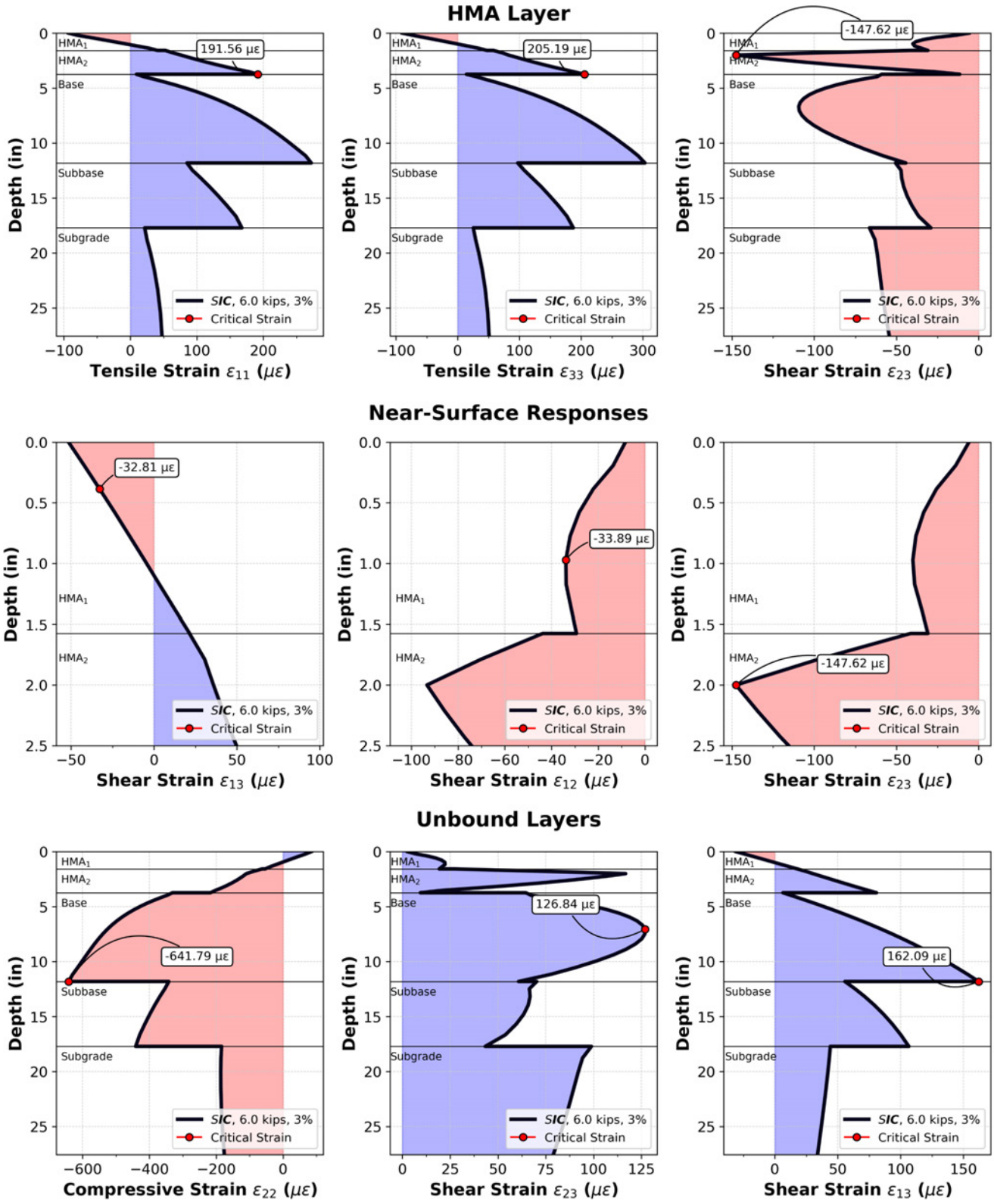

Figure 117. Graph. Summary of pavement responses of low volume section to a 6-kip steering axle load (P1) at 3% slip ratio.

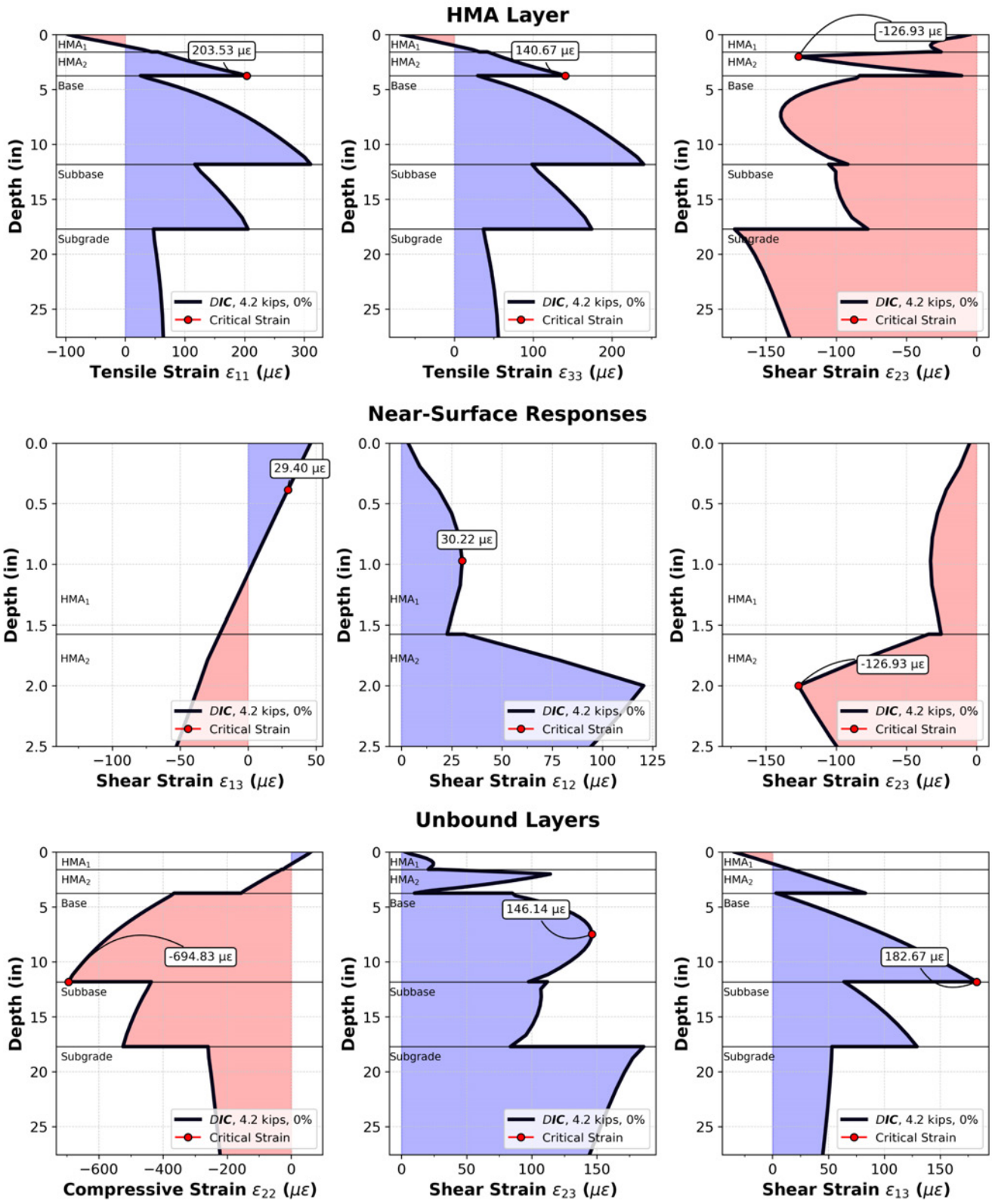

Figure 118. Graph. Summary of pavement responses of low volume section to a 4.2-kip DTA axle load (P2) at 0% slip ratio.

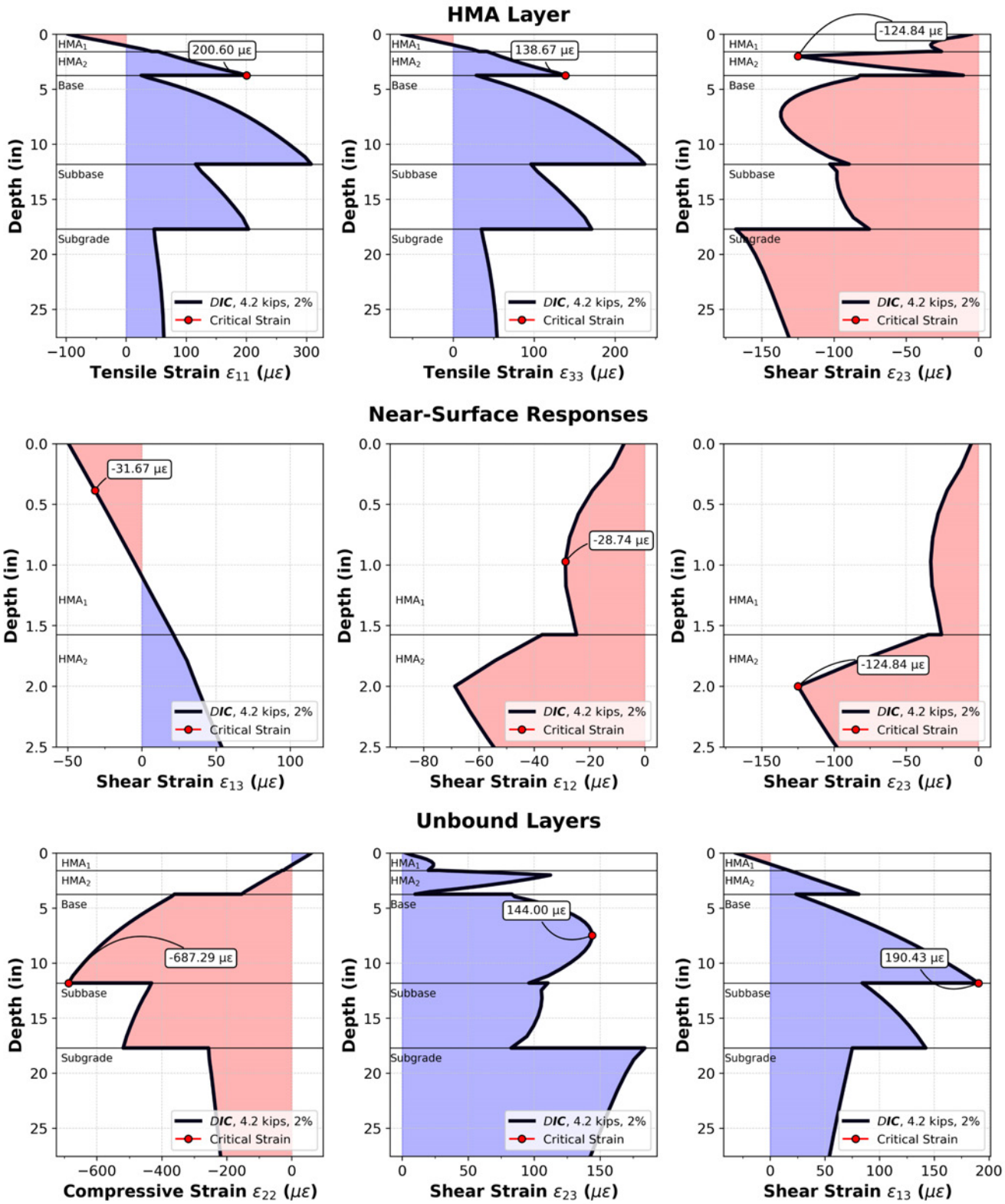

Figure 119. Graph. Summary of pavement responses of low volume section to a 4.2-kip DTA axle load (P2) at 2% slip ratio.

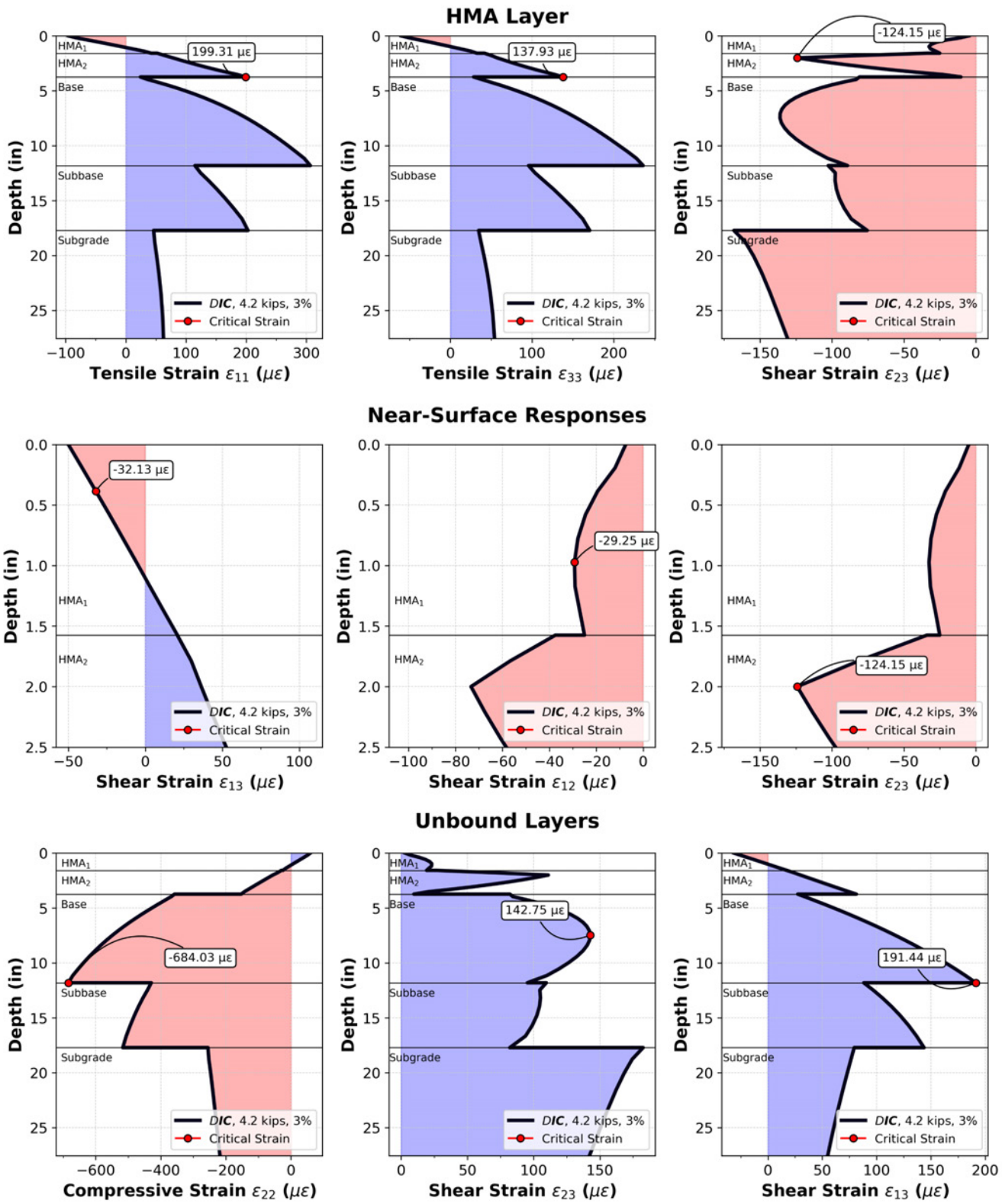

Figure 120. Graph. Summary of pavement responses of low volume section to a 4.2-kip DTA axle load (P2) at 3% slip ratio.

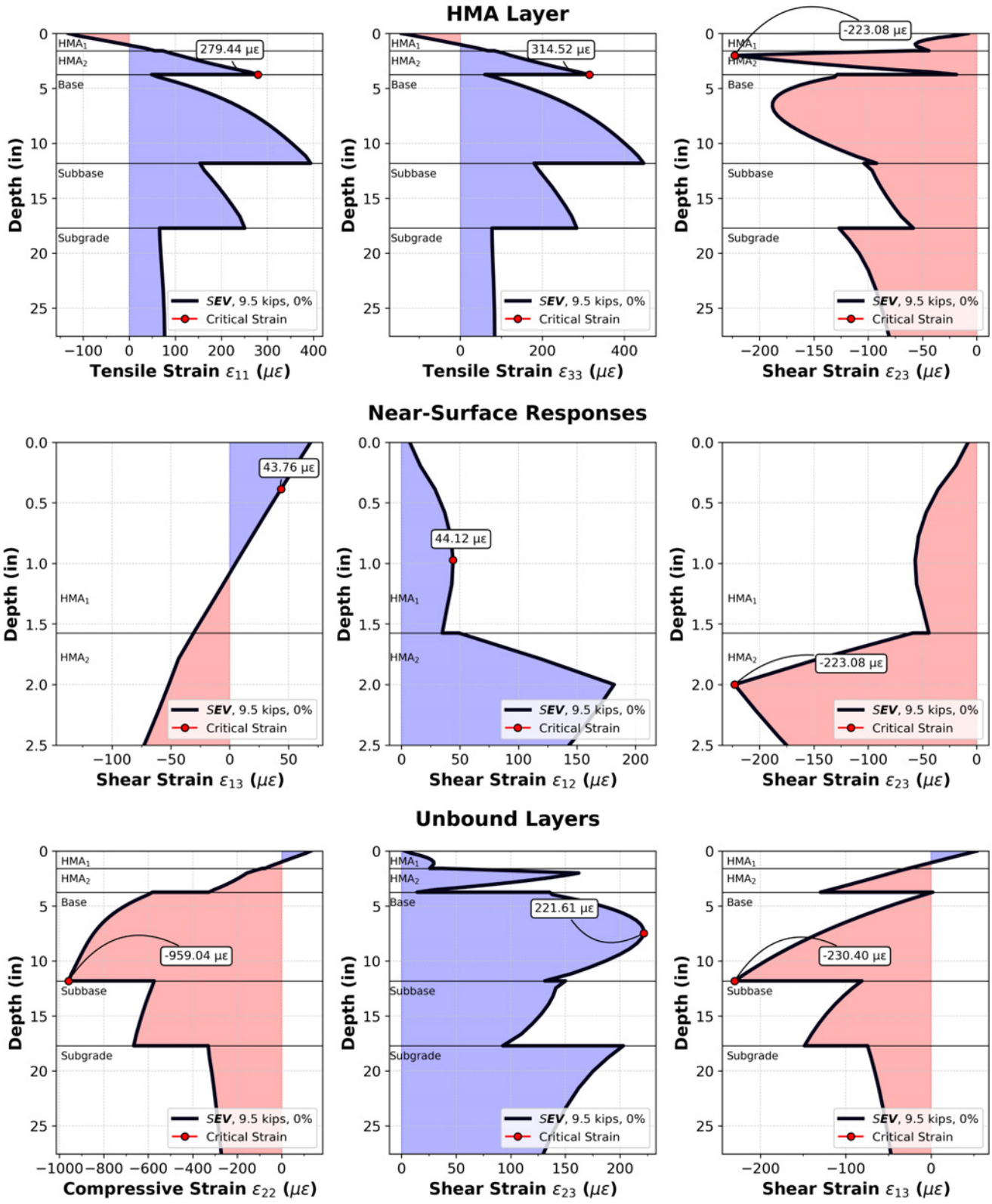

Figure 121. Graph. Summary of pavement responses of low volume section to a 9.5-kip steering axle load (P3) at 0% slip ratio.

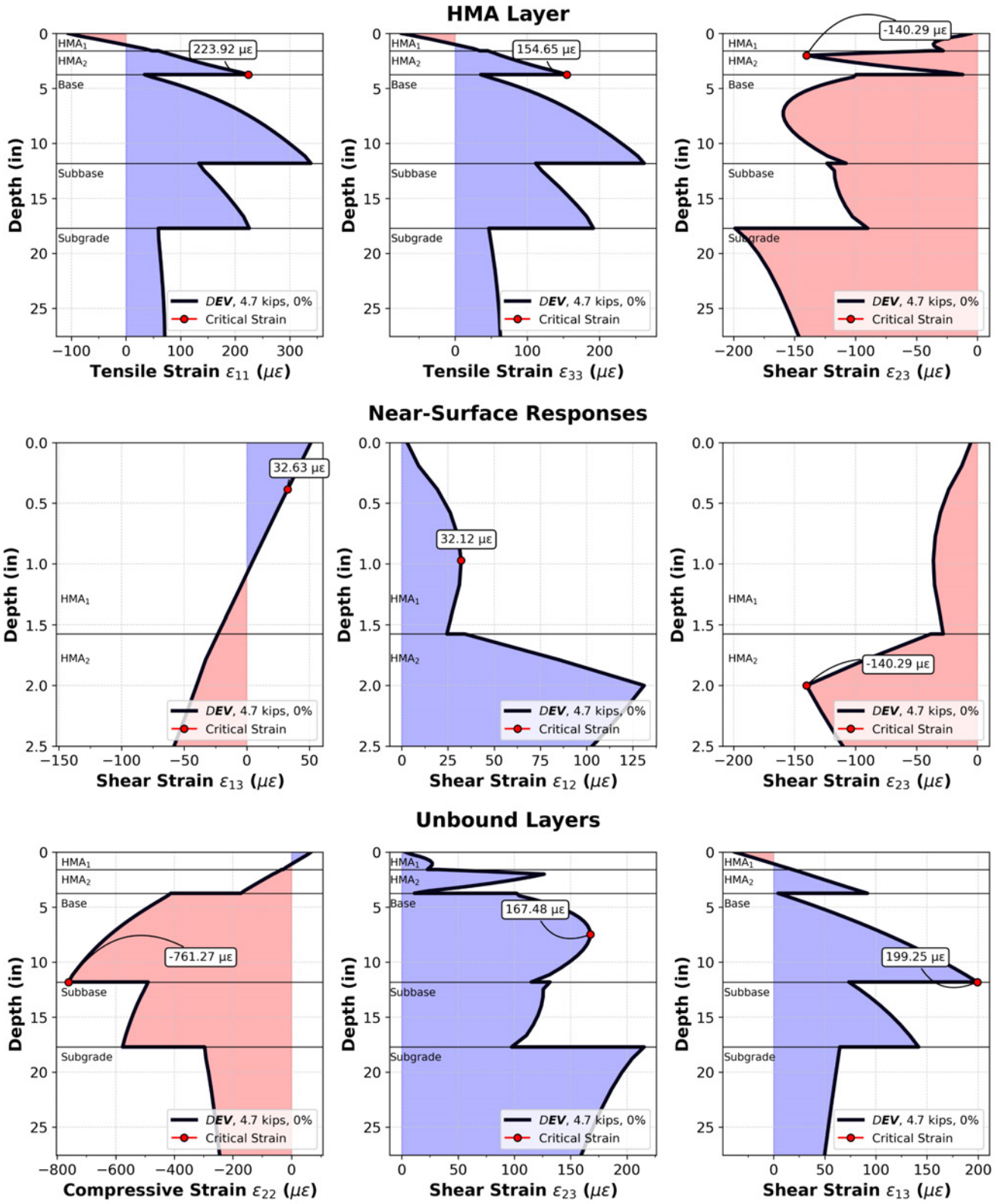

Figure 122. Graph. Summary of pavement responses of low volume section to a 4.7-kip DTA axle load (P4) at 0% slip ratio.

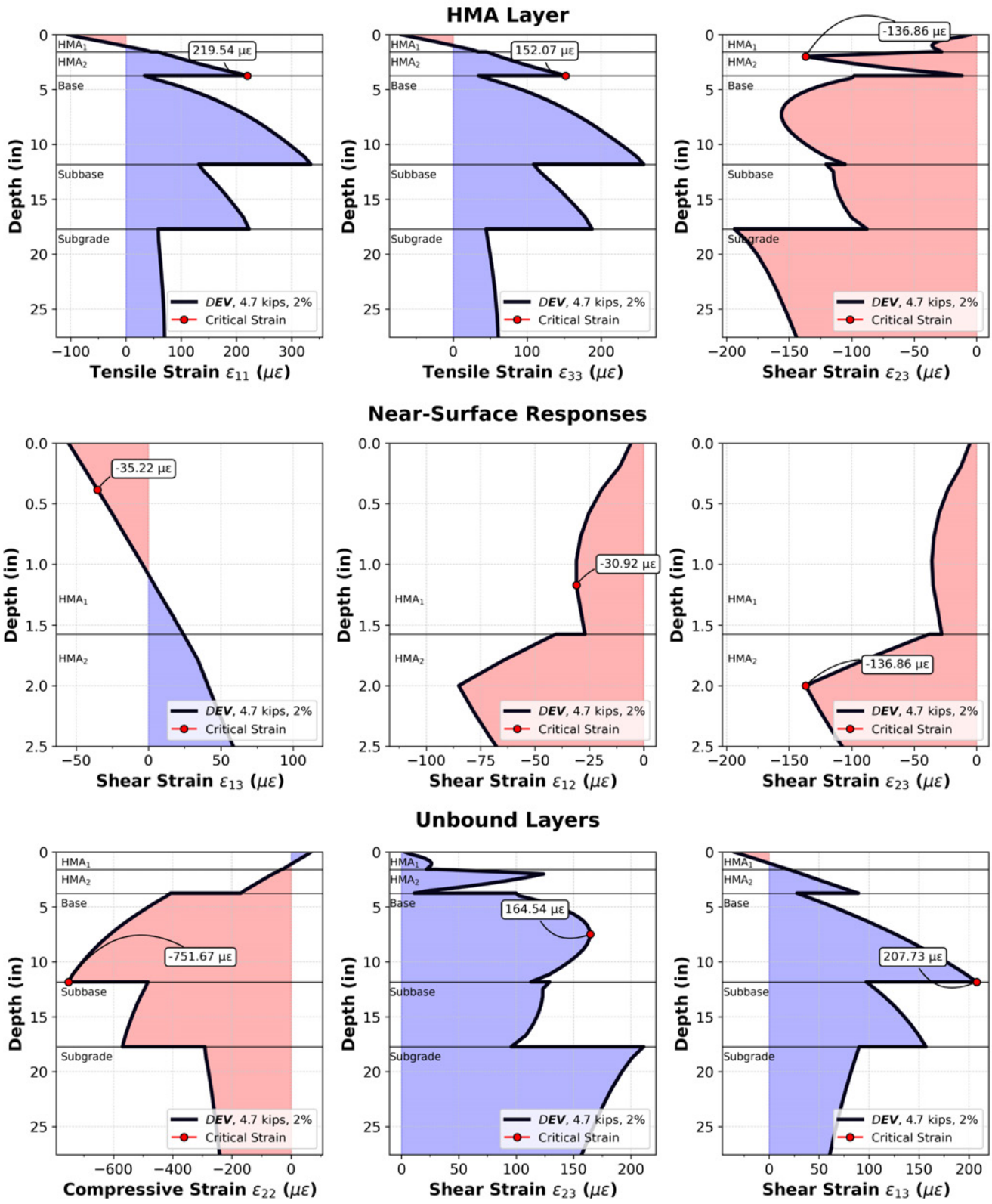

Figure 123. Graph. Summary of pavement responses of low volume section to a 4.7-kip DTA axle load (P4) at 2% slip ratio.

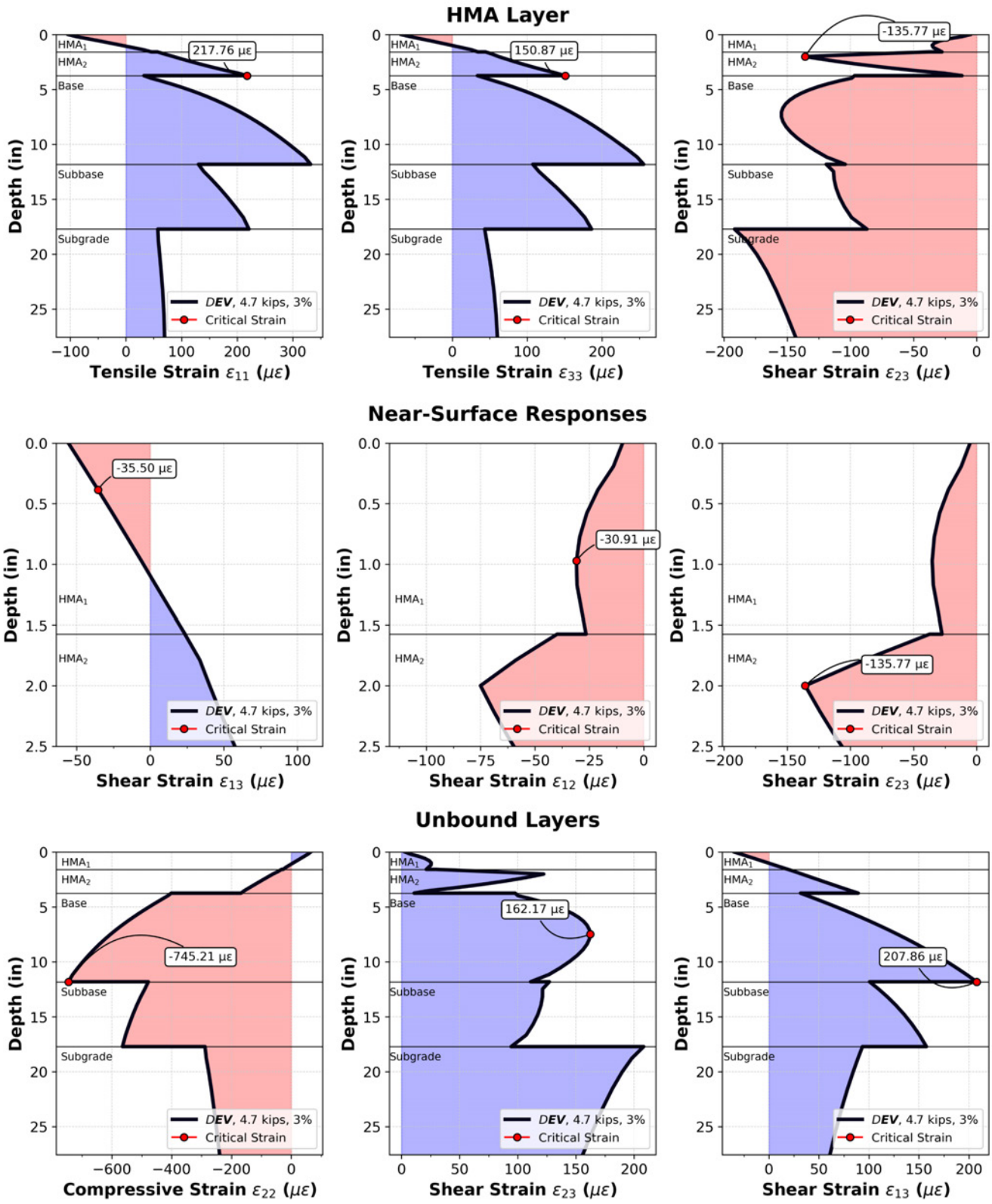

Figure 124. Graph. Summary of pavement responses of low volume section to a 4.7-kip DTA axle load (P4) at 3% slip ratio.

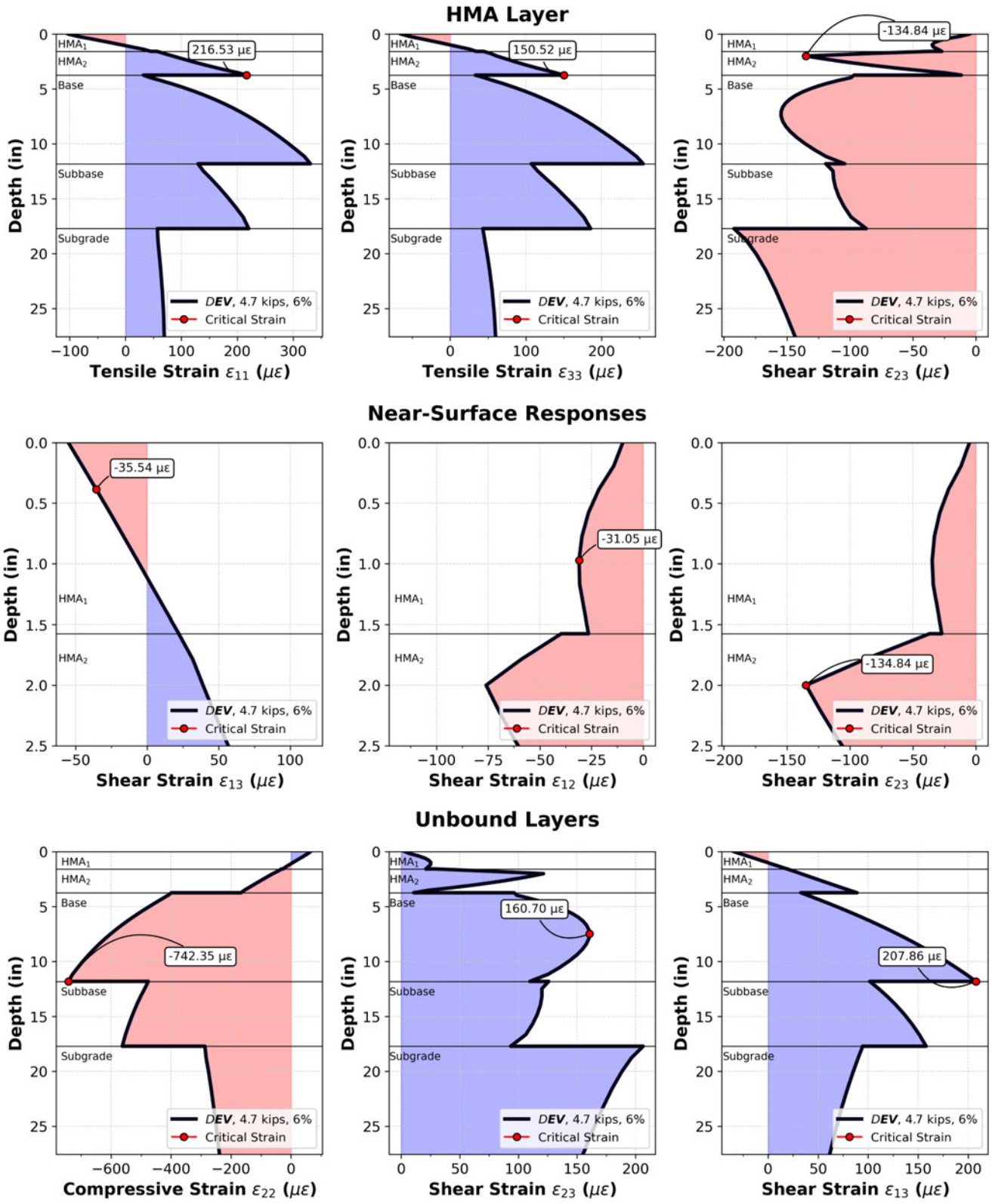

Figure 125. Graph. Summary of pavement responses of low volume section to a 4.7-kip DTA axle load (P4) at 6% slip ratio.

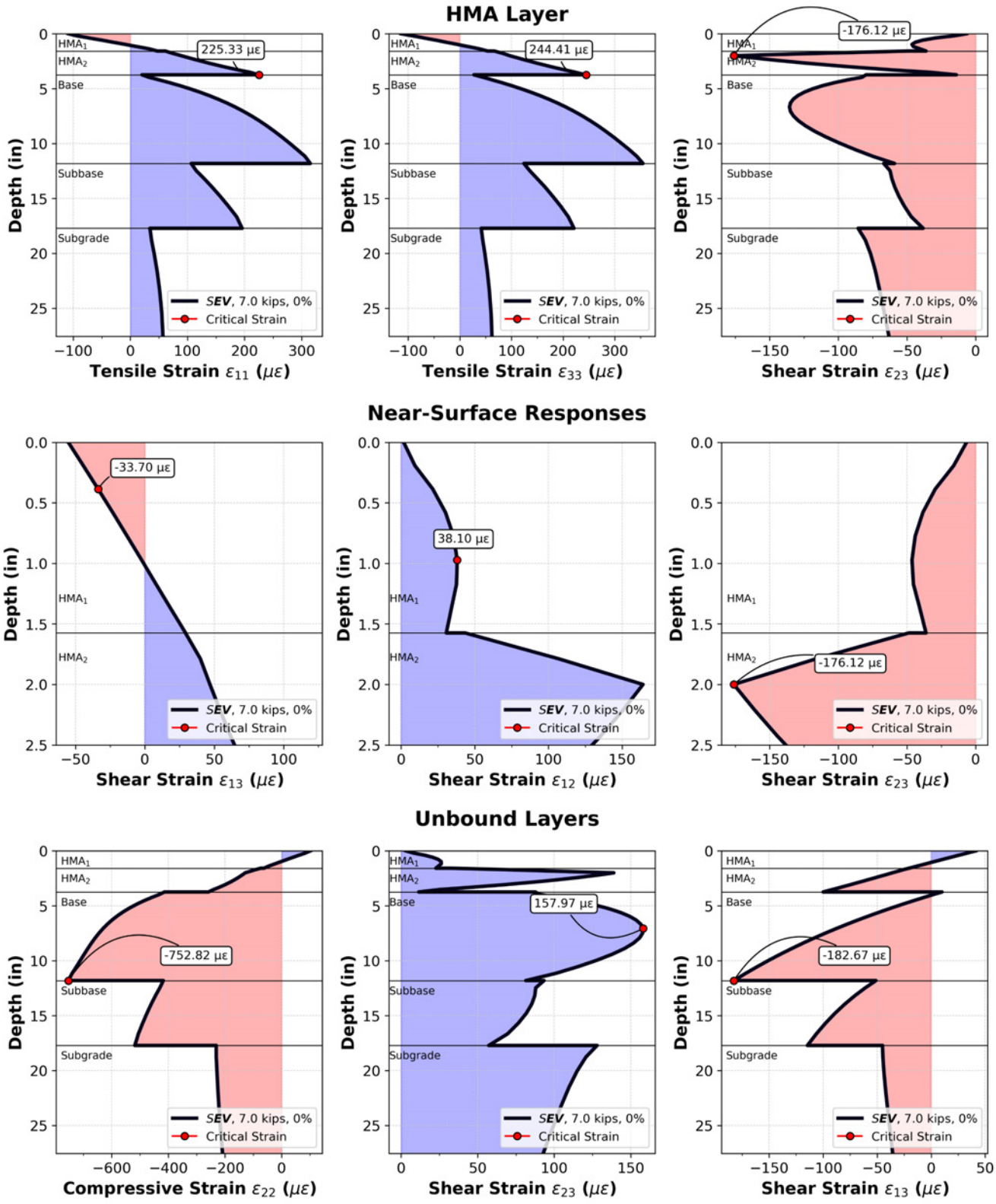

Figure 126. Graph. Summary of pavement responses of low volume section to a 7.0-kip steering axle load (P5) at 0% slip ratio.

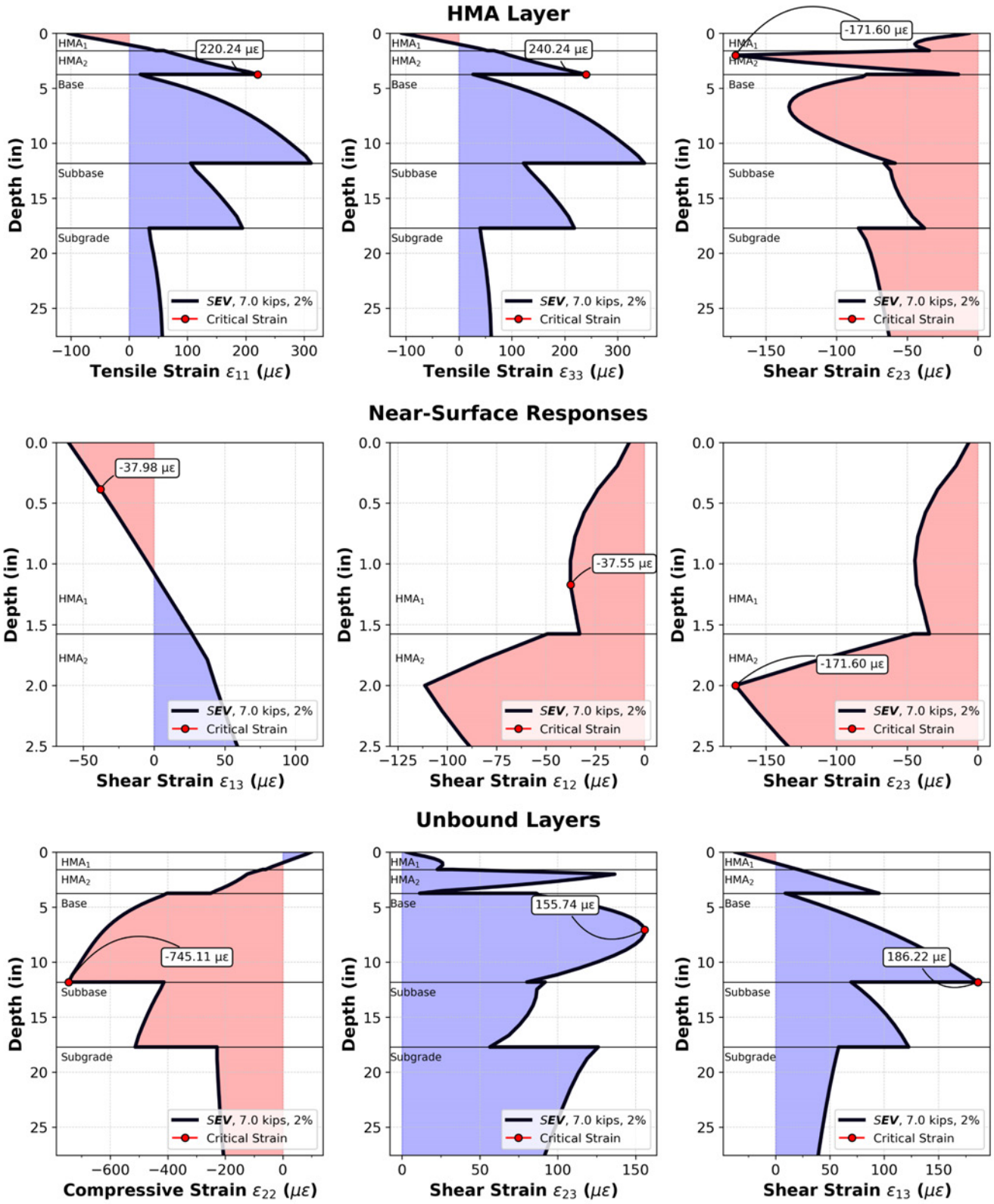

Figure 127. Graph. Summary of pavement responses of low volume section to a 7.0-kip steering axle load (P5) at 2% slip ratio.

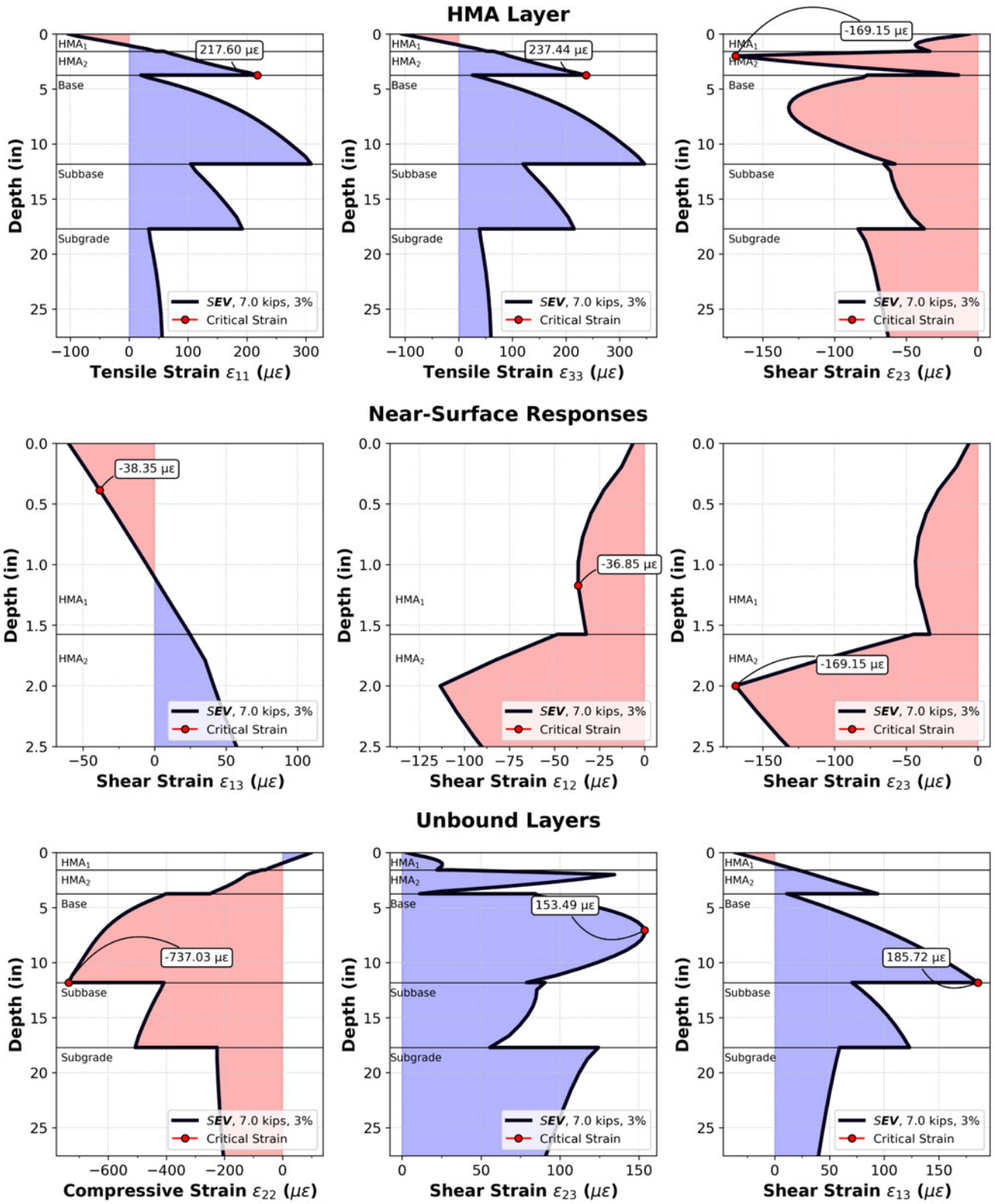

Figure 128. Graph. Summary of pavement responses of low volume section to a 7.0-kip steering axle load (P5) at 3% slip ratio.

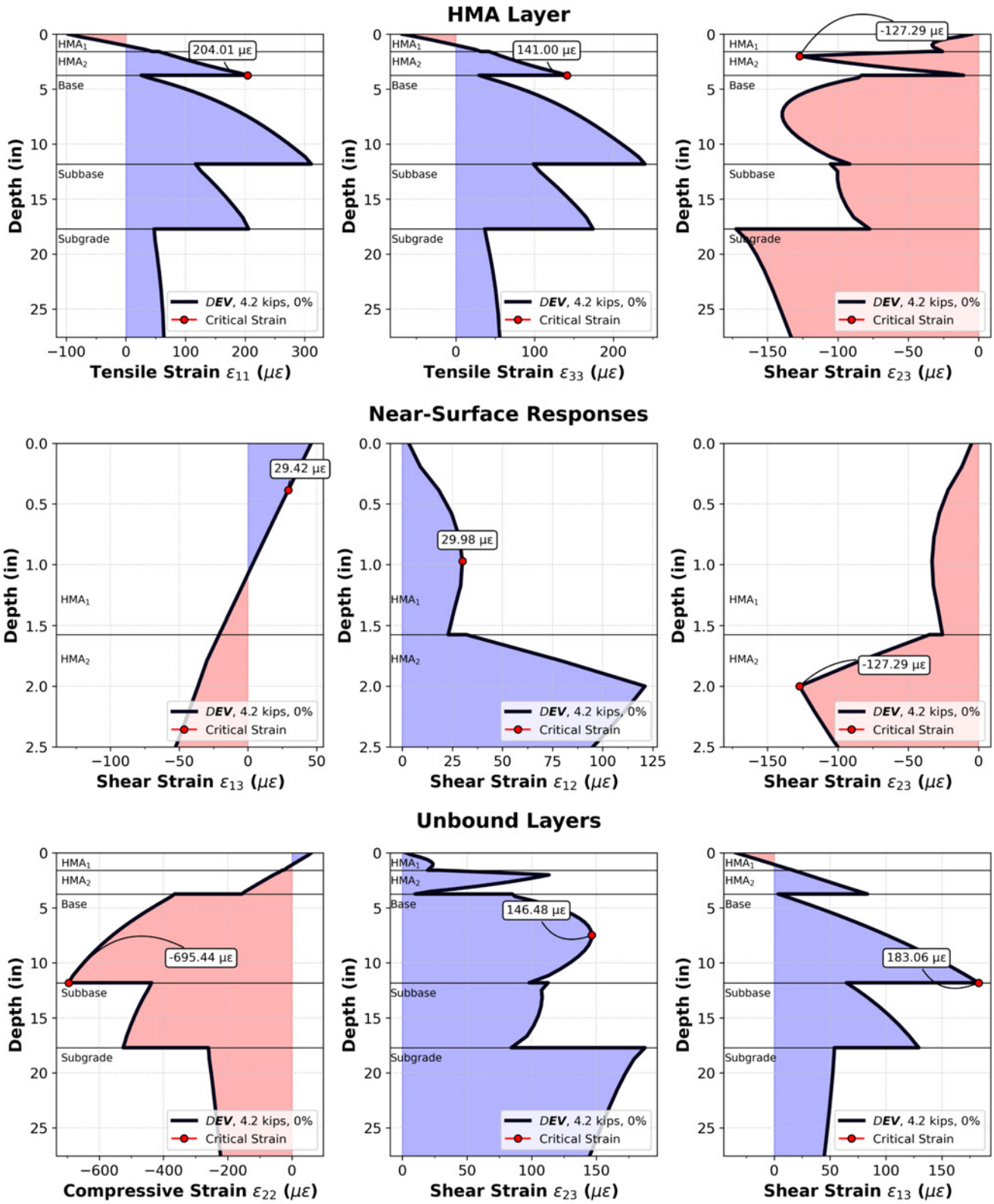

Figure 129. Graph. Summary of pavement responses of low volume section to a 4.2-kip DTA axle load (P6) at 0% slip ratio.

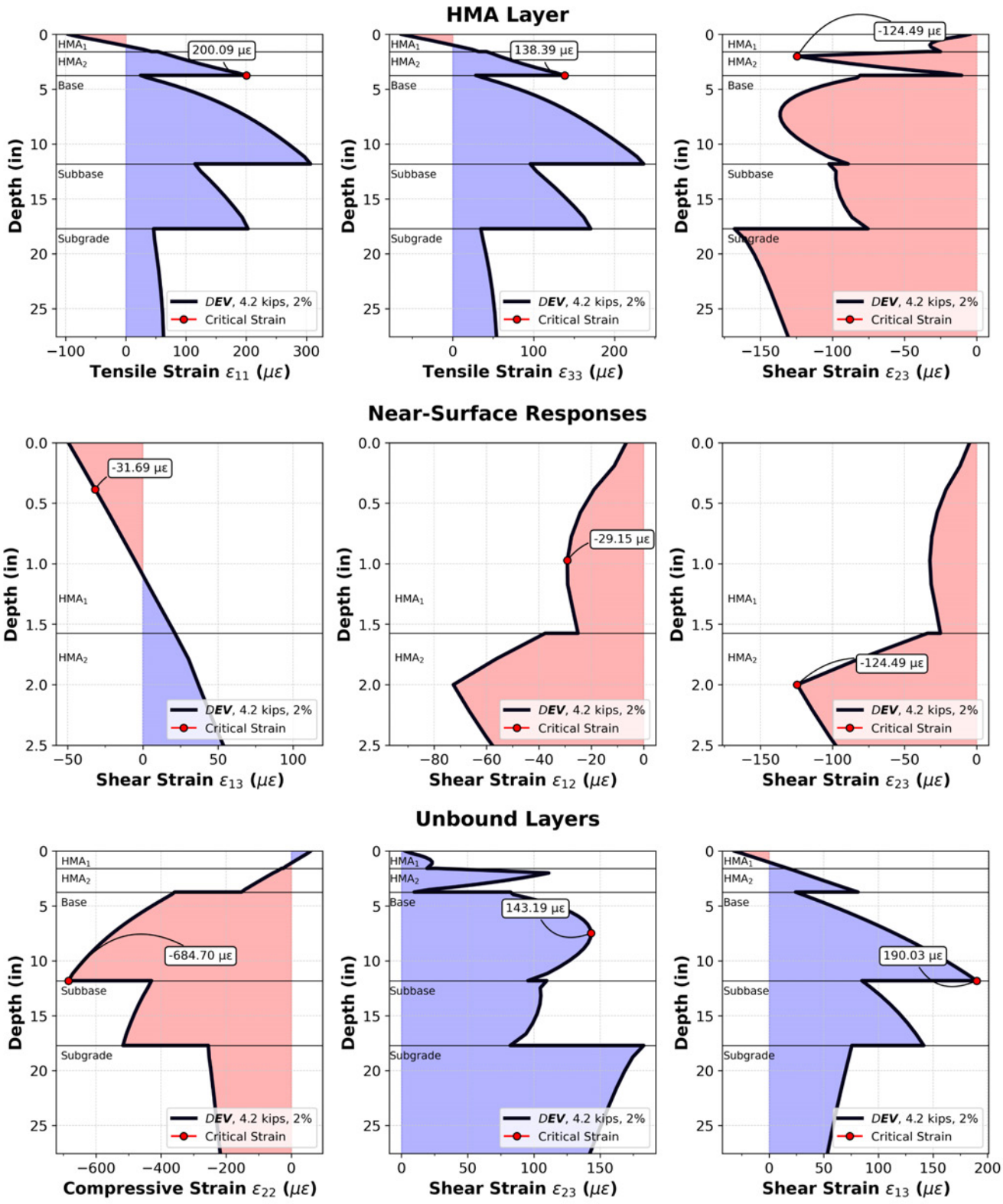

Figure 130. Graph. Summary of pavement responses of low volume section to a 4.2-kip DTA axle load (P6) at 2% slip ratio.

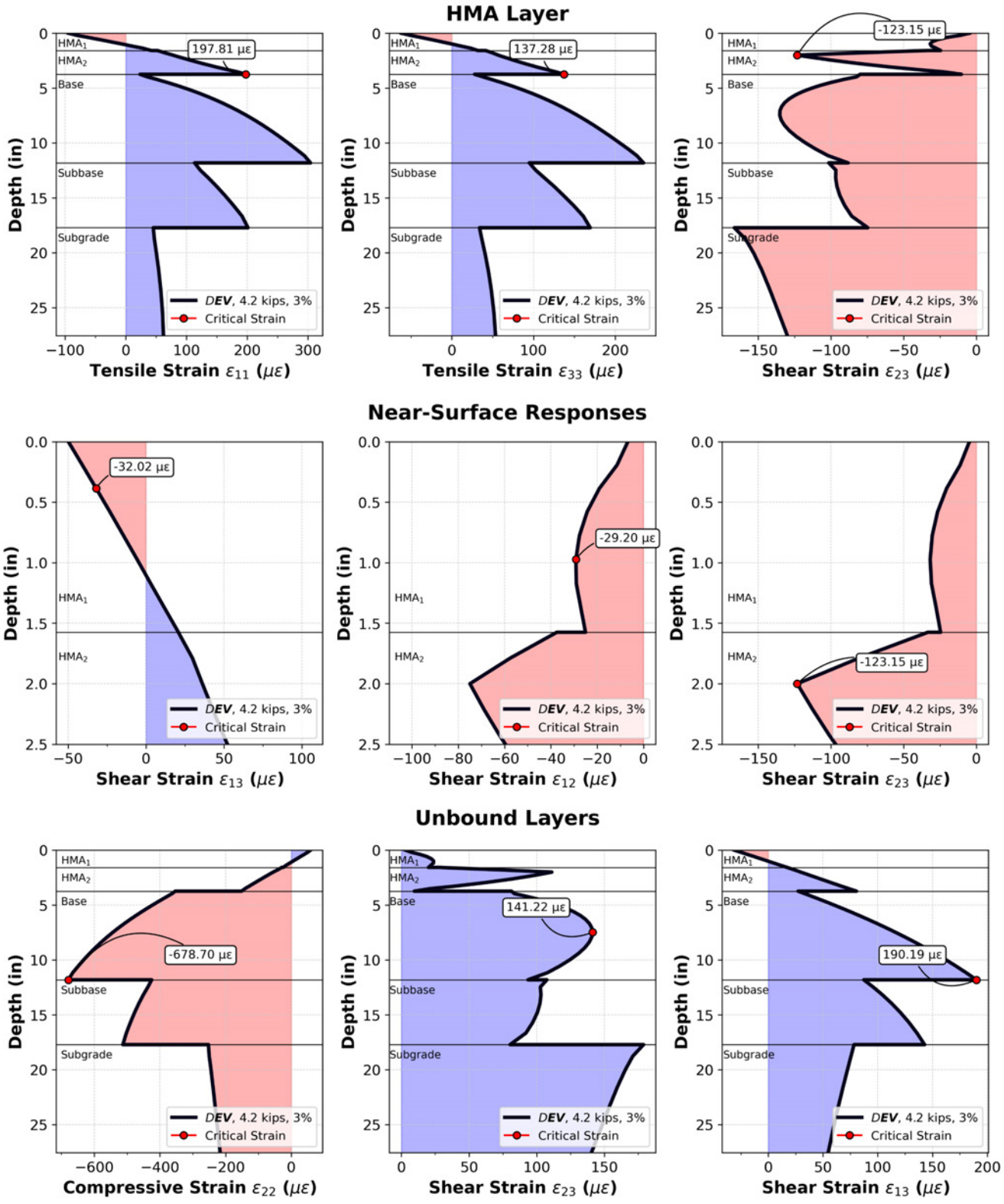

Figure 131. Graph. Summary of pavement responses of low volume section to a 4.2-kip DTA axle load (P6) at 3% slip ratio.

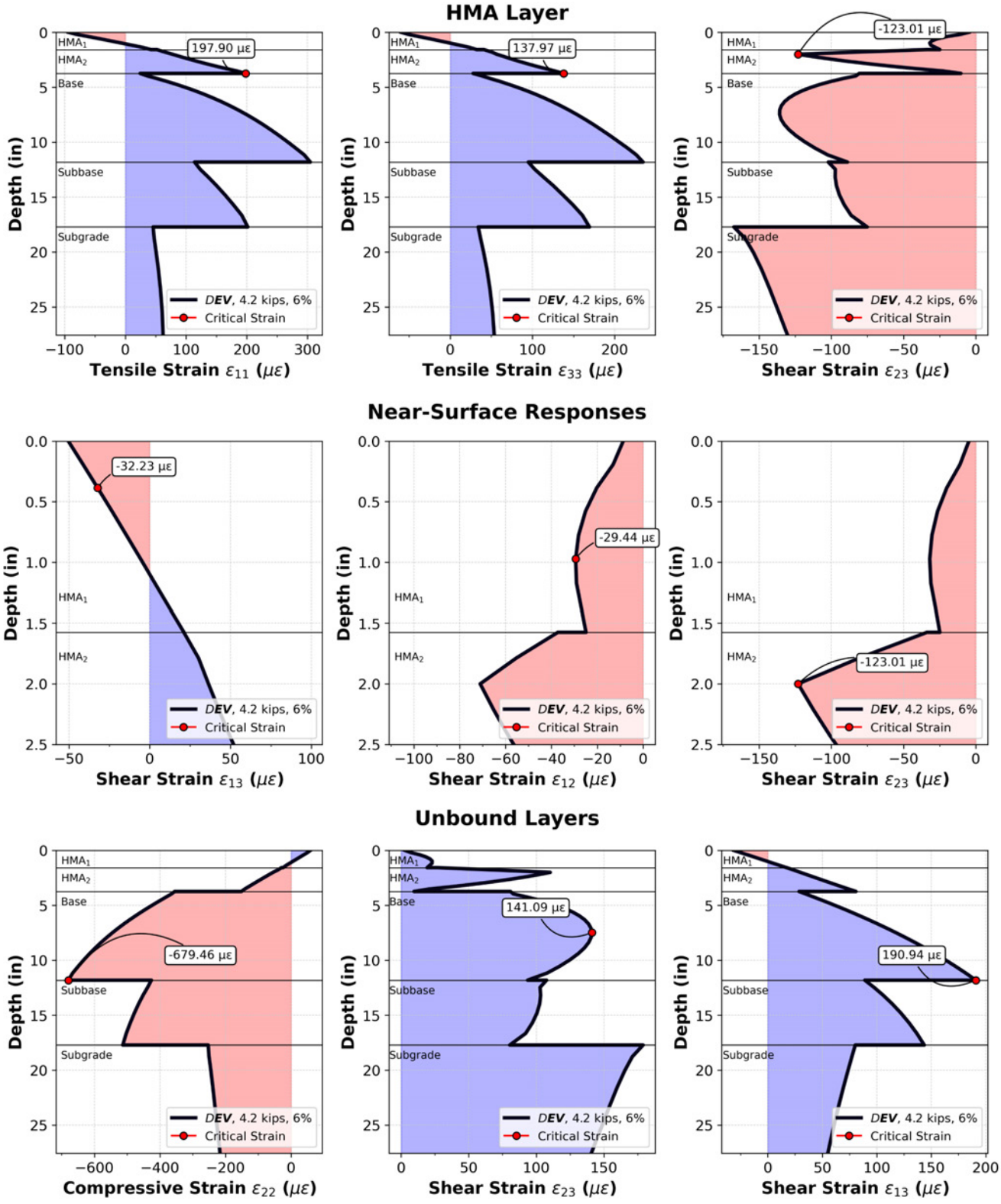

Figure 132. Graph. Summary of pavement responses of low volume section to a 4.2-kip DTA axle load (P6) at 6% slip ratio.

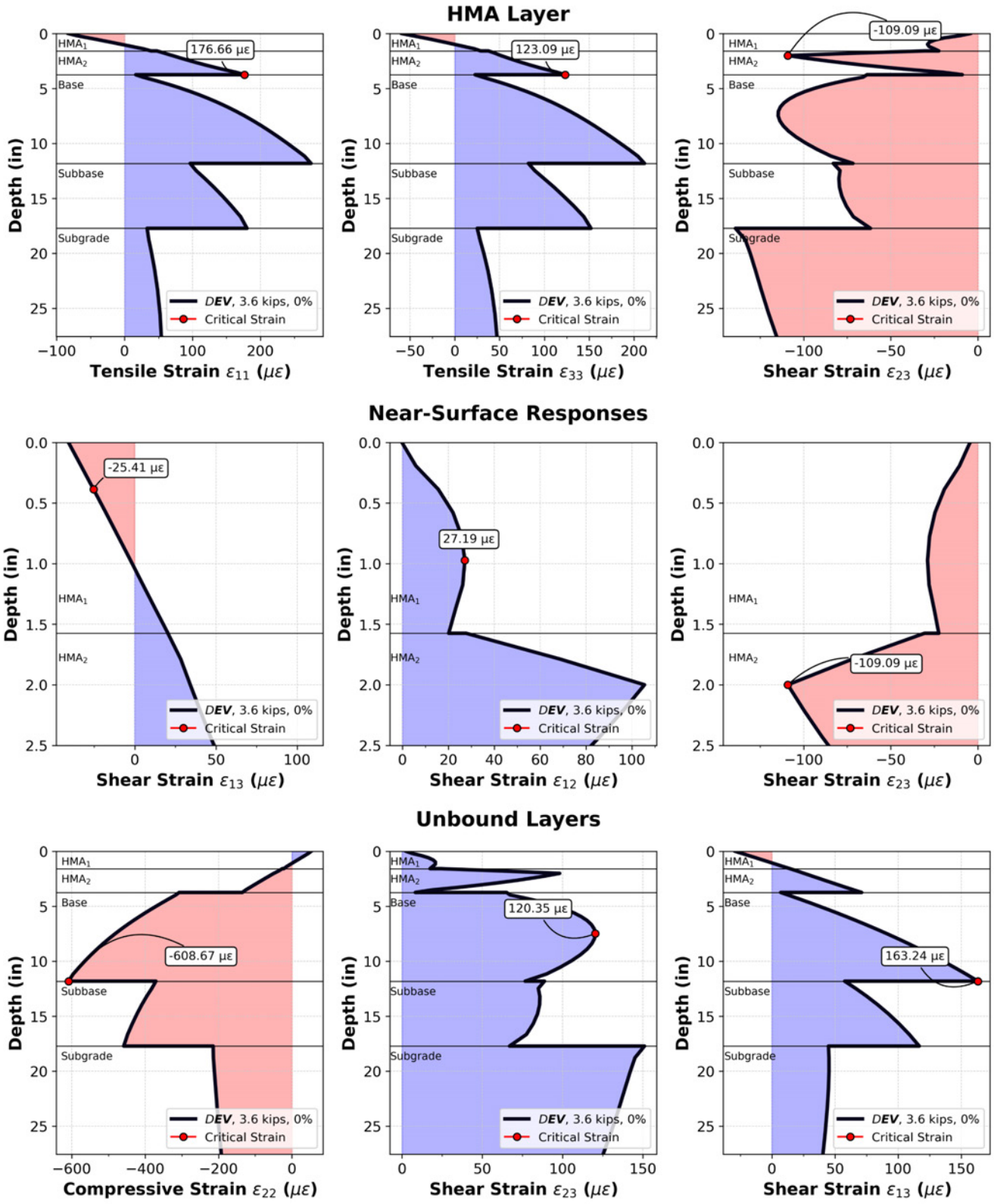

Figure 133. Graph. Summary of pavement responses of low volume section to a 3.6-kip DTA axle load (P7) at 0% slip ratio.

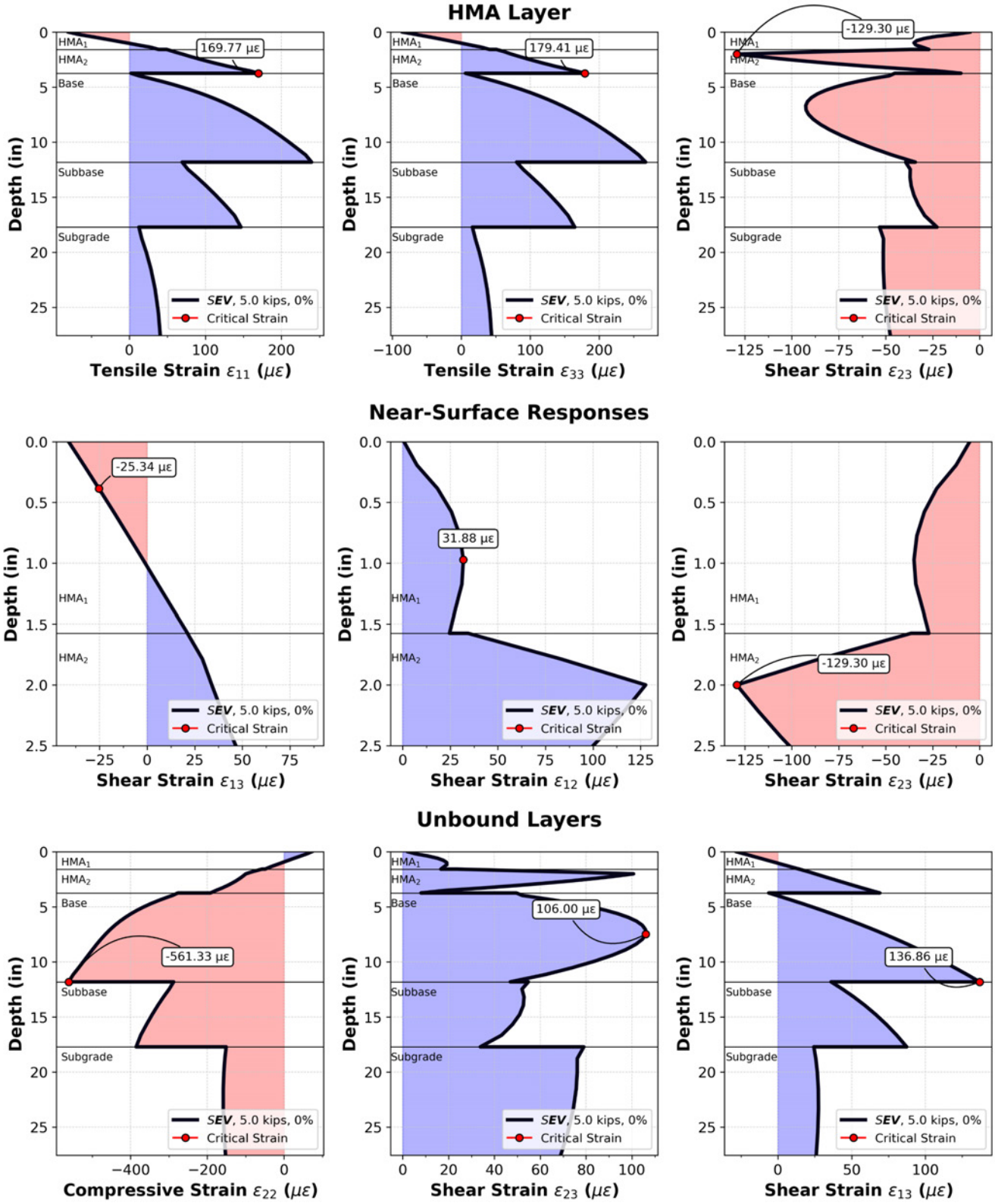

Figure 134. Graph. Summary of pavement responses of low volume section to a 5.0-kip steering axle load (P8) at 0% slip ratio.

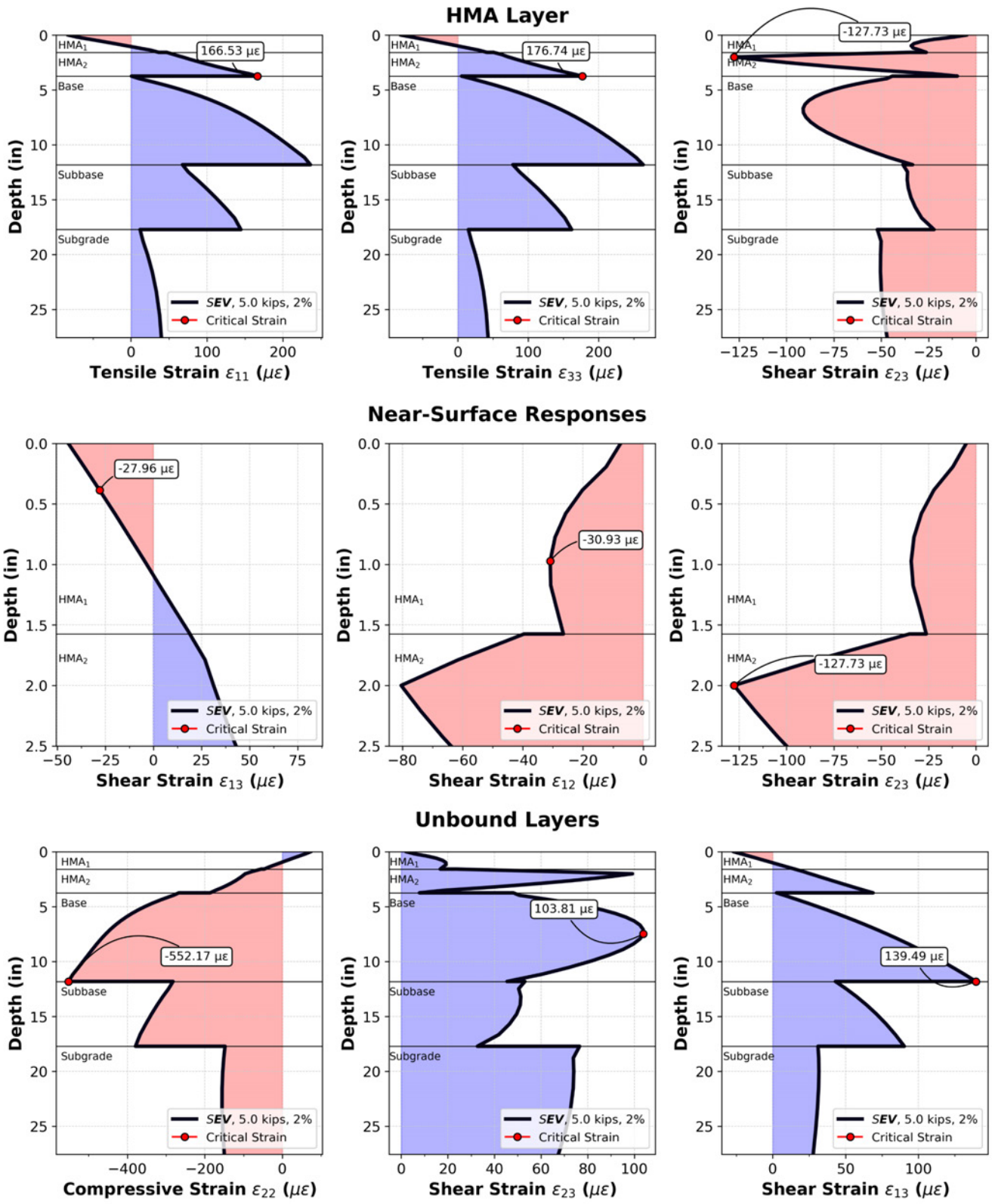

Figure 135. Graph. Summary of pavement responses of low volume section to a 5.0-kip steering axle load (P8) at 2% slip ratio.

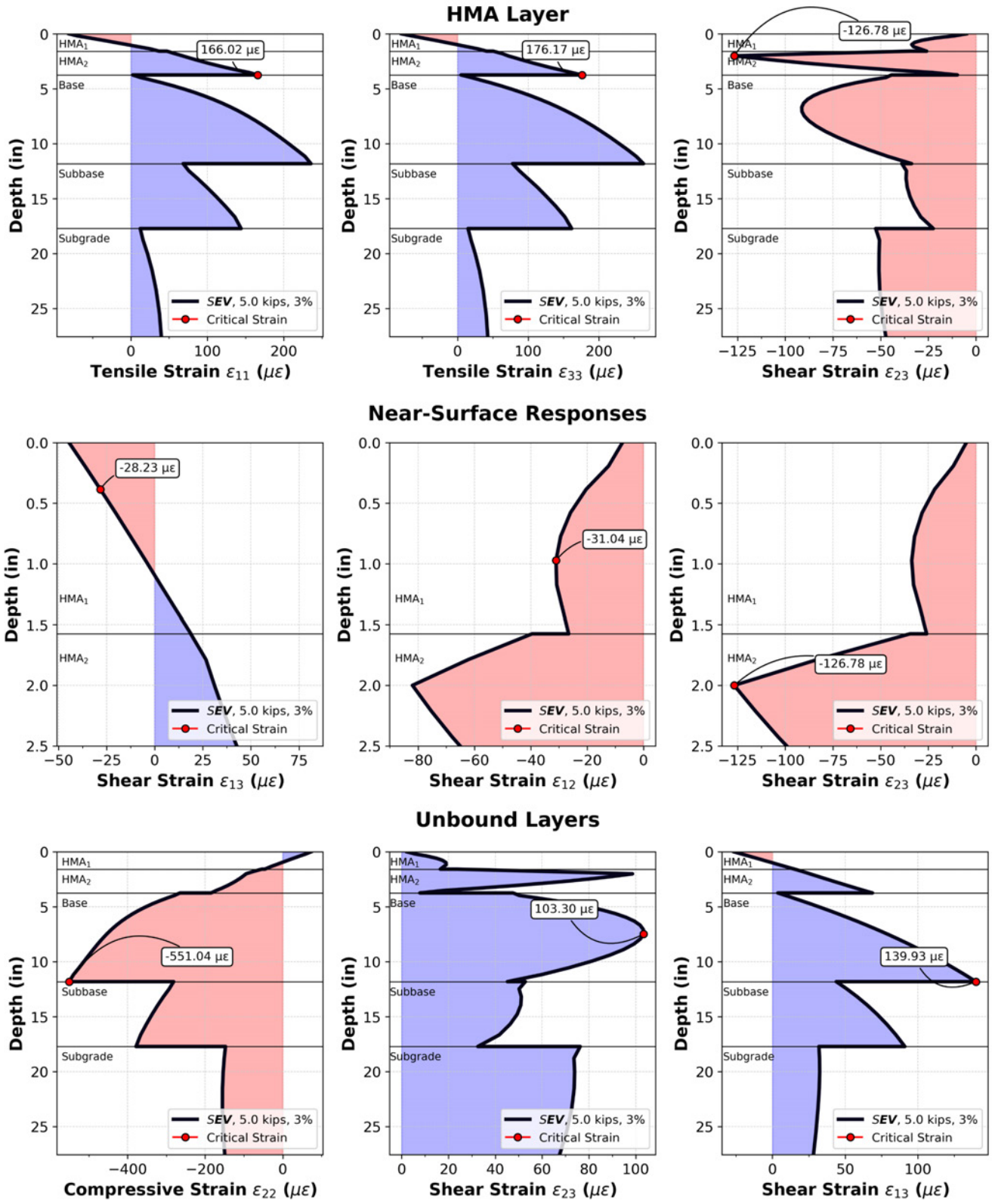

Figure 136. Graph. Summary of pavement responses of low volume section to a 5.0-kip steering axle load (P8) at 3% slip ratio.

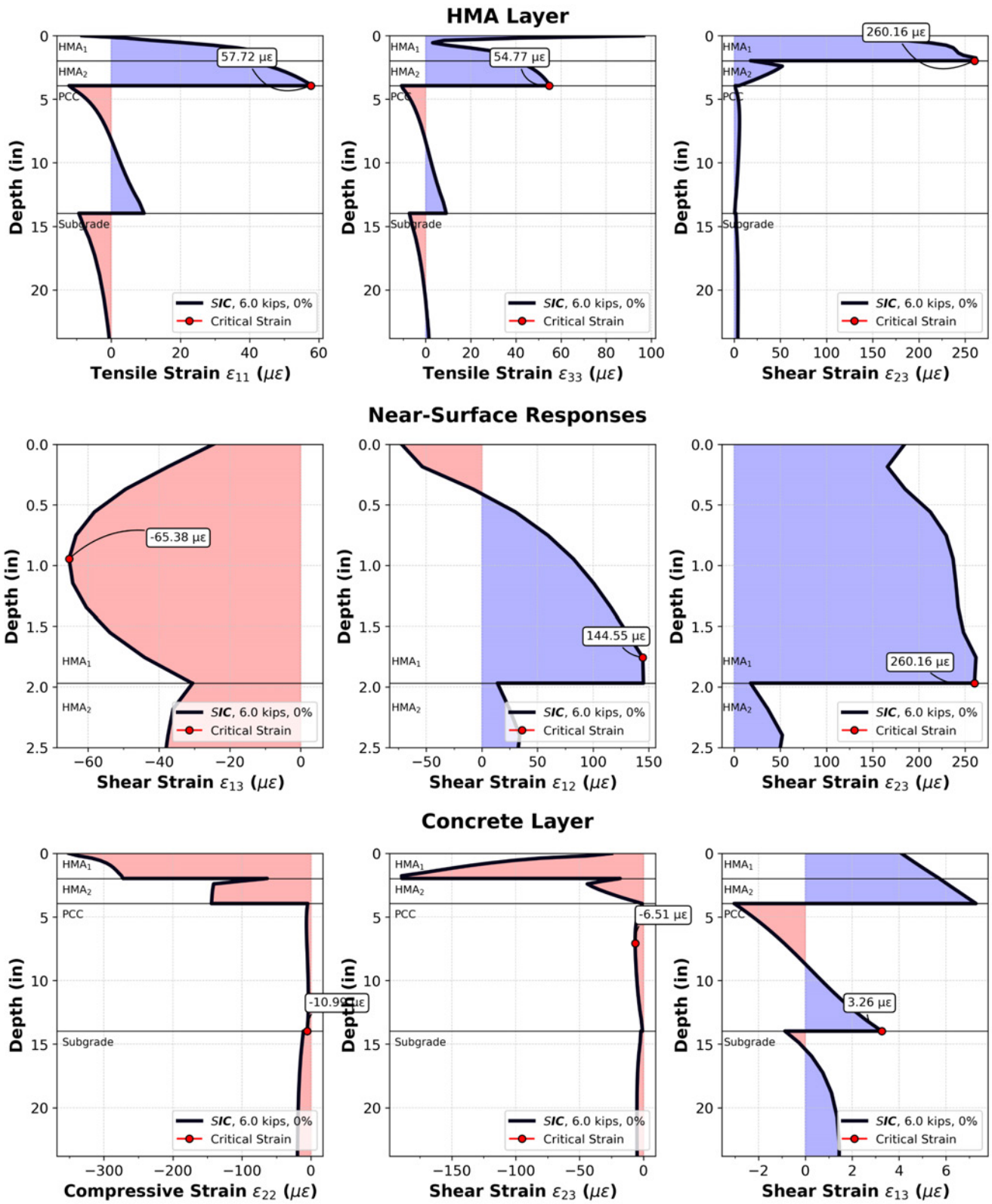

Figure 137. Graph. Summary of pavement responses of SMA overlay section to a 6-kip steering axle load (P1) at 0% slip ratio.

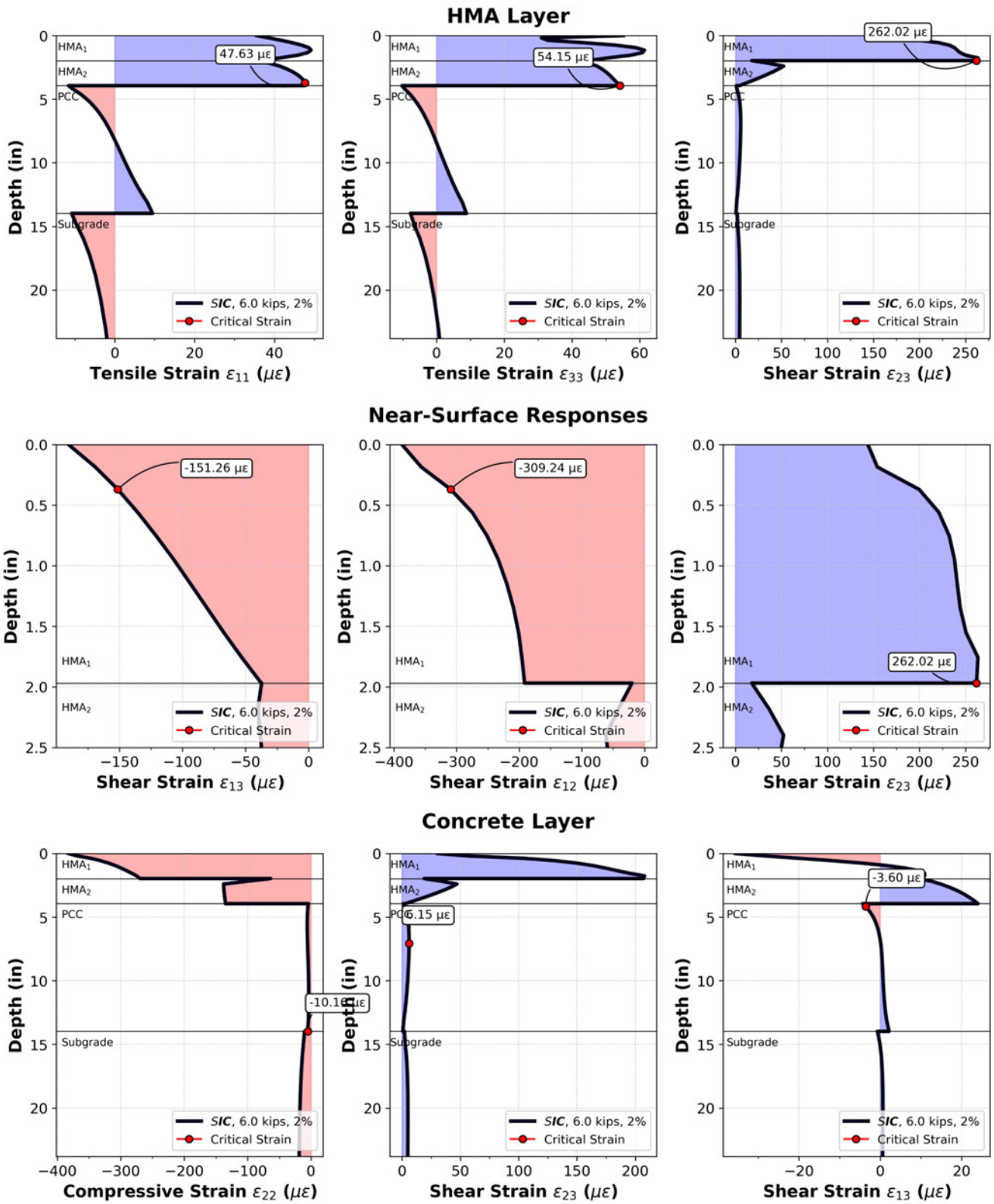

Figure 138. Graph. Summary of pavement responses of SMA overlay section to a 6-kip steering axle load (P1) at 2% slip ratio.

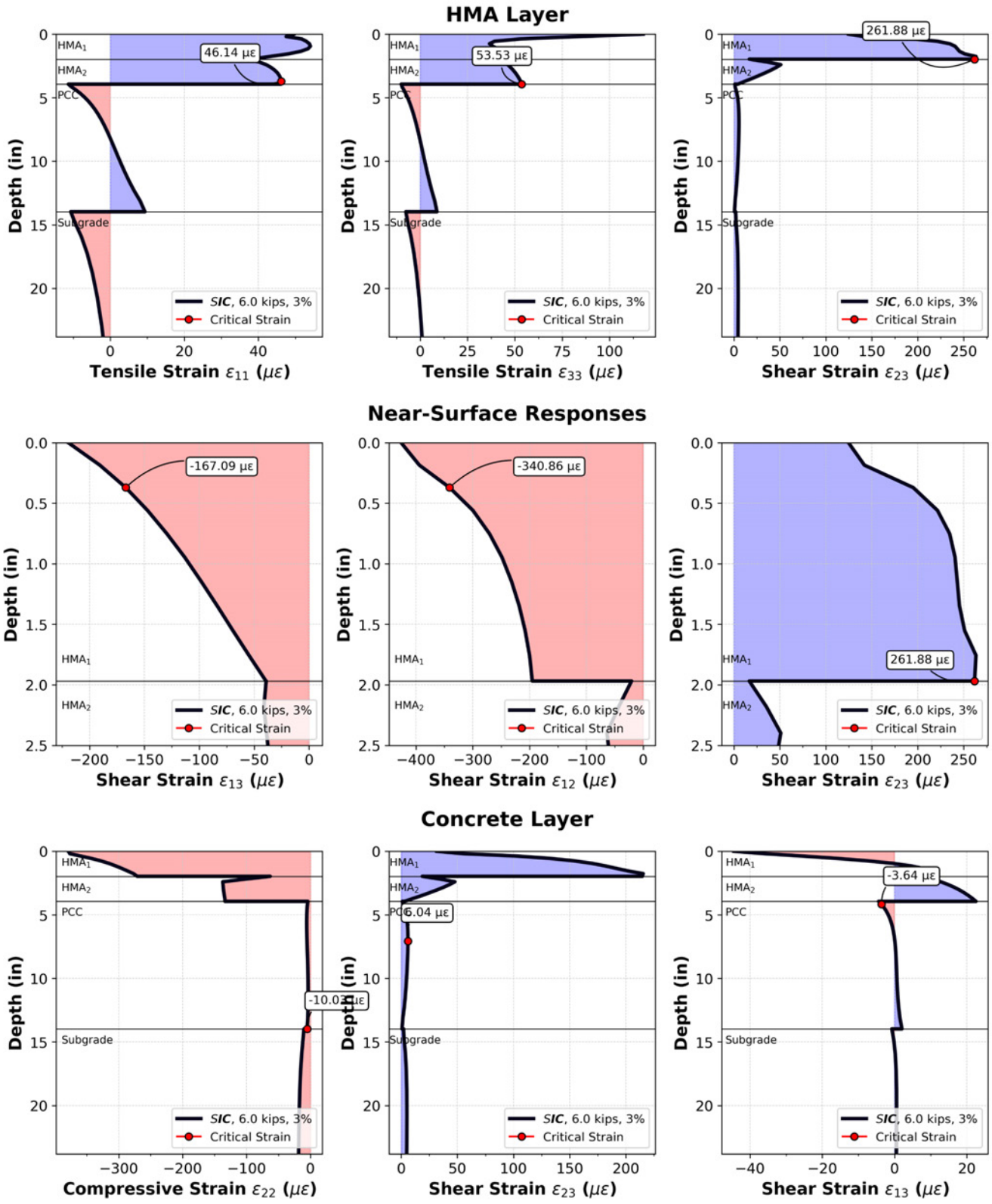

Figure 139. Graph. Summary of pavement responses of SMA overlay section to a 6-kip steering axle load (P1) at 3% slip ratio.

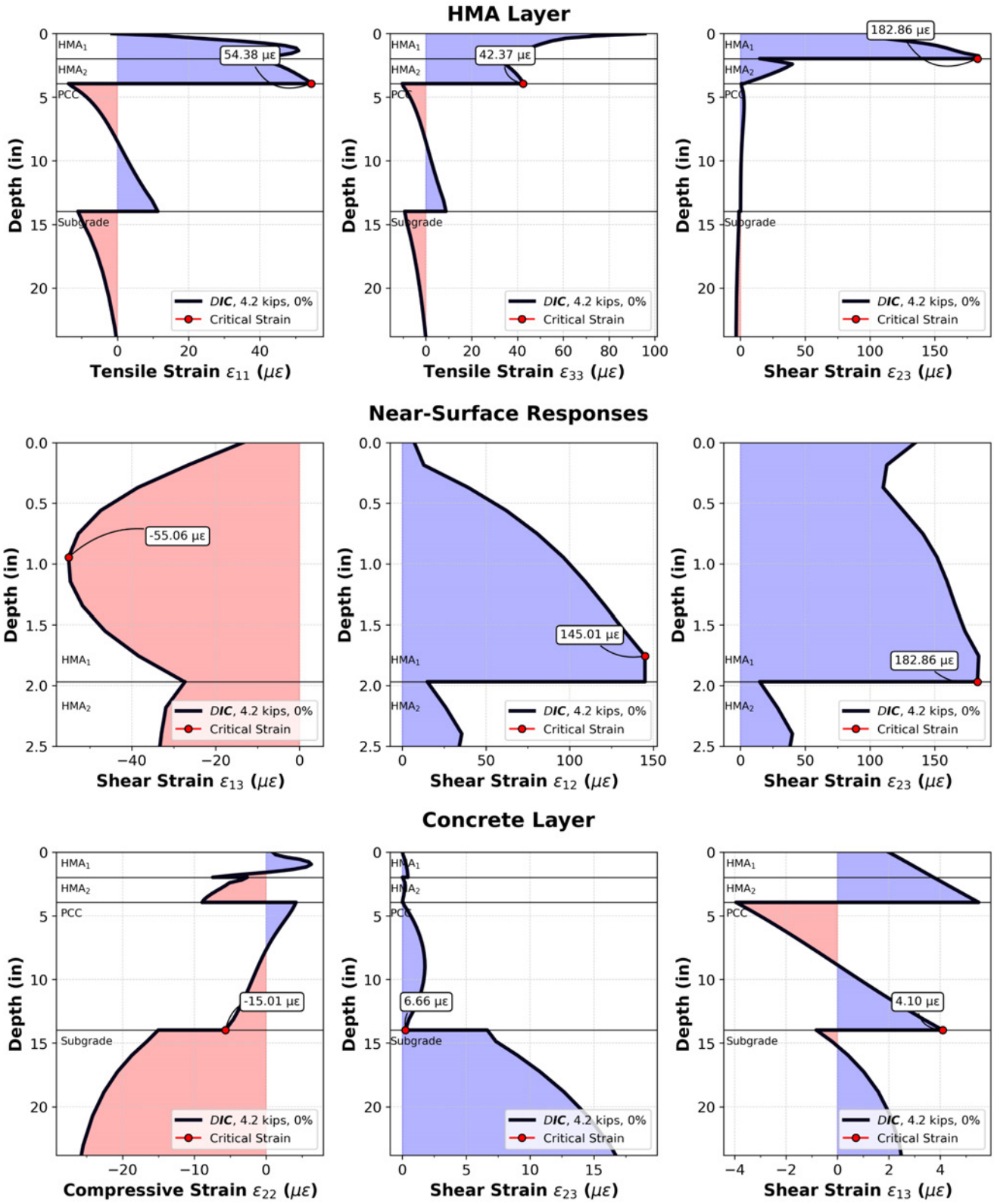

Figure 140. Graph. Summary of pavement responses of SMA overlay section to a 4.2-kip DTA axle load (P2) at 0% slip ratio.

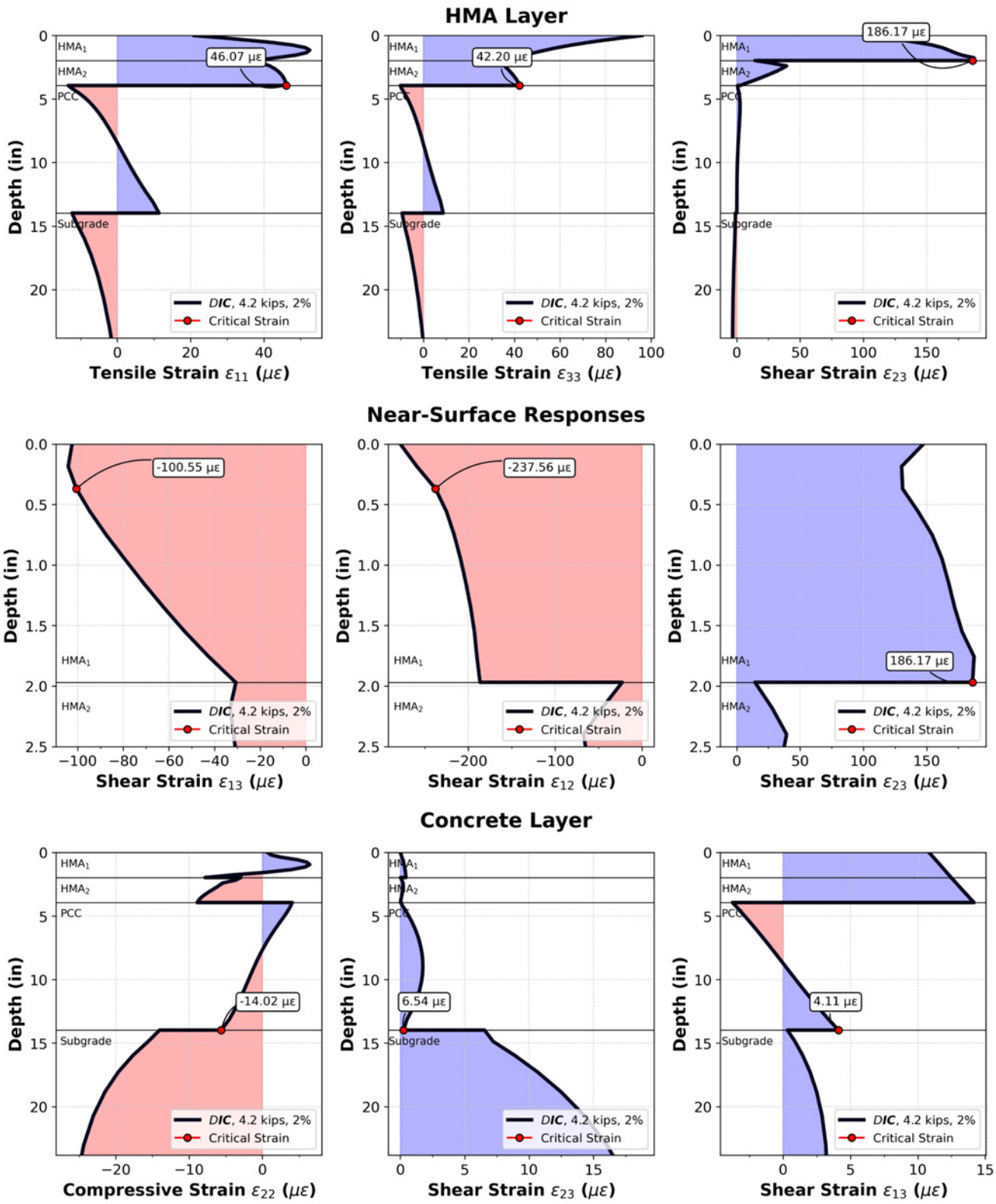

Figure 141. Graph. Summary of pavement responses of SMA overlay section to a 4.2-kip DTA axle load (P2) at 2% slip ratio.

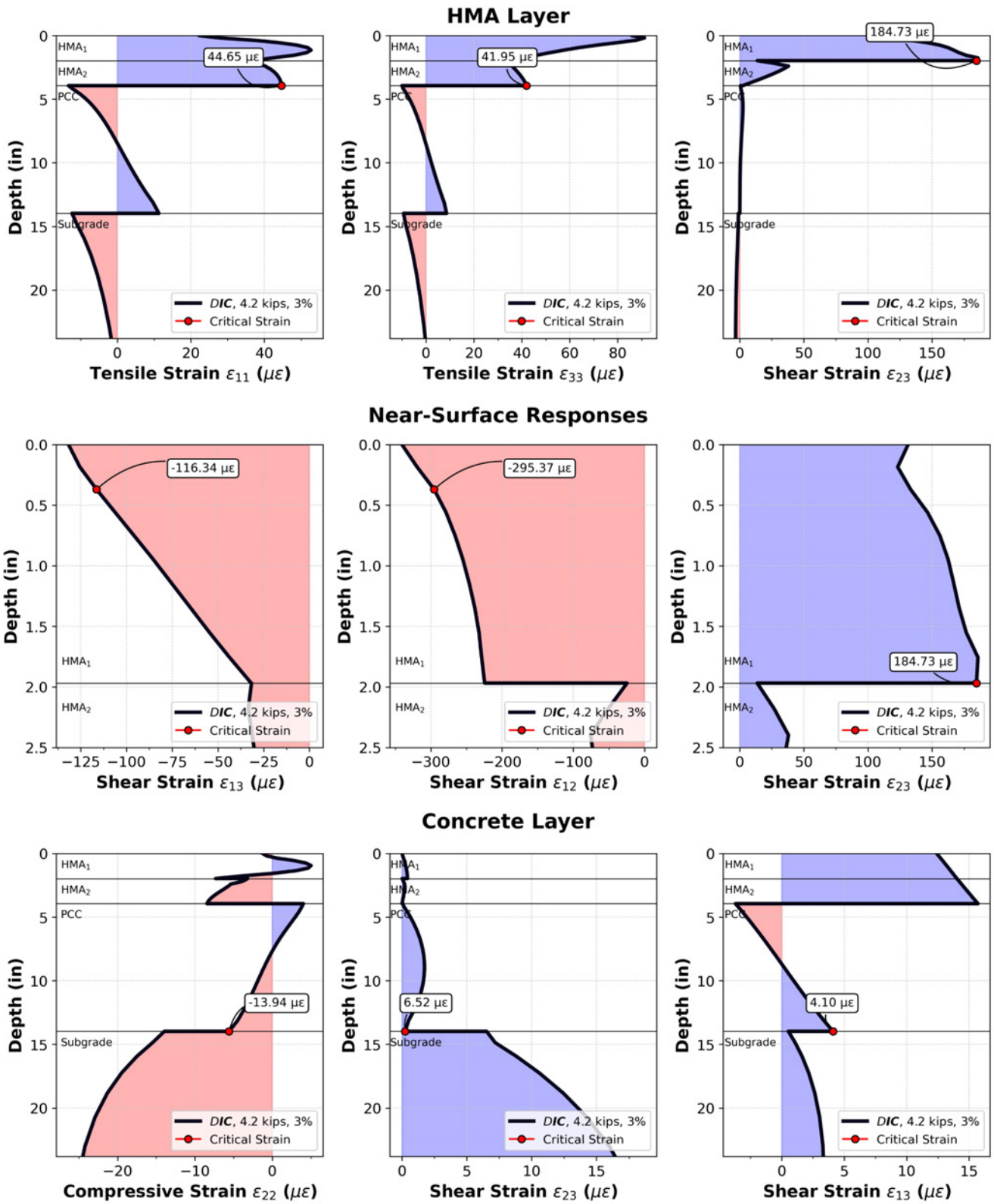

Figure 142. Graph. Summary of pavement responses of SMA overlay section to a 4.2-kip DTA axle load (P2) at 3% slip ratio.

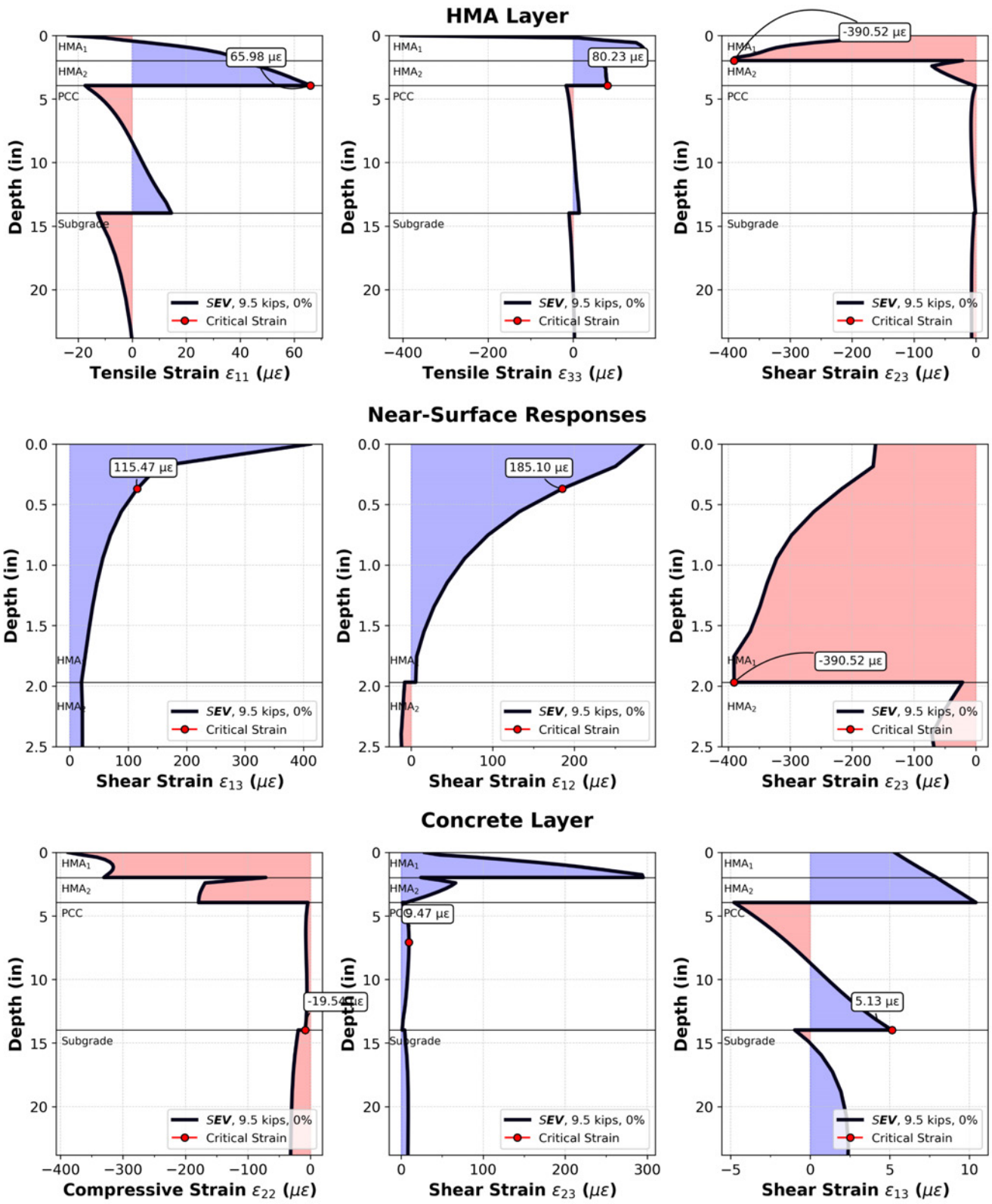

Figure 143. Graph. Summary of pavement responses of SMA overlay section to a 9.5-kip steering axle load (P3) at 0% slip ratio.

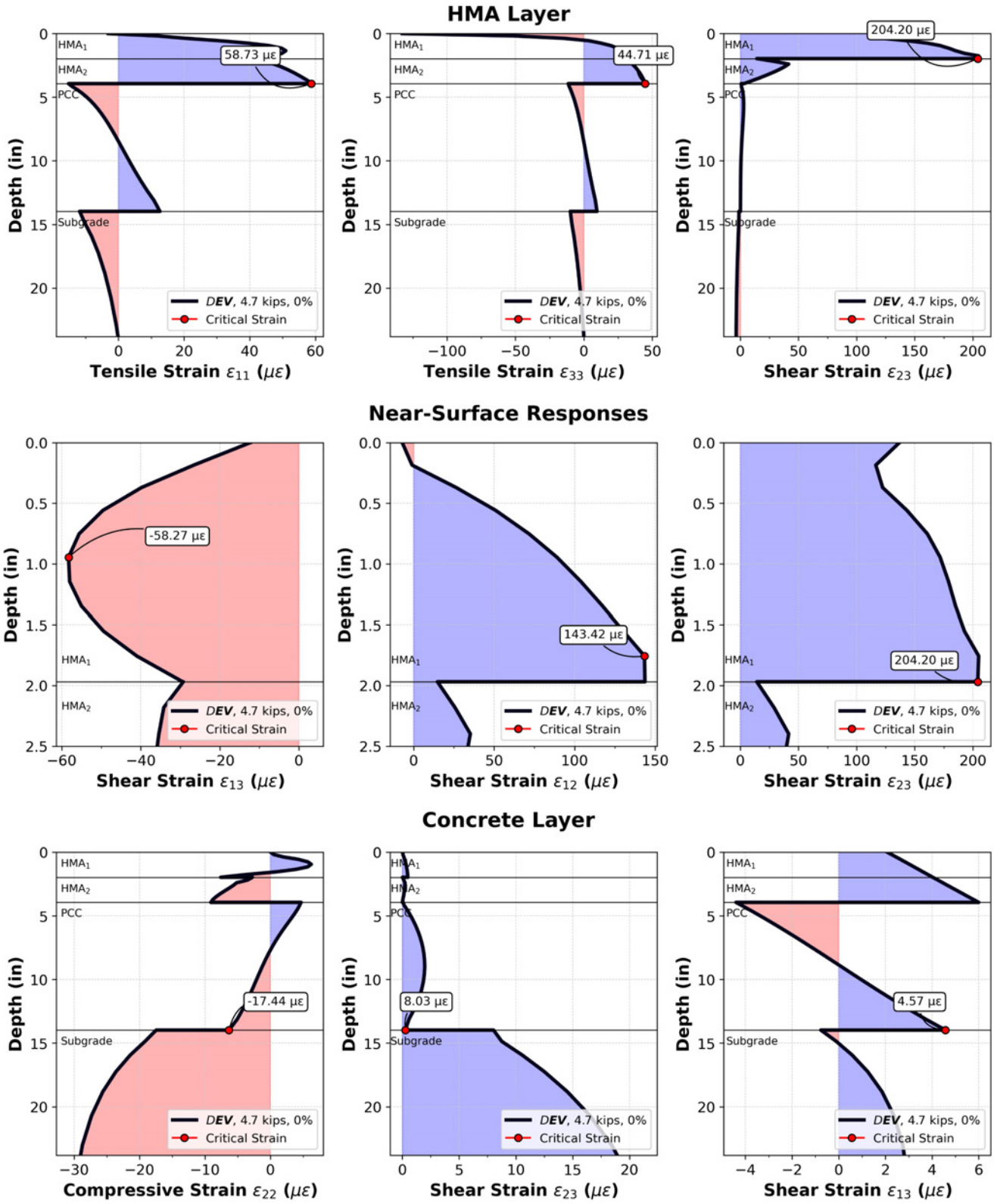

Figure 144. Graph. Summary of pavement responses of SMA overlay section to a 4.7-kip DTA axle load (P4) at 0% slip ratio.

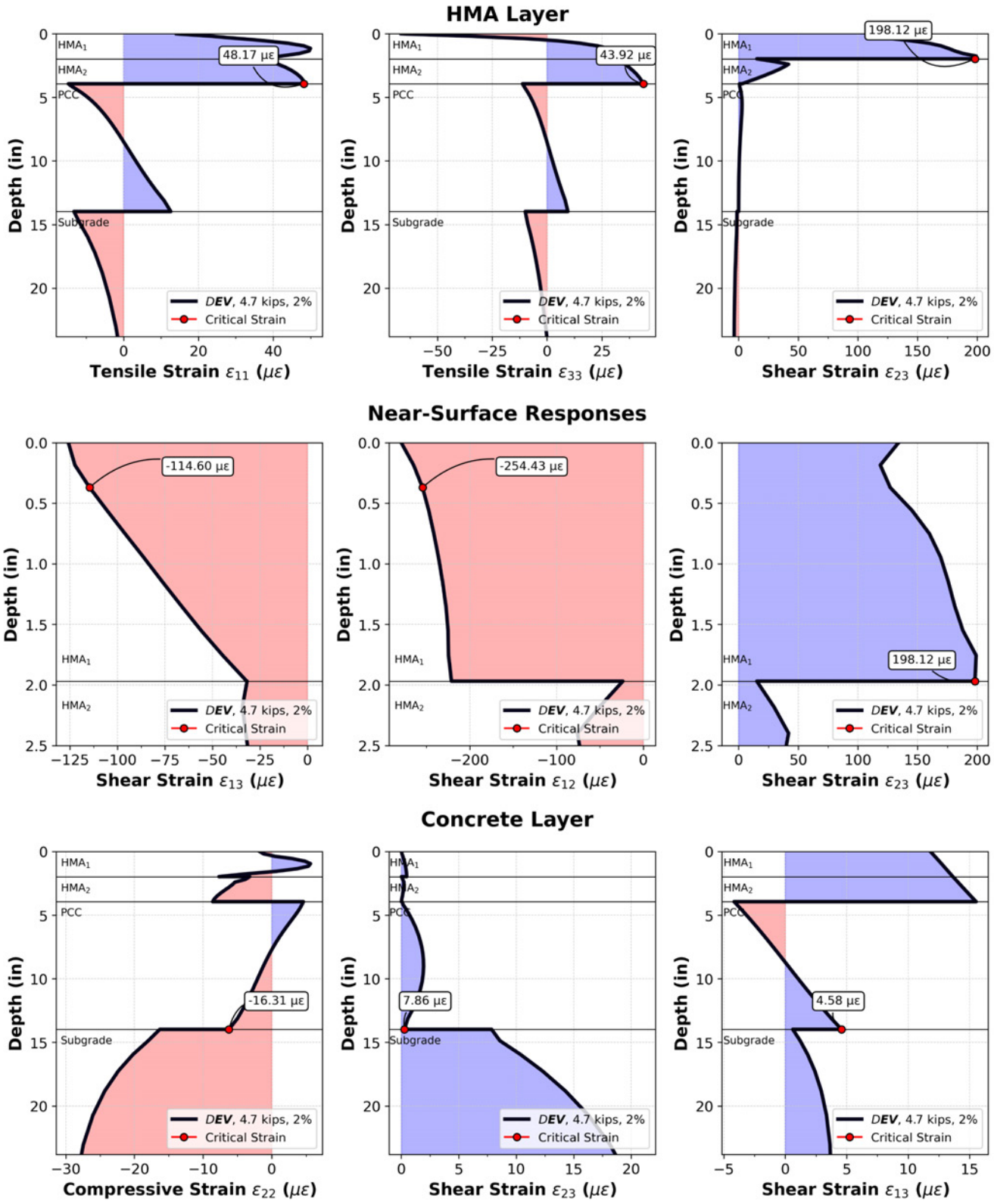

Figure 145. Graph. Summary of pavement responses of SMA overlay section to a 4.7-kip DTA axle load (P4) at 2% slip ratio.

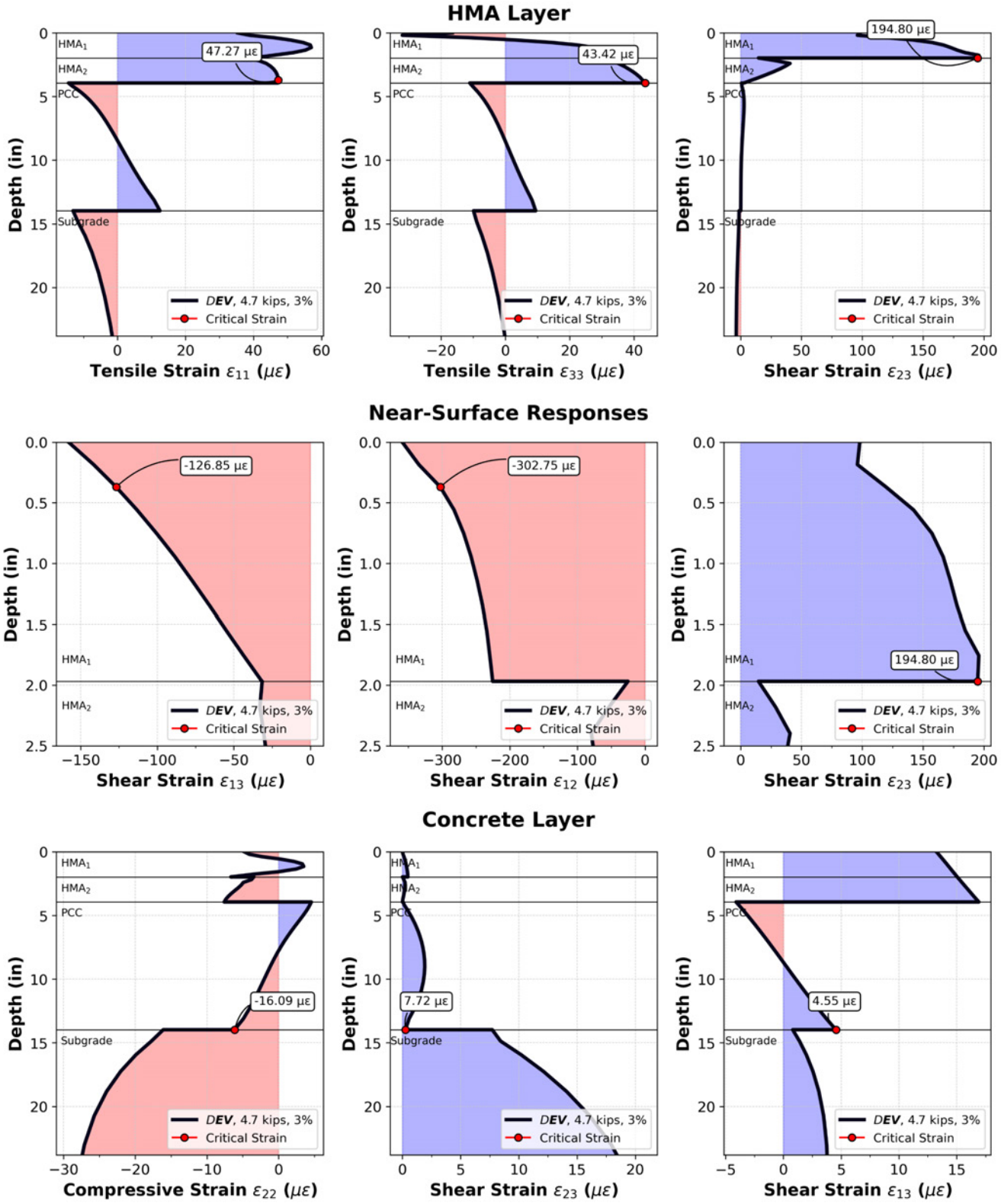

Figure 146. Graph. Summary of pavement responses of SMA overlay section to a 4.7-kip DTA axle load (P4) at 3% slip ratio.

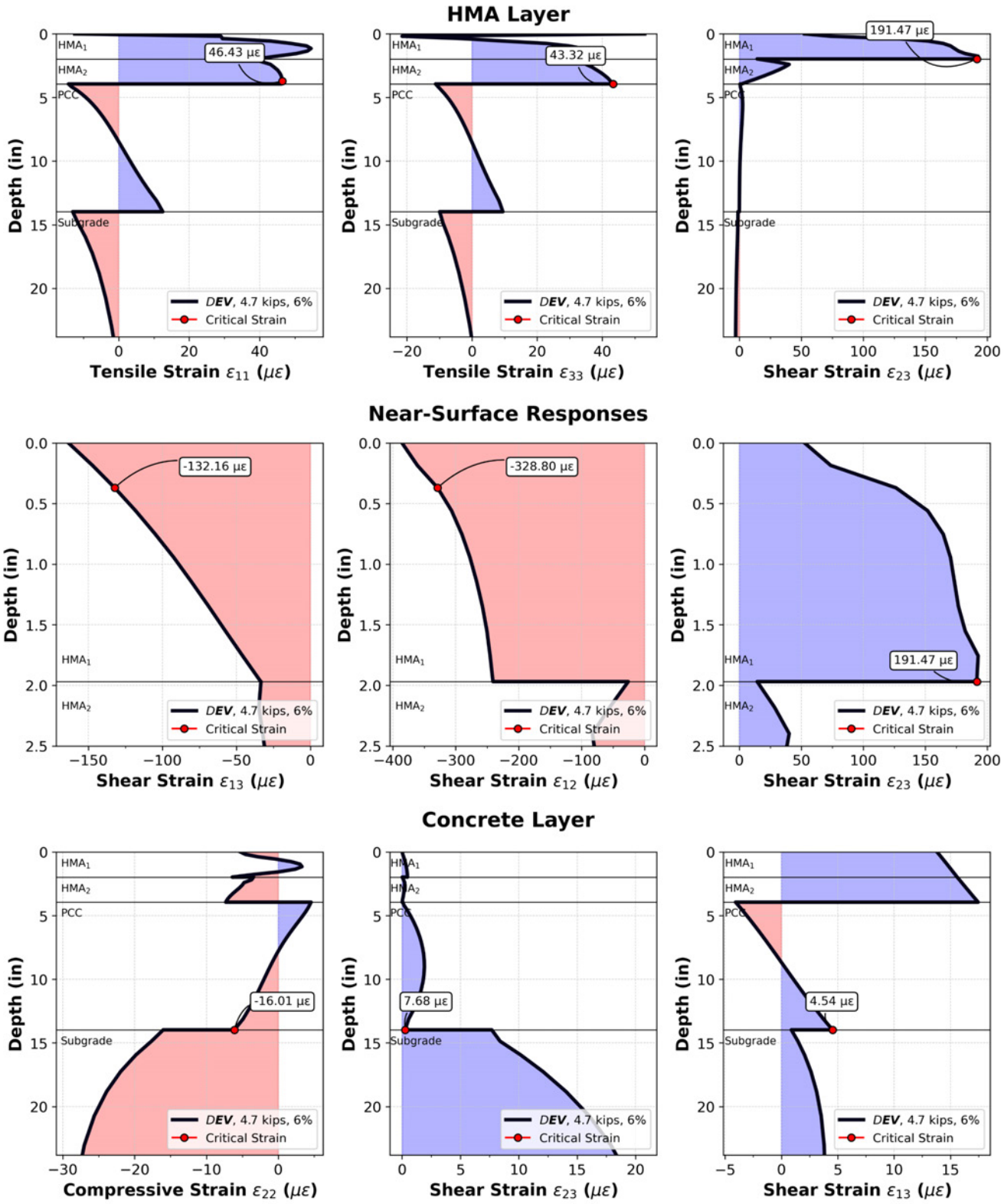

Figure 147. Graph. Summary of pavement responses of SMA overlay section to a 4.7-kip DTA axle load (P4) at 6% slip ratio.

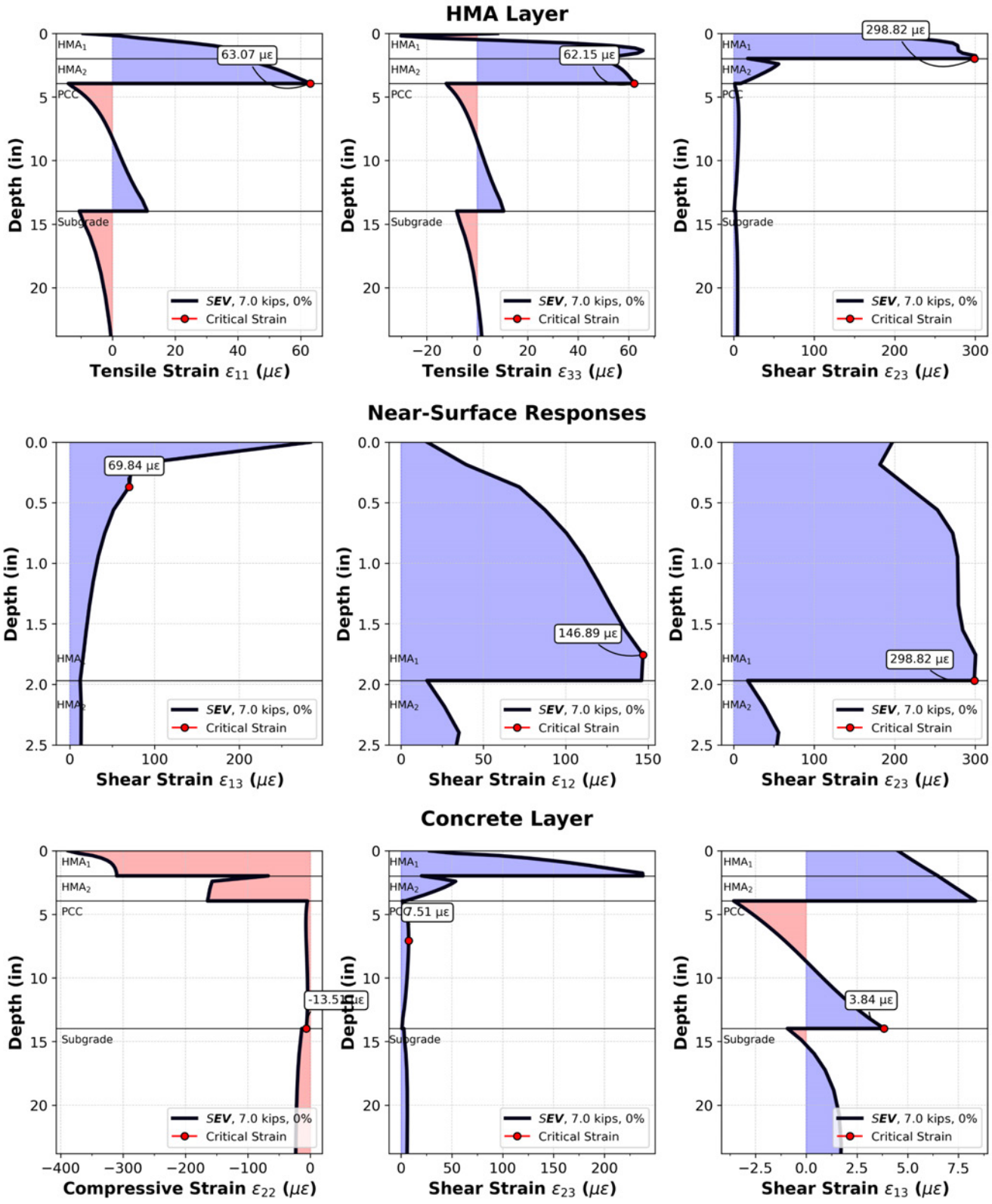

Figure 148. Graph. Summary of pavement responses of SMA overlay section to a 7.0-kip steering axle load (P5) at 0% slip ratio.

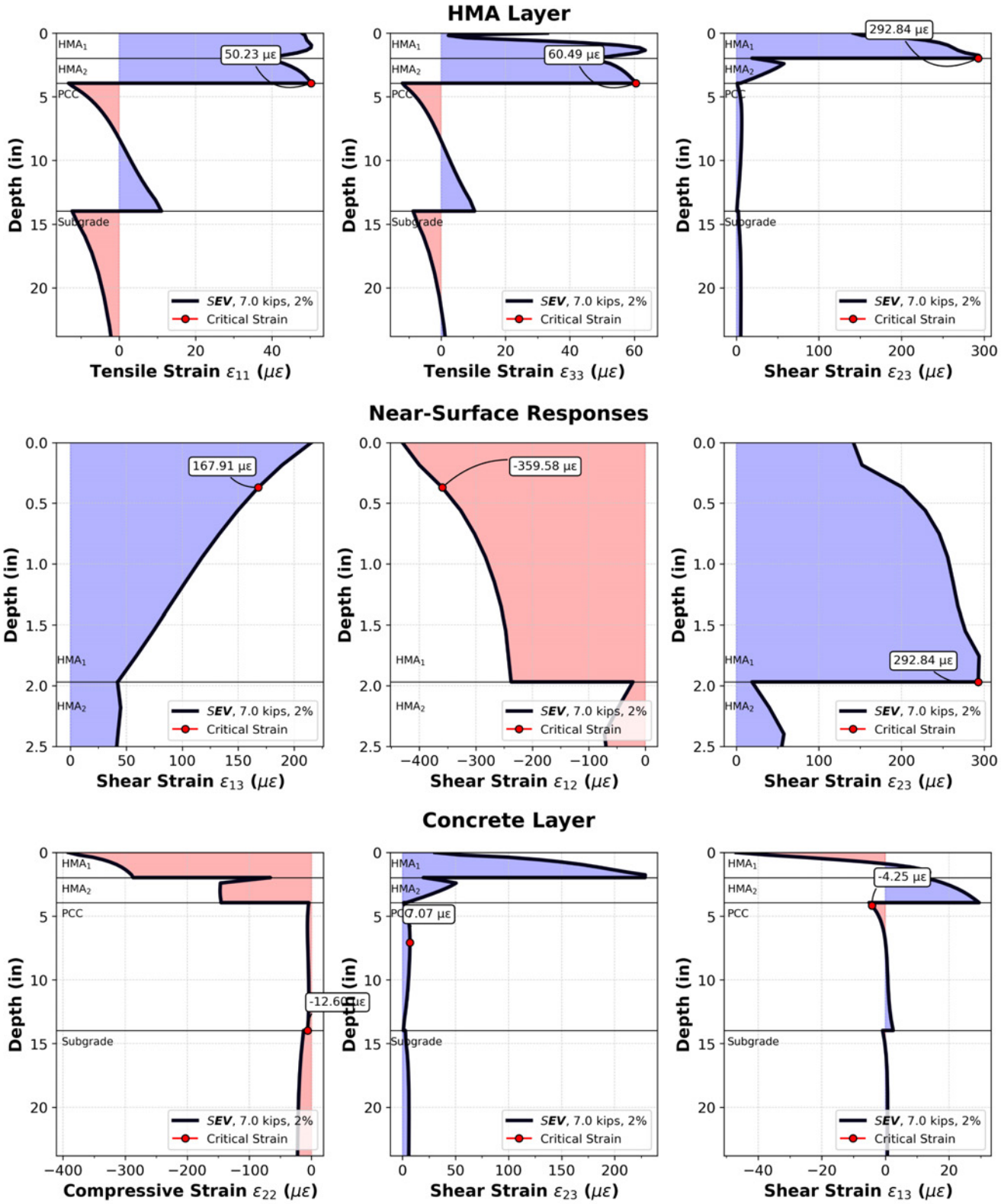

Figure 149. Graph. Summary of pavement responses of SMA overlay section to a 7.0-kip steering axle load (P5) at 2% slip ratio.

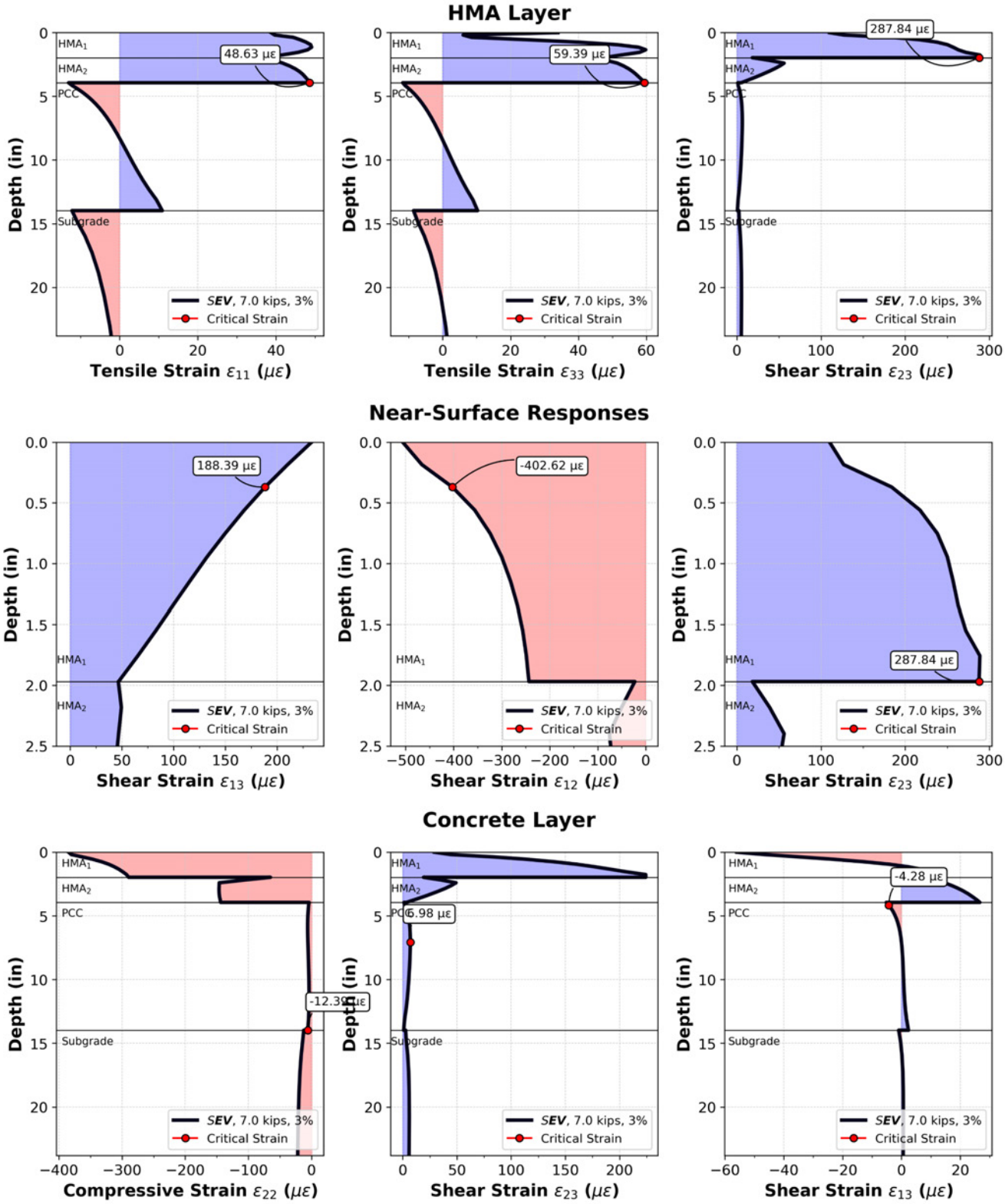

Figure 150. Graph. Summary of pavement responses of SMA overlay section to a 7.0-kip steering axle load (P5) at 3% slip ratio.

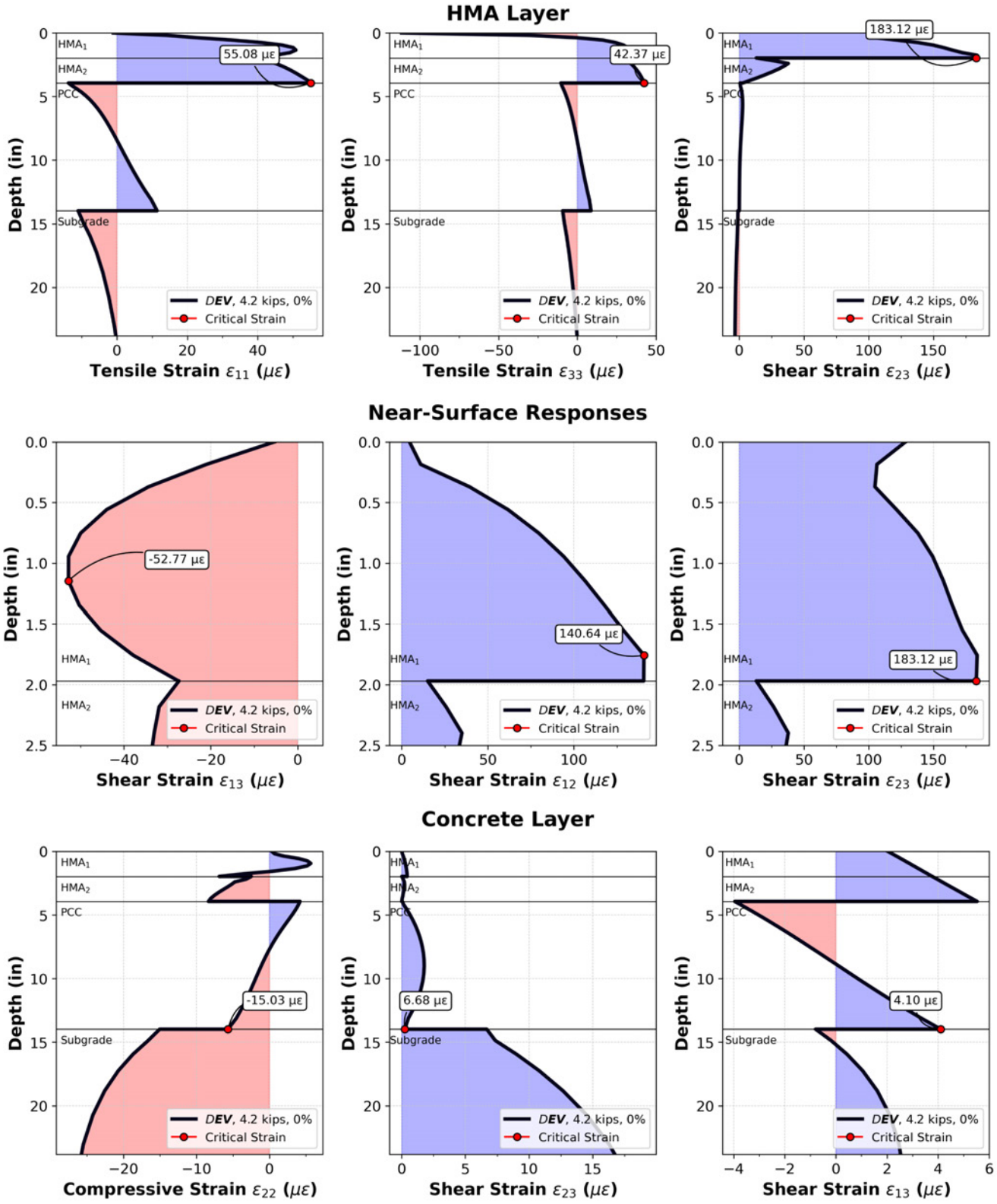

Figure 151. Graph. Summary of pavement responses of SMA overlay section to a 4.2-kip DTA axle load (P6) at 0% slip ratio.

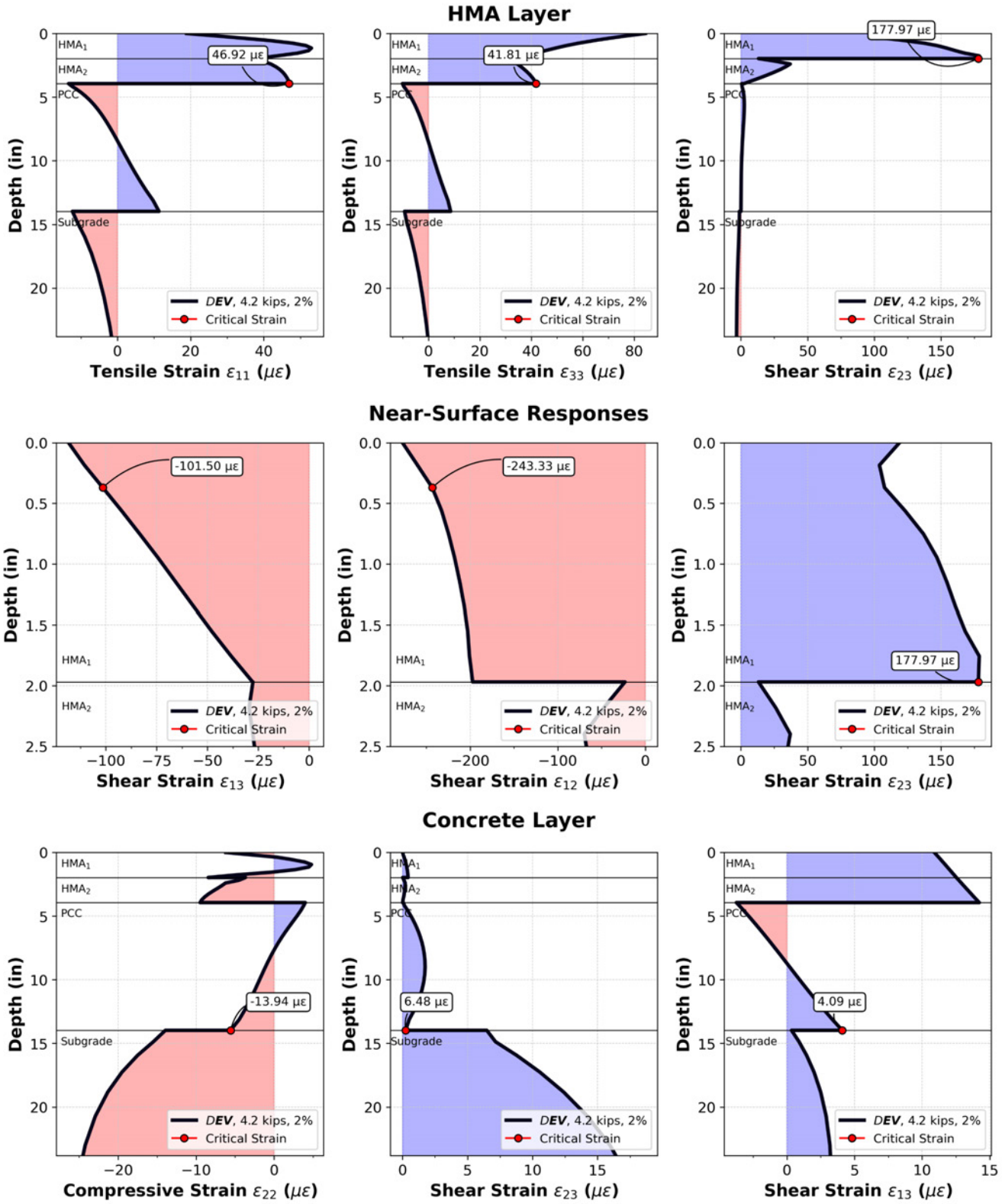

Figure 152. Graph. Summary of pavement responses of SMA overlay section to a 4.2-kip DTA axle load (P6) at 2% slip ratio.

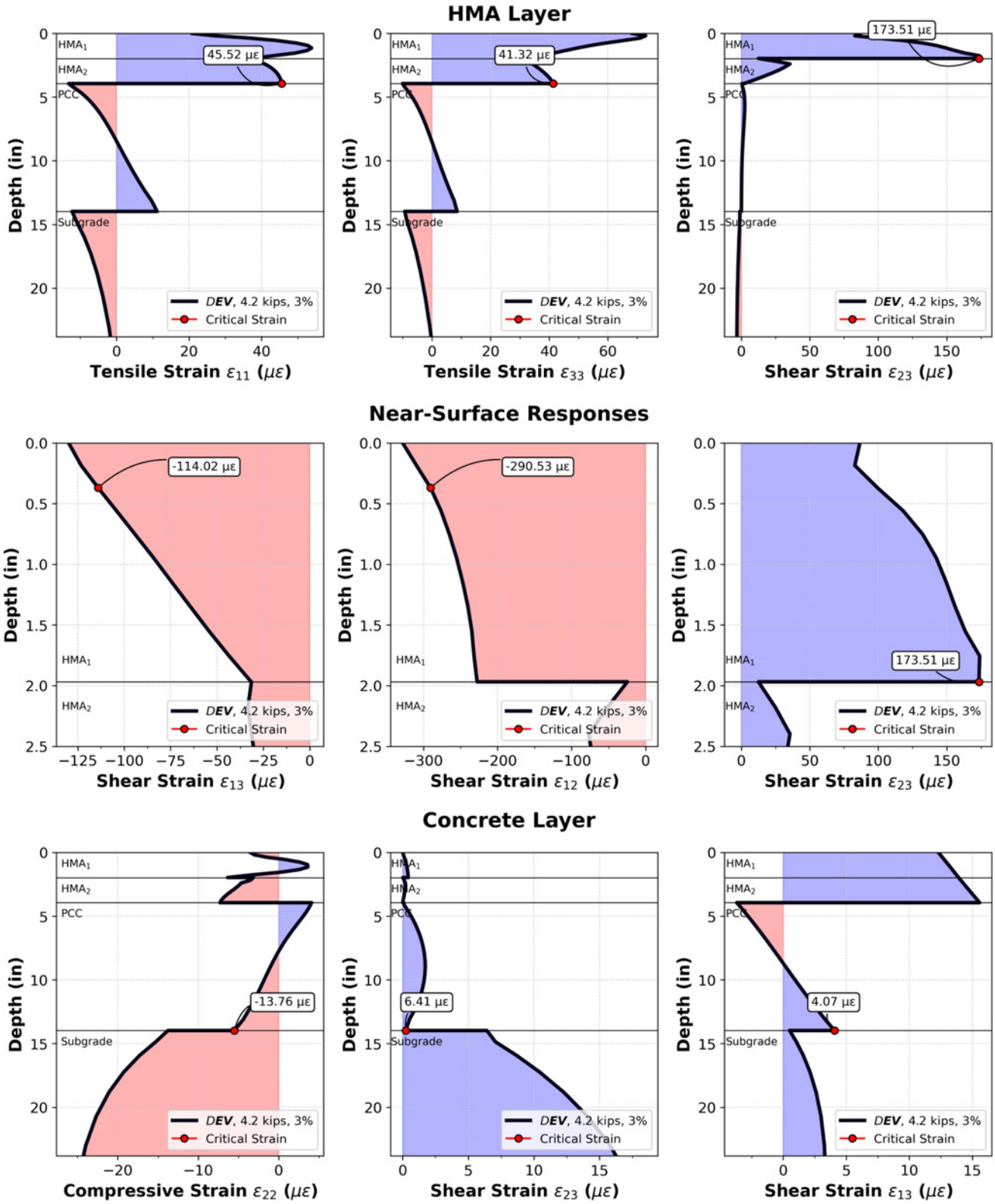

Figure 153. Graph. Summary of pavement responses of SMA overlay section to a 4.2-kip DTA axle load (P6) at 3% slip ratio.

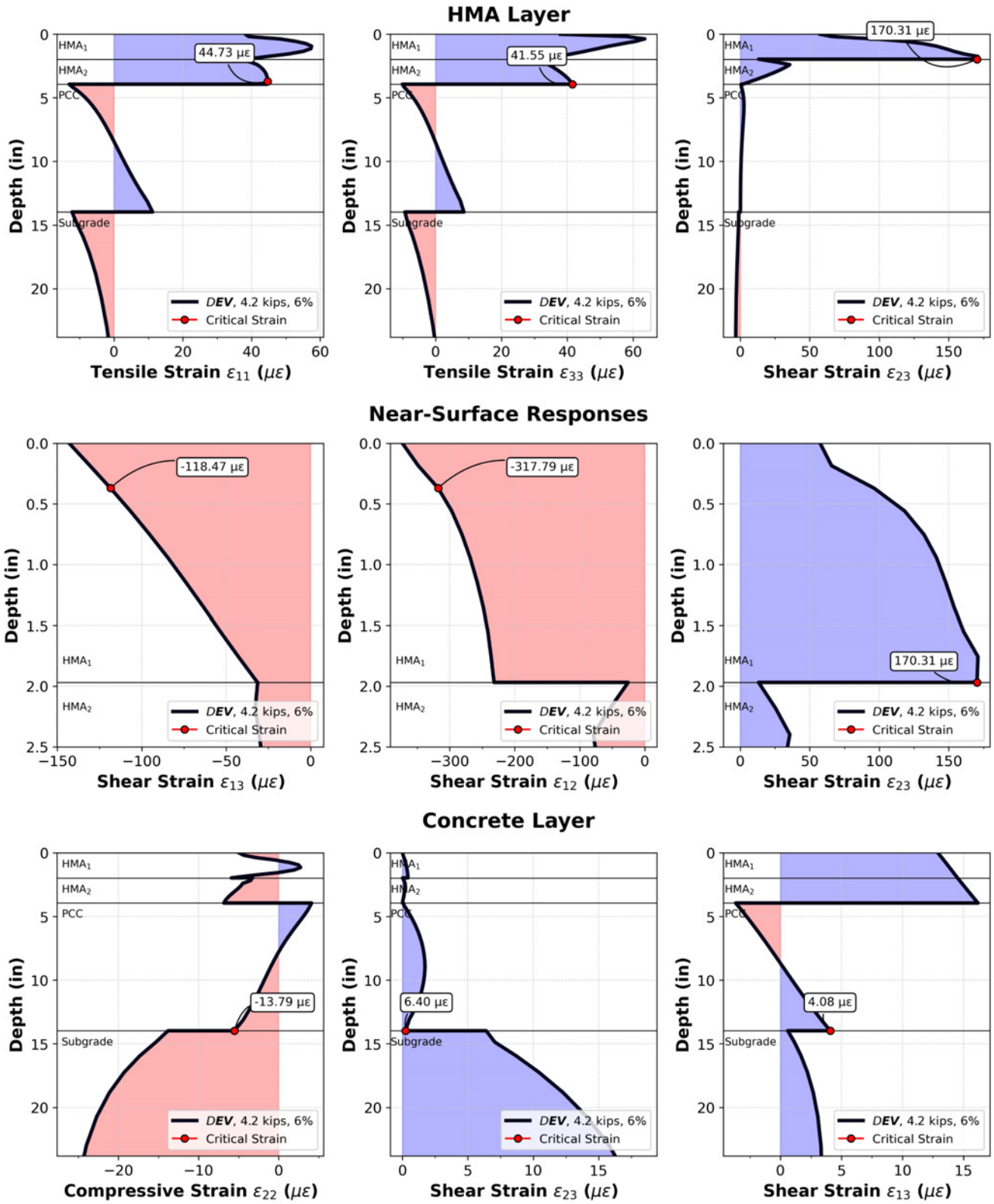

Figure 154. Graph. Summary of pavement responses of SMA overlay section to a 4.2-kip DTA axle load (P6) at 6% slip ratio.

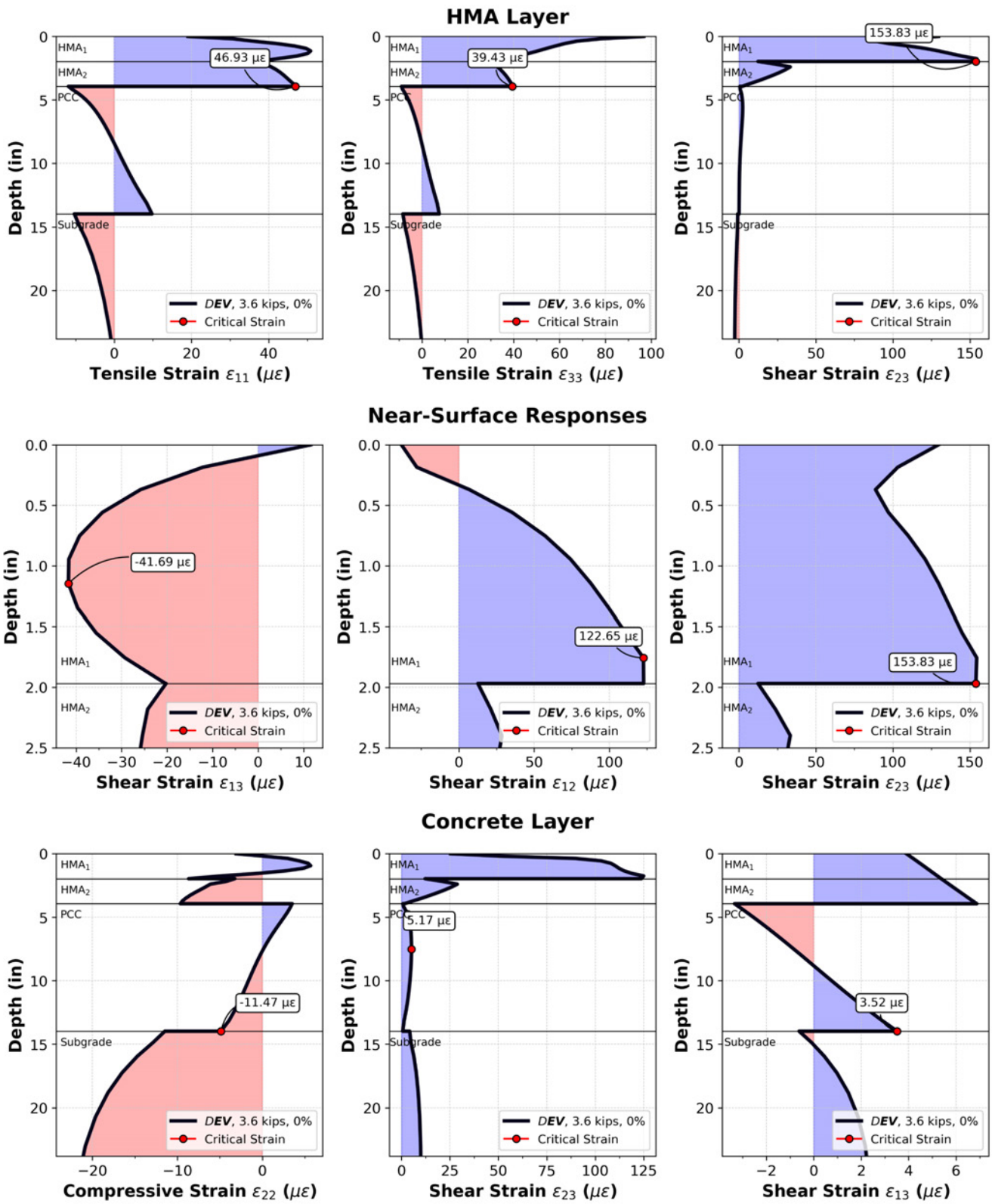

Figure 155. Graph. Summary of pavement responses of SMA overlay section to a 3.6-kip DTA axle load (P7) at 0% slip ratio.

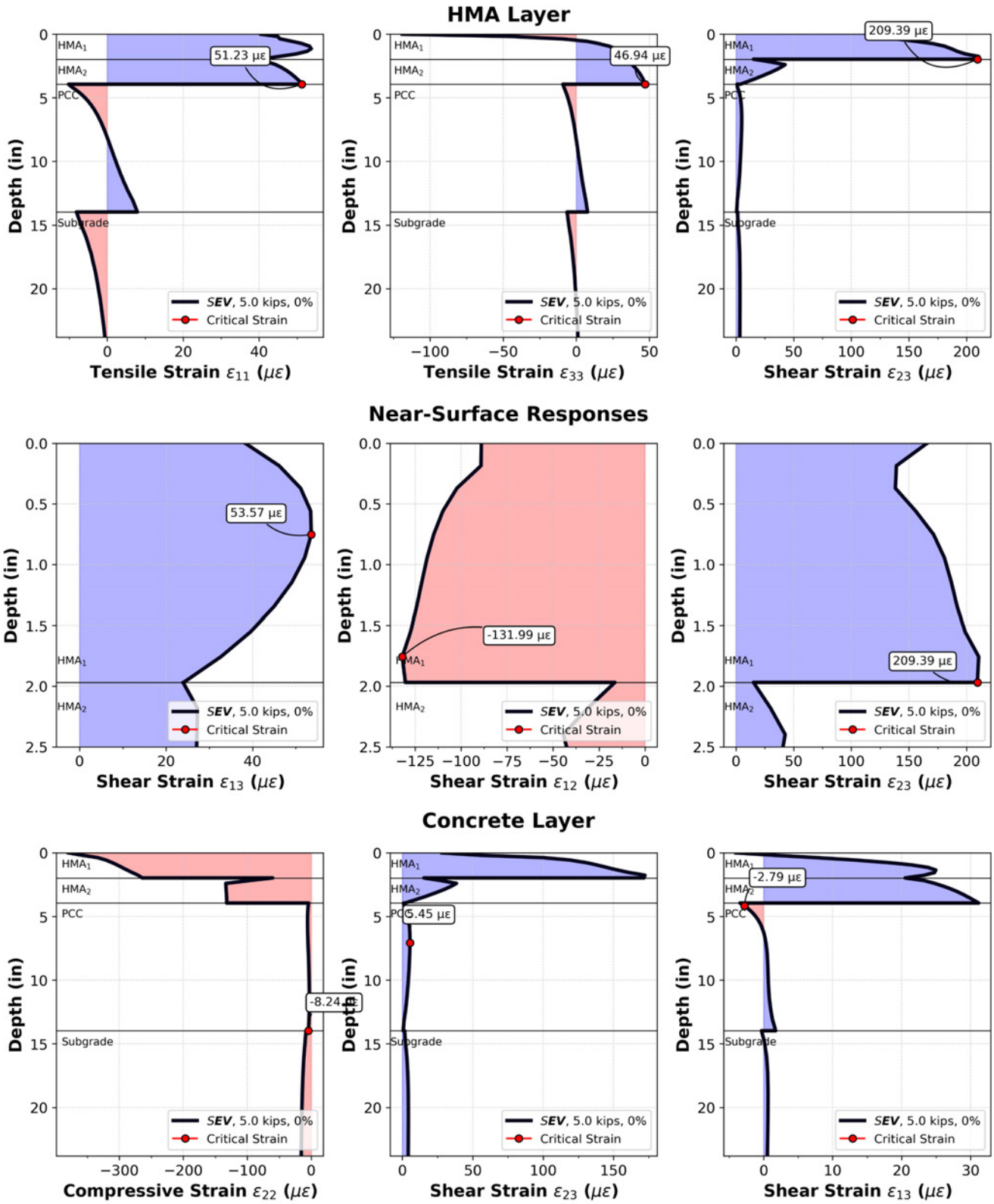

Figure 156. Graph. Summary of pavement responses of SMA overlay section to a 5.0-kip steering axle load (P8) at 0% slip ratio.

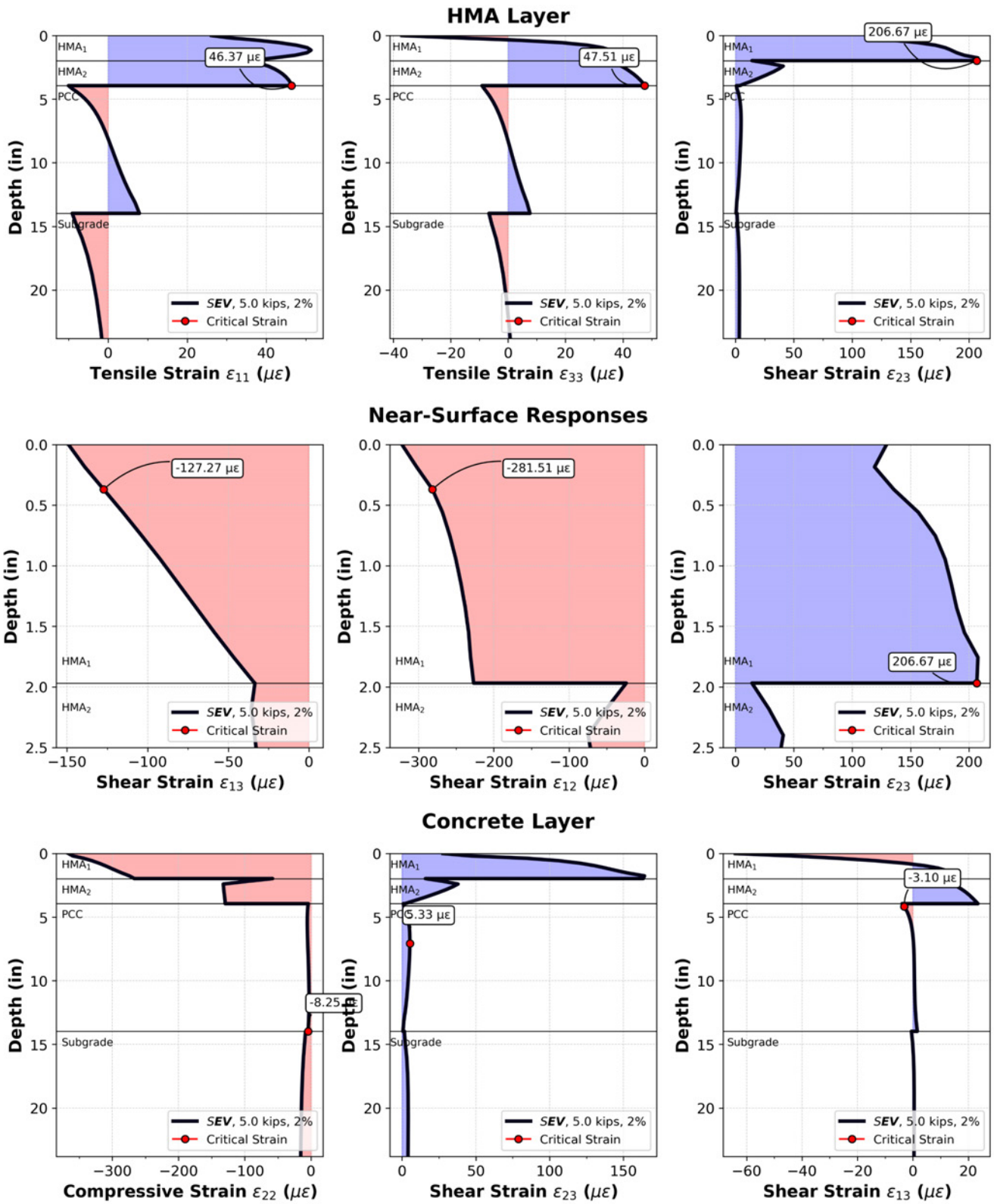

Figure 157. Graph. Summary of pavement responses of SMA overlay section to a 5.0-kip steering axle load (P8) at 2% slip ratio.

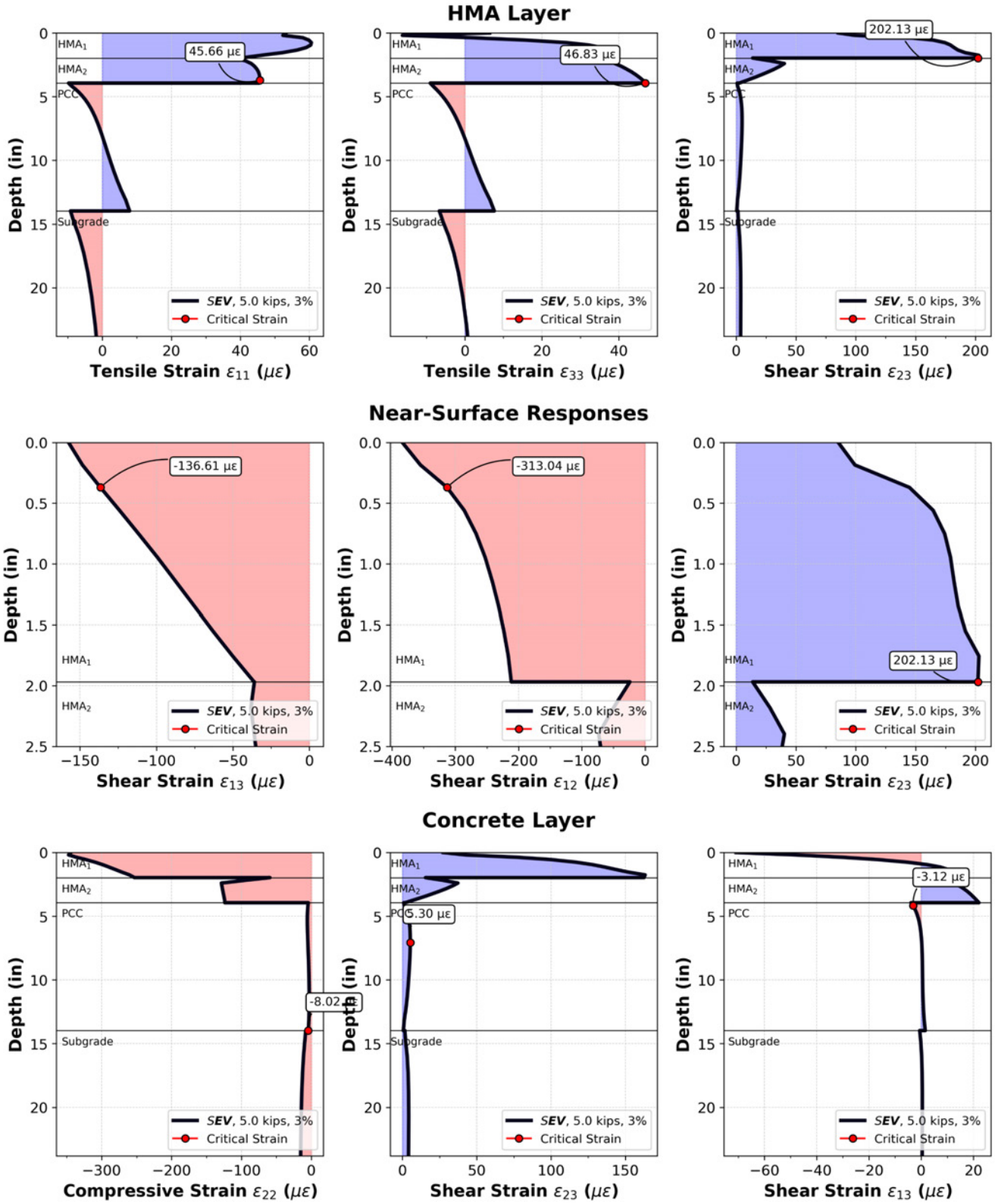

Figure 158. Graph. Summary of pavement responses of SMA overlay section to a 5.0-kip steering axle load (P8) at 3% slip ratio.


Illinois Department
of Transportation


ILLINOIS